OBSERVATIONS, DYNAMICS AND PREDICTABILITY OF THE

MESOSCALE CONVECTIVE VORTEX EVENT OF 10–13 JUNE 2003

A Thesis

by

DANIEL PATRICK HAWBLITZEL

Submitted to the Office of Graduate Studies of
Texas A&M University
in partial fulfillment of the requirements for the degree of

MASTER OF SCIENCE

May 2005

Major Subject: Atmospheric Sciences

OBSERVATIONS, DYNAMICS AND PREDICTABILITY OF THE

MESOSCALE CONVECTIVE VORTEX EVENT OF 10-13 JUNE 2003

A Thesis

by

DANIEL PATRICK HAWBLITZEL

Submitted to Texas A&M University
in partial fulfillment of the requirements
for the degree of

MASTER OF SCIENCE

Approved as to style and content by:

_____
Fuqing Zhang
(Chair of Committee)

_____
Craig Epifanio
(Member)

_____
John W. Nielsen-Gammon
(Member)

_____
Robert Hetland
(Member)

_____
Richard E. Orville
(Head of Department)

May 2005

Major Subject: Atmospheric Sciences

ABSTRACT

Observations, Dynamics and Predictability of the Mesoscale Convective Vortex Event of

10-13 June 2003. (May 2005)

Daniel Patrick Hawblitzel, B.S., University of Missouri – Columbia

Chair of Advisory Committee: Dr. Fuqing Zhang

This study examines the dynamics and predictability of the mesoscale convective

vortex (MCV) event of 10-13 June 2003 which occurred during the Bow Echo and

Mesoscale Convective Vortex Experiment (BAMEX). The MCV formed from a

preexisting upper-level disturbance over the southwest United States on 10 June and

matured as it traveled northeastward. The BAMEX field campaign provided a relatively

dense collection of upper air observations through dropsondes on 11 June during the

mature stage of the vortex. While several previous studies have focused on analysis of

the dynamics and thermodynamics of observed and simulated vortices, few have

addressed the ability to predict MCVs using numerical models. This event is of

particular interest to the study of MCV dynamics and predictability given the

anomalously strong and long-lived nature of the circulation and the dense data set.

The first part of this study explores the dynamics of this MCV through an in-

depth analysis of data from the profiler network and BAMEX dropsonde observations, in

addition to the conventional surface and sounding observations as well as radar and

satellite images. Next, issues relating to model performance are addressed through an

evaluation of two state-of-the-art mesoscale models with varying resolutions. It is

determined that the ability of a forecast model to accurately predict this MCV event is

directly related to its ability to simulate convection. It is also shown that the convective-

resolving Weather Research and Forecast (WRF) model with horizontal grid increments

of 4 km displays superior performance in its simulation of this MCV event. Finally, an

ensemble of 20 forecasts using mesoscale model MM5 with horizontal grid increments

of 10 km are employed to evaluate probabilistically the dynamics and predictability of

the MCV through the examination of the ensemble spread as well as the correlations

between different forecast variables among ensemble members. It is shown that after

MCV development, the ensemble mean performs poorly while individual ensemble

members with good forecasts of convection at all stages of the MCV also forecast the

midlevel vortex well. Furthermore, correlations among ensemble members generally

support the findings in the observational analysis and in previous literature.

ACKNOWLEDGMENTS

First and foremost, my sincerest thanks are owed to my advisor, Dr. Fuqing Zhang. This thesis would not have been possible without your support, both financial and intellectual. Thank you for you patience as I juggled my time between research, classes, friends and family, and of course storm chasing. I am very appreciative of the time you dedicated to me and my work, and for your guidance. I would also like to thank my other committee members, Dr. John Nielsen-Gammon, Dr. Craig Epifanio and Dr. Robert Hetland for their expertise and assistance both in and outside of the classroom, to which I owe much of my knowledge and understanding of science, which served as a backbone to this thesis. A special thanks to Dr. Nielsen-Gammon for his extra last-second help for this thesis over the Easter holiday weekend.

I want to thank my wonderful parents, Warren and Patti Hawblitzel for your infinite support throughout my time at Texas A&M. Thank you for making sure I never went bankrupt and that my desk drawer was always full of sweets to keep me going through the day. Also thanks to my sister Meggie.

A giant thanks to my friends at Texas A&M who made my time here unforgettable. The wonderful friends I met here are too many to list, but I especially want to thank Chrissy Smith for your unending friendship and support, and for walking beside me through my journey at Texas A&M from the day we met at orientation to defending our theses on the same day. Thank you to all those who kept my spirits alive throughout my time in Aggieland. I also want to thank my labmates Altug Aksoy,

TABLE OF CONTENTS

Page

LIST OF FIGURES

FIGURE   Page

FIGURE   Page

FIGURE   Page

FIGURE   Page

CHAPTER I

INTRODUCTION

1.1. Case summary

On the evening of 10 June 2003, a severe mesoscale convective system (MCS) moved across Oklahoma and formed a significant region of stratiform precipitation behind it. Within a few hours, rotation became evident within this stratiform rain region, signifying the development of a mesoscale convective vortex, or MCV. As this midlevel vortex persisted through the afternoon of 11 June and moved into the lower Ohio Valley, severe convection initiated in and near the MCV circulation. In addition, a relatively strong surface cyclone developed beneath the MCV circulation over the Ohio Valley during the evening of 11 June. The circulation remained evident on satellite and radar through early on 14 June over western New York state, making it a rare long-lived MCV event. Such long-lasting MCVs have been linked to severe weather episodes and severe flooding events, such as the Johnstown (PA) flooding event of 1977 (Bosart and Sanders, 1981). One of the most interesting aspects of an MCV is its ability to regenerate convection, and in turn increase both its intensity and duration. However, since the longevity of an MCV circulation itself is highly dependent on secondary convection and its feedback, the current ability to predict such long-lived MCVs is still in question.

This thesis follows the style and format of *Monthly Weather Review*.

The MCV of 11 June 2003 is of particular interest because it occurred during the Bow-Echo and MCV Experiment, or BAMEX, which was conducted from 20 May to 6 July 2003 at the Mid-America Regional Airport near St. Louis, Missouri (Davis et al., 2004). One of the main goals of this experiment was to better understand the lifecycle of MCVs, including the development of an MCV within a parent MCS, its role in triggering convection during the subsequent diurnal cycle , the feedback of such convection onto the MCV, and the overall predictability of MCVs and related convection. To capture the thermodynamic structure of MCVs and their parent MCSs, a Learjet equipped with dropsondes was used to explore such systems that formed in the BAMEX domain, which covered an area extending roughly 1000 km in each direction from Mid-America Regional Airport. The MCVs sampled by the BAMEX campaign were the first to have an available dense sounding data set. The dropsonde data has provided a detailed look at MCV circulations that was previously only available through satellite, radar and numerical simulations. Five mature MCV cases were documented during BAMEX, with the 11 June MCV, hereafter referred to as the BAMEX IOP (Intense Observation Period) 8 MCV, being the most intense and longest-lived MCV case.

1.2 Background on MCVs

1.2.1 Potential vorticity

For a column in the atmosphere, potential vorticity (PV), expressed as the ratio of

vorticity to the height of that column, is constant following the fluid column (Rossby, 1940), such that

$$P = (f + \zeta_\theta)/\Delta = \text{constant},\tag{1.1}$$

where P represents potential vorticity, ζ_θ is the isentropic vorticity and Δ represents layer thickness as $\Delta = -\delta p/g$. By assuming a frictionless and adiabatic system and using the hydrostatic approximation in a manner similar to Ertel (1942), Eq. 1.1 can be rewritten as,

$$P = -g(f + \mathbf{k} \cdot \nabla_\theta \times \mathbf{v})/(\partial p/\partial \theta),\tag{1.2}$$

where P is referred to as Ertel potential vorticity, or EPV, although this paper will maintain the term "potential vorticity" for this variable. In other words, potential vorticity is defined as the product of isentropic vorticity and the vertical stratification of isentropic surfaces. Since this value remains constant in an adiabatic process, it follows that as isentropic surfaces become vertically separated, the atmosphere responds with increased vorticity in that layer.

1.2.2. Convection and potential vorticity

The nature of PV in a non-adiabatic atmospheric process, such as in the case of convective latent heating, is particularly important to the evolution of an MCV. Several studies (e.g. Haynes and McIntyre, 1987; Thorpe, 1985; Raymond and Jiang, 1990) showed that latent heat release in the mid troposphere acts to redistribute potential vorticity such that a positive PV anomaly develops below the area of latent heating and a negative anomaly above it (Fig. 1.1). Since increased potential vorticity yields lower
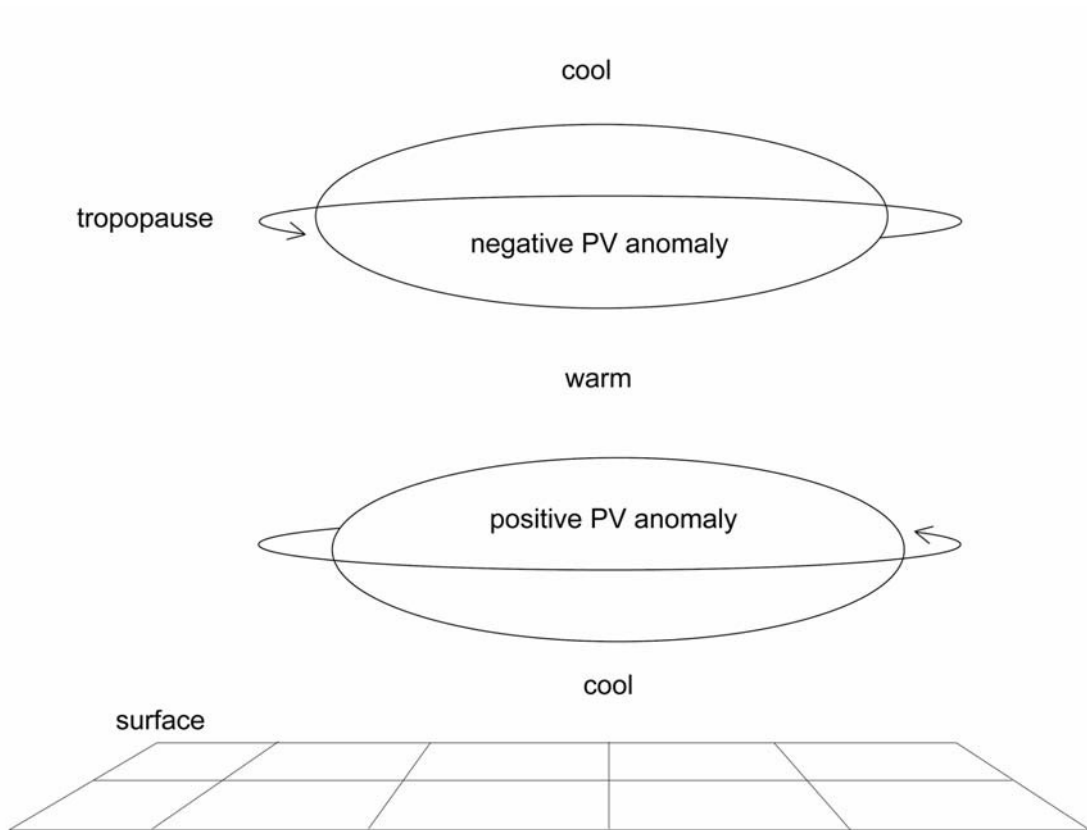
FIG. 1.1. Postulated structure of potential vorticity anomalies produced by a region of convection and the associated changes in temperature and wind structure. Adapted from *Raymond and Jiang* [1990].

 heights (Rossby, 1940), balanced winds respond by circulating cyclonically around a

positive potential vorticity anomaly and anticyclonically around a negative anomaly.

Thus, widespread convection would theoretically yield increased potential vorticity and

a resulting cyclonic circulation in the lower troposphere, and decreased potential

vorticity and anticyclonic rotation in the upper troposphere. Consistent with this model,

Raymond and Jiang (1990) idealized MCVs as potential vorticity anomalies induced by

convective latent heating in the mid troposphere (Fig. 1.1). This theoretical dynamic and

thermodynamic MCV structure has been well documented by both observational studies

and numerical simulations (e.g., Bosart and Sanders, 1981; Zhang and Fritsch, 1986;

Bartels and Maddox, 1991; Trier et al., 2000a; Rogers and Fritsch, 2001).

1.2.3. Preexisting vorticity and MCV formation

For the Raymond and Jiang (1990) PV mechanism to take place, the convective

heating must result in a net warming of the atmosphere so that a balanced atmospheric

response results through a lowering of height and an adjustment to the wind field. This

process will be favored when the reduction of the local Rossby radius of deformation,

defined as the final horizontal length scale over which the height field must adjust to

reach equilibrium (Holton, 1972), is reduced to a scale comparable to, or smaller than,

the horizontal scale of convective heating (Rogers and Fritsch, 2001). The local Rossby

radius is given by,

$$L_R = \frac{NH}{f + \zeta}, \tag{1.3}$$

where N is the Brunt-Väisälä frequency and H is the scale height of the disturbance. Thus, the local Rossby radius will be lowered in an area of strong environmental vertical vorticity, such as a midlevel shortwave. Schubert et al. (1980) confirmed that diabatic heating will be more efficient in creating a net warming of the atmosphere when convection initiates in a region of existing ambient vorticity.

Several additional studies have investigated the importance of the merging of small-scale PV perturbations into one larger disturbance (e.g. Ritchie and Holland, 1997; Davis and Bosart, 2001). These studies illustrated the importance of a preexisting disturbance that organizes convection and acts to focus the resulting PV anomalies. The merger of several PV perturbations can result in a much larger-scale, cohesive PV anomaly which will in turn be associated with a more significant balanced response from the atmosphere (Davis and Bosart, 2001). These studies illustrate the importance a preexisting vortex can have on the eventual development of an MCV through the lowering of the local Rossby radius and the role as a focusing mechanism for convectively-induced potential vorticity perturbations.

1.2.4. Vorticity analysis

Kirk (2003) further examined the dynamical evolution of mesoscale convective vortices by separating the vertical vorticity equation into terms representing horizontal vorticity advection, vertical vorticity advection, convergence, tilting, and vorticity transfer through friction. By examining the contribution of each term to simulated vortex development of two MCVs, he found that there is not a specific method by which

MCV formation takes place. His numerical simulations showed that the rotation in one MCV was initiated by the tilting term and was further intensified by convergence acting on vorticity at all levels. Another MCV case was initiated by low-level convergence followed by vertical advection of vorticity at mid-levels.

In addition to Kirk (2003), numerous other studies have diagnosed vortex development within an MCS through studies of various MCVs, yielding differing results. Chen and Frank (1993) predicted that vortex tilting is responsible for initial circulation growth at mid-levels, and this region of maximum vorticity descends with time. Zhang and Fritsch (1988) showed that low-to-midlevel convergence was primarily responsible for MCV growth. They predicted that latent heat release creates a vortex at low-levels and this vortex is expanded upward through convergence. Olsson and Cotton (1997) similarly theorized that latent heat release initiated the vortex at lower levels, however they speculated that tilting became the dominant term after vortex initiation and that convergence was insignificant. Bartels and Maddox (1991) predict that to a first approximation, MCV development can be explained via simple quasigeostrophic theory, specifically convergence acting on planetary vorticity. The disparity in the above studies shows how complex MCV formation is, and suggests that MCVs can potentially form in a variety of ways.

1.2.5. Low-level vortex growth and secondary convection

Many studies have shown that convection near an MCV center has significant amplification effects (e.g. Tracton 1973; Ritchie and Holland 1997; Montgomery and

Enagonio 1998). In fact, as described by Trier et al. (2000b), secondary convection is crucial in extending the lifetime of an MCV. Convective heating in the midlevels of the atmosphere can work to increase the amplitude of an existing PV anomaly if the convection occurs coincident with it, or it can produce a new MCV altogether. Since the magnitude of the warm core increases, the balanced response is to further lower the heights beneath the warm anomaly, where PV would increase (Raymond and Jiang, 1990). Furthermore, Rogers and Fritsch (2001) provide an alternate explanation of this process through an examination of the hypsometric equation as written in Hirschberg and Fritsch (1991):

$$\frac{\partial z(p_b)}{\partial t} = \frac{R}{g} \int_{p_b}^{p_t} \frac{\partial T_v}{\partial t} d \ln p, \tag{1.4}$$

where T_v is virtual temperature, p_b and p_t are two arbitrary pressure levels, with p_t high enough such that $\partial z(p_t)/\partial t = 0$. Thus warming in the middle troposphere would yield lower heights at the bottom of the layer of warming. A resulting balanced cyclonic circulation and convergence can then develop or intensify at the surface. In extreme cases, this convectively-enhanced surface convergence can further escalate convection, in turn lengthening the lifetime of an MCV. Such a process may have been a factor in the long duration of the BAMEX IOP 8 MCV.

Past studies have shown that another important factor in vortex intensification is the type of precipitation produced in the circulation center (Anthes et al. 1983; Gyakum 1983). Due to locations of vertical velocities, MCS-related stratiform precipitation tends to focus latent heating in the middle troposphere, while convective processes distribute

latent heating into the lower troposphere (Hertenstein and Schubert 1991, Houze et al. 2004; Fig. 1.2). Rogers and Fritsch (2001) found that vortex penetration to the surface was most favorable when latent heating was focused in the lower troposphere. Eq. 1.4 suggests that heating in the lower troposphere will lower heights below that layer, which may be very near the surface. Thus, convection close to the vortex center would be most favorable for a strengthened low-level vortex and surface cyclone development.

Another factor leading to vortex intensification at the surface is the reduction of static stability in the lower levels. Hoskins et al. (1985) write the vertical influence of a PV perturbation as

$$D = \frac{(f_{loc}\zeta_a)^{1/2}L}{N},$$
(1.5)

where D is the vertical influence of a PV perturbation, L is the horizontal scale of the perturbation, and f_{loc} is a local background rotation term. The depth of a vortex will increase when the horizontal scale of a disturbance is increased (Holton, 1972), as can happen with mergers of smaller PV anomalies (Davis and Bosart, 2001) or by the addition of convective heating. The vertical penetration will also be increased when local stability is decreased, and when this reduction occurs in the lower troposphere, vortex penetration to the surface will be enhanced. Such a reduction in lowlevel stability can result from a weakening of a surface cold pool or moistening of lowlevels to a moist adiabatic thermodynamic profile through vertical motions, or the creation of a lowlevel adiabatic thermal profile through time-averaged lifting in the boundary layer (Rogers and Fritsch, 2001).
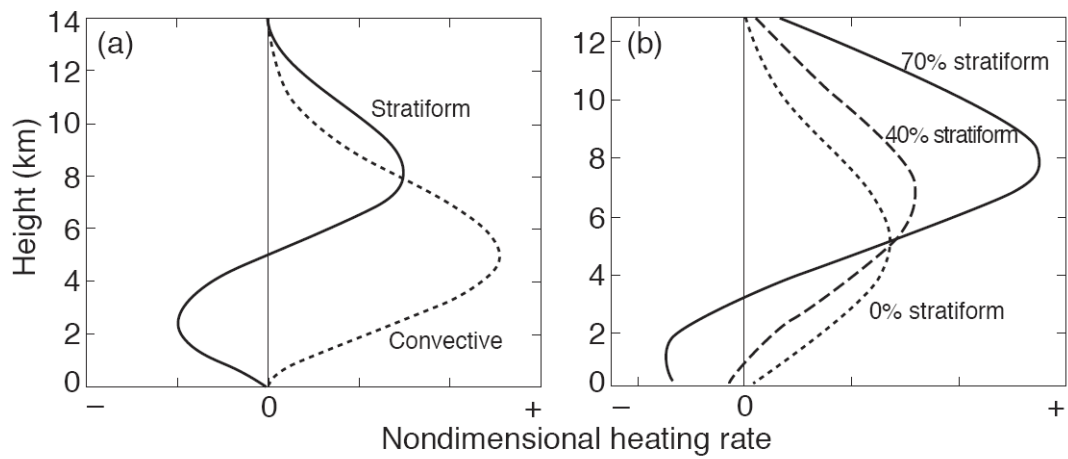
FIG. 1.2. (a) Idealized profiles of net heating associated with convective and stratiform precipitation in a mesoscale convective system. The x-axis is nondimensional until precipitation amounts are specified for the convective and stratiform regions. (b) Profiles of net heating by a mesoscale convective system with different fractions of stratiform precipitation. From *Houze et al.* [2004].

1.2.6. Vertical displacements and instability

Secondary convection, and thus a long-lived MCV, is most favored in an environment of moderate to high instability (Trier et al., 2000b). Absolute thermodynamic instability will be achieved when a conditionally unstable source layer is sufficiently saturated so as to eliminate the distance between the source level and the LFC, resulting in an elimination of convective inhibition. Vertical displacements greatly affect the destabilization that occurs within a vortex and can lead to convective redevelopment. Trier et al. (2000b) noted that time integrated vertical lifting is anticipated to be one of the most important factors in convective redevelopment.

Trier et al. (2000b) found that secondary convection typically occurs downshear, near the outer periphery of the MCV circulation. As noted by Raymond and Jiang (1990), the downshear side of an MCV is usually characterized by isentropic ascent, with descent on the upshear side. Trier et al. (2000b) further found that the ascent was usually strongest near the radius of maximum winds. Additionally, a thermally-direct solenoidal circulation can exist at the edge of a cloud shield or surface cold pool, which Trier et al. (2000b) speculated would enhance upward motion on the downshear periphery of an MCV. This effect, combined with any remnant outflow boundaries ahead of an MCV, would favor convection along the outer periphery of an MCV circulation. Convection was found to usually shift upshear toward the MCV center during the evening and overnight hours. Through numerical simulation, Trier et al. (2000b) proposed that several hours of vertical displacements downshear of an MCV combined with vertical tilt would bring conditionally unstable air from the downshear

quadrant to a region above the vortex center later in the day, creating an absolutely

unstable airmass conducive to late evening convection near the center and thus further

strengthening the vortex. Several other complicating factors, such as the diurnal

temperature cycle, synoptic fronts and the low-level jet may help determine when and

where secondary convection occurs.

Considering the potential vorticity structure of an MCV, two upglide/downglide

possibilities within a PV anomaly can be considered, as illustrated by Raymond and

Jiang (1990) and given in Fig. 1.3. The first possibility is that ambient shear acts on PV-

induced slanted isentropes to produce isentropic upglide. The second possibility is a

PV-induced circulation acting on ambient isentropes. Raymond (1992) also noted that

vertical motion may arise as shear-induced changes in the PV distribution influence

isentropic surfaces in lower levels. This mechanism has yet to be confirmed through

detailed observational data, but was demonstrated by numerical simulations of Trier et

al. (2000b), who showed that the greatest such vertical displacements within an MCV

range from downshear for a moderate MCV to 90 degrees to the left of downshear for a

strong MCV in weak shear. Fritsch et al. (1994) provided a more detailed theory of

isentropic influence from an MCV and this concept is illustrated in Fig. 1.4.

Trier et al. (2000b) showed that instability is increased in the downshear portion

of an MCV, and greatly decreased upshear. Cyclonic low-level circulation will usually

advect colder air into the upshear side, which lowers the mean theta-e of the boundary

layer and thus reduces instability. Subsidence behind the MCV warms the atmosphere

above the boundary layer which further increases convective inhibition (CIN). The
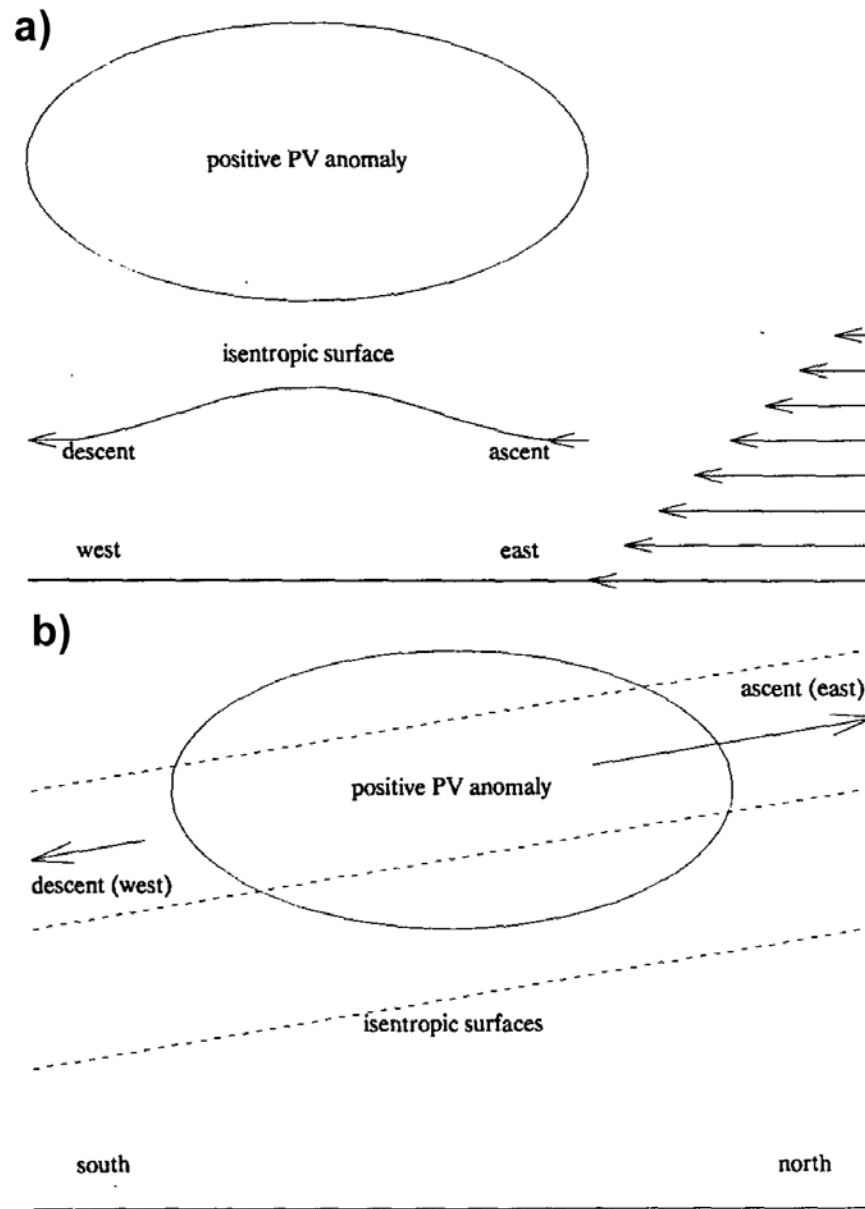
FIG. 1.3. Sketches of mechanisms by which lifting might occur in the presence of a potential vorticity anomaly in shear. The ambient shear is confined to the east-west plane. (a) Ambient shear is limited to below the potential vorticity anomaly here for clarity. In a frame in which the anomaly is stationary, the relative environmental wind causes flow on the perturbation isentropic surface caused by the potential vorticity anomaly. Ascent and descent occurs as illustrated. (b) View of the potential vorticity anomaly from the east. The tilted isentropic surfaces (dashed lines) are associated with uniform ambient westerly shear through the depth of the illustration. The cyclonic circulation around the anomaly causes ascent in the northward-moving air on the east side and descent in the southward-moving air on the west side as illustrated. From *Raymond and Jiang* [1990].
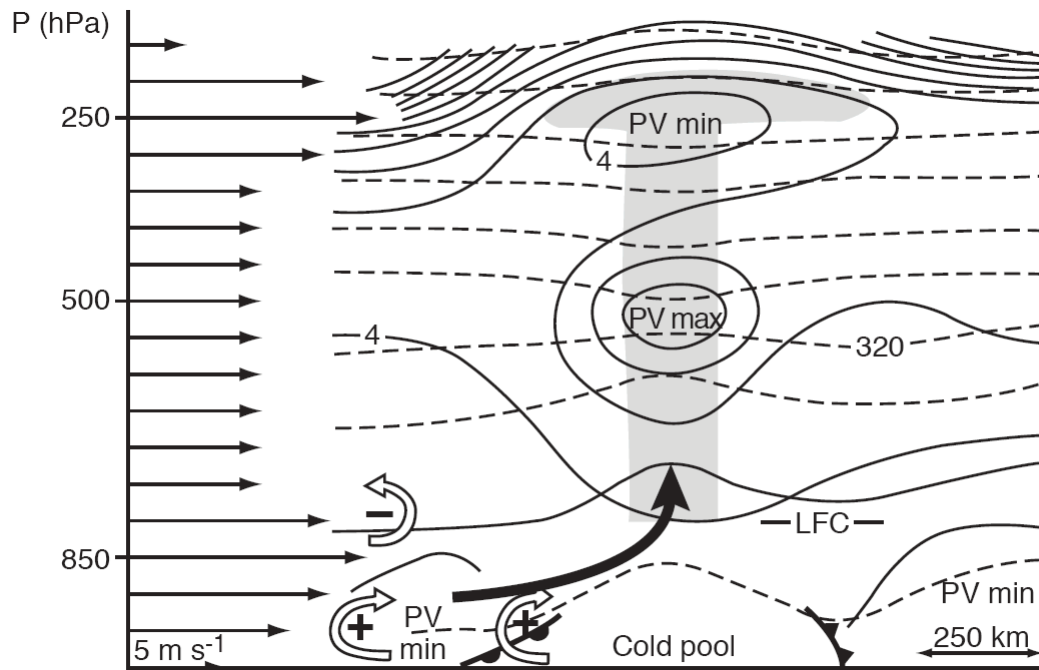
FIG. 1.4. Conceptual diagram of the structure and redevelopment mechanism of a mesoscale warm core vortex associated with an MCS. Thin arrows along the ordinate indicate the vertical profile of the environmental wind. Open arrows with plus or minus signs indicate the sense of the vorticity component perpendicular to the plane of the cross section produced by the cold pool and by the environmental vertical wind shear. The thick solid arrow indicates the updraft axis created by the vorticity distribution. Frontal symbols indicate outflow boundaries. Dashed lines are potential temperature (5 K intervals) and solid lines are potential vorticity (2×10^{-7} m^2 s^{-1} K kg^{-1} intervals). The system is propagating left to right at about 5-8 m s^{-1} and is being overtaken by air of high equivalent potential temperature in the low-level jet. Air overtaking the vortex ascends isentropic surfaces, reaches its level of free convection (LFC), and thereby initiates deep convection. Shading indicates cloud. From *Fritsch et al.* [1994].

opposite holds true in the downshear side of an MCV circulation which is typically characterized by persistent mesoscale lifting and vortex-induced warm air advection in the lower levels. In addition, larger vortices are more likely to be associated with atmospheric destabilization because of greater magnitude and depth of upward displacements. The time-averaged lifting acts to shift the vertical thermodynamic profile in the boundary layer toward adiabatic and thus decrease low level stability. Trier et al. (2000b) further proposed that the most significant role of the mesoscale lifting downshear may be to saturate the ~1 km deep layer above the mixing layer. This air becomes absolutely unstable and does not require additional forcing for convection to occur, unlike the conditionally unstable boundary layer below it. Additionally, Rogers and Fritsch (2001) note that such moist ascent can result when a low-level jet of high theta-e air is forced to rise over a surface cold pool. As the moist air within the low-level jet ascends, it moistens the layer above the boundary layer which can lead to an absolutely unstable layer above the surface cold pool.

Trier et al. (2000b) also found through simulation that vortex tilting can favor atmospheric destabilization and convective redevelopment near the vortex center. Numerical studies (Davis and Weissman 1994; Olsson and Cotton 1997) have identified an MCV as a feature in which potential temperature and vertical vorticity are quasi-balanced, with a warm core structure in the middle and upper troposphere and cold core structure in the lower troposphere, as well as near the tropopause (Zhang and Fritch 1987). Thus, as ambient shear tilts the vortex, it would theoretically remain balanced through the displacement of its associated upper level negative temperature anomaly

away from the center of circulation in the direction of vortex tilt (Raymond 1992). This process places the upper-level cold anomaly over an area of higher theta-e air on the downshear periphery of the vortex, thus furthering instability in that region.

1.2.7. Ambient shear

Trier et al. (2000a) performed a climatological study of MCV environments. They found that most long-lived MCVs occurred in environments of weak shear, both in the lower troposphere and through the vortex layer. Although shear helps to sustain secondary convection, it also works against a vortex by tilting and weakening it. Trier et al. (2000b) showed that the most critical factors for determining vortex longevity, aside from secondary convection, are its aspect ratio, L/H, and the strength of the ambient vertical shear, $\partial u/\partial z$. An approximate vortex timescale can be derived by taking the ratio of these two parameters, yielding $\tau \sim L/\Delta U$. Thus, they proposed that vortex longevity is favored in cases of broad vortices and/or vortices occurring in weak shear. Broad vortices are especially favored because they induce greater vertical displacements and generally penetrate deeper into the lower atmosphere, where the source layer for vertical motion comes from higher theta-e air in the boundary layer. Also, vertical shear will not tilt a vortex enough such that warm subsided air on the upshear flank would overlie saturated unstable air in the lower levels downshear, as could happen with a smaller vortex or a medium-sized vortex in strong shear.

While significant vertical displacement has been found to occur within small vortices in strong shear, Trier et al. (2000b) found that the maximum displacement

occurs with strong vortices in average shear. Since shear can act to reduce stability and favor upward displacements through balanced lifting, it was speculated that at least some ambient shear is needed to favor secondary convection. They also noted that stronger shear yields a smaller vortex, which in turn yields weaker vertical motion and is least favorable for convection. They concluded that for this reason, secondary convection is less likely to occur in strongly sheared or very weakly sheared environments.

1.3. Background on ensemble forecasting and mesoscale predictability

The high sensitivity of an MCV to convective processes has serious impacts on predictability. It was demonstrated by Zhang et al. (2002, 2003, 2005) that small-scale error in the presence of moist convection can significantly impact mesoscale predictability due to strong upscale error growth, similar to that forseen by Lorenz (1969). Because of this uncertainty, Buizza and Chessa (2002) note the significance of including stochastic perturbations in the global ensemble prediction system at the European Center for Medium-Range Weather Forecasts (ECMWF). It has been documented that prediction skill can be significantly improved when data assimilation techniques account for uncertainties in initial conditions, including the specifications of background error covariance (e.g. Cohn and Parrish 1991; Daley 1992; Evensen 1994; Cohn 1997; Talagrand 1997). For this reason, ensemble forecasting was introduced as a considerable step in improving the state of numerical weather prediction (Tracton and Kalnay 1993; Molteni et al. 1996; Toth and Kalnay 1997). As a set of forecasts generated through different stochastic perturbations among initial conditions, ensemble

forecasting not only promises the best estimate of the future atmospheric state, it also

details uncertainties associated with the best estimate and provides valuable information

for estimating the flow-dependent background error covariance (Evensen 1994).

Zhang (2005) introduced an investigation into the dynamics and structure of

mesoscale error covariance in an explosive extratropical cyclogenesis event. He

demonstrated that underlying balanced dynamics and effects of moist convection

determined the characteristics and structure of error growth. Through analysis of error

covariance structure, relationships among several atmospheric variables and processes

can be further investigated. However, few studies have applied this technique to

investigate error covariance structure in a small scale event highly dependent on

convective processes, such as an MCV.

1.4. Objectives and methodology

The primary objective of this study is to provide further insight into the dynamics

and predictability of mesoscale convective vortices through a case study of the BAMEX

IOP 8 MCV. This objective will be carried out in three parts. First, the structure and

kinematics of the IOP 8 MCV will examined using observations, including the relatively

dense upper-air data set acquired through the BAMEX campaign. Next, the MCV will

be put to a more detailed dynamic analysis through deterministic numerical simulations.

The theoretical literature regarding MCV dynamics in section 1.2 will be used as a

framework in diagnosing the dynamics of the IOP 8 MCV. Finally, ensemble forecasts

will be employed to provide an alternate assessment of the dynamics of the MCV, as

well as to provide a statistical test of both the MCV-related theories presented by previous literature and the conclusions reached through the analyses of observations and deterministic forecasts in this paper. Further detail regarding the numerical models employed for this study is given in Chapter III.

1.5. Outline of thesis

Following the introduction to MCV dynamics, mesoscale predictability and objectives of this research, an overview of BAMEX IOP 8 will be presented (Chapter II). This will include an analysis of radar, satellite, surface and upper air observations. Chapter III will detail the numerical models employed by this study and give a first look at the predictability issues surrounding the MCV. In Chapter IV, a new approach to assessing MCV predictability is introduced through the use of ensemble forecasting. Lastly, Chapter V will include a summary and discussion of the results.

CHAPTER II

OBSERVATIONAL IOP 8 ANALYSIS

2.1. Introduction

As mentioned in Galarneau and Bosart (2004), the period of 5–14 June 2003 was characterized by a strong subtropical jet extending from southeast of Hawaii east-northeastward to the Mississippi Valley and North Atlantic. Within this strong jet, multiple disturbances propagated through the central United States, generating several significant convective rounds and a few MCVs. This active pattern coincided with the BAMEX field campaign and provided several noteworthy research cases, one of which was the long-lived MCV of BAMEX IOP 8. Beginning as a widespread convective episode on 10 June over New Mexico, this system is of particular interest because of its rare longevity (over 60 hours), multiple periods of convection, and its transition into a baroclinic system. In this chapter, the evolution of the IOP 8 MCV is investigated using analyses of observational data, including radar, satellite, surface and upper air observations, including dropsonde data recorded specifically for the BAMEX project. The analysis focuses on two significant stages of this MCV. The first stage is the formation of a mature MCV from a severe MCS in Oklahoma on late 10 June. The second stage includes a round of secondary convection that developed over the MCV as it moved into the Ohio Valley as well as growth of the midlevel vortex down to the surface during the local afternoon of 11 June.

2.2. MCV precursor: West Texas MCS and resulting midlevel circulation

Figure 2.1 displays the large-scale 300 hPa pattern at 0000 UTC 10 June, 21

hours before the initiation of the Oklahoma MCS that eventually led to the formation of

the MCV. A cutoff low was situated over southern California, with a secondary

negatively-tilted shortwave trough extending from Arizona to near El Paso, Texas.

Ahead of this feature, two large areas of 250 hPa divergence were analyzed over central

New Mexico and the Texas/New Mexico border. At the same time, the large-scale flow

at 500 hPa over the southwestern United States was from the southwest and was fairly

weak, giving way to weak midlevel ridging over the Southern and Central Plains (Fig.

2.2). A weak midlevel shortwave was present over New Mexico, evidenced by the

anomalous northwesterly wind measured at Albuquerque.

Under this large scale flow pattern, a large MCS formed from convection over

the high plains of eastern New Mexico and southwest Texas (Fig. 2.3). The strongest

part of the MCS moved southeastward into south central Texas overnight. While the

bulk of the west Texas activity moved southward into central Texas by 0900 UTC (Fig.

2.3d), radar loops showed a weak cyclonic circulation within the stratiform rain region

over the central Texas/New Mexico border around 0600 UTC (not detectible in the static

images provided in Fig. 2.3). This weak circulation can be traced on radar and satellite

loops throughout the day of 10 June as it crosses the Texas panhandle into western

Oklahoma later that evening. Furthermore, the 1200 UTC 10 June 500 hPa analysis in

Fig. 2.4 clearly shows evidence of a closed cyclonic midlevel circulation over west

Texas at that time, between the easterly wind measured at Amarillo, Texas and the
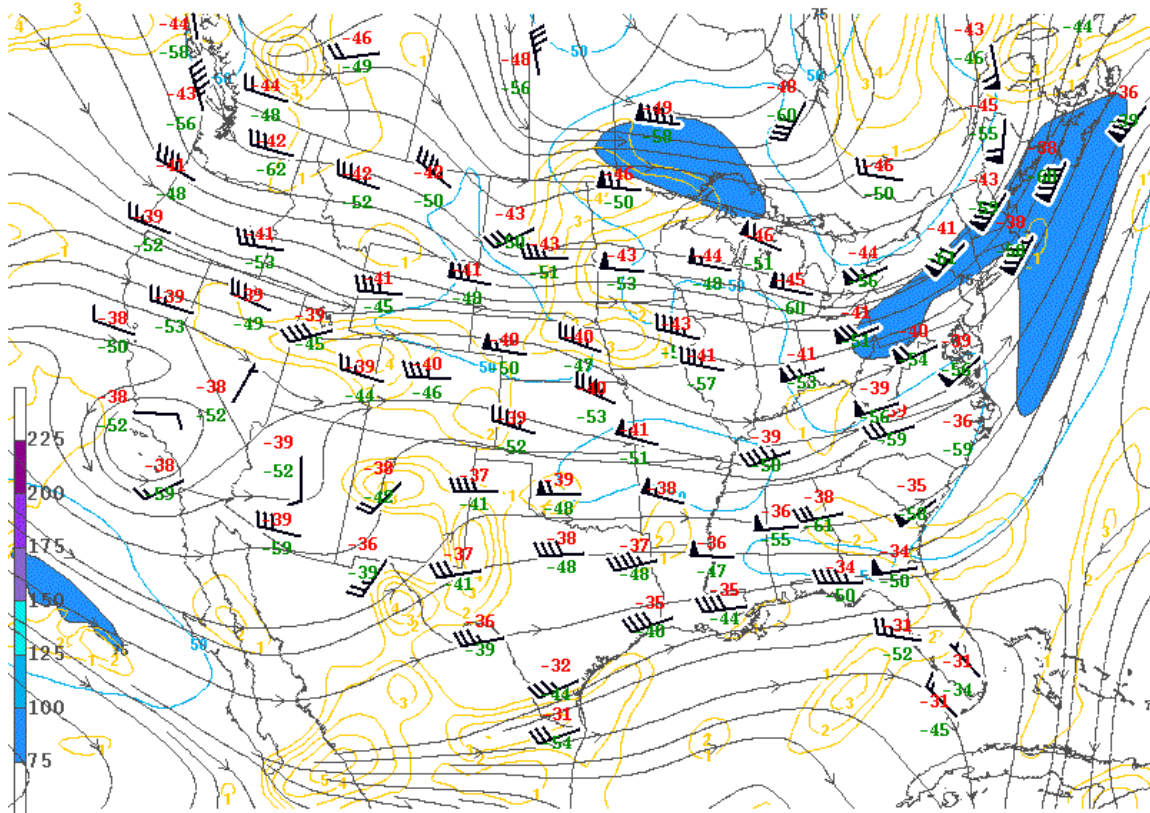
FIG. 2.1. 300 hPa observations of wind (full barb denotes 10 kt), temperature (red) and dewpoint (green) in degrees C at 0000 UTC 10 June. Gray contours denote streamlines, divergence is contoured in yellow and filled contours are isotachs. Image from the Storm Prediction Center.
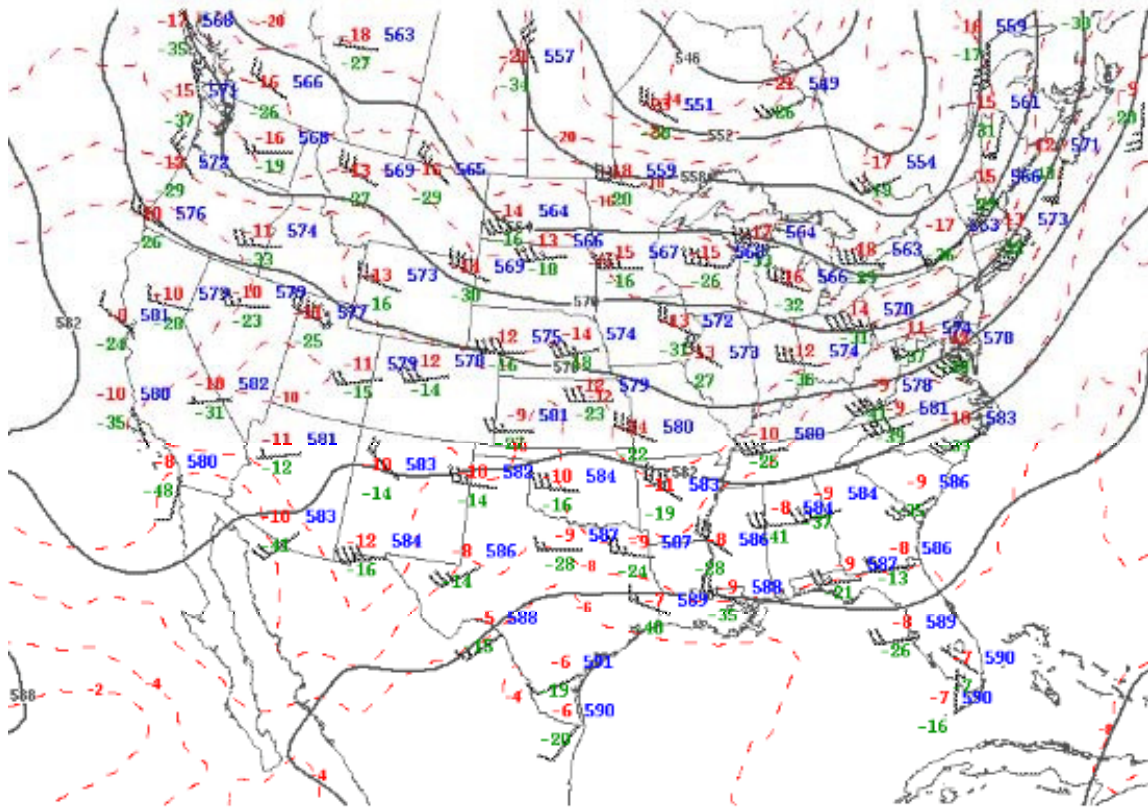
FIG. 2.2. 500 hPa observations of wind (full barb denotes 10 kt), height (blue in dm), temperature (red) and dewpoint (green) in degrees C at 0000 UTC 10 June. Gray contours denote isoheights contoured every 6 dm and dashed red contours are temperature every 2 degrees C. Image from the Storm Prediction Center.
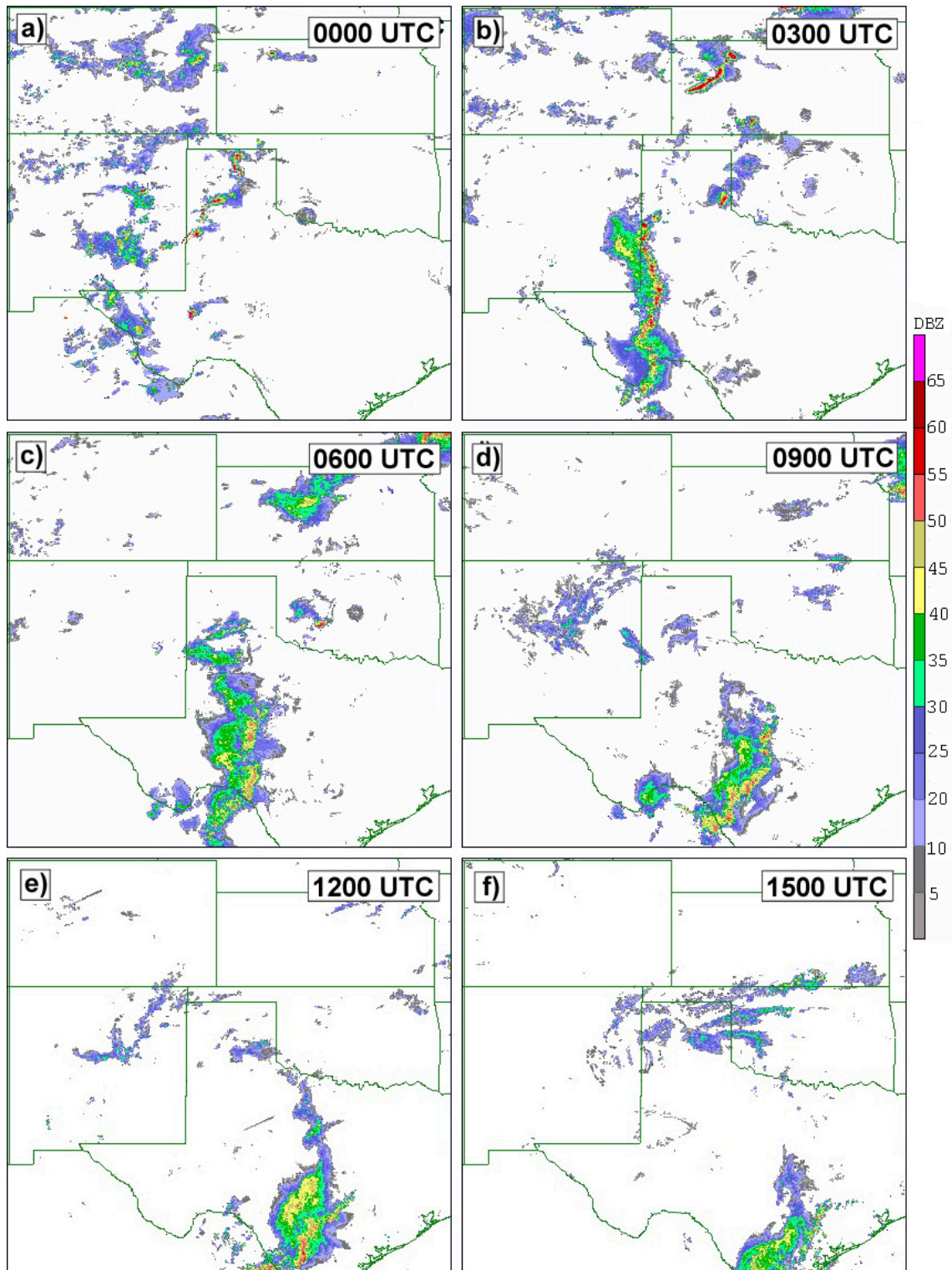
FIG. 2.3. Radar reflectivity from 0000 UTC to 0900 UTC 10 June.

westerly wind measured at Midland, Texas, and between the northerly and southerly 500

hPa winds measured at Albuquerque, New Mexico and Fort Worth, Texas respectively.

This circulation coincides with the detected circulation south of Amarillo on radar loops

at that time (static image presented in Fig. 2.3e). Figure 2.4 shows a considerable

deepening of the shortwave trough over the twelve hour period following the analysis in

Fig. 2.2. It appears through radar and upper air observations that the convection over

New Mexico and West Texas during early 10 June had significant amplification effects

on the midlevel shortwave, though the degree to which convection acted to strengthen

the shortwave cannot be determined with the conventional observation network alone,

and will be examined further in Chapters III and IV.

2.3 Stage I: MCV formation

The synoptic-scale setup at 0000 UTC 11 June 2003 included a negatively-tilted

upper level shortwave trough that extended through the southern Plains and the

associated 500 hPa shortwave over southern Kansas and northern Oklahoma (Figs. 2.5,

2.6). The closed circulation at 500 hPa that had been evident 12 hours earlier (Fig. 2.4)

was no longer detectable at this time, though continuous but weak deepening of the

shortwave was observed as it moved over western Oklahoma and the Texas Panhandle.

At the surface, a weak frontal boundary extended from a low over the Great Lakes

through Kansas and northwestern Oklahoma, where it met with a surface trough that

extended southward through western Oklahoma and into northwest Texas (Fig. 2.7). As

seen in Fig. 2.8, cloud cover associated with convective debris from the previous night
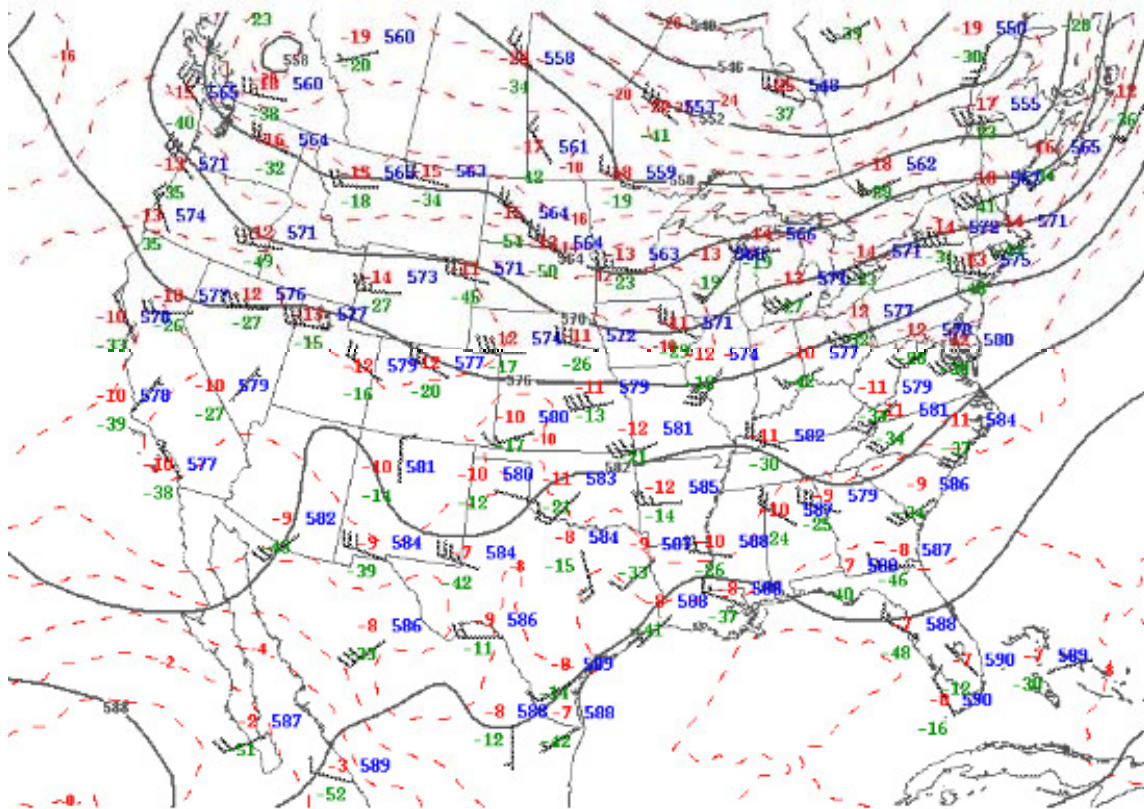
FIG. 2.4. 500 hPa observations of wind (full barb denotes 10 kt), height (blue in dm), temperature (red) and dewpoint (green) in degrees C at 1200 UTC 10 June. Gray contours denote isoheights contoured every 6 dm and dashed red contours are temperature every 2 degrees C. Image from the Storm Prediction Center.
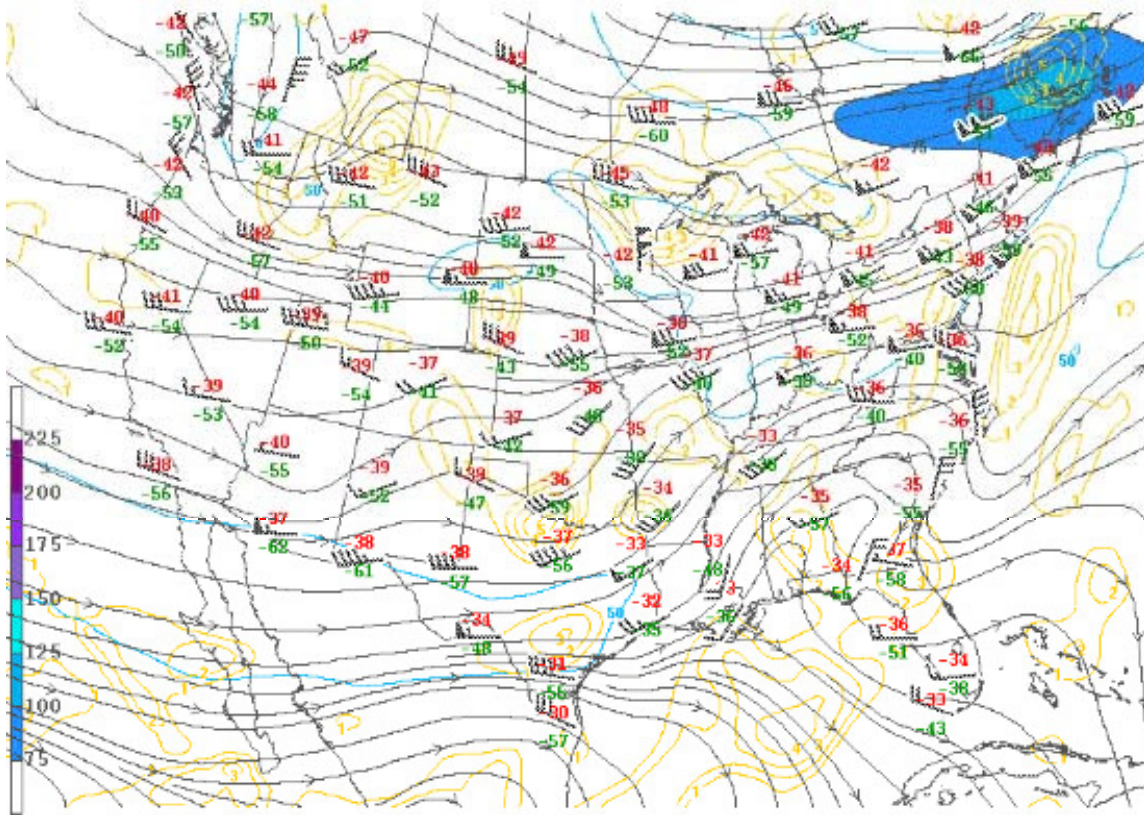
FIG. 2.5. 300 hPa observations of wind (full barb denotes 10 kt), temperature (red) and dewpoint (green) in degrees C at 0000 UTC 11 June. Gray contours denote streamlines and filled contours are isotachs. Image from the Storm Prediction Center.
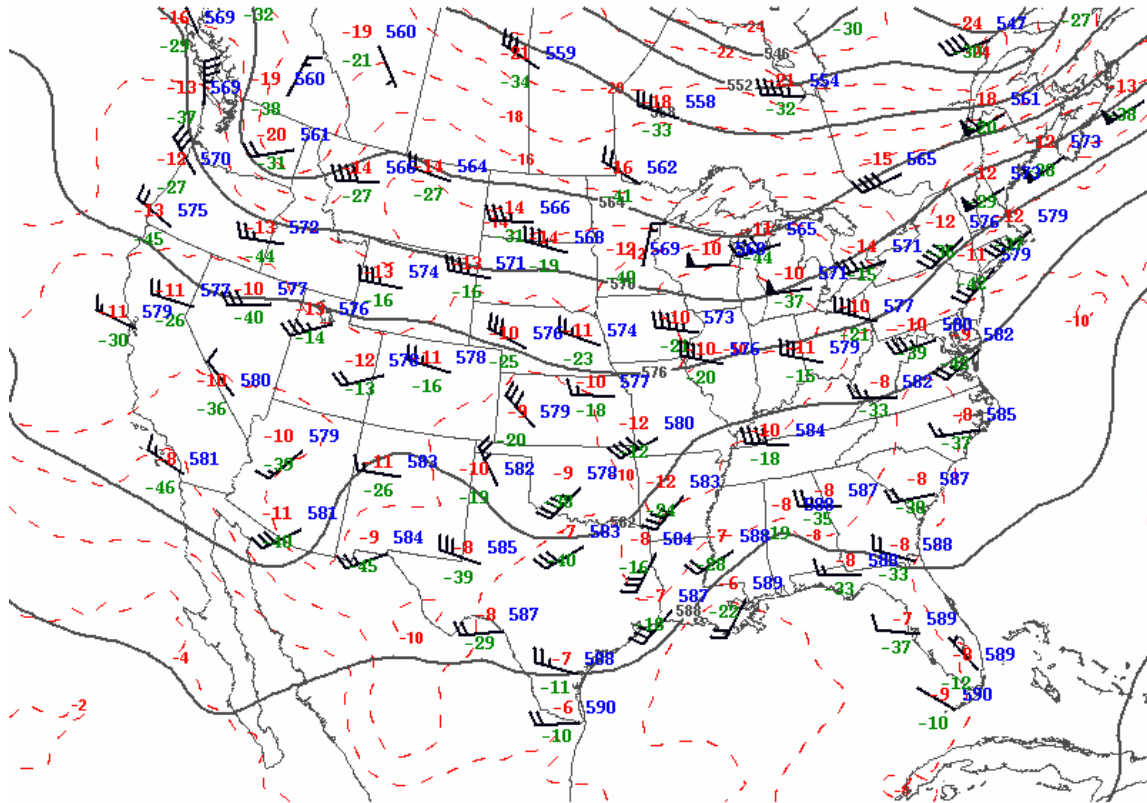
FIG. 2.6. 500 hPa observations of wind (full barb denotes 10 kt), height (blue in dm) temperature (red) and dewpoint (green) in degrees C and height (blue) in dm at 0000 UTC 11 June. Gray contours denote isoheights contoured every 6 dm and dashed red contours are temperature every 2 degrees C. Image from the Storm Prediction Center.
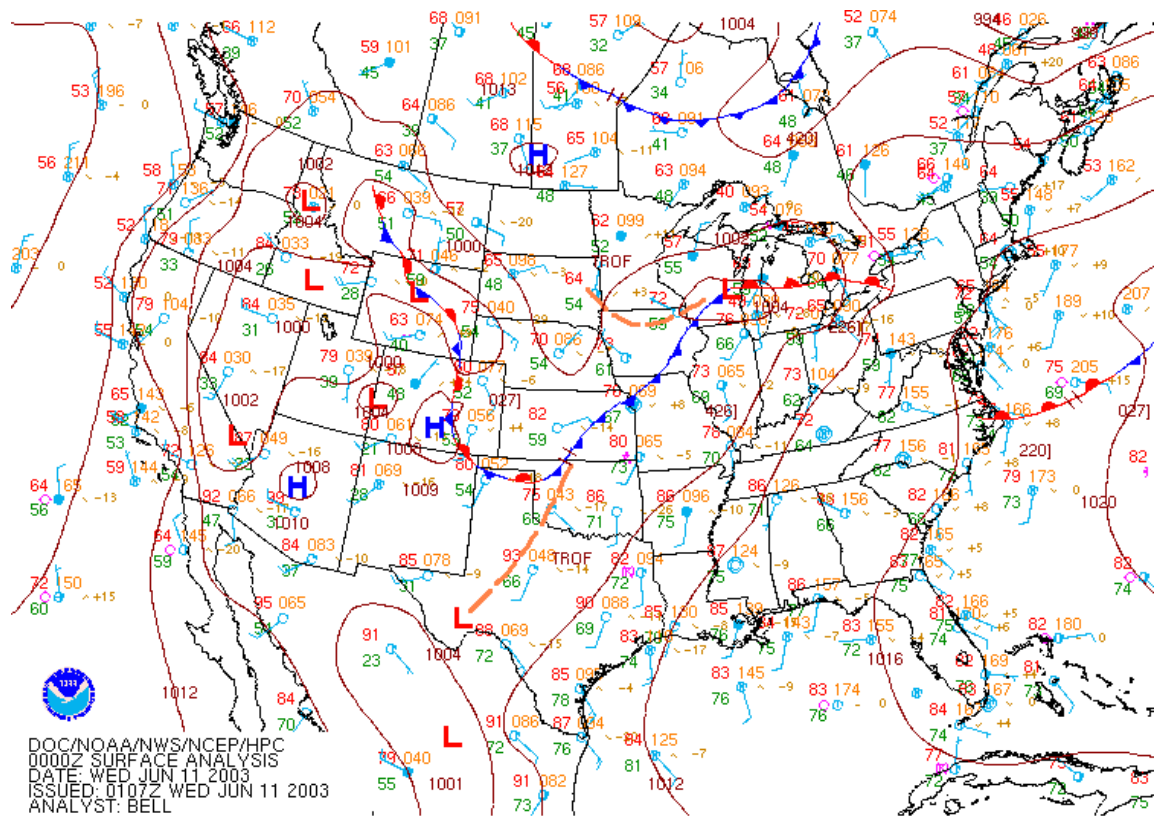
FIG. 2.7. Surface analysis valid at 0000 UTC 11 June 2003. Image from the Hydrometeorological Prediction Center.
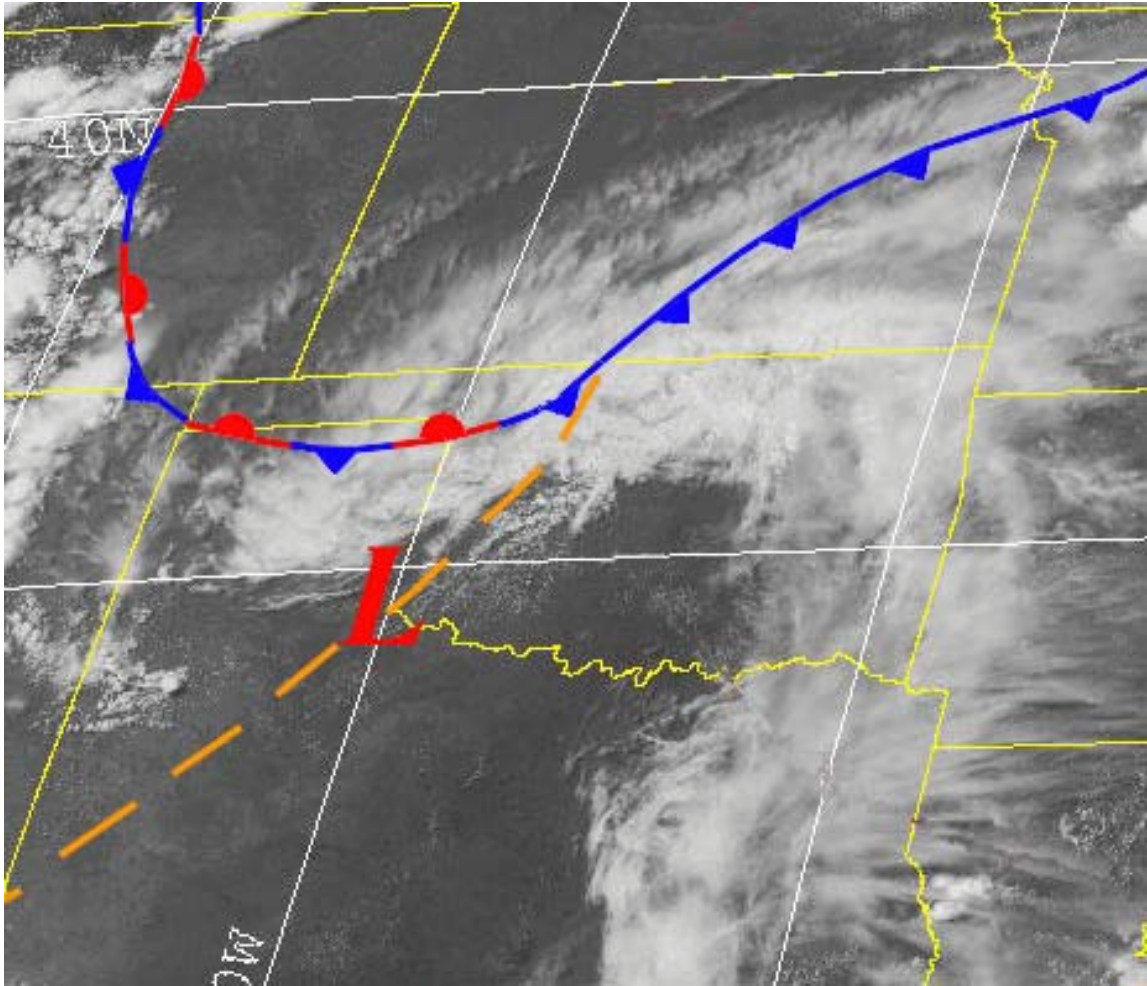
FIG. 2.8. 2-km Ch. 1 GOES-12 imagery at 1956 UTC 10 June.

had spread over western and northern Oklahoma throughout the day of 10 June, enhancing the local temperature gradient ahead of the front and behind the surface trough, as is evident in the 2100 UTC subjective surface analysis in Fig. 2.9.

The airmass ahead of the frontal boundary was moderately unstable with convective potential energy (CAPE) values exceeding 2000 J/kg as evidenced in the Norman, Oklahoma sounding from 00Z 11 June (Fig.2.10). Surface convergence along the trough and cold front provided enough forcing to initiate convection in northwest Oklahoma around 2100 UTC as seen on radar (Fig. 2.11a). Aided by large-scale ascent provided by the upper-level trough (Figs. 2.5, 2.6), the area of convection quickly expanded southward along the surface trough and by 0000 UTC 11 June the convection had merged into an MCS which extended from north central Oklahoma through the southwest corner of the state, or roughly 250 km in length (Fig. 2.11 b). The line was strongest around 0300 UTC (Fig. 2.11c), and by 0600 UTC more than 50 reports of high wind and large hail were reported across Oklahoma and extreme northern Texas. An extensive stratiform rain region formed behind the MCS around 0300 UTC, leading to a strong surface cold pool by 0600 UTC (surface temperatures in the lower to mid 60s; Fig. 2.12) which helped push the strong convection across all of Oklahoma overnight. By 0900 UTC (Fig. 2.11e), the MCS had weakened in western Arkansas but a large area of light-to-moderate rain (roughly 200 km in diameter) remained across eastern Oklahoma and western Arkansas. A weak circulation within the stratiform region over eastern Oklahoma became evident in radar reflectivity animations by 0600 UTC (denoted by an
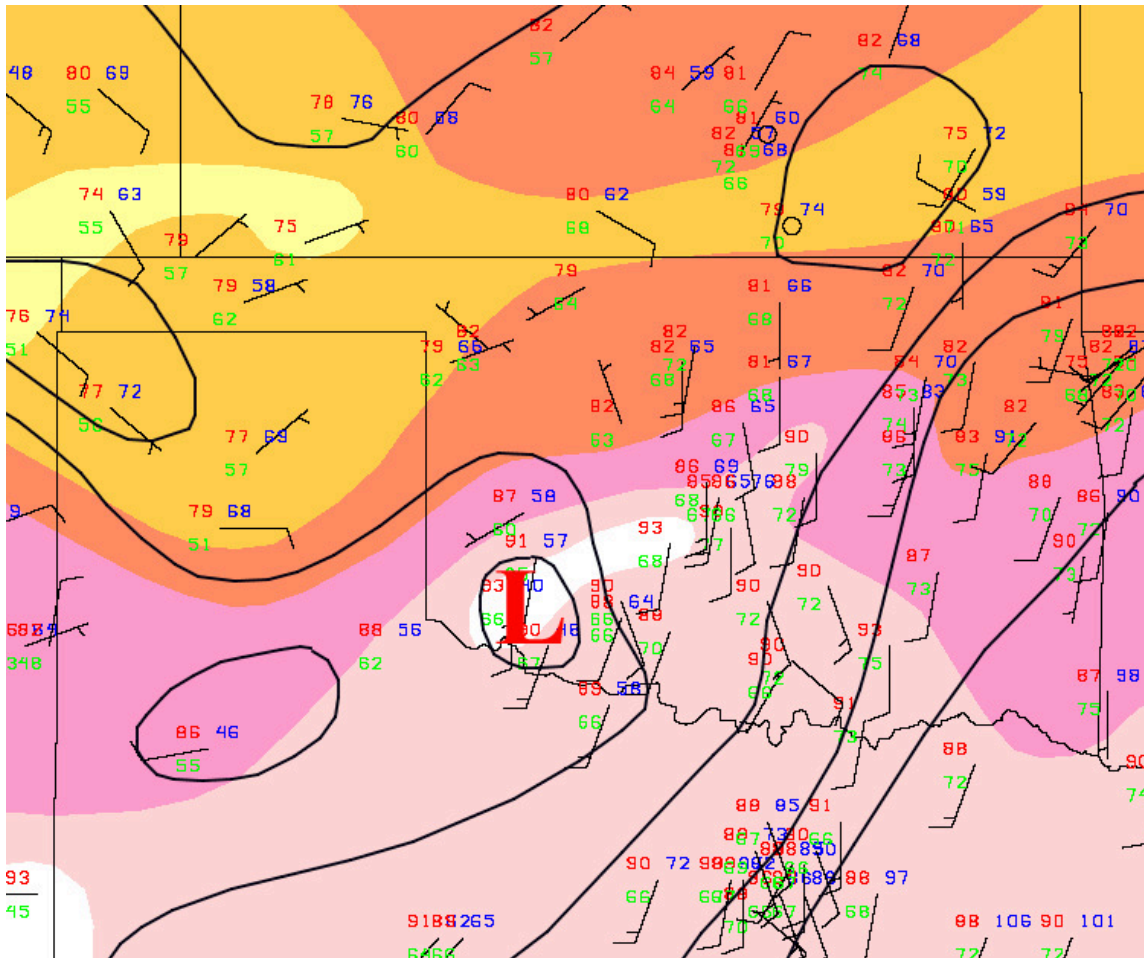
FIG. 2.9. Surface analysis valid 2100 UTC 10 June. Temperature plotted in red, dewpoint in green and surface pressure (minus 1000 and multiplied by 10) in blue. One full barb denotes 10 kt. Black contours denote isobars analyzed every millibar and temperature shaded every 4 degrees Fahrenheit.
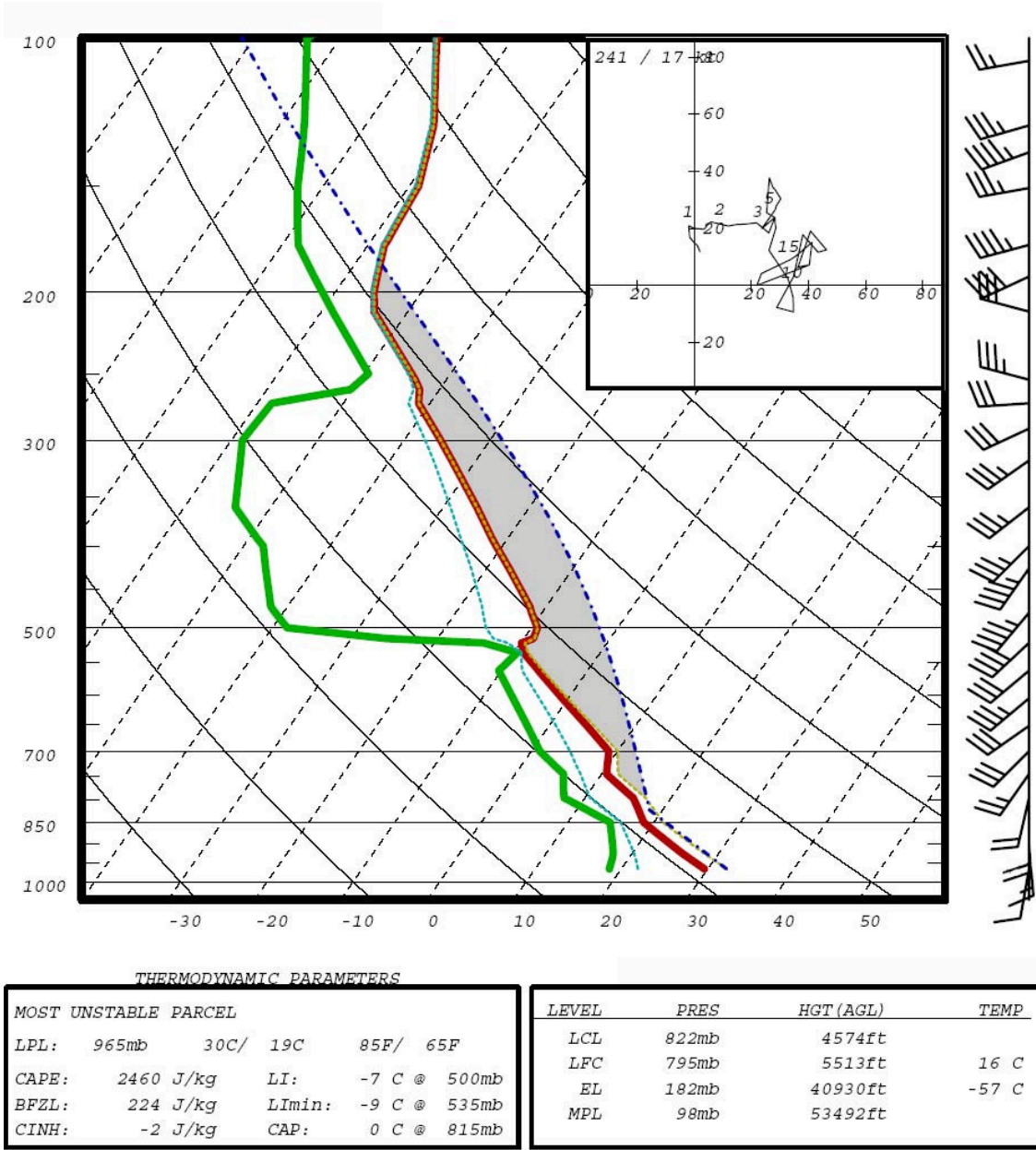
FIG. 2.10. 0000 UTC 11 June KOUN RAOB sounding. Temperature in red, dewpoint in green, wet-bulb temperature in dashed cyan and virtual temperature dashed yellow. Lifted surface parcel trajectory (using virtual temperature) denoted by dark blue dotted line.
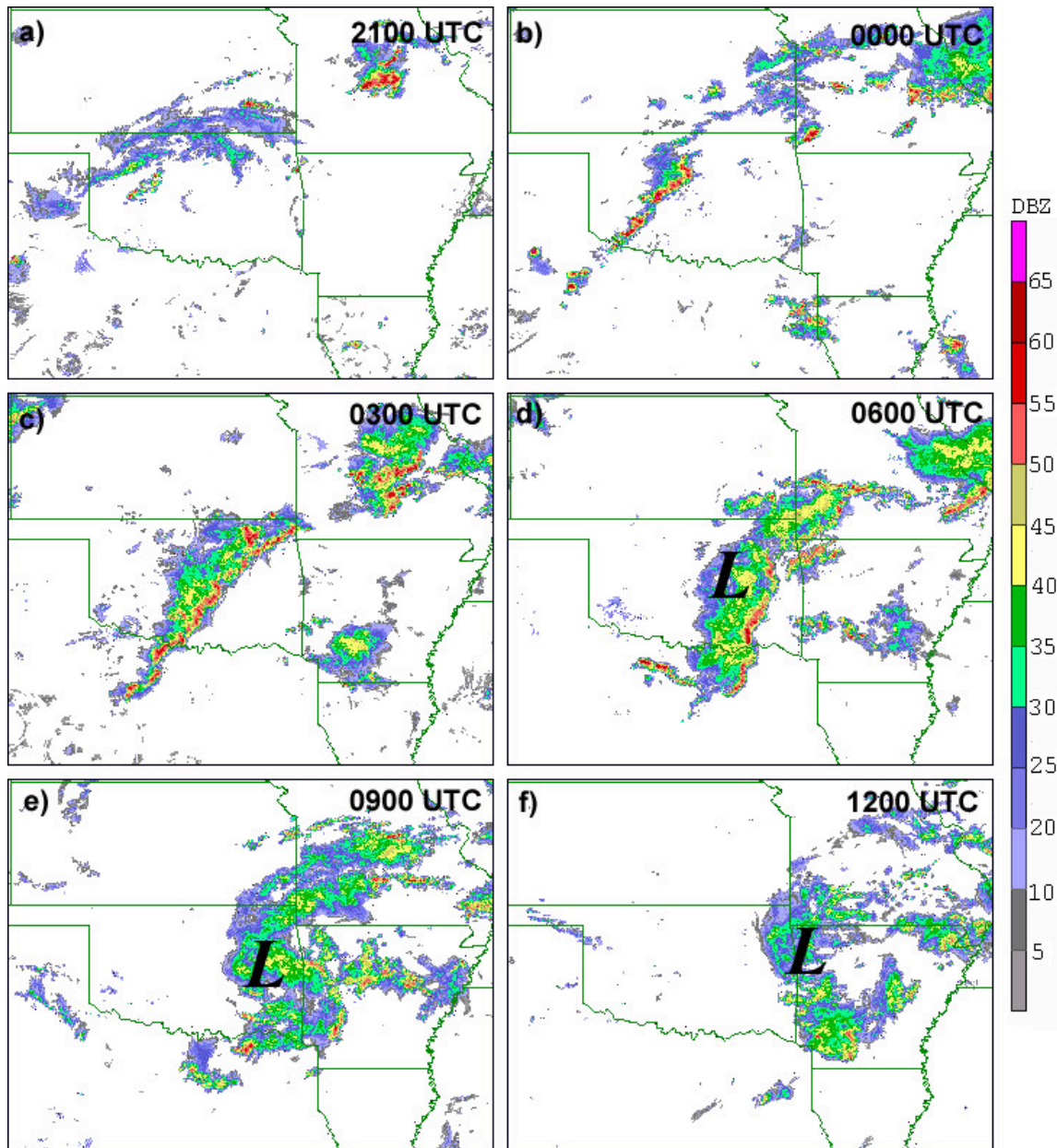
FIG. 2.11. WSR88D reflectivity from 2100 UTC 10 June to 1200 UTC 11 June. "L" denotes approximate location of midlevel circulation.
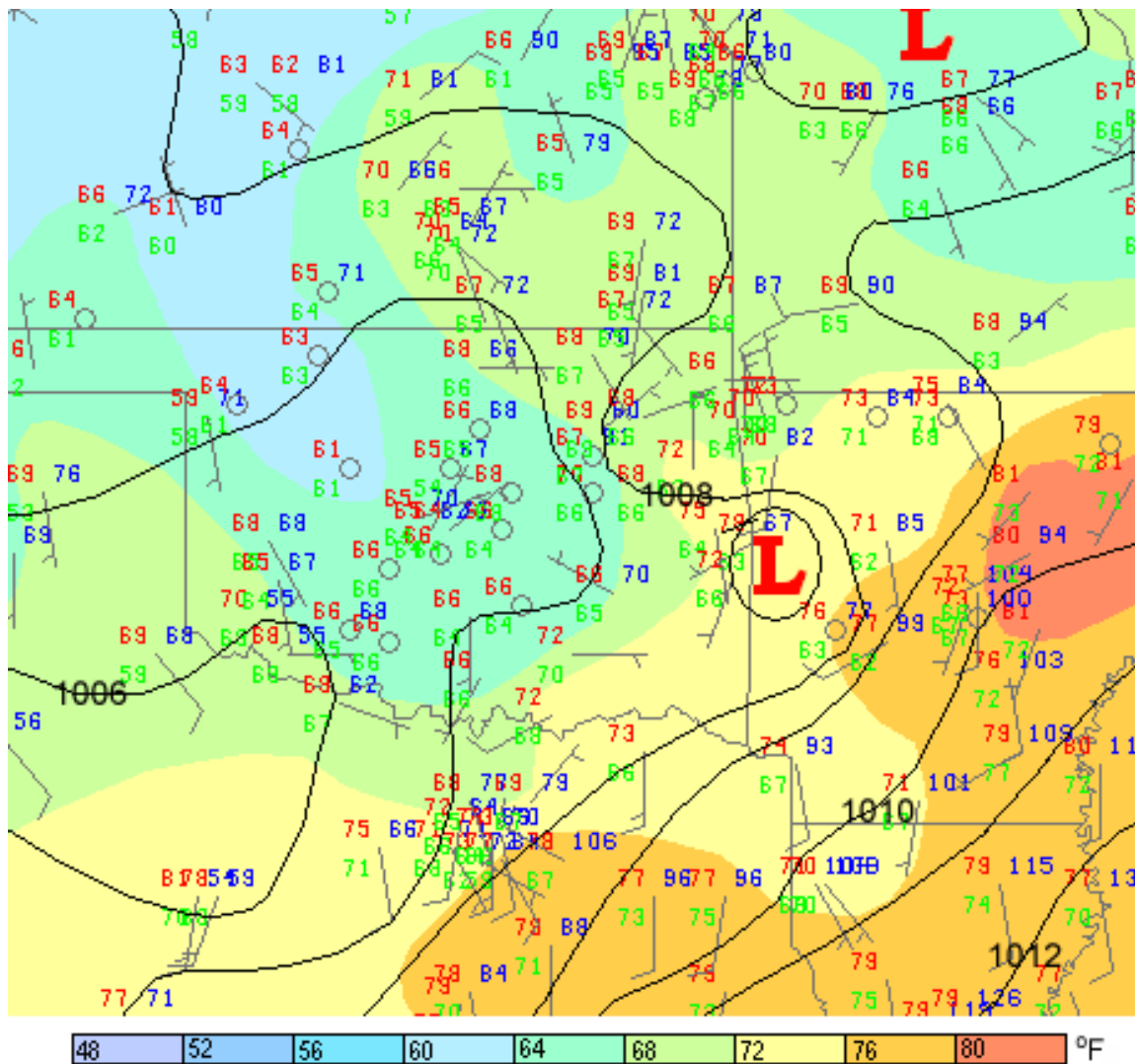
FIG. 2.12. Surface analysis valid 0600 UTC 11 June. Temperature plotted in red, dewpoint in green and surface pressure (minus 1000 and multiplied by 10) in blue. One full barb denotes 10 kt. Black contours denote isobars analyzed every millibar.

"L" in Fig. 2.11d). The circulation grew in strength and size and by 1200 UTC 11 June

it was extremely well-defined over northeast Arkansas (Fig. 2.11 f).

By analyzing nearby wind profilers during the development stages of the MCV,

it becomes apparent that the MCS and related MCV developed directly in the vicinity of

the midlevel shortwave trough. 500 hPa analyses of 0000 11 June UTC RAOB data (Fig.

2.6) and 600 hPa wind profiler data in Fig. 2.13 suggest that the midlevel trough was

located from southwest to northeast across northwest Oklahoma, with the axis in the

general vicinity of Lamont, Oklahoma (LMN). This location puts the trough slightly

behind the MCS at that time. At 0200 UTC (Fig. 2.13c), the Lamont profiler measured a

22 knot 356-degree wind, which veered to 28 knots at 39 degrees an hour later (Fig.

2.13d), after the stratiform rain region had passed overhead. The difference between the

two wind vectors is a due east wind at 9 knots. Tracing the midlevel circulation on radar

back from 1200 UTC would suggest the developing vortex would be over central

Oklahoma at 0300 UTC (Fig. 2.11c), or due south of Lamont. The easterly difference in

wind vectors measured in Lamont between 0200 UTC and 0300 UTC confirms a

developing circulation due south of that location. Additionally, the Purcell, Oklahoma

profiler, located south of the estimated circulation at that time, detected a westerly 600

hPa at 0400 UTC (Fig. 2.13e) which veered to northwesterly by 0600 UTC (Fig. 2.13g),

further suggesting the presence of a developing circulation over central Oklahoma.

Finally, the Haskell, OK profiler measured a sharp veering of 600 hPa winds between

0700 UTC and 0800 UTC (Figs. 2.13h–i), a difference of 20 knots at 336 degrees. The

added north-northwesterly wind implies the passage of the circulation to the east of
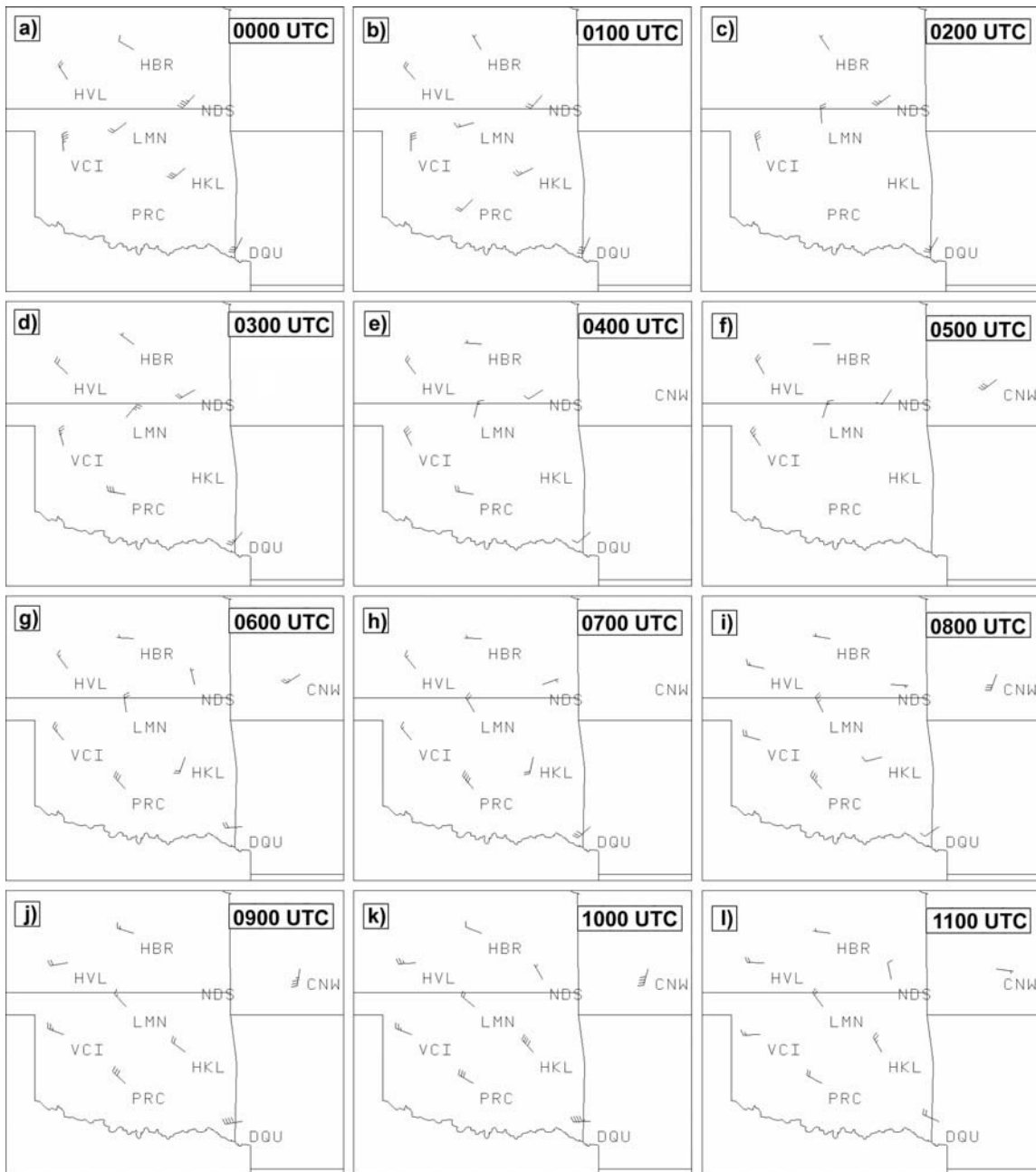
FIG. 2.13. 11 June 600 hPa observations from the NOAA Wind Profiler Network. One full barb denotes 10 kt.

Haskell after 0800 UTC, which further proves the vortex to be over eastern Oklahoma at

0800 UTC. Evidence of the midlevel cyclonic circulation continued to be detected

through 1100 UTC when Conway, MO (CNW) detected an easterly wind (Fig. 2.13l),

suggesting the vortex to be south of that location at that time. This circulation is

strongest in wind profiler data at 500 and 600 hPa. Above this level, there is no

evidence of a closed circulation at any time, and below 600 hPa the signs of circulation

are much weaker. No circulation is evident at any time at 925 hPa (additional levels not

shown).

2.4 Stage II: Secondary convection and surface vortex development

This section analyzes the evolution of the MCV during the next diurnal cycle in

which secondary convection became a significant factor. Figure 2.14 shows radar

reflectivity at three-hour intervals from 1500 UTC 11 June to 0600 UTC 12 June,

capturing the convective event during the day. By 1500 UTC 11 June (Fig. 2.14a),

convection had already restrengthened on the southern periphery of the circulation, near

Little Rock, Arkansas. At the same time, isolated thunderstorms began to develop

across a large portion of the southeast United States. These cells merged into several

convective lines through the afternoon of 11 June (Fig. 2.14b–c), and embedded bow

echoes resulted in widespread high wind reports from eastern Arkansas across northern

parts of Mississippi and Alabama and into much of Tennessee. Convection on the south

side of the MCV circulation expanded and merged into a weak MCS which moved

southward through Arkansas and Mississippi during the evening (Fig. 2.14d–f).
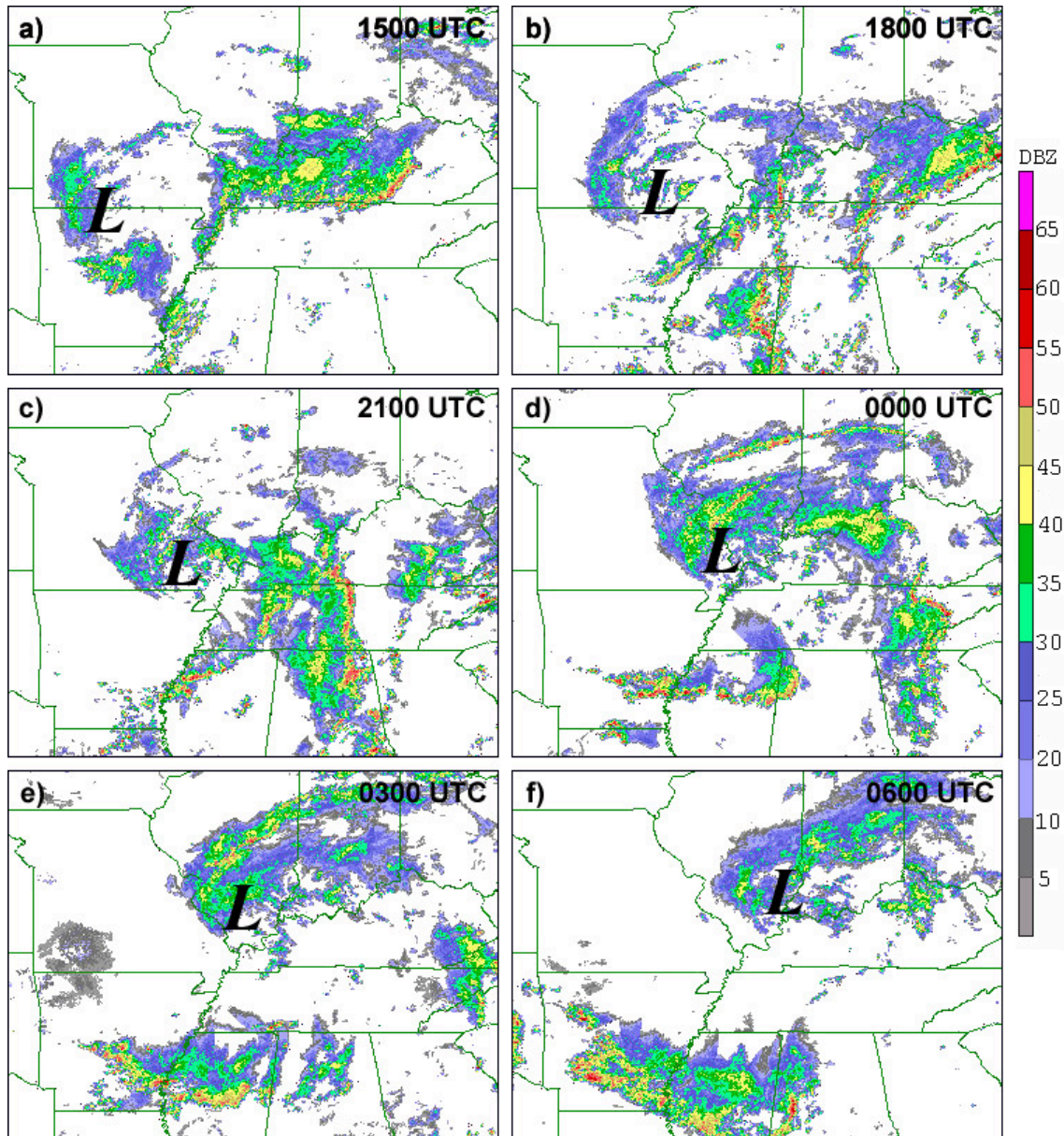
FIG. 2.14. WSR88D reflectivity from 1500 UTC 11 June to 0600 UTC 12 June. "L" denotes approximate location of midlevel circulation.

Additionally, at 0000 UTC 12 June, a line of severe thunderstorms developed along the cold front in central Illinois on the north side of the MCV circulation (Fig. 2.14d). These storms produced five reported weak tornadoes in Sangamon and Logan counties in Illinois.

Closer to the MCV circulation itself, isolated weak convection initiated around 1800 UTC in southeast Missouri (Fig. 2.14b), about 50 km east of the midlevel circulation center. Additional weak convection formed near and slightly west of the MCV circulation through 2000 UTC as shown in Springfield, Missouri and Paducah, Kentucky reflectivity images in Figs. 2.15 and 2.16 respectively. This activity diminished by 0000 UTC 12 June (Fig. 2.14d), however the area of light to moderate rain with embedded convection on the northern and western sides of the MCV expanded through 0300 UTC 12 June (Fig. 2.14e), after which radar reflectivity decreased across all sections of the MCV and surrounding areas. The circulation on radar remained evident through this time as the MCV moved across southern Illinois, and signs of a cyclonic circulation were apparent all through the overnight into the local morning hours of 12 June as it entered Ohio (Fig. 2.17a–d).

At the surface, a weak surface low of 1007 hPa appeared in the surface analysis over western Arkansas (ahead of the MCS) at 0600 UTC (Fig. 2.12). The surface low deepened to 1006 hPa at 0900 UTC over northwest Arkansas (Fig. 2.18), and the cold pool associated with the MCS had overspread the area as the MCS passed overhead (Fig. 2.11e). The observed midlevel circulation on radar was still about 150 km to the southwest over east central Oklahoma at this time. By 1200 UTC (Fig. 2.19), as the
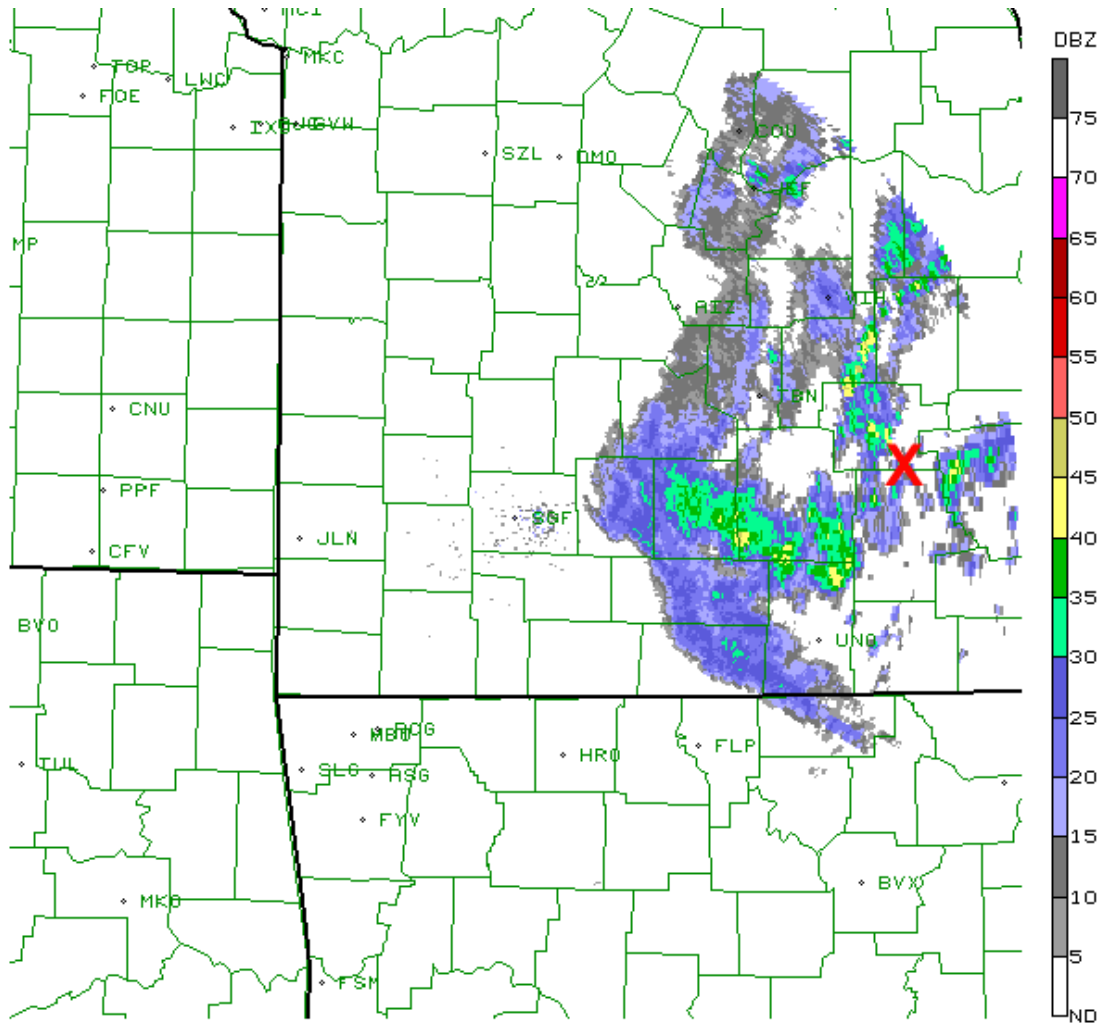
FIG. 2.15. Springfield, Missouri WSR-88D reflectivity at 1933 UTC 11 June. Red 'X' denotes approximate center of midlevel circulation.
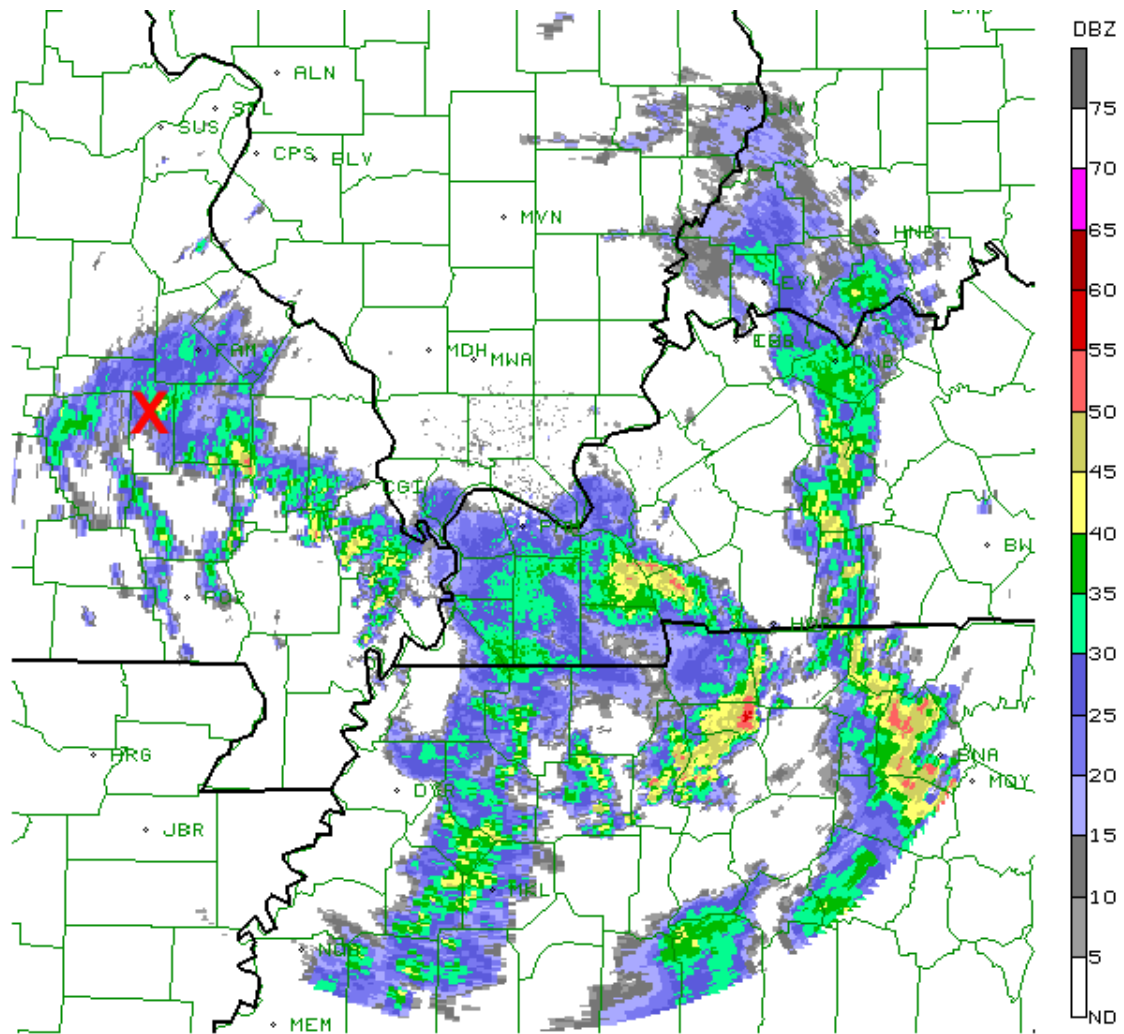
FIG. 2.16. Paducah, Kentucky WSR-88D reflectivity at 1959 UTC 11 June. Red 'X' denotes approximate center of midlevel circulation.
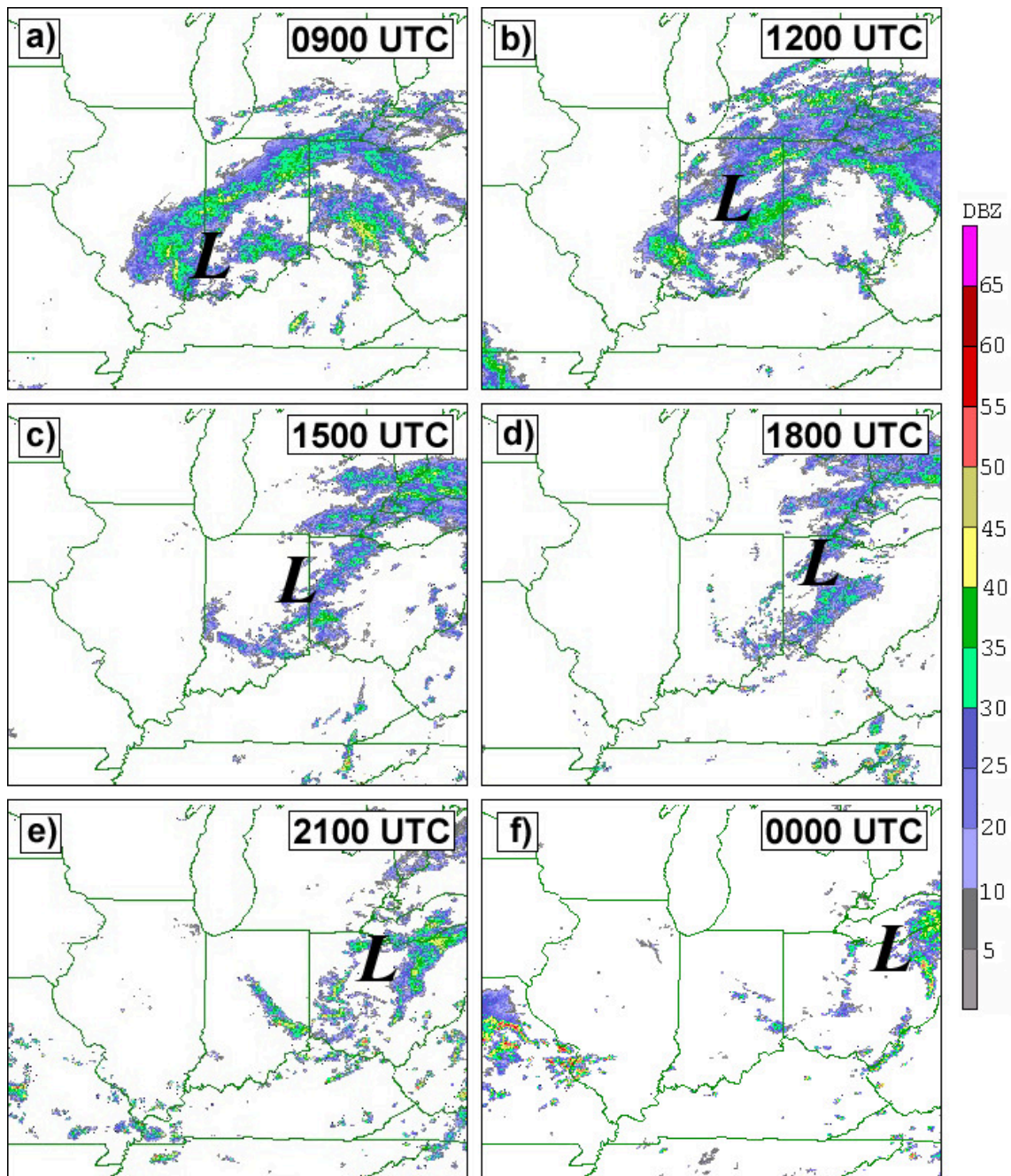
FIG. 2.17. WSR88D reflectivity from 0900 UTC 12 June to 0000 UTC 13 June. "L" denotes approximate location of midlevel circulation.
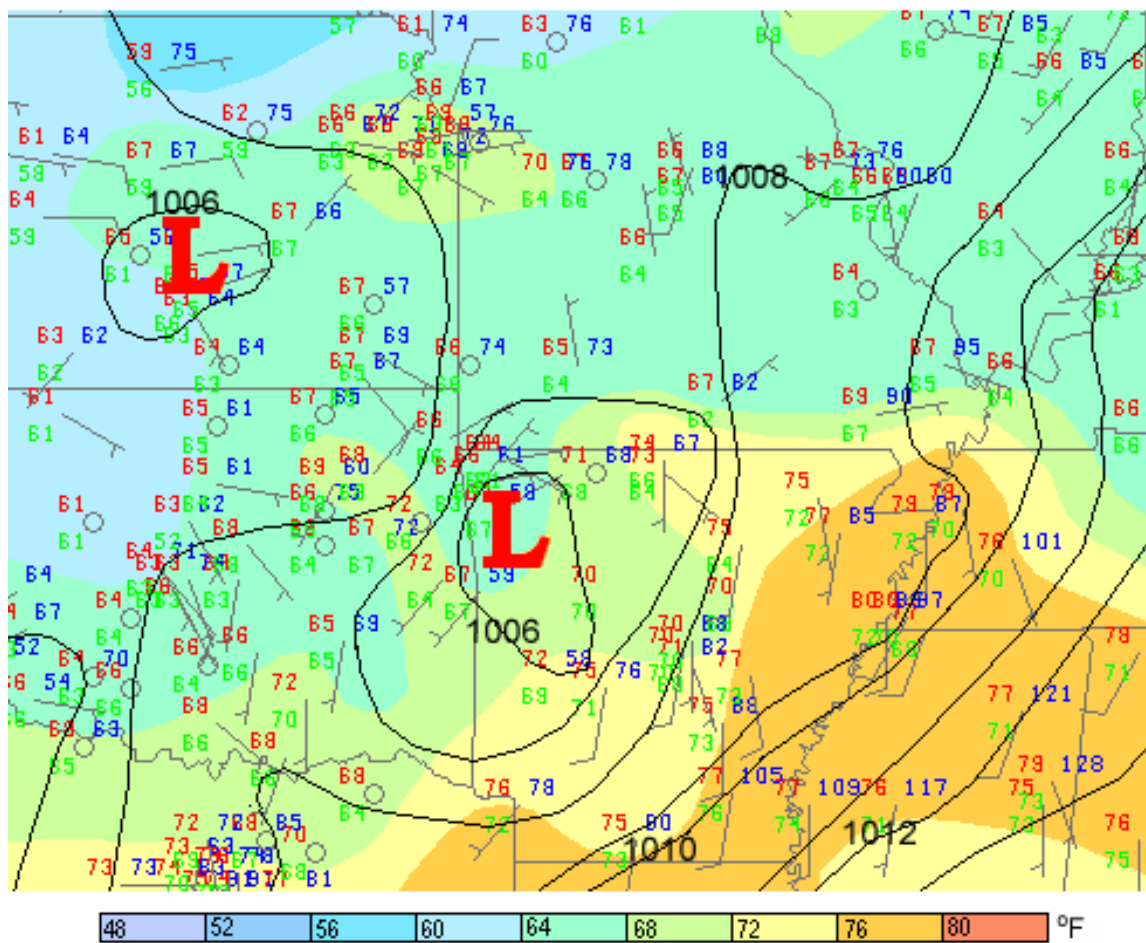
FIG. 2.18. Surface analysis valid 0900 UTC 11 June. Temperature plotted in red, dewpoint in green and surface pressure (minus 1000 and multiplied by 10) in blue. One full barb denotes 10 kt. Black contours denote isobars analyzed every millibar.
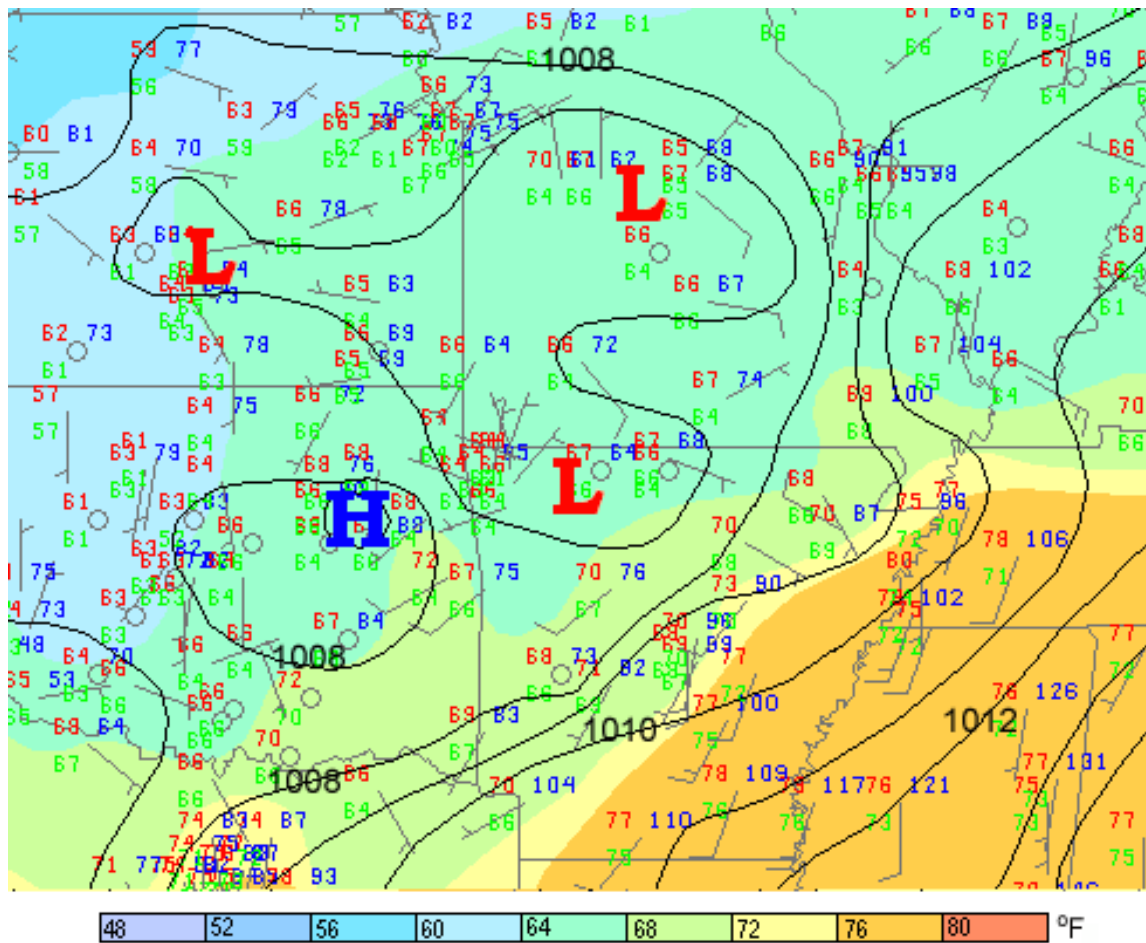
FIG. 2.19.   Surface analysis valid 1200 UTC 11 June. Temperature plotted in red, dewpoint in green and surface pressure (minus 1000 and multiplied by 10) in blue. One full barb denotes 10 kt. Black contours denote isobars analyzed every millibar.

midlevel circulation moved over northwest Arkansas and closer to the vicinity of the

surface low, the surface analysis showed evidence of a closed surface circulation with

increased easterly winds to the north of the circulation center. While the surface low

was situated within cool temperatures at this time, the mesohigh associated with the

convective cold pool appeared to be stationed over northeast Oklahoma. Three hours

later (Fig. 2.20), the surface low had moved into south central Missouri, and was

displaced about 100 km from the surface cold pool over southwest Missouri. The low

was still analyzed at 1007 hPa at this time, however the surface circulation continued to

become better defined. By 1800 UTC (Fig. 2.21), the surface low had deepened to

below 1006 hPa and was still displaced about 100 km from the cold pool. It was around

this time that new convection has formed near the MCV center, and at 2100 UTC (Fig.

2.22), the surface cyclone had maintained its intensity but was situated in a new surface

cold pool. Through 0000 UTC 12 June (Fig. 2.23), the surface cyclone maintained its

intensity, until it showed signs of restrengthening over southeast Illinois at 0600 UTC

(not shown). Over the next six hours, the cyclone deepened to below 1004 hPa, but by

1200 UTC (Fig. 2.24) it had merged with the nearby frontal boundary and began to show

signs of becoming an extratropical system.

At 1600 UTC 11 June, the BAMEX project began releasing dropsondes into the

MCV. Twenty-three dropsondes were released through 1902 UTC, capturing the

structure of the MCV in all quadrants as the vortex reached its mature stage and began to

reinitiate convection along its downshear periphery. The location of each dropsonde

overlain onto visible satellite imagery is given in Fig. 2.25. Figures 2.26 through 2.32
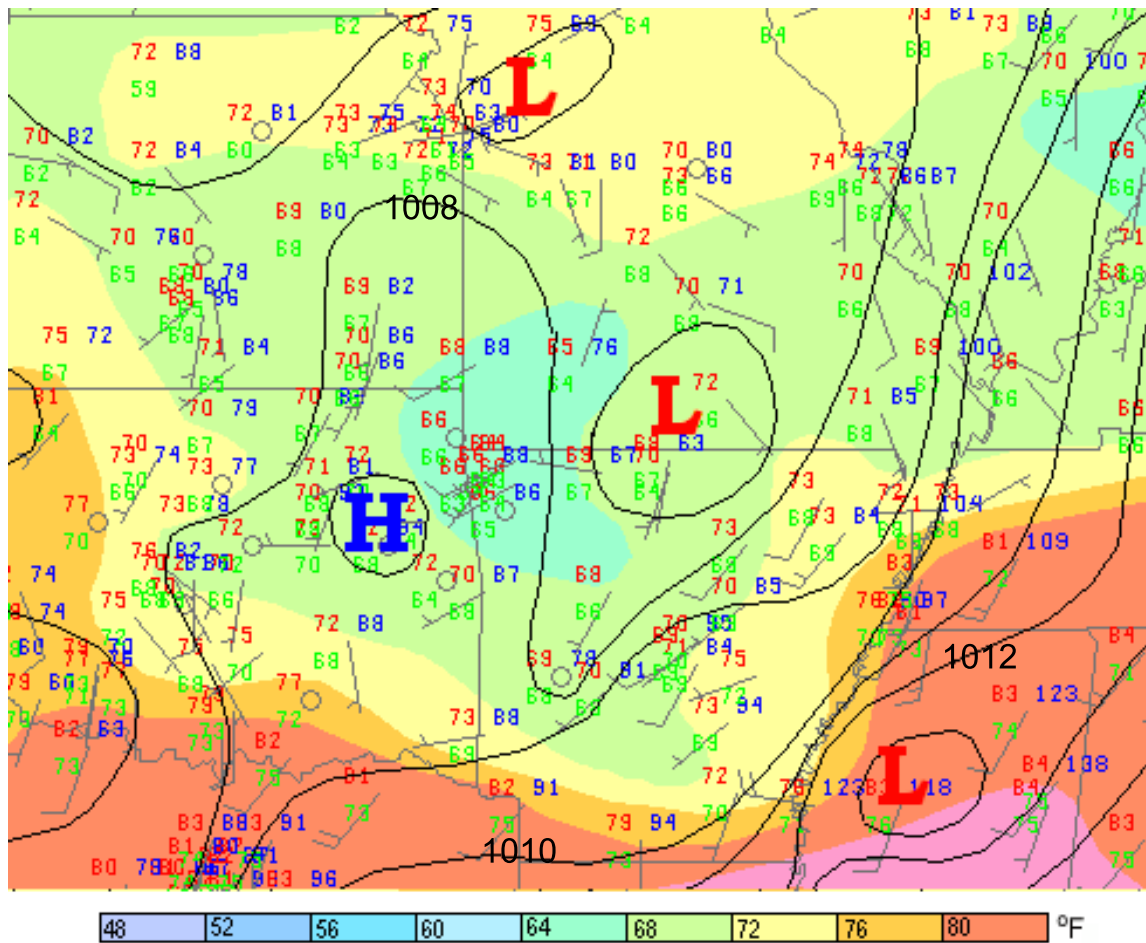
FIG. 2.20. Surface analysis valid 1500 UTC 11 June. Temperature plotted in red, dewpoint in green and surface pressure (minus 1000 and multiplied by 10) in blue. One full barb denotes 10 kt. Black contours denote isobars analyzed every millibar.
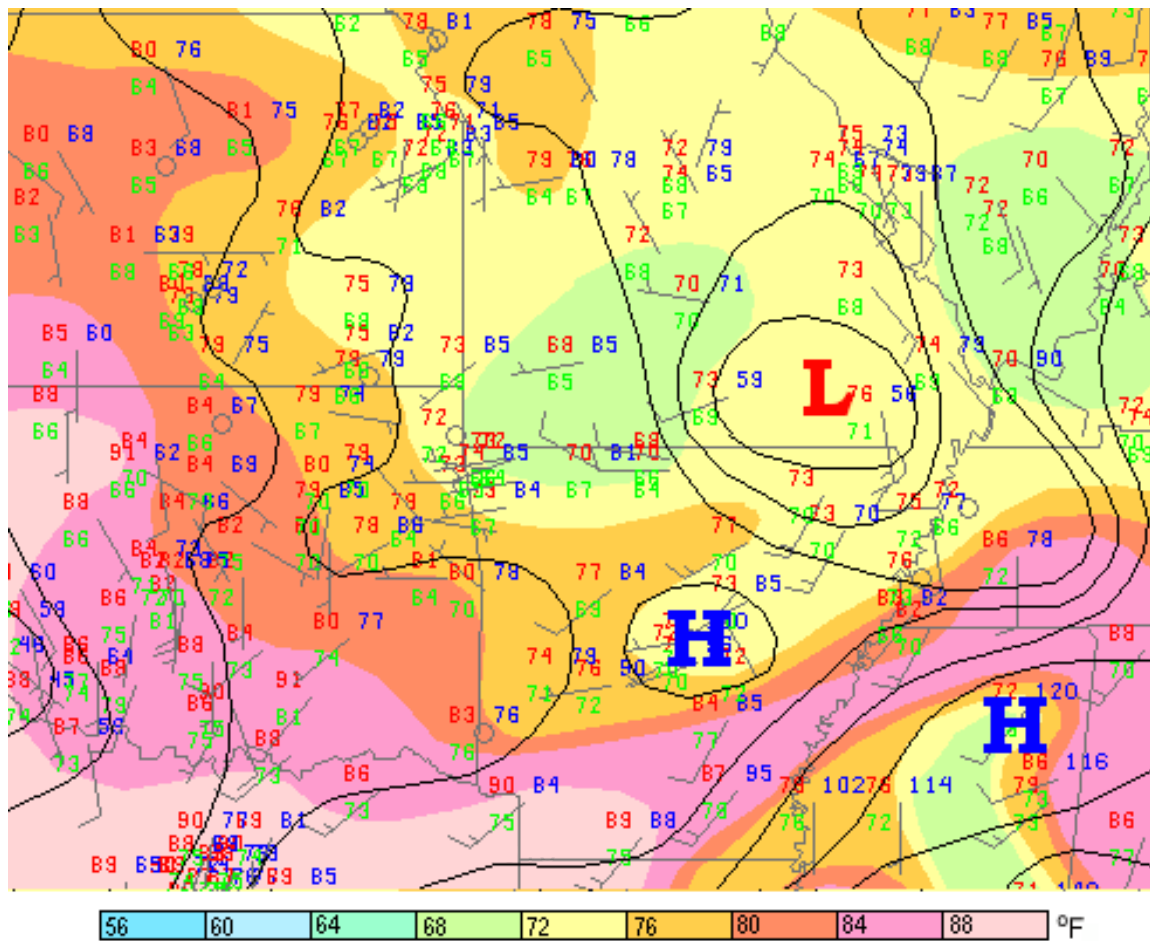
FIG. 2.21. Surface analysis valid 1800 UTC 11 June. Temperature plotted in red, dewpoint in green and surface pressure (minus 1000 and multiplied by 10) in blue. One full barb denotes 10 kt. Black contours denote isobars analyzed every millibar.
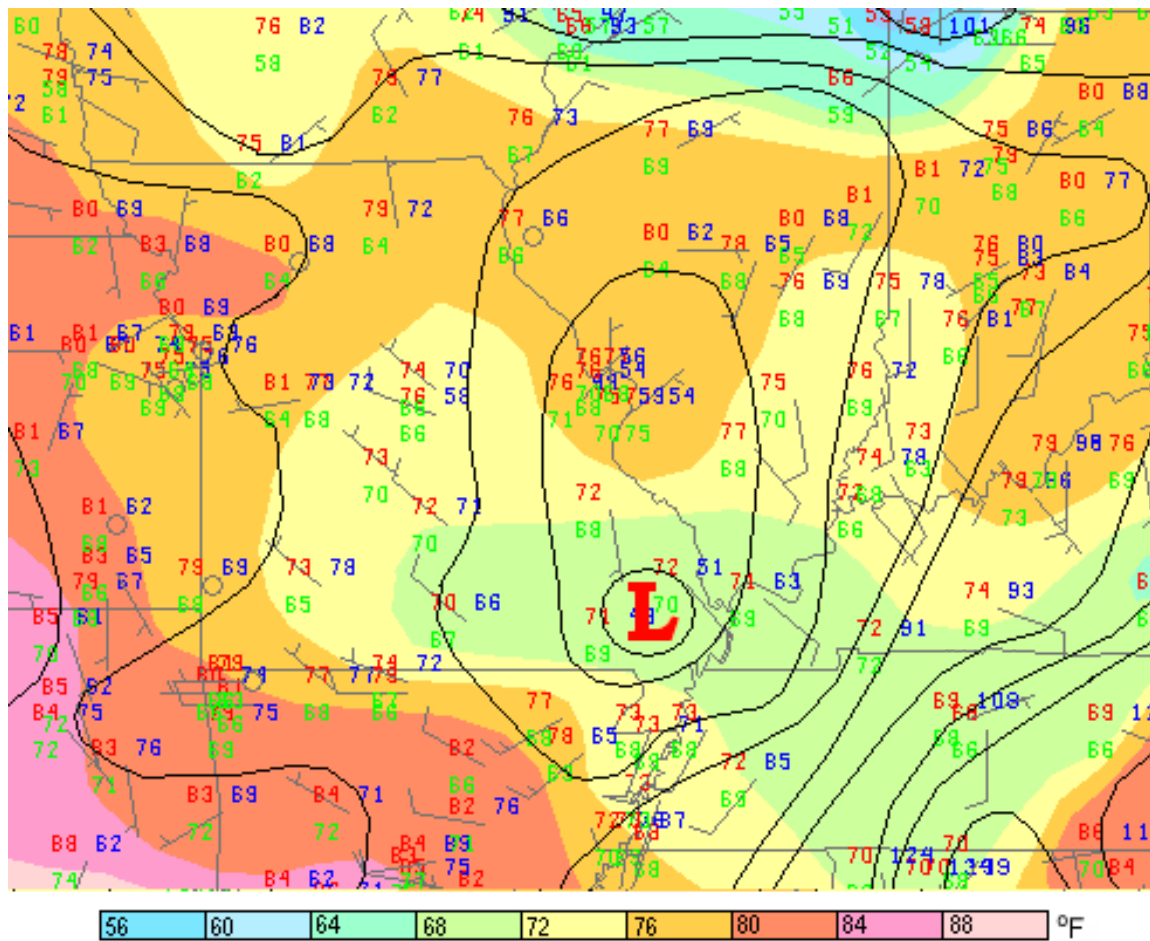
FIG. 2.22. Surface analysis valid 2100 UTC 11 June. Temperature plotted in red, dewpoint in green and surface pressure (minus 1000 and multiplied by 10) in blue. One full barb denotes 10 kt. Black contours denote isobars analyzed every millibar.
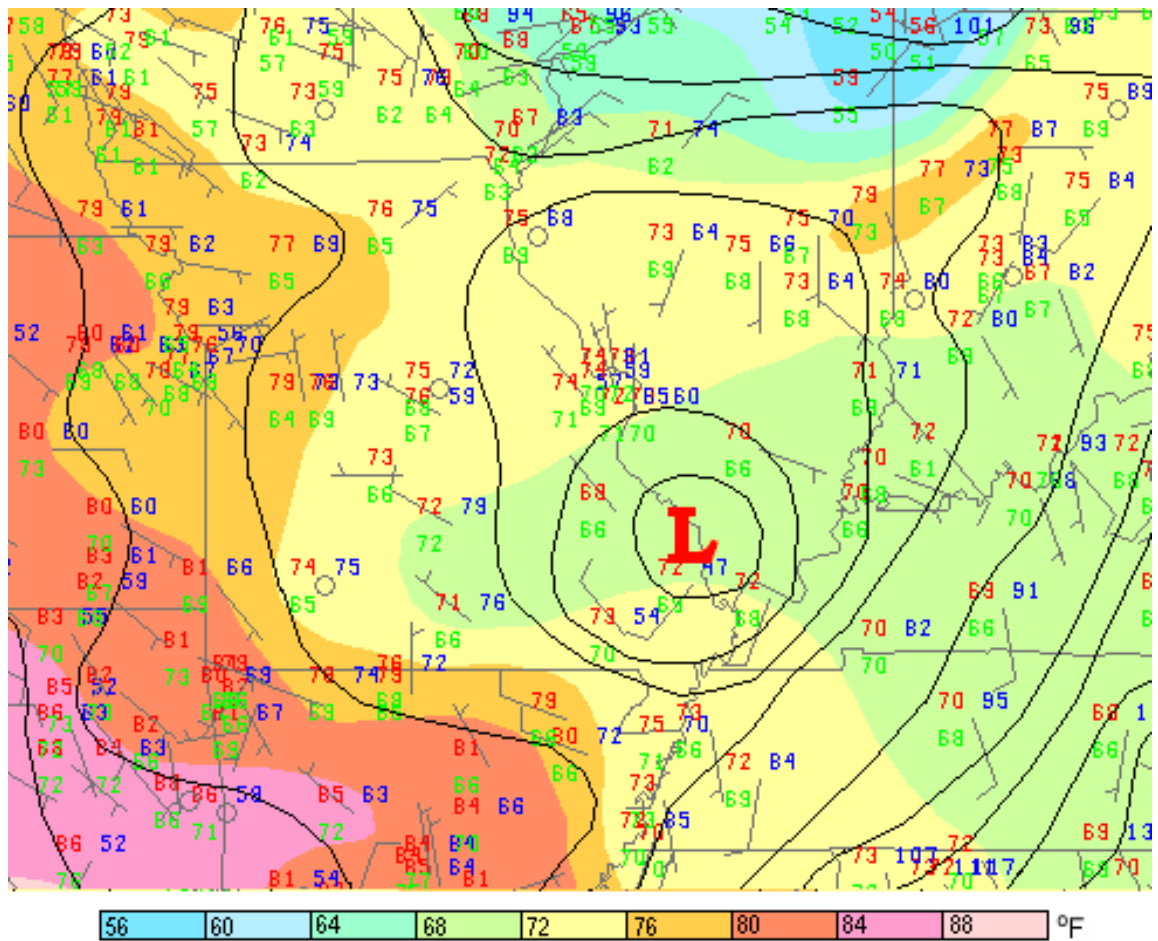
FIG. 2.23. Surface analysis valid 0000 UTC 12 June. Temperature plotted in red, dewpoint in green and surface pressure (minus 1000 and multiplied by 10) in blue. One full barb denotes 10 kt. Black contours denote isobars analyzed every millibar.
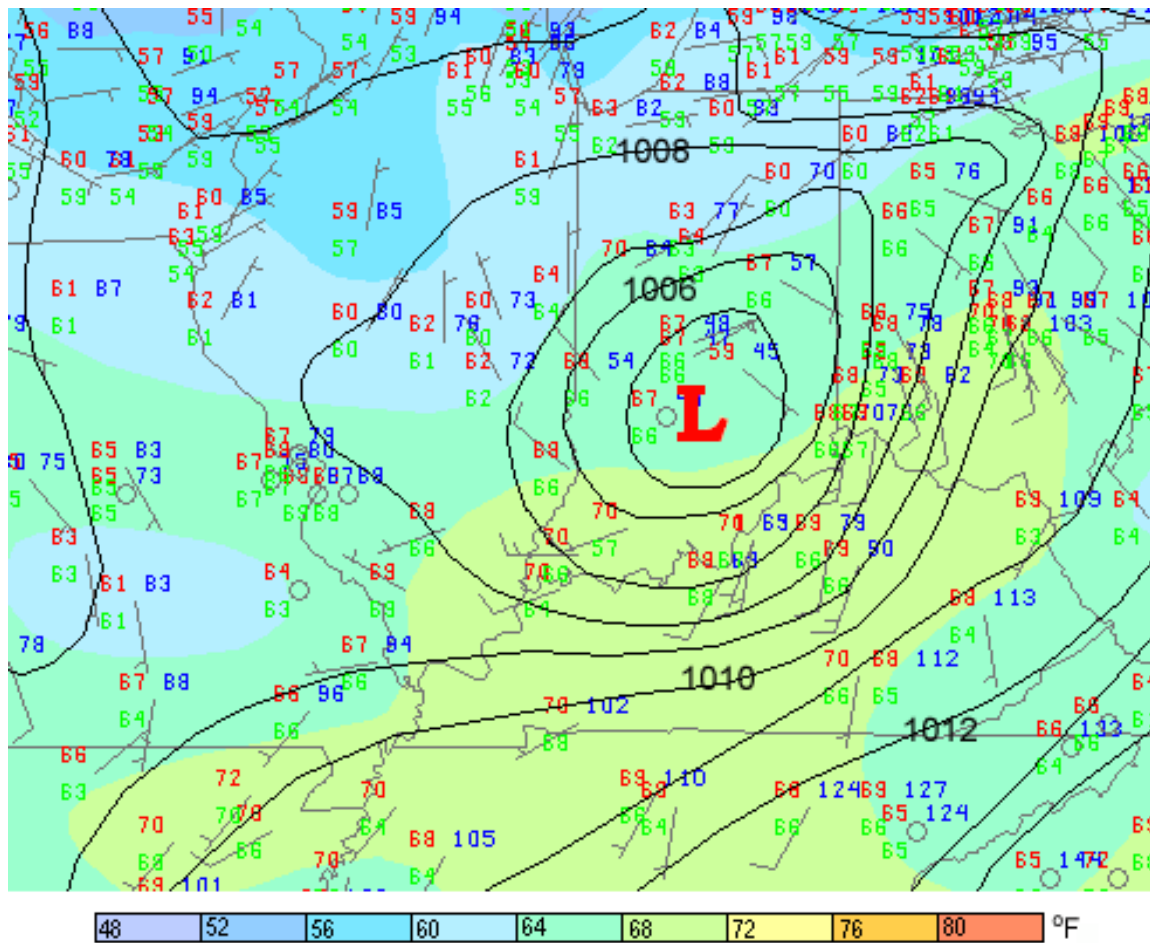
FIG. 2.24. Surface analysis valid 1200 UTC 12 June. Temperature plotted in red, dewpoint in green and surface pressure (minus 1000 and multiplied by 10) in blue. One full barb denotes 10 kt. Black contours denote isobars analyzed every millibar.
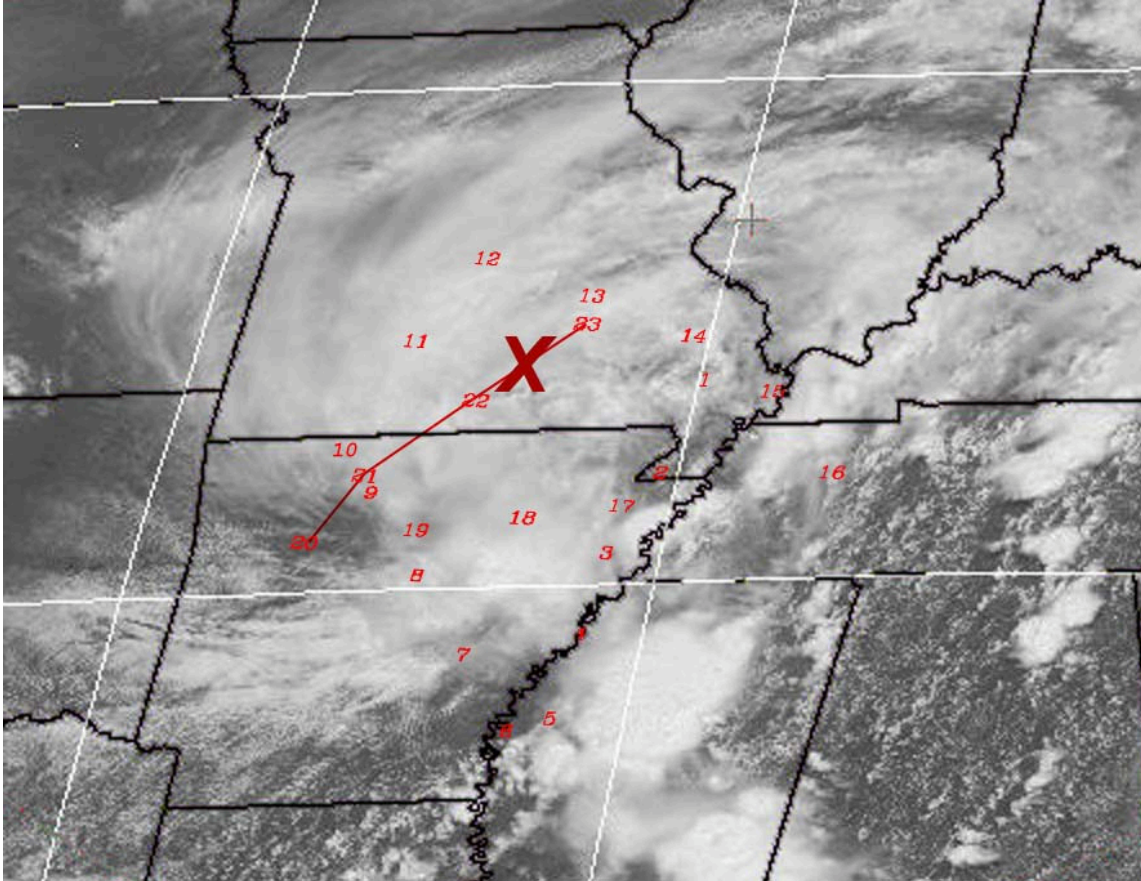
FIG. 2.25. Dropsonde locations overlain onto 1700 UTC 11 June NOAA GOES-10 1-km visible satellite imagery. Numbers correspond to the sequence in which each dropsonde was released. Gray cross denotes Mid-America Regional Airport. Red 'X' denotes approximate center of midlevel circulation. Red line denotes location of vertical cross section in Fig. 2.33.
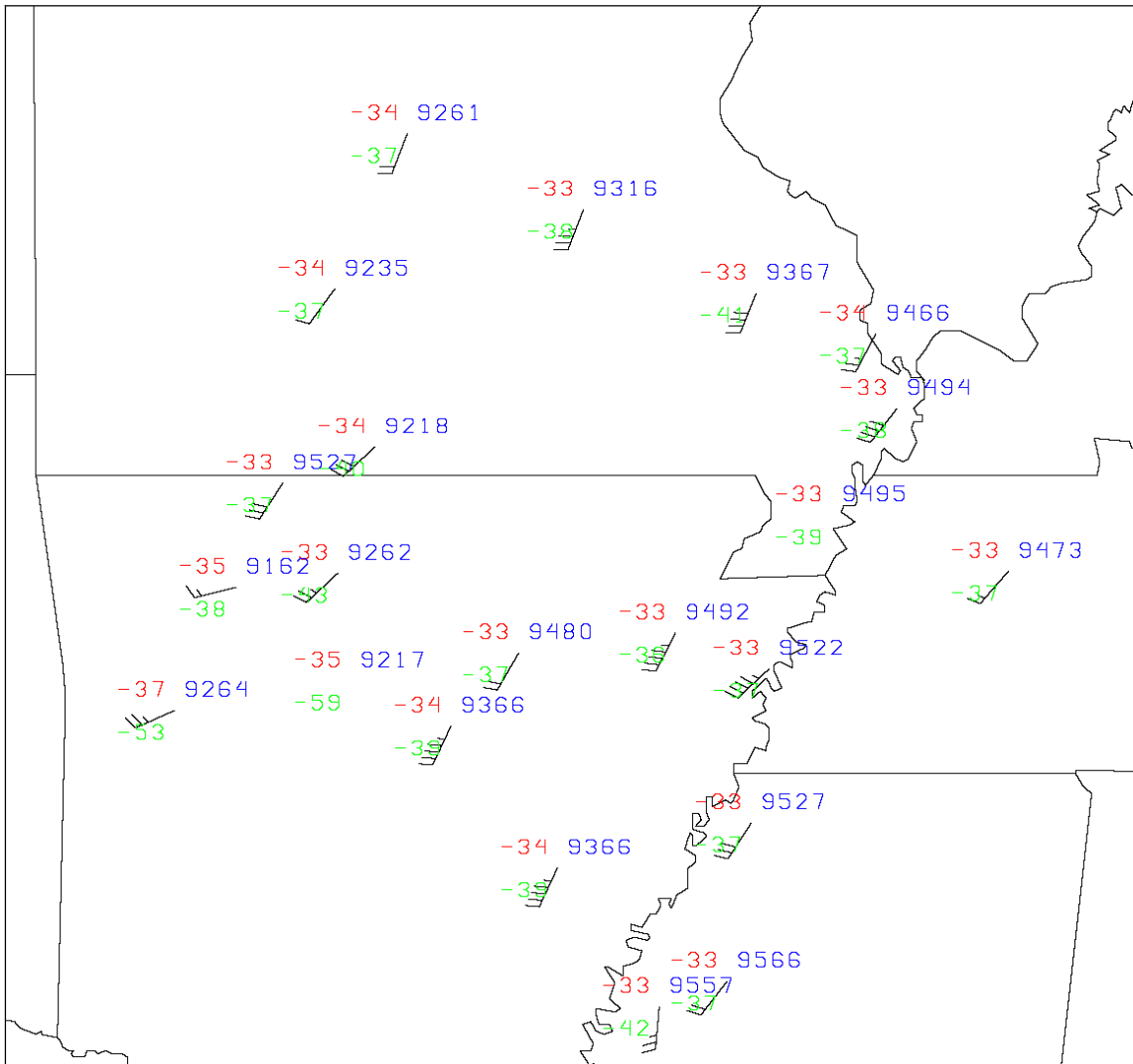
FIG. 2.26. 300 hPa BAMEX dropsonde observations of temperature (red, in degrees Celsius), dewpoint (green), height (blue, in meters) and wind (one full barb denotes 10 knots). Data adjusted with respect to approximate MCV center at 1730 UTC 11 June.
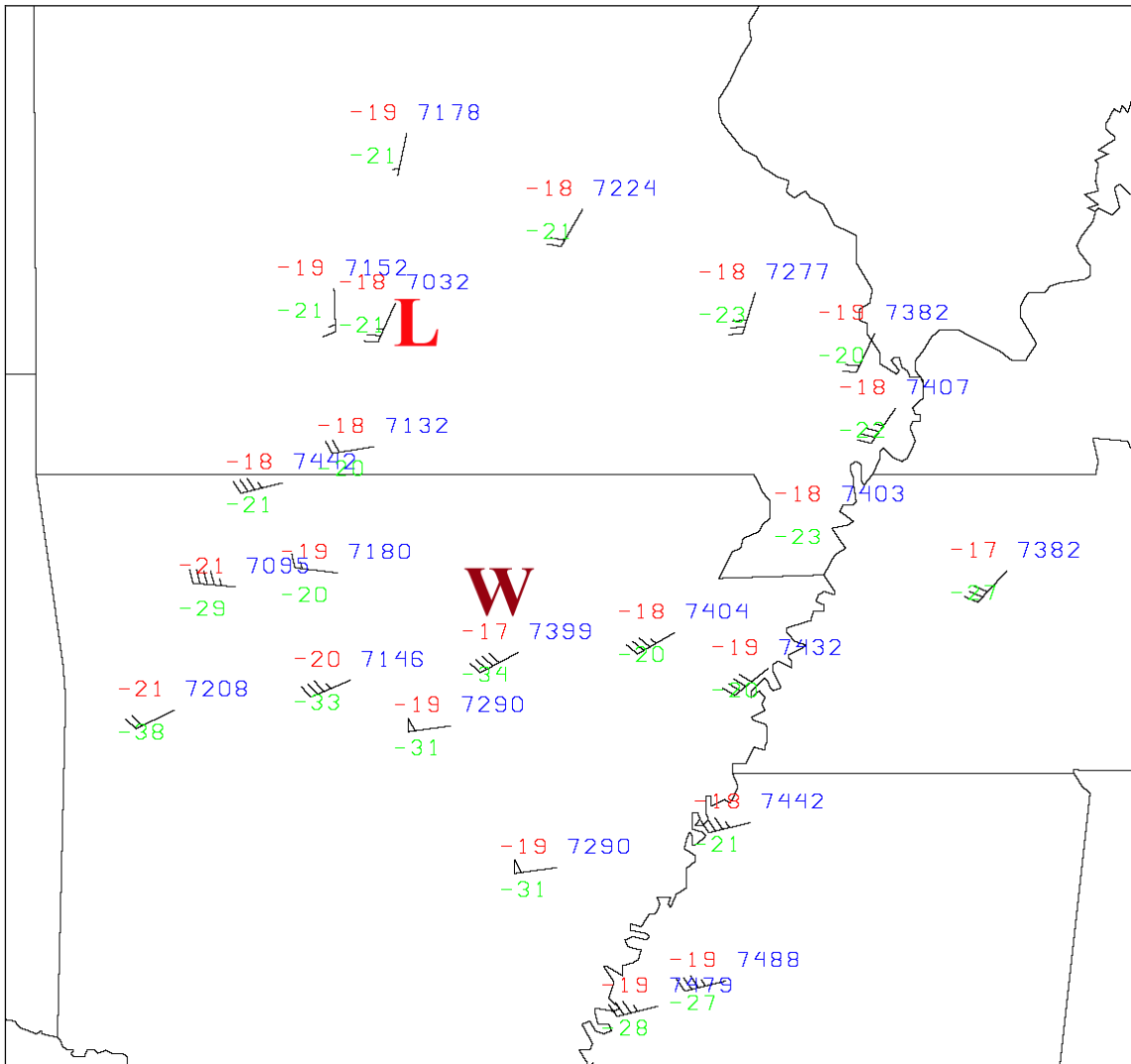
FIG. 2.27. 400 hPa BAMEX dropsonde observations of temperature (red, in degrees Celsius), dewpoint (green), height (blue, in meters) and wind (one full barb denotes 10 knots). Red '*L*' denotes approximate location of height minimum and maroon *'W'* denotes approximate location of warm core. Data adjusted with respect to approximate MCV center at 1730 UTC 11 June.
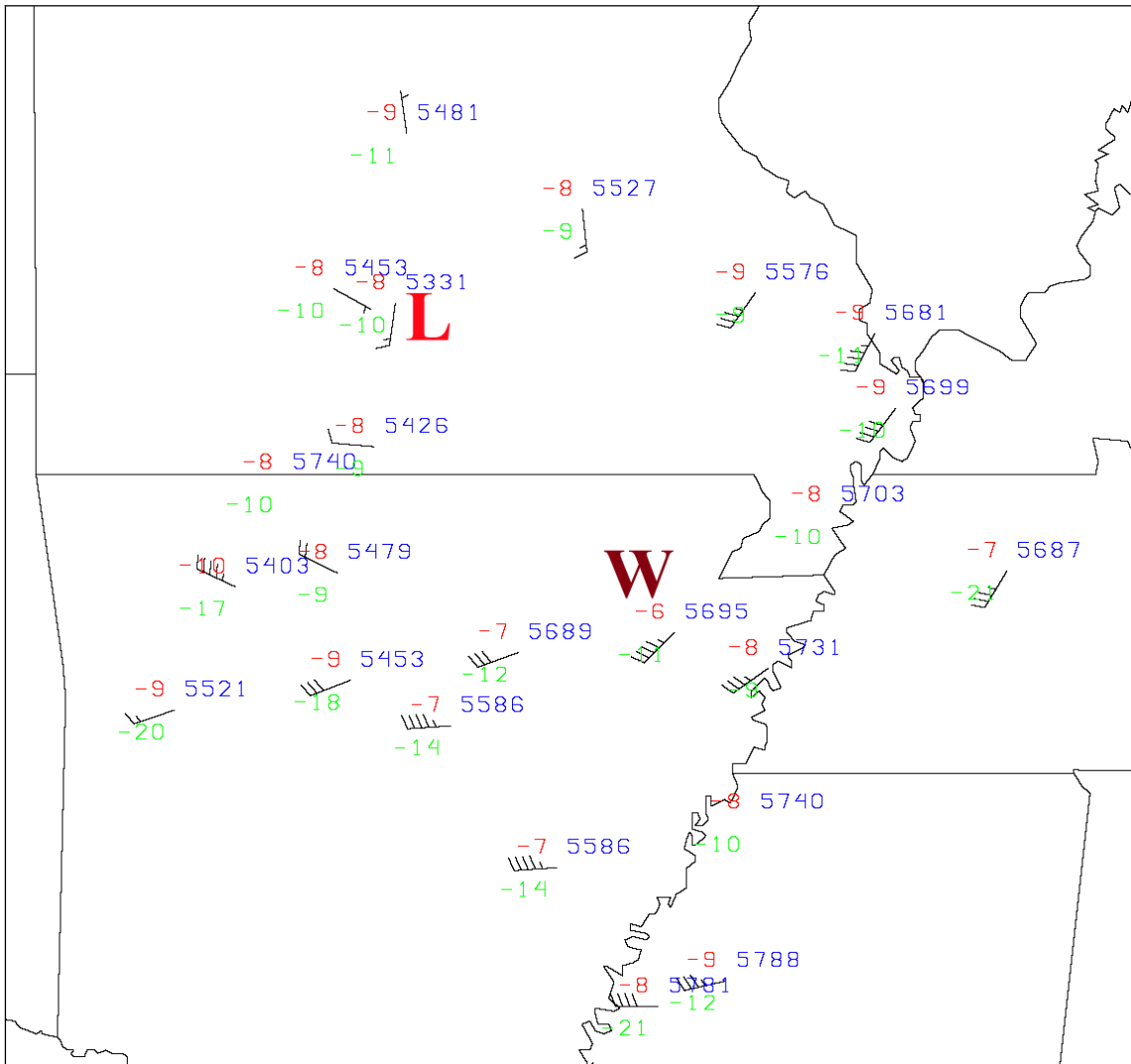
FIG. 2.28. 500 hPa BAMEX dropsonde observations of temperature (red, in degrees Celsius), dewpoint (green), height (blue, in meters) and wind (one full barb denotes 10 knots). Red '*L*' denotes approximate location of height minimum and maroon *'W'* denotes approximate location of warm core. Data adjusted with respect to approximate MCV center at 1730 UTC 11 June.
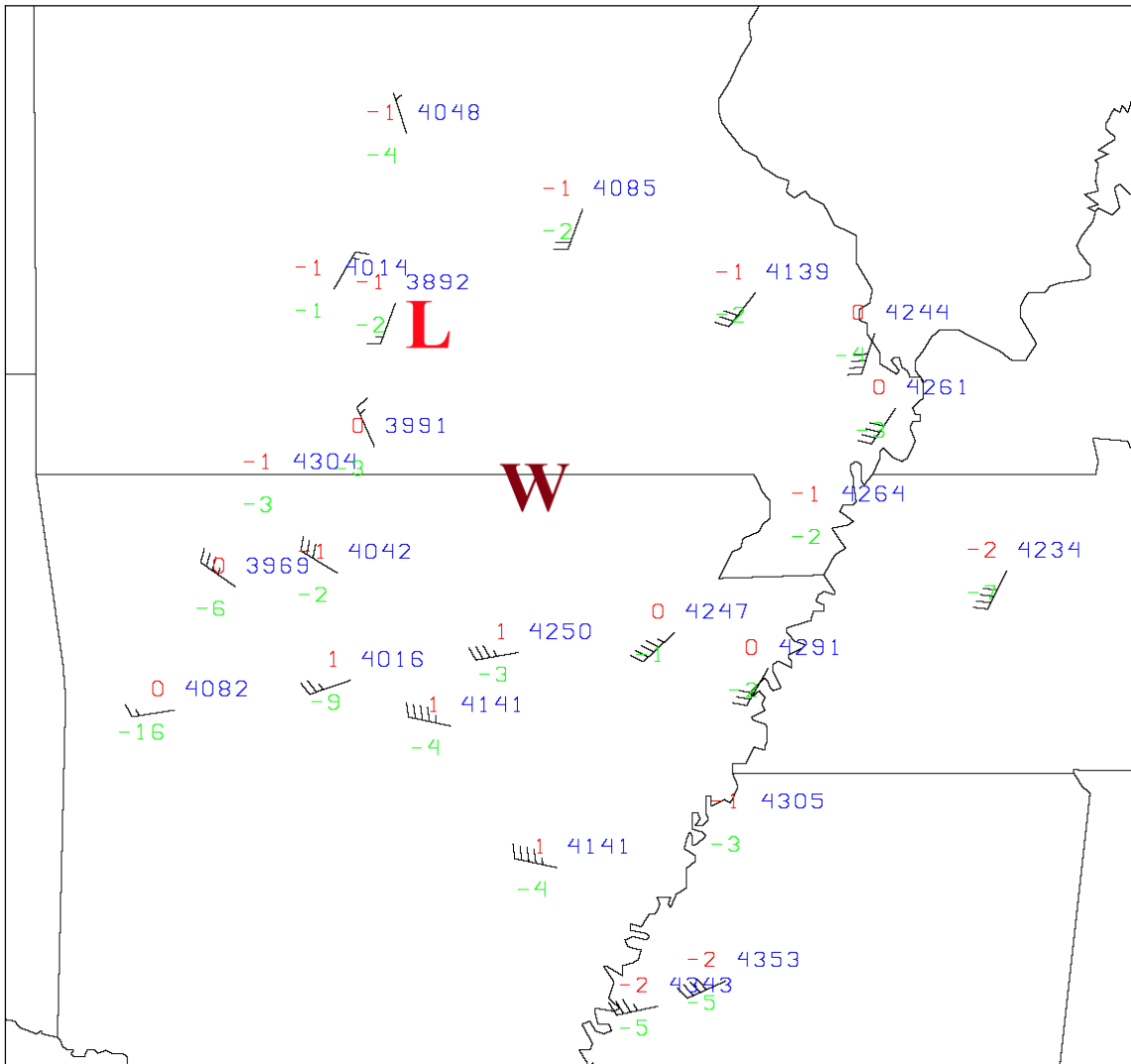
FIG. 2.29. 600 hPa BAMEX dropsonde observations of temperature (red, in degrees Celsius), dewpoint (green), height (blue, in meters) and wind (one full barb denotes 10 knots). Red '*L*' denotes approximate location of height minimum and maroon *'W'* denotes approximate location of warm core. Data adjusted with respect to approximate MCV center at 1730 UTC 11 June.
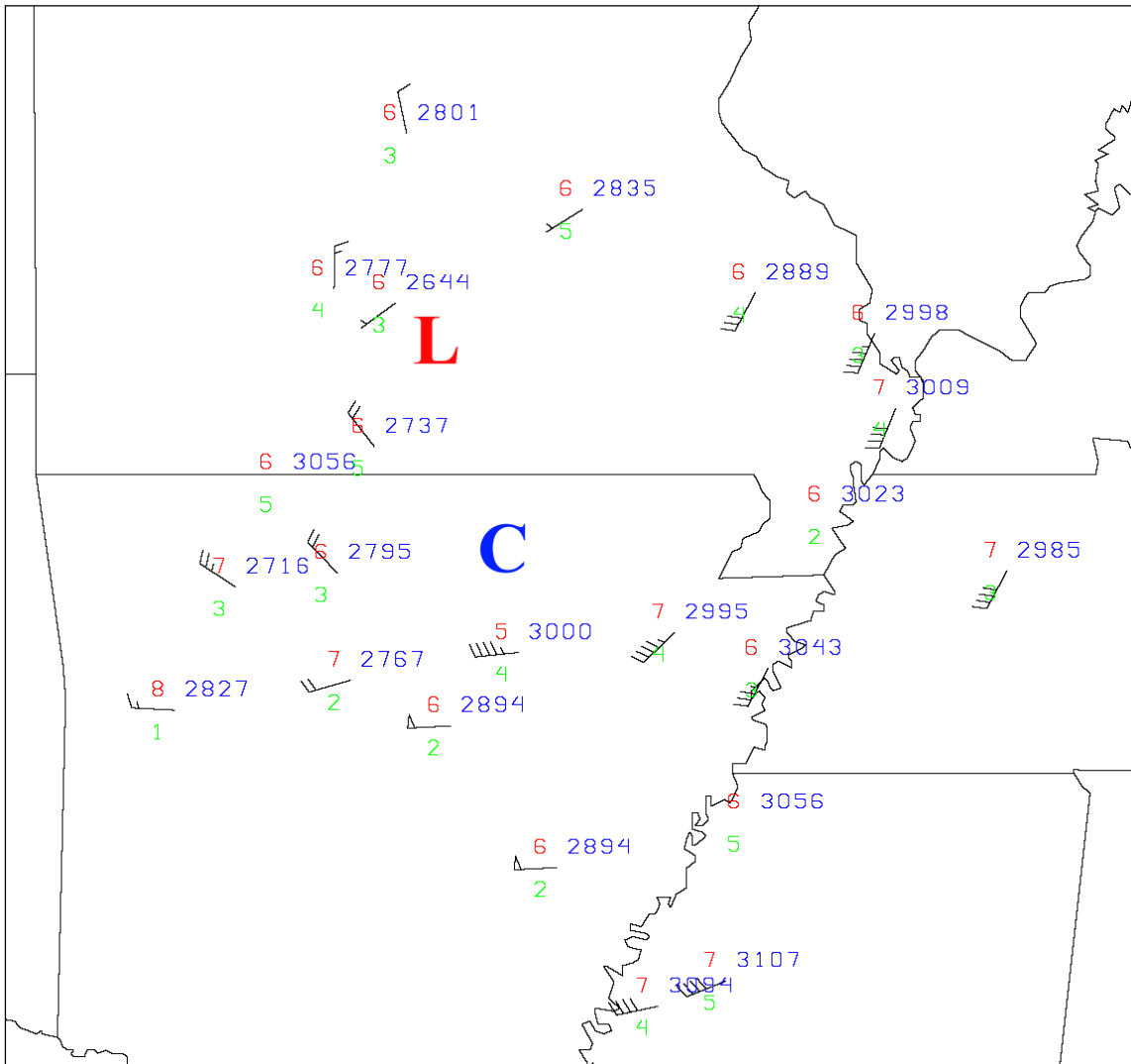
FIG. 2.30. 700 hPa BAMEX dropsonde observations of temperature (red, in degrees Celsius), dewpoint (green), height (blue, in meters) and wind (one full barb denotes 10 knots). Red '*L*' denotes approximate location of height minimum and blue *'C'* denotes approximate location of cold core. Data adjusted with respect to approximate MCV center at 1730 UTC 11 June.
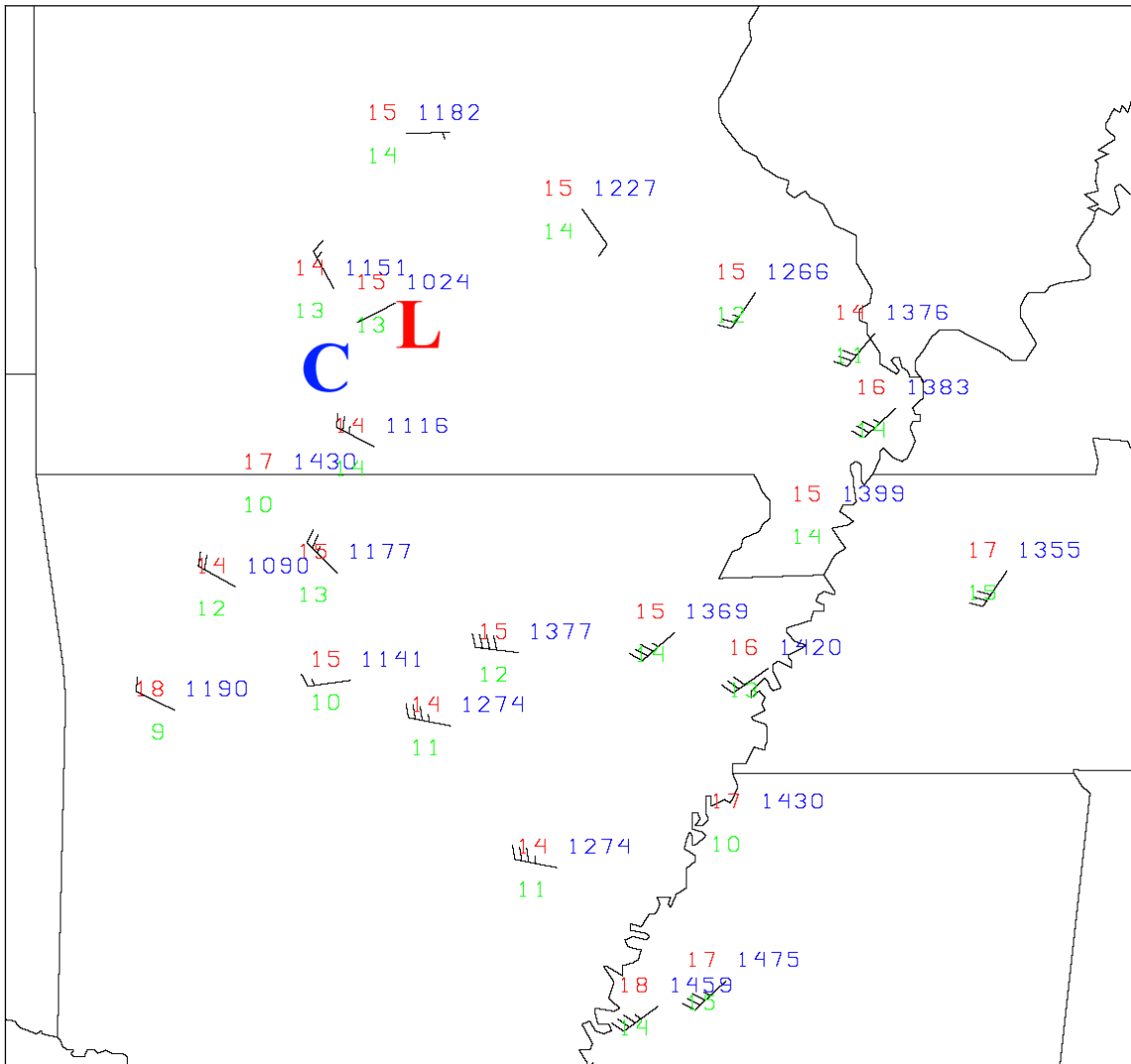
FIG. 2.31. 850 hPa BAMEX dropsonde observations of temperature (red, in degrees Celsius), dewpoint (green), height (blue, in meters) and wind (one full barb denotes 10 knots). Red '*L*' denotes approximate location of height minimum and blue *'C'* denotes approximate location of cold core. Data adjusted with respect to approximate MCV center at 1730 UTC 11 June.
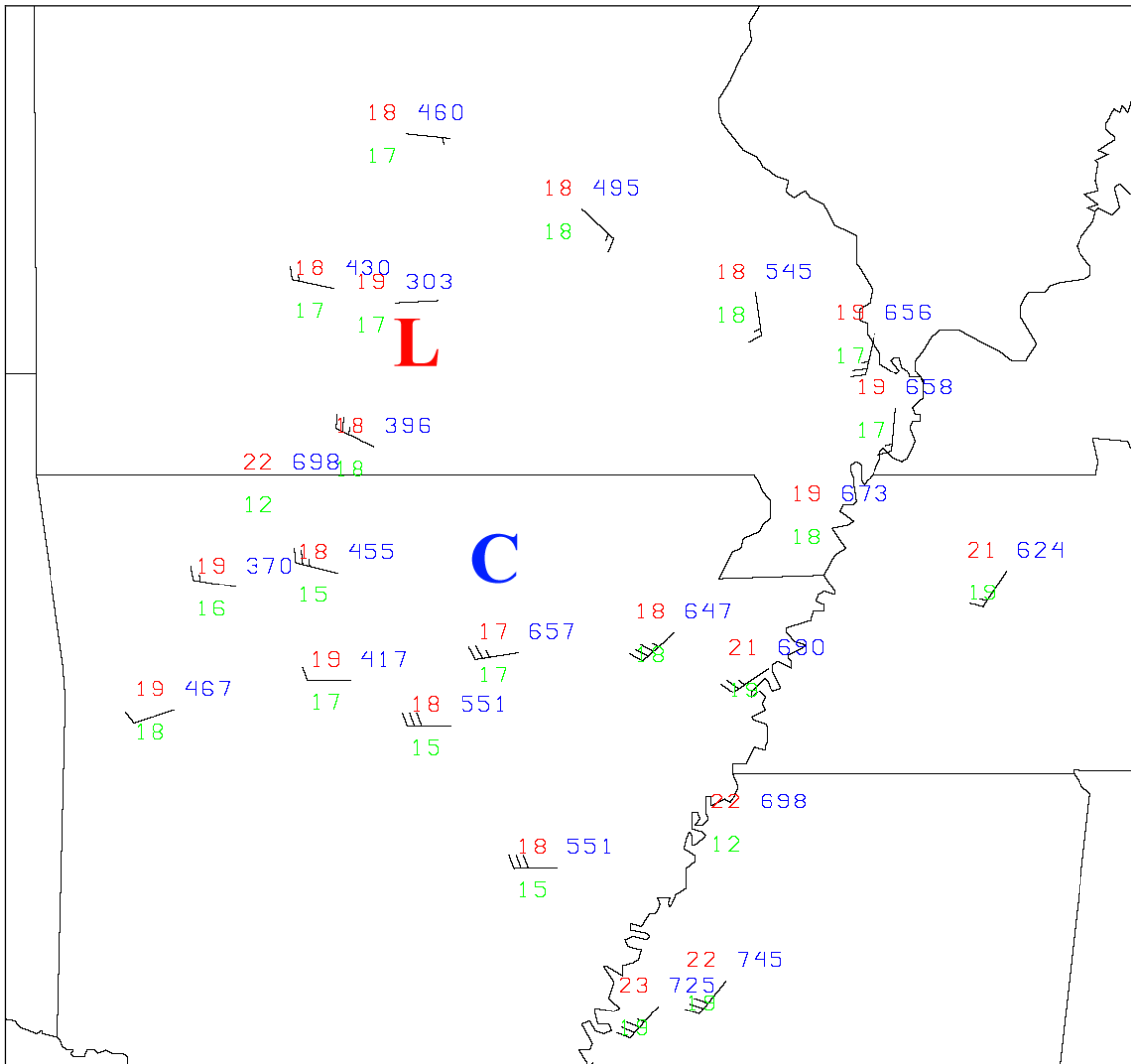
FIG. 2.32. 925 hPa BAMEX dropsonde observations of temperature (red, in degrees Celsius), dewpoint (green), height (blue, in meters) and wind (one full barb denotes 10 knots). Red '*L*' denotes approximate location of height minimum and blue *'C'* denotes approximate location of cold core. Data adjusted with respect to approximate MCV center at 1730 UTC 11 June.

present the dropsonde height, temperature, dewpoint and wind observations for several

levels from 925 hPa to 300 hPa, adjusted in space to match the respective location to the

MCV center at 1730 UTC. The dropsondes detected a low-level cold core structure

through 700 hPa (Figs. 2.30– 2.32, and a warm core from 600 hPa up to the tropopause

(Figs. 2.26–2.29). This temperature structure would suggest that the maximum PV was

concentrated between 600 and 700 hPa where the vertical potential temperature gradient

was greatest between the low-level cold core and upper level warm core. Theoretically,

this pattern would give an enhanced cyclonic circulation in the area of maximum PV and

an increased anticyclonic influence in the lower and upper levels, and is confirmed as

the strongest cyclonic influence relative to background flow is evident in plots at 500

and 600 hPa (Figs. 2.29 and 2.30) while higher plots suggest an open wave structure up

through 400 hPa. Additional cyclonic vorticity is evident at 700 hPa, and a closed

circulation is detected at 850 and 925 hPa which was not evident in wind profiler data

roughly twelve hours earlier (not shown). The circulation center at all levels appears to

be near the central Missouri/Arkansas border. The evidence of low-level cyclonic

vorticity in the dropsonde data suggests growth of a low-level circulation, given the

absence of a sustained low-level vortex in the profiler data between 0000 UTC and 1200

UTC 11 June. The development of the low-level vortex will be explored in greater

detail in Chapter IV.

Figure 2.33 shows a cross section of dropsonde data from southwest to northeast

across the MCV circulation, using four consecutive dropsonde releases (cross section

denoted as red line in Fig. 2.25). Potential temperature is contoured in green, and height
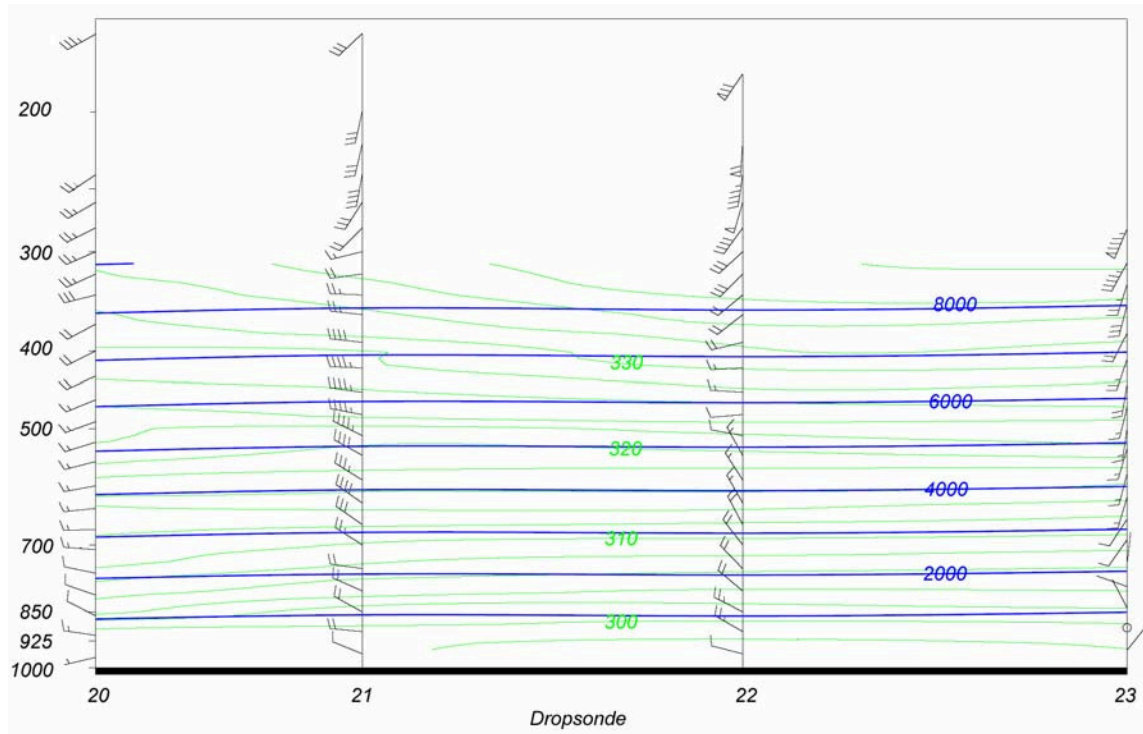
FIG. 2.33. Southwest to northeast-oriented cross section across four dropsondes (denoted as a red line in Fig. 2.20). Potential temperature represented by green contours and heights denoted in blue. One full barb denotes 10 knots.

in blue. The surface cold pool is very evident in this cross section, appearing to be at

maximum strength beneath the 304 K surface and slightly to the southwest of dropsonde

22. In the middle troposphere, significant warming, most likely due to the convective

latent heating of the previous night, appears to have taken place between the 324 K and

338 K isentropic surfaces (roughly between 500 and 300 hPa), and between dropsondes

22 and 23. It was shown in Figs. 2.26 – 2.32 that dropsonde 23 measured the lowest

heights at every level which places the lowest heights in this cross section to the

northeast of the cold pool and near the upper-tropospheric warm anomaly.

To further examine the thermodynamic structure of this system, observations at

the 330 K isentropic surface are shown in Fig. 2.34 (roughly 400 hPa; Fig. 2.27). Plots

at this level show that the highest pressures of that surface were measured in northern

Arkansas, very close to the circulation centers detected at 500 and 600 hPa in Figs. 2.28

and 2.29 respectively. This vertical structure matches the Raymond and Jiang (1990)

model placing the midlevel vortex below the warmest upper-tropospheric temperature

anomaly. At the same time, dropsonde data at the 302 K surface in Fig. 2.35 (roughly

850 hPa) shows that close to the MCV, the height of that surface is highest over

southwest Missouri, where the low-level cold pool is strongest. Contradictory to the

simple Raymond and Jiang model (1990), this location displaces the cold pool center

roughly 150 km west of the low-level circulation seen in the 925 hPa plot in Fig. 2.32

and the 1800 UTC surface analysis in Fig. 2.21. The significance of the location of the

surface cold pool with respect to the deepening low-level circulation will be examined in

much greater detail using in Chapter IV.

63
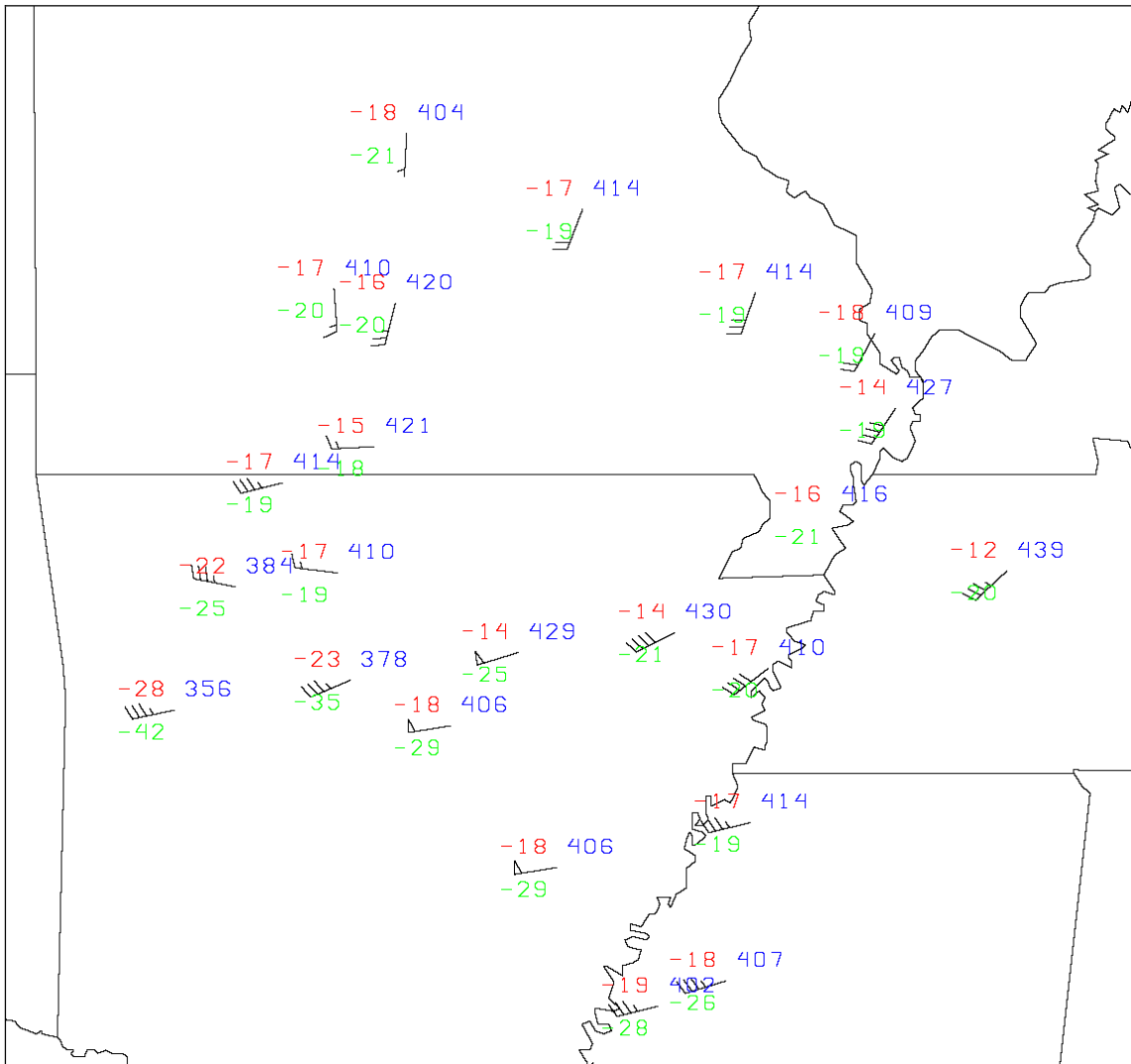
FIG. 2.34. BAMEX dropsonde observations of temperature (red, in degrees Celsius), dewpoint (green), pressure (blue, in hPa) and wind (one full barb denotes 10 knots) at the 330 K surface. Data adjusted with respect to approximate MCV center at 1730 UTC 11 June.
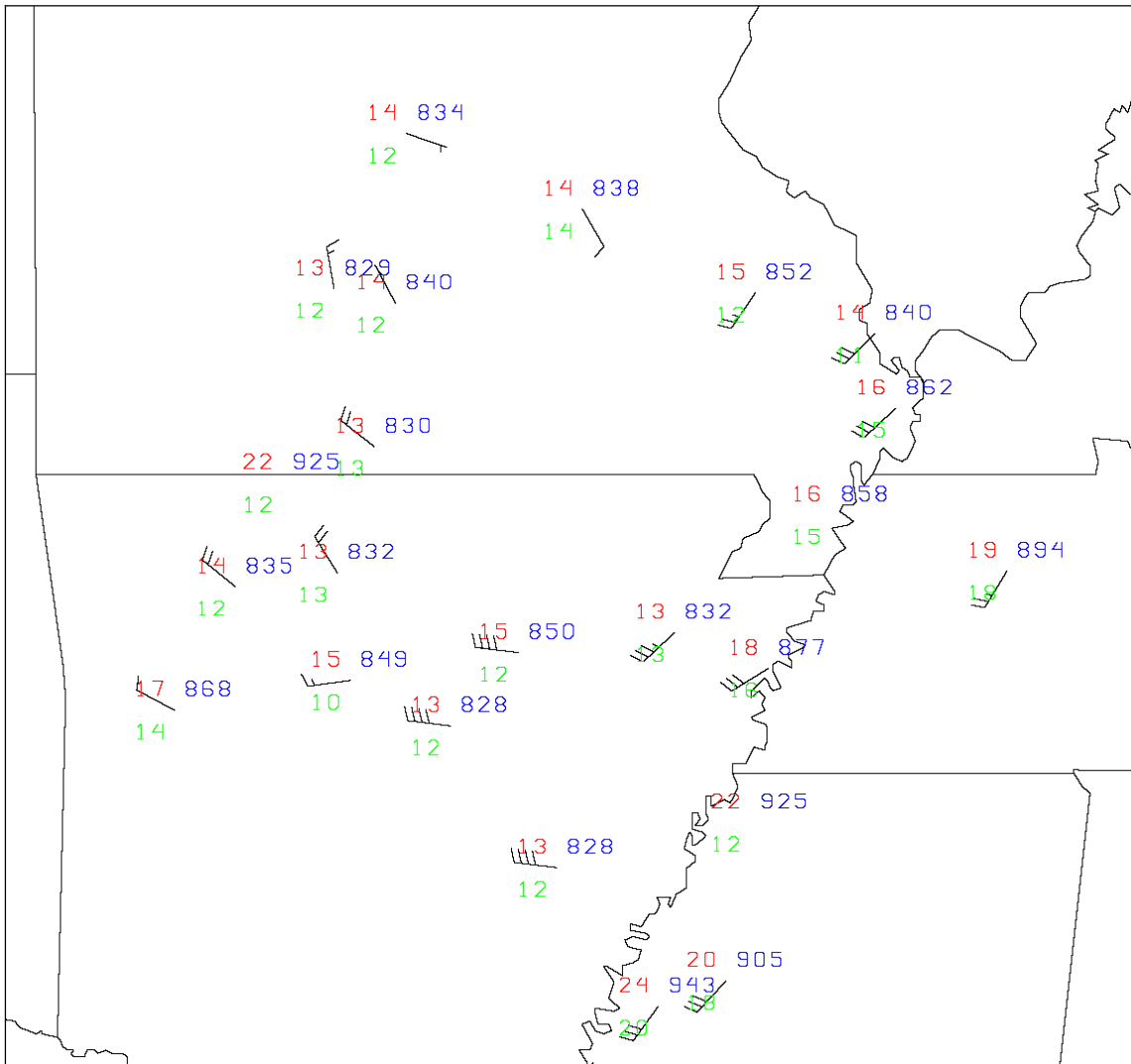
FIG. 2.35. BAMEX dropsonde observations of temperature (red, in degrees Celsius), dewpoint (green), pressure (blue, in hPa) and wind (one full barb denotes 10 knots) at the 302 K surface. Data adjusted with respect to approximate MCV center at 1730 UTC 11 June.
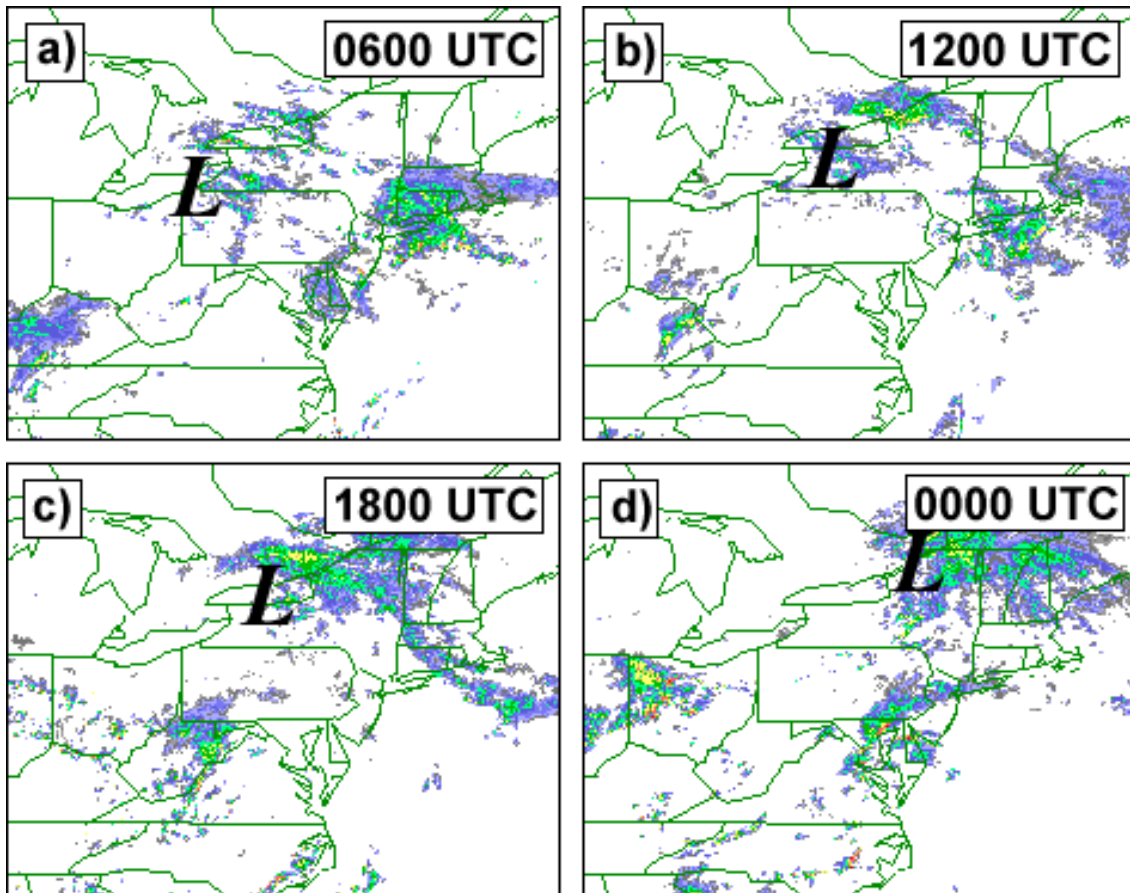
FIG. 2.36.   WSR88D reflectivity from 0600 UTC 13 June to 0000 UTC 14 June.

A second convective episode, albeit much weaker, was triggered during the local afternoon hours of 12 June over eastern Ohio (Fig. 2.17e–f). The circulation continued to be evident on radar overnight into the local morning of 13 June as it entered New York state (Fig. 2.36). After 0000 UTC 14 June (Fig. 2.36d), the circulation was no longer evident on radar, having last been noted in northeast New York and southeast Ontario. Thus, the circulation lasted on radar a total of about 66 hours, from 0600 UTC 11 June to 0000 UTC 14 June and had traveled a distance of over 2200 km from east central Oklahoma to northeast New York state. However, this study will only focus on the time period between 0000 UTC 10 June and 0000 UTC 12 June, capturing the West Texas convection, the MCS over Oklahoma, and the first secondary convective episode during the local afternoon of 11 June.

2.5 Summary and discussion

Convection during the local morning hours of 10 June over New Mexico and western Texas may have played an important role in the eventual evolution of the IOP 8 MCV. Weak midlevel circulation behind this convection, evident in radar loops, hints that an enhancement of the existing midlevel shortwave or even an MCV may have resulted from this early morning activity. Extrapolating the circulation forward through time shows that the Oklahoma MCS later that evening fired very close to the remnants of the convection from that morning. As was described in 1.2.3, stronger ambient vorticity will theoretically help lower the local Rossby radius of deformation so that convection will be more efficient in yielding a net warming of the troposphere, and hence aiding the

formation of an MCV. It is possible that the convection from earlier that day enhanced

the relative vorticity within the midlevel shortwave, and supported MCV formation

through a decreased Rossby radius when convection fired later that evening.

Additionally, it was shown that remnant cloud cover had enhanced surface temperature

gradients near a boundary in Oklahoma which may have further aided in convective

development. The importance of the early morning convection of 10 June to the

eventual evolution of the Oklahoma MCS and resulting MCV will be explored in much

greater detail in Chapters III and IV.

　　　　According to the simple model of Raymond and Jiang (1990), PV will be

increased in areas directly below the maximum midlevel warming and directly above the

low-level cold pool, where vertical potential temperature gradients are strongest. The

BAMEX dropsondes supported the former case, in which the lowest heights were

detected immediately below region of warmest midlevel temperatures. It also appears

that the strongest midlevel circulation was near the location of the midlevel height

minimum. However, an analysis of the 302 K surface (representing the top of the cold

pool) shows that the height of that level was highest to the west and south of the

midlevel circulation at 1800 UTC instead of directly below it. As noted in the surface

analysis, the surface circulation associated with the MCV was displaced roughly 100 km

east of the remnant surface cold pool. However, the degree to which the center of

circulation at low- and midlevels was displaced due to interaction between

environmental and MCV-induced shear is unknown. The surface vortex directly beneath

the midlevel MCV begins to strengthen around 1500 UTC (Fig. 2.20) when the MCV

becomes displaced ahead of the surface cold pool. By 1800 UTC, weak convection formed directly over the surface vortex which is when the surface pressure begins to fall. Additionally, widespread convection fires several hundred kilometers ahead of the MCV around 1500 UTC. It is possible that the displacement of the surface vortex into warmer low-level temperatures allowed for the midlevel vortex to extend farther downward due to an increase in vertical penetration depth resulting from decreased stratification of potential temperature surfaces in a warmer environment (discussed in section 1.2.5). It also appears possible that convection during the local afternoon of 11 June played a role in the downward development of the MCV, as the surface vortex deepened as weak convection developed directly overhead. The reason behind the downward vorticity growth cannot to be determined using strictly the observations provided in this chapter. The exact role of secondary convection and strength and location of the surface cold pool in the downward growth of the MCV and the evolution of the surface vortex will be explored in much greater detail through numerical simulations in Chapters III and IV.

CHAPTER III

INTRODUCTION TO MCV PREDICTABILITY THROUGH DISCREPANCY IN

MODEL FORECASTS

3.1. Introduction

Preceding the investigation of the IOP 8 MCV dynamics via numerical

simulation in Chapter IV, this chapter gives a brief overview of eight separate model

simulations of the IOP 8 MCV in an effort to illustrate the extreme sensitivity of MCV

predictability to the forecast models. The analysis focuses especially on differences in

horizontal model resolution and convective parameterization and the corresponding

impacts on MCV prediction. This chapter also gives a brief introduction to the model

that will be employed for the in-depth dynamic analyses using probabilistic forecasts in

Chapter IV, and outlines issues surrounding each model.

3.2. Model description

The first model employed is the recently developed Weather Research and

Forecast model, or WRF (Michalakes et al. 2001). The WRF model was introduced with

the goal of developing an advanced mesoscale forecast and assimilation system, and to

accelerate research advances into operations. This study uses version 1.3 of the WRF

run on a real-time configuration at NCAR. The WRF was run at two horizontal

resolutions: a 10-km resolution (WRF-10), which employs cumulus and microphysics

parameterizations and a 4-km resolution (WRF-4) which employs microphysics to explicitly predict convection. WRF-4 uses 500 × 500 horizontal grid points, and WRF-10 is run using 310 × 244 grid points, both with 35 vertical levels. Both WRF-4 and WRF-10 use the Yonsei University (YSU) boundary layer scheme (Noh et al. 2001), and Lin Microphysics scheme (derived from the original scheme in Lin et al.; 1983). The WRF-10 forecasts use an updated version of the Kain-Fritsch convection scheme (Kain and Fritsch 1993). No nesting of WRF is used. All domains are initialized using output from the latest available operational Eta model (Black, 1994). Lateral boundary conditions are specified from 3-hour output from the corresponding Eta forecast. Each model run extends 36 hours from two initializations at 0000 UTC on 10 and 11 June, providing four separate WRF forecasts.

The second model employed is the two-way nested NCAR/PSU nonhydrostatic Mesoscale Model (MM5), version 2 (Dudhia 1993), initialized at 0000 UTC on 10 and 11 June, extending 48 hours from each initialization at three-hour forecast increments. The model is run at both 10-km (MM5-10) and 30-km (MM5-30) horizontal resolutions. MM5-10 uses 310 × 244 horizontal grid points, and MM5-30 uses 190 × 120 horizontal grid points. Both versions use 27 vertical layers and employ the Mellor-Yamada PBL scheme (Mellor and Yamada 1982) and the Reisner microphysics scheme with graupel (Reisner et al. 1998). MM5-30 utilizes the Grell cumulus parameterization scheme (Grell 1993) and MM5-10 forecasts convection explicitly. Both versions use the operational 6-hour Eta model as lateral boundary conditions. The model domains for both the WRF and MM5 simulations are given in Fig. 3.1.
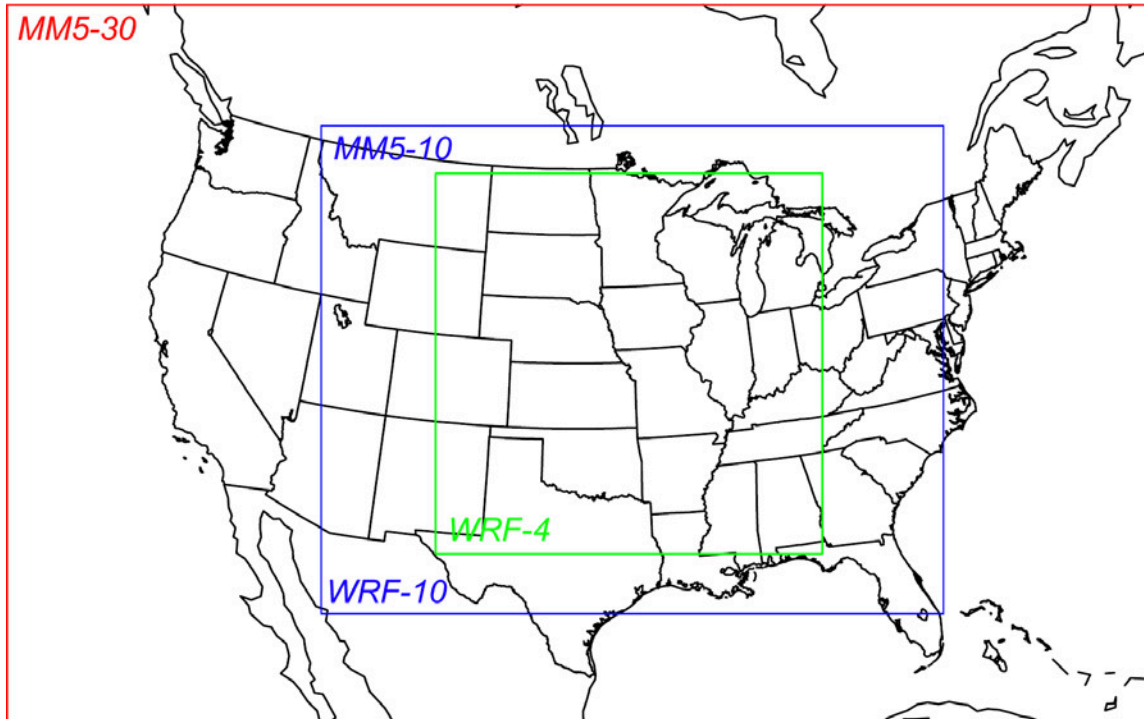
FIG. 3.1. Model domains for MM5-30 (red), MM5-10 and WRF-10 (blue) and WRF-4 (green).

3.3. Model comparison

It is first necessary to choose the model which shows the best performance in predicting each stage of the MCV lifecycle, in particular the initial MCS and midlevel vortex formation (stage I), and secondary convection and vortex growth at the surface (stage II). As will be described in later sections, three of the four models show worse performance in forecasting the MCS when initialized at 0000 UTC on 11 June compared to their respective forecasts initialized on the 10th. Additionally, WRF forecasts only extend 36 hours from initialization, and the simulations initialized on 10 June do not cover stage II of the MCV. Therefore, the part of the model comparison regarding stage I of the MCV will analyze those models run at 0000 UTC on 10 June (denoted hereafter as WRF-4A, etc.) and stage II will be evaluated using those models initialized at 0000 UTC 11 June (denoted WRF-4B, etc.).

3.3.1. MCV precursor: West Texas MCS and resulting midlevel circulation

As described in Chapter II, a weak MCV or an enhancement of the midlevel wave had resulted from convection over New Mexico and west Texas earlier on 10 June (Fig. 2.3). Of the four model simulations, MM5-30A appears to have the best performance for this early stage, with forecast strong convection and associated strong midlevel vorticity (Fig. 3.2). This same model forecasts an area of 10×10^{-5} s^{-1} relative vorticity over northwest Texas at 1500 UTC (Fig. 3.2c). Even though there is little convection simulated in MM5-10, it forecasts relatively high midlevel vorticity in the same area at 1500 UTC (Fig. 3.3c), stronger than that by MM5-30. Neither WRF-10

FIG. 3.2. MM5-30 initialized 0000 UTC 10 June forecast of reflectivity (shaded), 500 hPa relative vorticity (red solid in 10^{-5} s^{-1}, contoured every 10^{-4} s^{-1}) and 500 hPa heights (m) at 3-hour intervals beginning 0900 UTC 10 June.
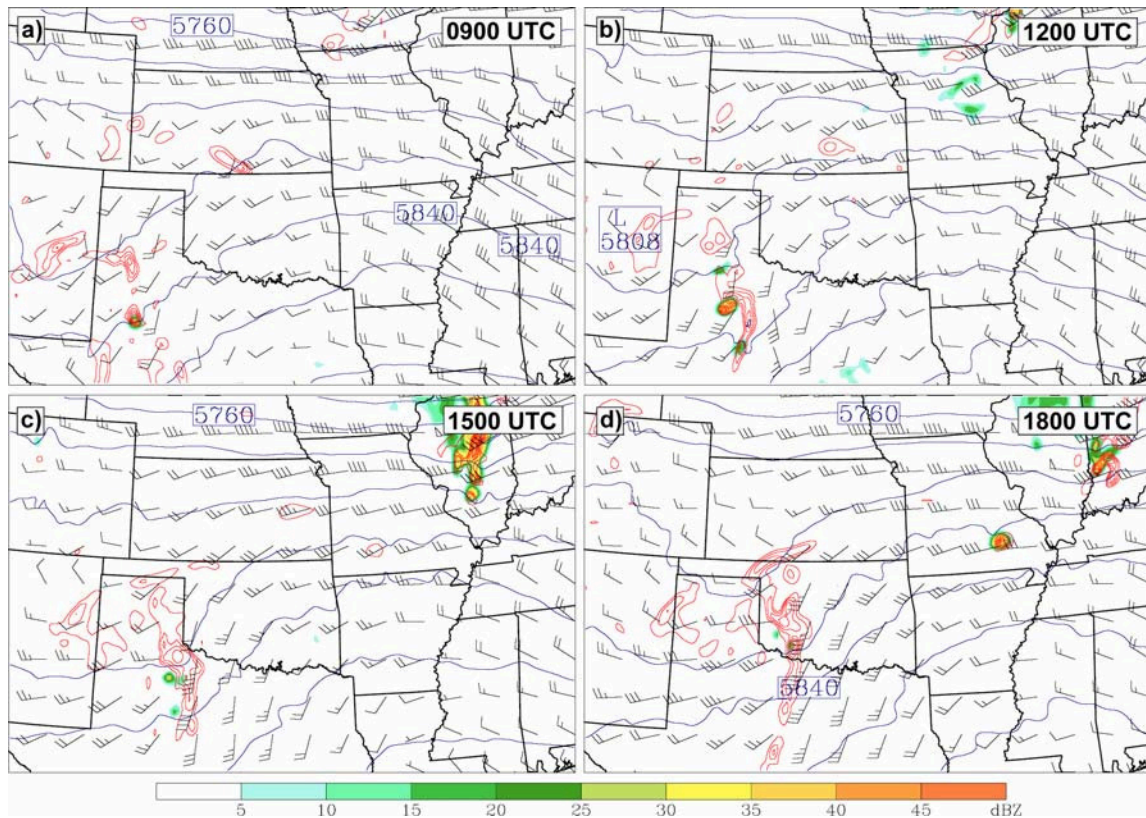
FIG. 3.3. MM5-10 initialized 0000 UTC 10 June forecast of reflectivity (shaded), 500 hPa relative vorticity (red solid in 10^{-5} s^{-1}, contoured every 10^{-4} s^{-1}) and 500 hPa heights (m) at 3-hour intervals beginning 0900 UTC 10 June.
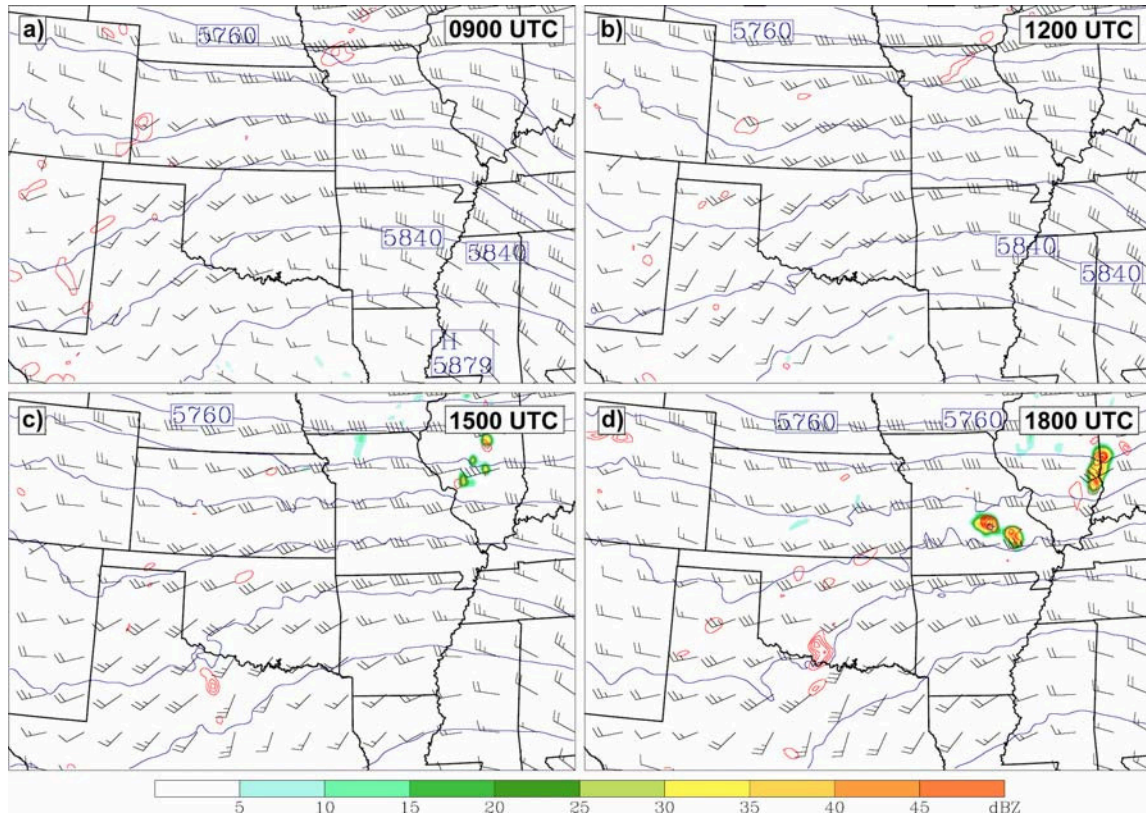
FIG. 3.4. WRF-10 initialized 0000 UTC 10 June forecast of reflectivity (shaded), 500 hPa relative vorticity (red solid in 10^{-5} s^{-1}, contoured every 10^{-4} s^{-1}) and 500 hPa heights (m) at 3-hour intervals beginning 0900 UTC 10 June.
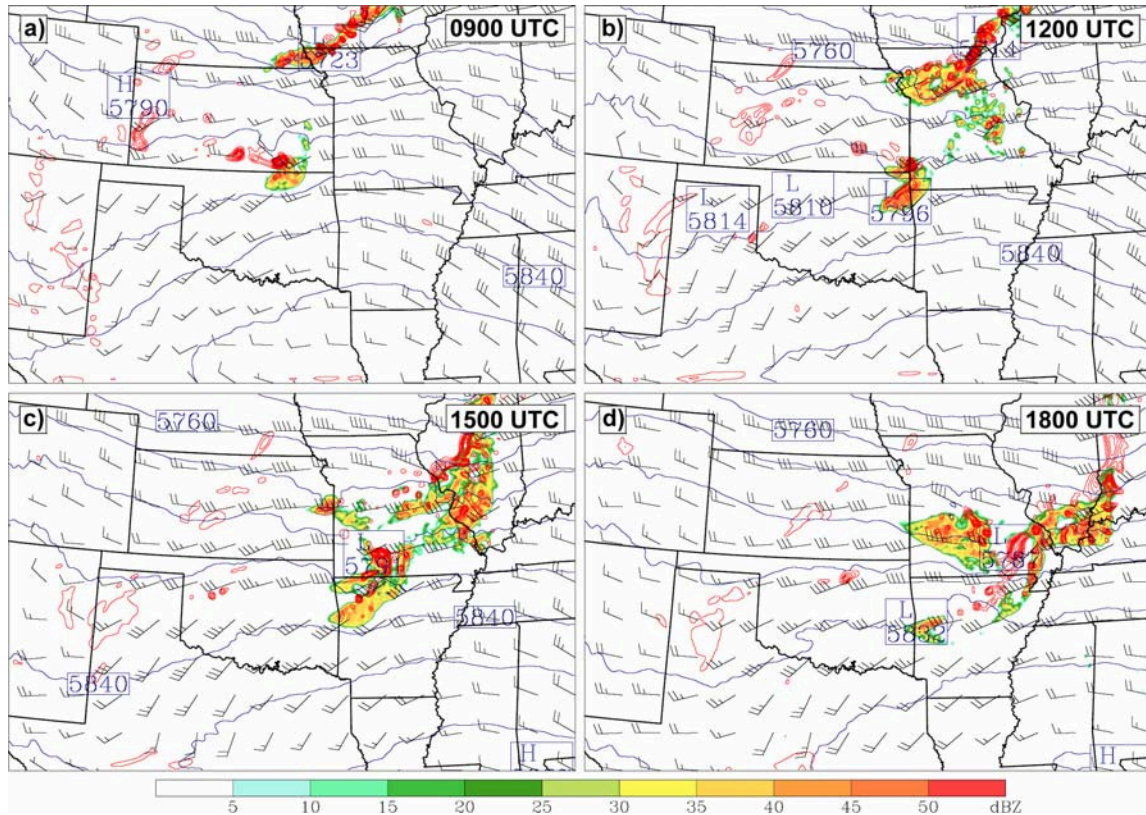
FIG. 3.5. WRF-4 initialized 0000 UTC 10 June forecast of reflectivity (shaded), 500 hPa relative vorticity (red solid in 10^{-5} s^{-1}, contoured every 10^{-4} s^{-1}) and 500 hPa heights (m) at 3-hour intervals beginning 0900 UTC 10 June.

nor WRF-4 forecasts convection over New Mexico or Texas at all during that time period (Figs. 3.4 and 3.5). Nonetheless, the WRF-4 forecasts an area of high positive relative vorticity in the vicinity of the midlevel shortwave at 1500 UTC 11 June (Fig. 3.5c) which is nearly absent in the WRF-10 forecasts. Comparison of the 24-hour forecast 500-hPa height and winds to those observed by 0000 UTC 11 June NOAA upper air soundings (Fig. 2.6) shows that the WRF-4 and both versions of the MM5 model forecast the midlevel trough reasonably well, with MM5-30 being the deepest and most consistent with the observed upper air data.

3.3.2. Stage I: MCV formation

All three model forecasts that predicted a vorticity maximum associated with the shortwave trough at 0000 UTC 11 June (MM5-30, MM5-10 and WRF-4) also forecast convection to initiate in the general vicinity of the vorticity center later in the afternoon/evening of 10 June (Figs. 3.6, 3.7 and 3.9). The forecast reflectivity and vorticity for each model is shown in Figs. 3.6–3.9. WRF-10, without a significant vorticity center, greatly underforecasts the Oklahoma MCS, and produces convection primarily in southern Missouri along the surface front (Fig. 3.8). Of the three models that predicted convection in the vicinity of the midlevel wave in Oklahoma and Kansas, the best performance comes from WRF-4 and MM5-10. MM5-30 produces widespread convection across northern Oklahoma and southern Kansas, yet does not show signs of any organized structure (Figs. 3.6d–f). Additionally, convection initiates at 0600 UTC, about nine hours too late, and likewise the peak convection is forecast 1500 UTC, also
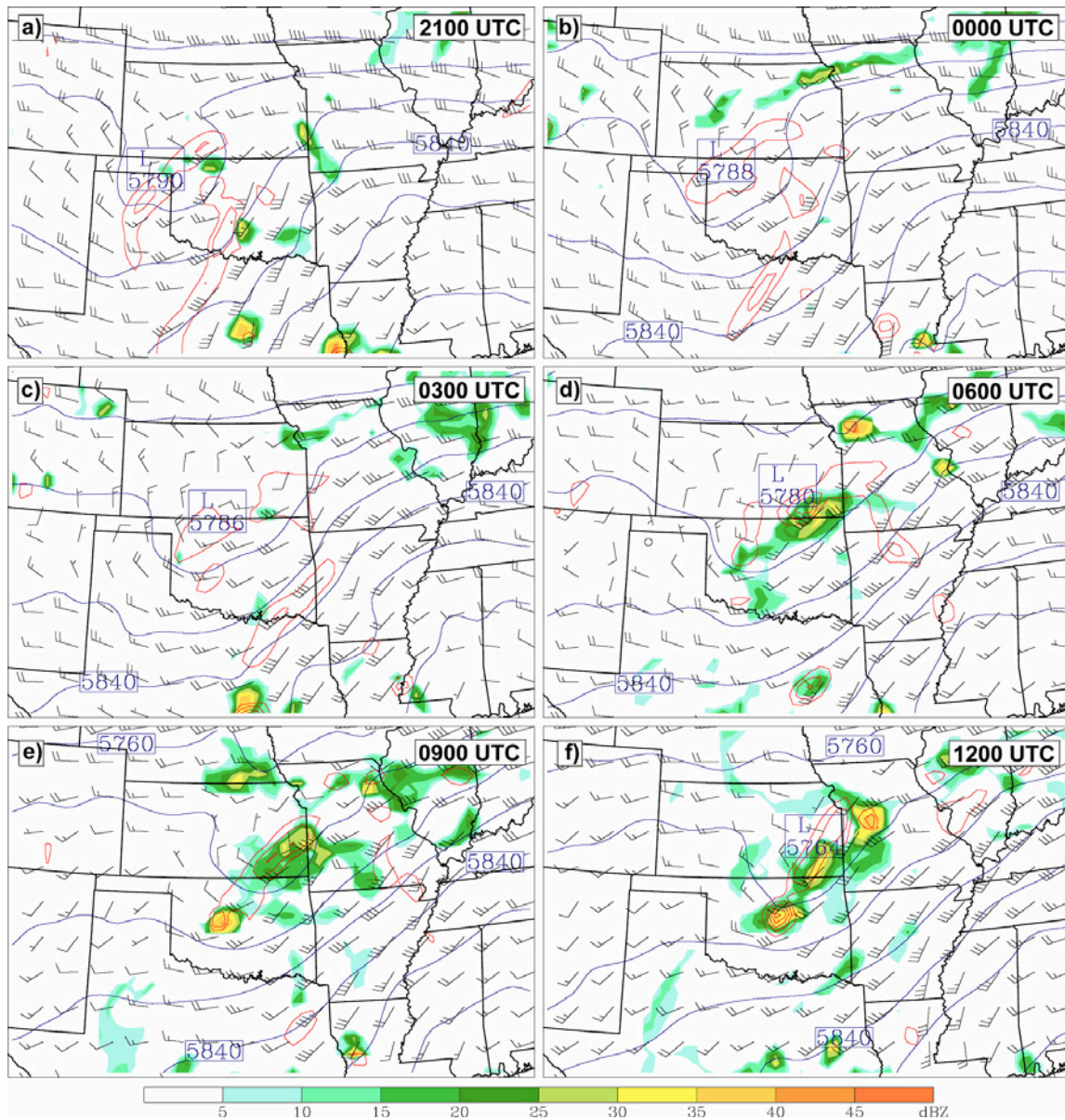
FIG. 3.6. MM5-30 initialized 0000 UTC 10 June forecast of reflectivity (shaded), 500 hPa relative vorticity (red solid in 10^{-5} s^{-1}, contoured every 10^{-4} s^{-1}) and 500 hPa heights (m) at 3-hour intervals beginning 2100 UTC 11 June.
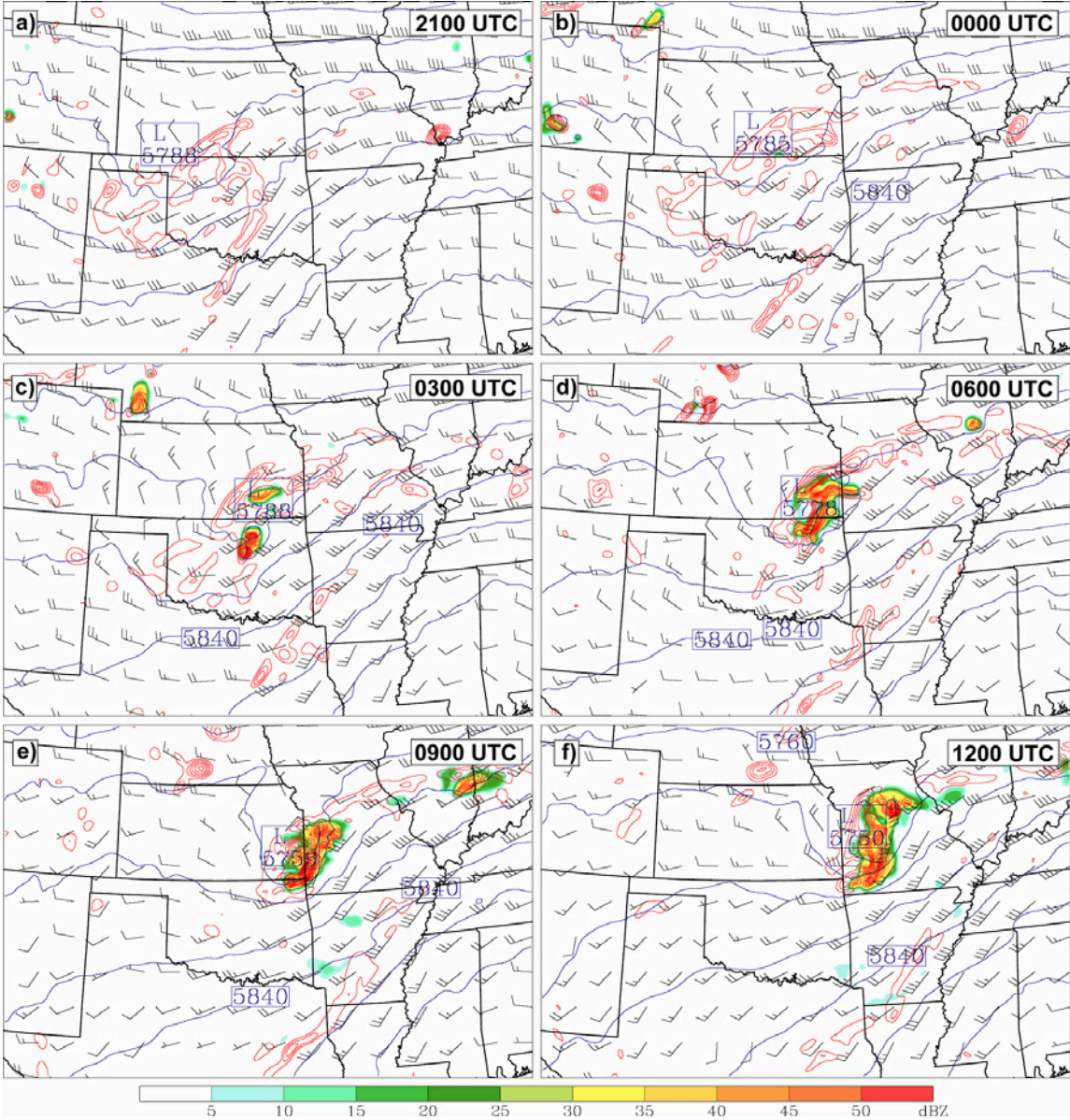
FIG. 3.7. MM5-10 initialized 0000 UTC 10 June forecast of reflectivity (shaded), 500 hPa relative vorticity (red solid in 10^{-5} s^{-1}, contoured every 10^{-4} s^{-1}) and 500 hPa heights (m) at 3-hour intervals beginning 2100 UTC 11 June.
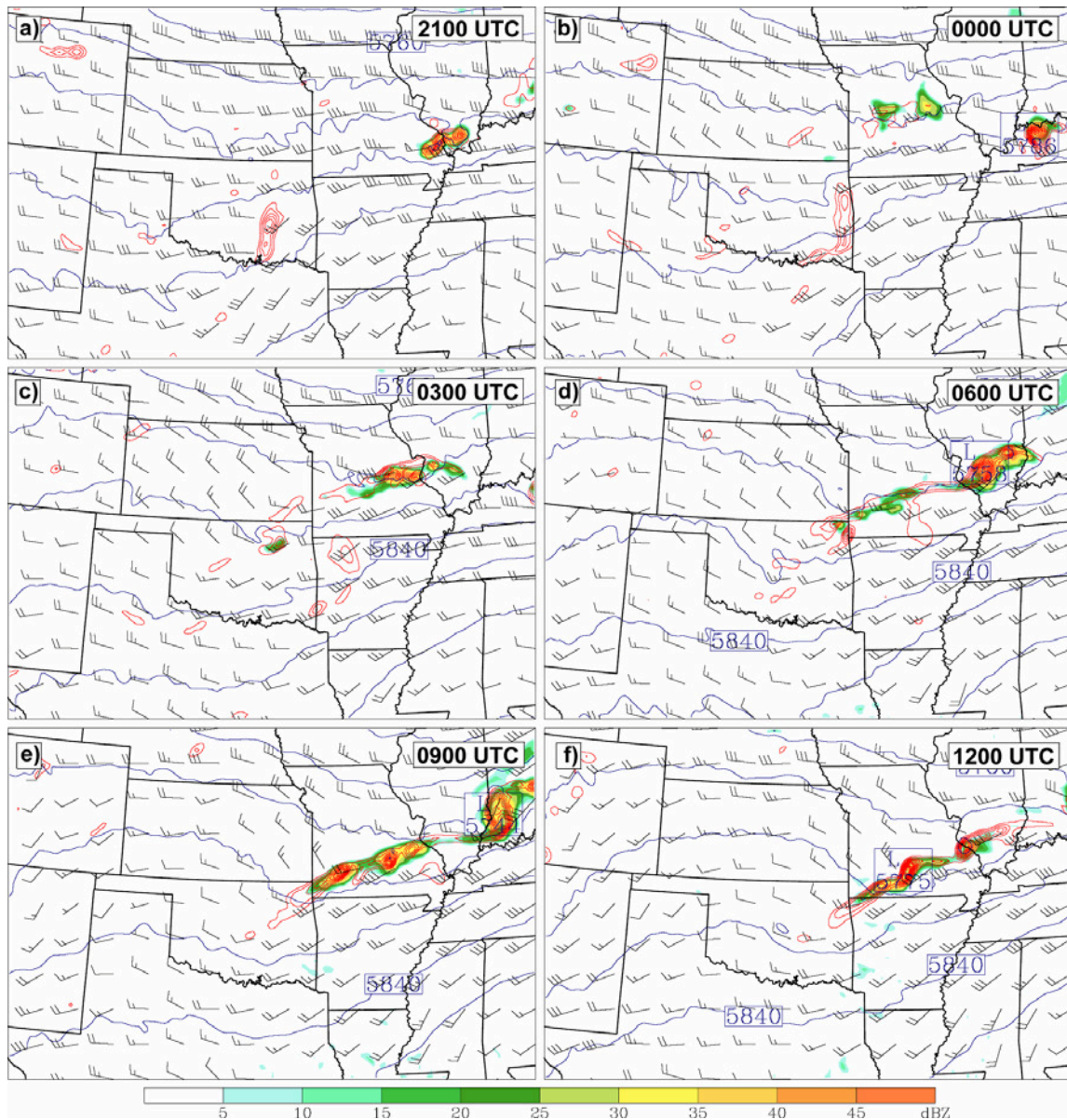
FIG. 3.8. WRF-10 initialized 0000 UTC 10 June forecast of reflectivity (shaded), 500 hPa relative vorticity (red solid in 10^{-5} s^{-1}, contoured every 10^{-4} s^{-1}) and 500 hPa heights (m) at 3-hour intervals beginning 2100 UTC 11 June.
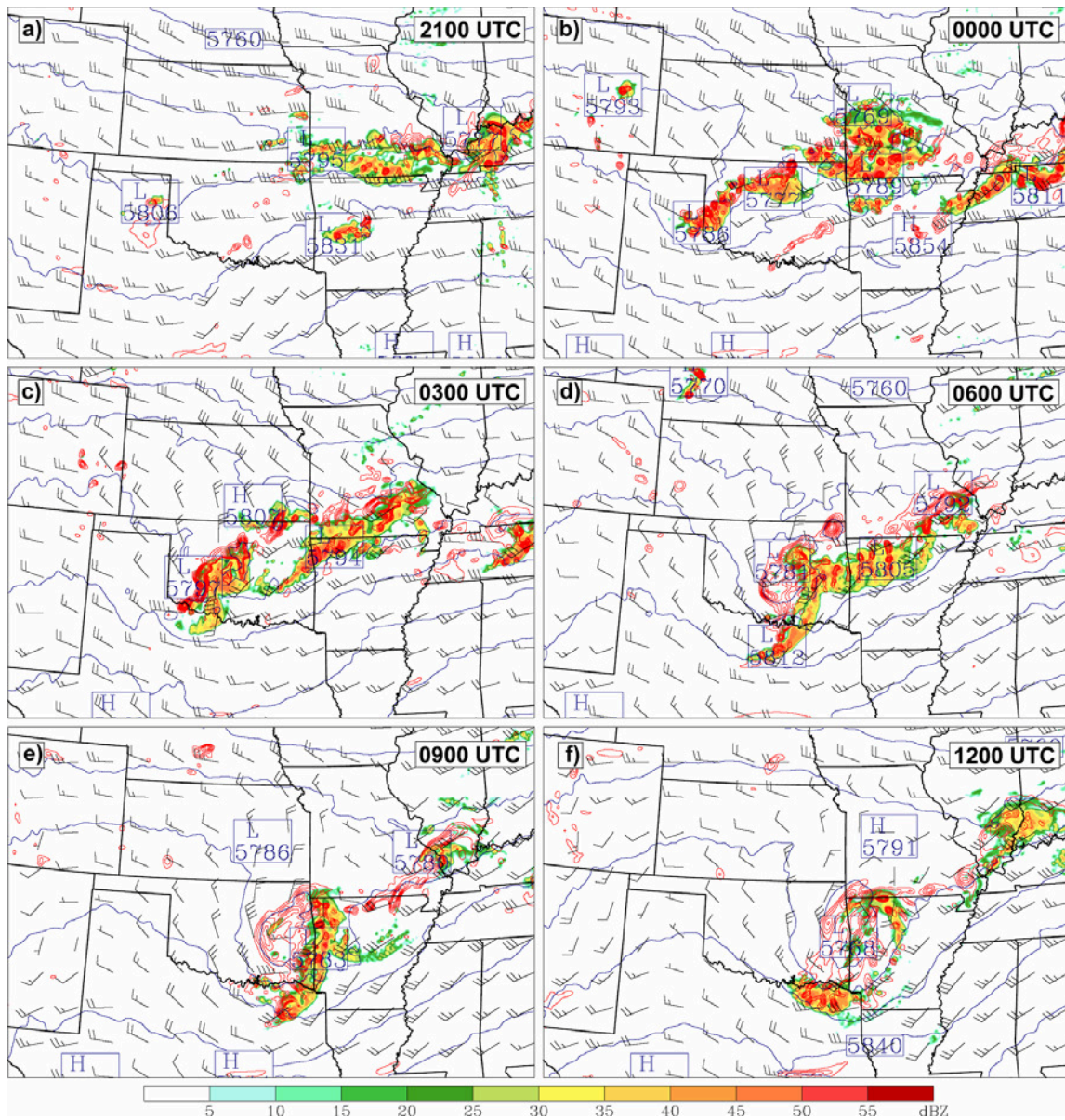
FIG. 3.9. WRF-4 initialized 0000 UTC 10 June forecast of reflectivity (shaded), 500 hPa relative vorticity (red solid in 10^{-5} s^{-1}, contoured every 10^{-4} s^{-1}) and 500 hPa heights (m) at 3-hour intervals beginning 2100 UTC 11 June.

about nine hours too late and 200 km too far west (not shown). Furthermore, the areal

coverage of convection appears too small to have a significant net warming of the

atmosphere. The resulting impact on midlevel vorticity is minimal and no closed

circulation is produced by MM5-30 at any level at any time.

While both models without convective parameterization (MM5-10 and WRF-4)

perform much better than their coarse-resolution counterparts in forecasting the MCV,

WRF-4 outperforms MM5-10 in almost all stages of initial convection and MCV

development. WRF-4 initiates convection in western Oklahoma and the Texas

panhandle along the surface front and ahead of the midlevel shortwave at 2100 UTC

(Fig. 3.9a), which is close to verification in Fig. 2.11a. On the other hand, in Fig. 3.7c it

is seen that MM5-10 initiates convection five hours later and 100 km too far east over

central Oklahoma. By 0300 UTC 11 June (Fig. 3.9c), WRF-4 merges convection into an

MCS and is very close to the actual timing of observed MCS development in Fig. 2.11c.

Conversely, MM5-10 does not merge convective cells until 0600 UTC (Fig. 3.7d),

which is roughly four hours too late. By 0600 UTC, WRF-4 displays impressive

accuracy in its forecast of the MCS over eastern Oklahoma in Fig. 3.9d, although little to

no stratiform rain is forecast behind the convective line at any time through 1200 UTC

hours. The forecast MCS weakens at 1200 UTC, which is about three hours later than

the actual MCS began to dissipate (Figs. 3.9f and 2.11e). By 1200 UTC, WRF-4

reflectivity forecasts hint at a midlevel circulation over northwest Arkansas, which again

is very close to the location of observed rotation on radar at that time. Meanwhile in Fig.

3.7f, MM5-10 forecasts the MCS to move into Missouri by 1200 UTC with no signs of weakening.

As WRF-4 outperforms the other three model forecasts in MCS initiation, coverage, timing, location and mode, it also shows the best performance in predicting the midlevel rotation and MCV formation. As described in Chapter II, the NOAA wind profiler network first measured an easterly component to 600 hPa winds at 0300 UTC over Lamont, Oklahoma (Fig. 2.13d). WRF-4 forecasts a similar northeasterly midlevel wind at 0600 UTC over northeast Oklahoma in Fig. 3.9d, which implies it develops the midlevel circulation about three hours too late. By 0900 UTC (Fig. 3.9e) it develops a closed 500 hPa low over northeast Oklahoma which deepens to 5762 meters by 1200 UTC over the Oklahoma/Arkansas border. MM5-10 develops the midlevel vortex in a similar fashion in Fig. 3.7d, with an easterly component to the wind north of the convection appearing at 0600 UTC as well. However, this model develops a closed low at 0700 UTC (not shown), 2 hours earlier than WRF-4, and deepens the 500 hPa low slightly further to 5750 m at 1200 UTC (Fig. 3.7f). The largest error in the MM5-10 MCV forecast is the placement of the vortex, as it forecasts the circulation center over western Missouri at 1200 UTC, or about 300 km too far to the north. Additionally, through 1200 UTC MM5-10 forecasts convection over a smaller area than what is forecast by WRF-4 and what is verified by radar.

3.3.3. Stage II: Secondary convection and surface vortex development

The second stage of the BAMEX IOP 8 MCV to be examined is the initiation of secondary convection and the growth of the MCV circulation at the surface during the local afternoon hours of 11 June. Although both versions of the MM5 which were initialized at 0000 UTC 10 June cover this time period, the WRF forecasts only cover 36 hours beyond that time, and thus the 10 June WRF simulations do not include this stage of the MCV. Therefore this part of the study examines those models initiated at 0000 UTC 11 June, using the same four models analyzed in section 3.3.1 and 3.3.2. Additionally, since the MM5-10 initialized at 0000 UTC 10 June is employed for the statistical predictability analysis in Chapter IV (for reasons to be explained later in this study), its forecasts will be included in the model comparison in this section.

Figures 3.10–3.13 show reflectivity and 500 hPa vorticity forecasts from each model during the secondary convection stage of the MCV. The convection forecasts are very poor among all models except theWRF-4 when compared to actual radar in Fig. 2.14. The most inaccurate forecasts come from MM5-30 and WRF-10 (Figs. 3.10 and 3.12 respectively), in which both forecast convection much too strong over the circulation center throughout the forecast period. Additionally, these two models confine convection to the immediate midlevel vortex center and the northern half of the circulation. This forecast does not verify with observed radar (Fig. 2.14), which shows a large area of scattered strong convection several hundred kilometers to the east of the circulation, and limited weak convection within the MCV itself. MM5-10 is only slightly better, as it does not forecast convection as strong directly over the circulation
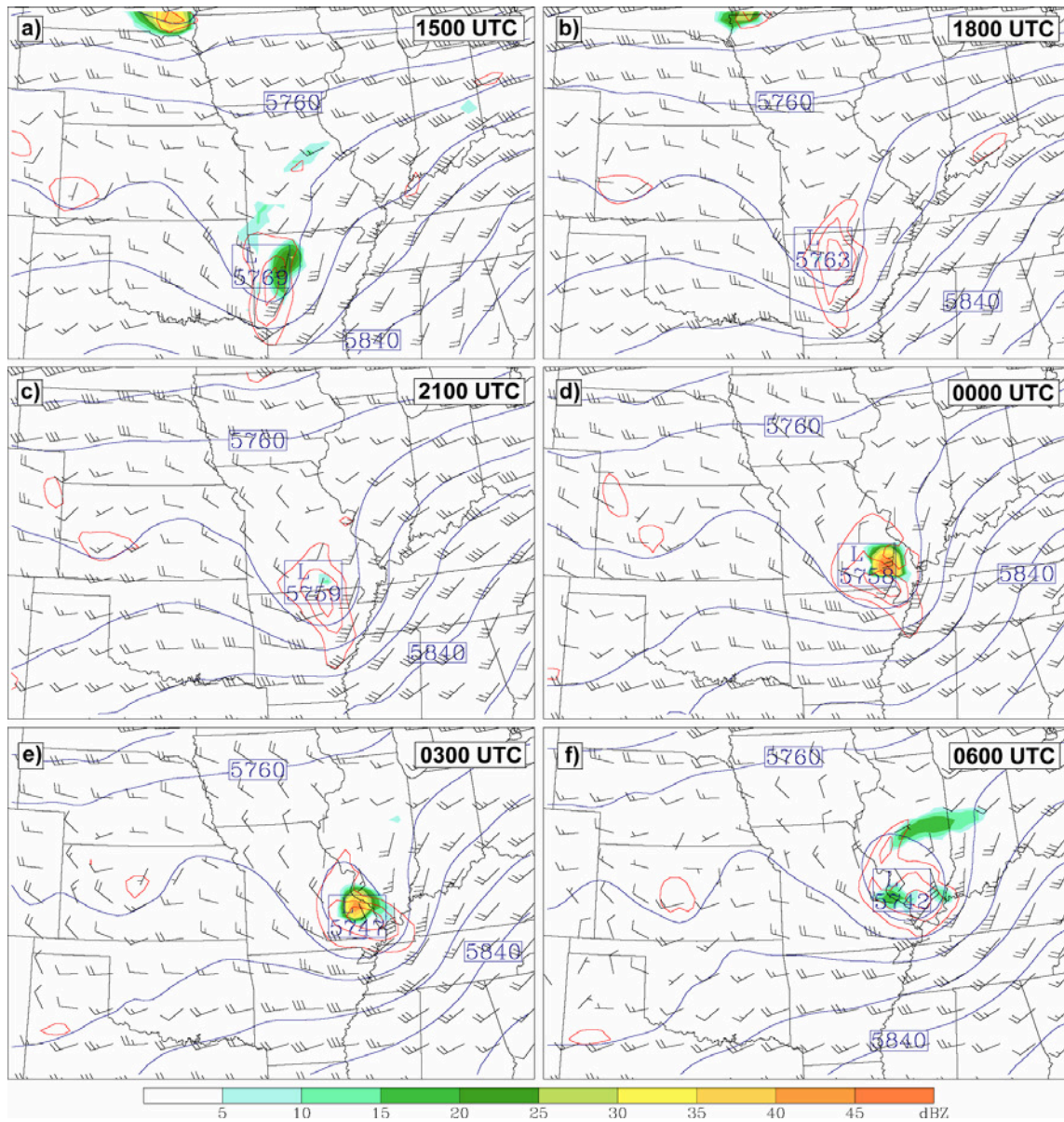
FIG. 3.10. MM5-30 initialized 0000 UTC 11 June forecast of reflectivity (shaded), 500 hPa relative vorticity (red solid in 10^{-5} s^{-1}, contoured every 10^{-4} s^{-1}) and 500 hPa heights (m) at 3-hour intervals beginning 1500 UTC 11 June.

FIG. 3.11. MM5-10 initialized 0000 UTC 11 June forecast of reflectivity (shaded), 500 hPa relative vorticity (red solid in 10^{-5} s^{-1}, contoured every 10^{-4} s^{-1}) and 500 hPa heights (m) at 3-hour intervals beginning 1500 UTC 11 June.
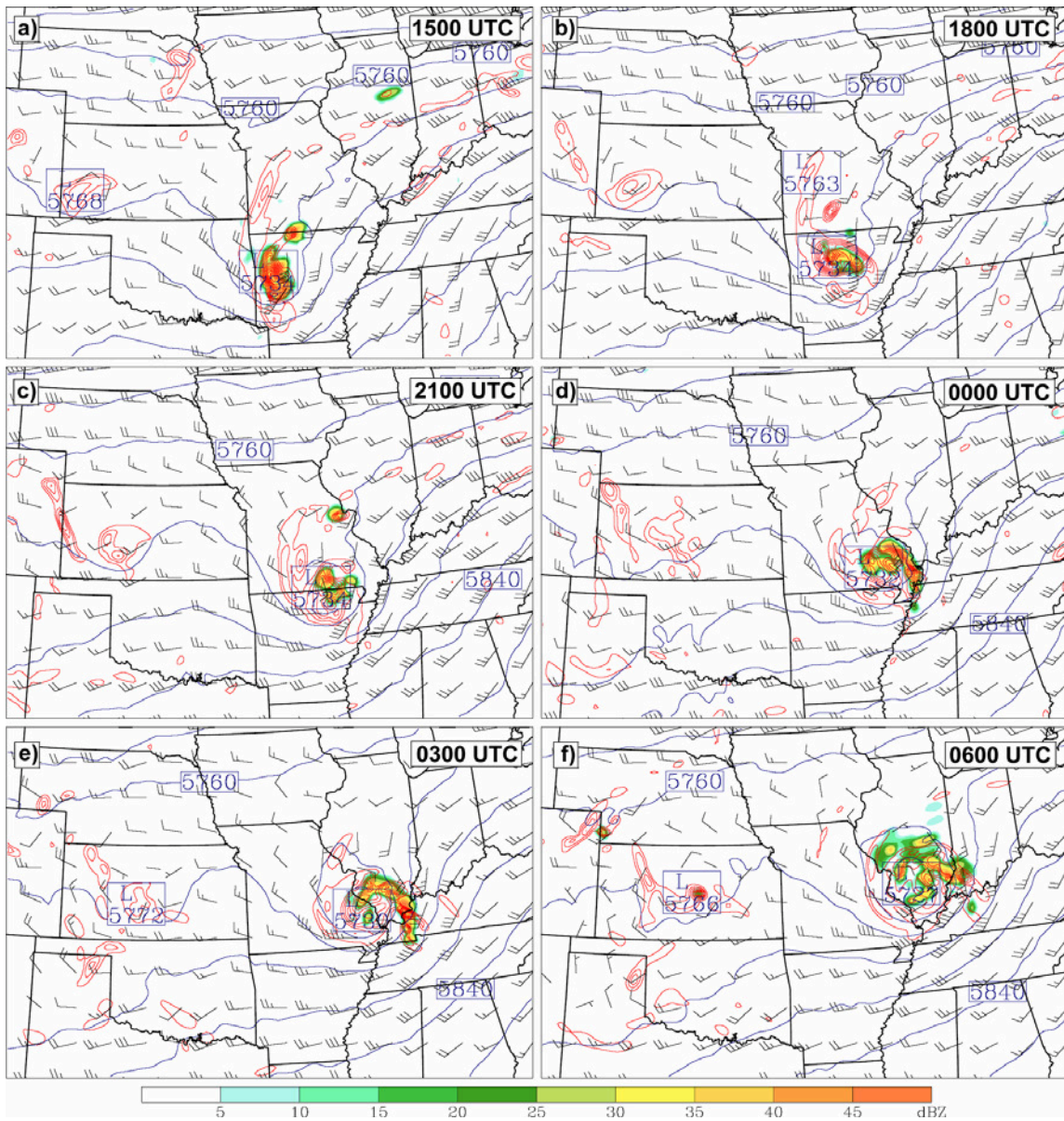
FIG. 3.12. WRF-10 forecast initialized 0000 UTC 11 June of reflectivity (shaded), 500 hPa relative vorticity (red solid in 10^{-5} s^{-1}, contoured every 10^{-4} s^{-1}) and 500 hPa heights (m) at 3-hour intervals beginning 1500 UTC 11 June.
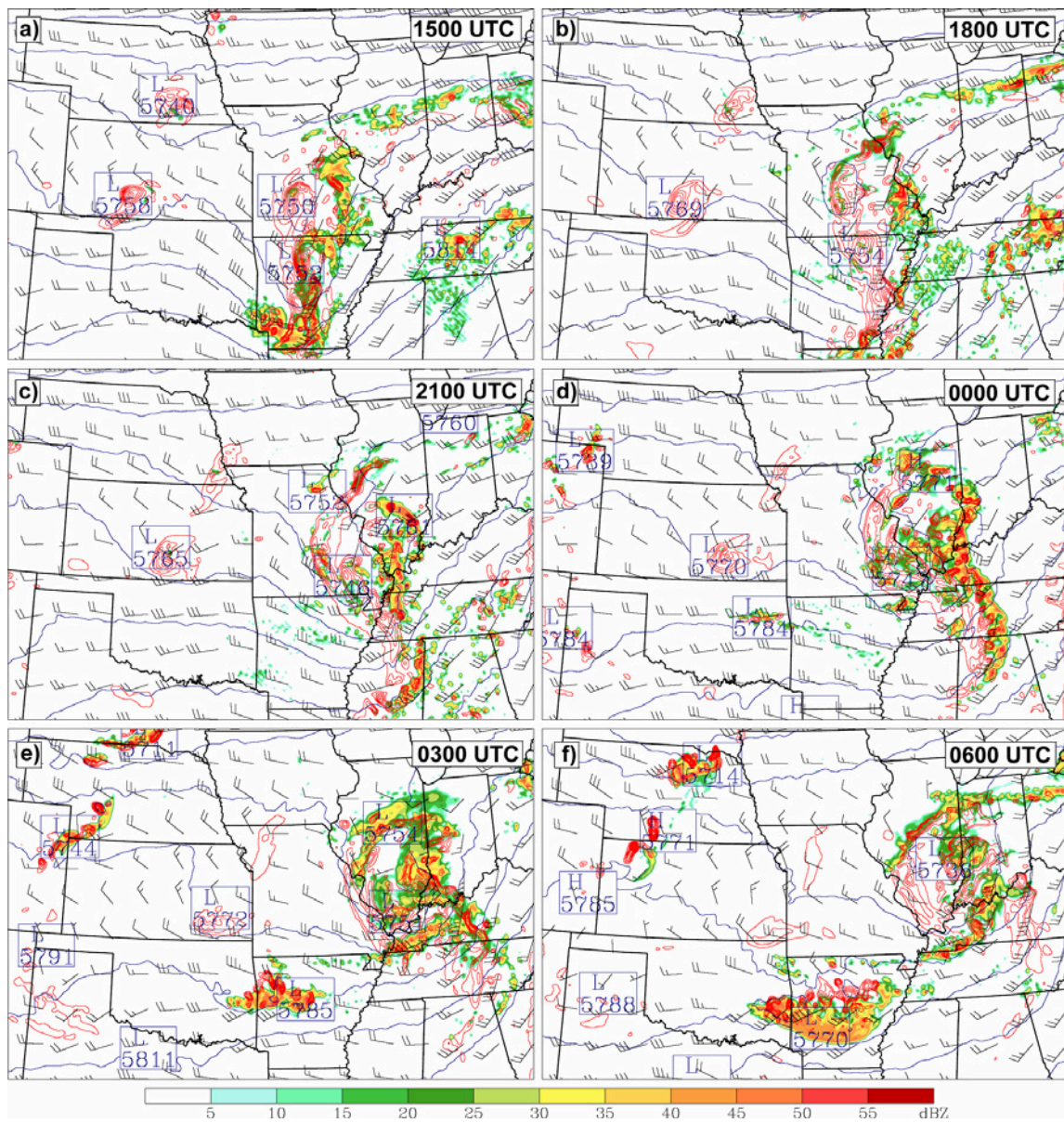
FIG. 3.13. WRF-4 initialized 0000 UTC 11 June forecast of reflectivity (shaded), 500 hPa relative vorticity (red solid in 10^{-5} s^{-1}, contoured every 10^{-4} s^{-1}) and 500 hPa heights (m) at 3-hour intervals beginning 1500 UTC 11 June.

center (Fig. 3.11). However, MM5-10 forecasts convection over a very limited area

close to the MCV itself, and keeps the convection near the MCV too strong. The most

accurate forecast of secondary convection comes again from WRF-4. This model

predicts a much more expansive area of convection through the afternoon of 11 June

(Fig. 3.13), and keeps much weaker convection over the MCV itself. In Fig. 3.14,

similar reflectivity forecasts are shown for MM5-10 forecasts but for the simulation

initialized at 0000 UTC 10 June (MM5-10A). A clearly defined midlevel circulation is

forecast at 1500 UTC (Fig. 3.14a) and relatively widespread convection is generated

both near the midlevel circulation center and in a band ahead of the MCV through 0000

UTC (Fig. 3.14b–d). These forecasts are superior to those forecast by the MM5-10

initialized at 0000 UTC 11 June (Fig. 3.12) which had forecasts very limited convection

and a weaker MCV. While not as accurate as WRF-4 during this stage of the MCV (Fig.

3.13), the MM5-10A forecast of secondary convection and MCV evolution in Fig. 3.14

still exhibits fine performance.

To compare MCV forecasts with the BAMEX dropsonde data from Chapter II,

WRF-4B forecasts of temperature, height and wind at four levels are given in Fig. 3.15.

Additionally, Fig. 3.16 gives similar forecasts from the MM5-10 model initialized at

0000 UTC 10 June, since this model adequately forecasts the MCV at this time and will

be further examined in Chapter IV. Similar to BAMEX dropsonde data, WRF-4

forecasts in Fig. 3.15 show a transition from a strong warm core system at 500 hPa (Fig.

3.15a; dropsonde data in Fig. 2.28) to a strong cold core at 850 hPa (Fig. 3.15d;

dropsonde data in Fig. 2.31). Like the dropsonde data, the WRF-4 forecasts a low in the
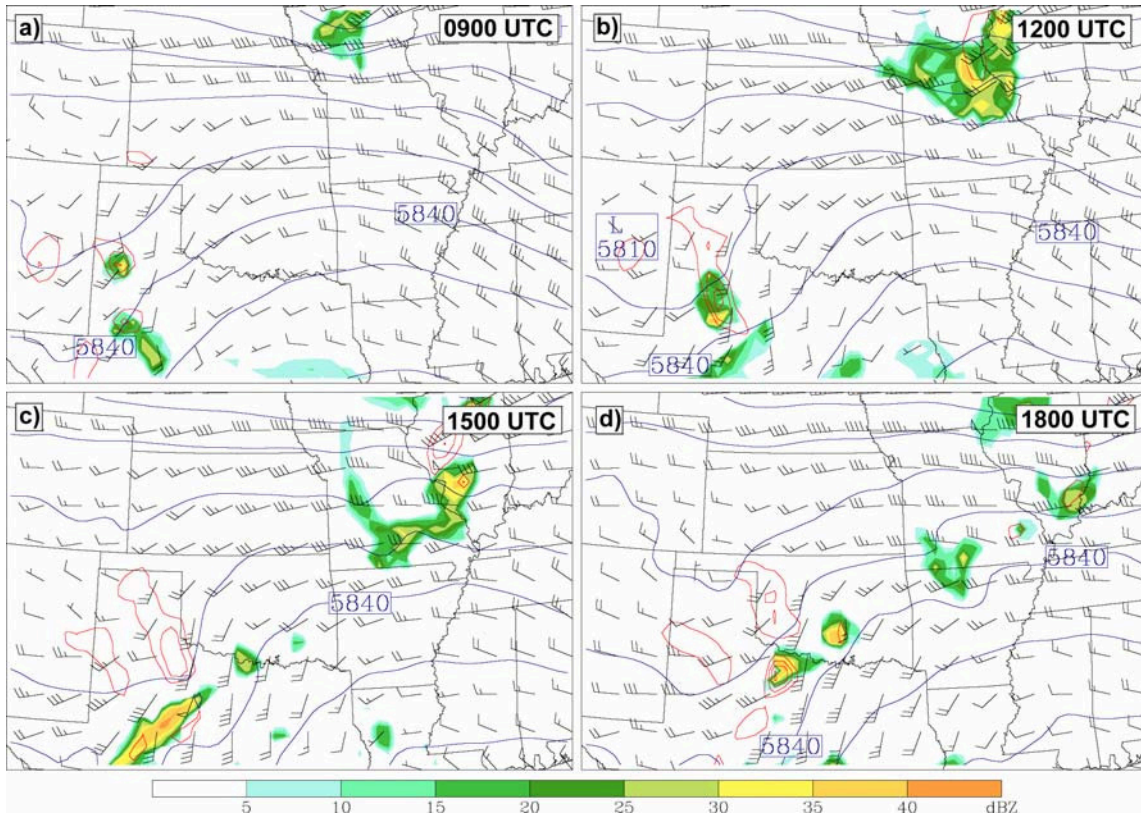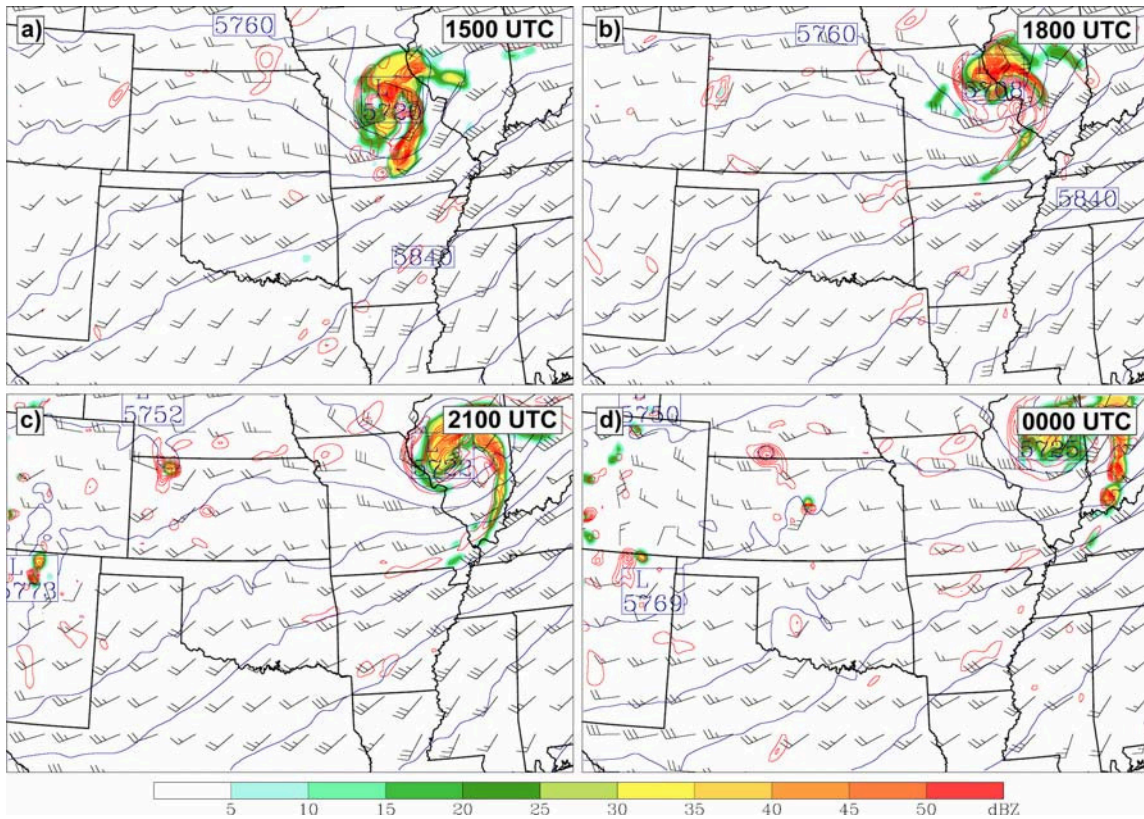
FIG. 3.14. MM5-10 initialized 0000 UTC 10 June forecast of reflectivity (shaded), 500 hPa relative vorticity (red solid in 10^{-5} s^{-1}, contoured every 10^{-4} s^{-1}) and 500 hPa heights (m) at 3-hour intervals beginning 1500 UTC 11 June.
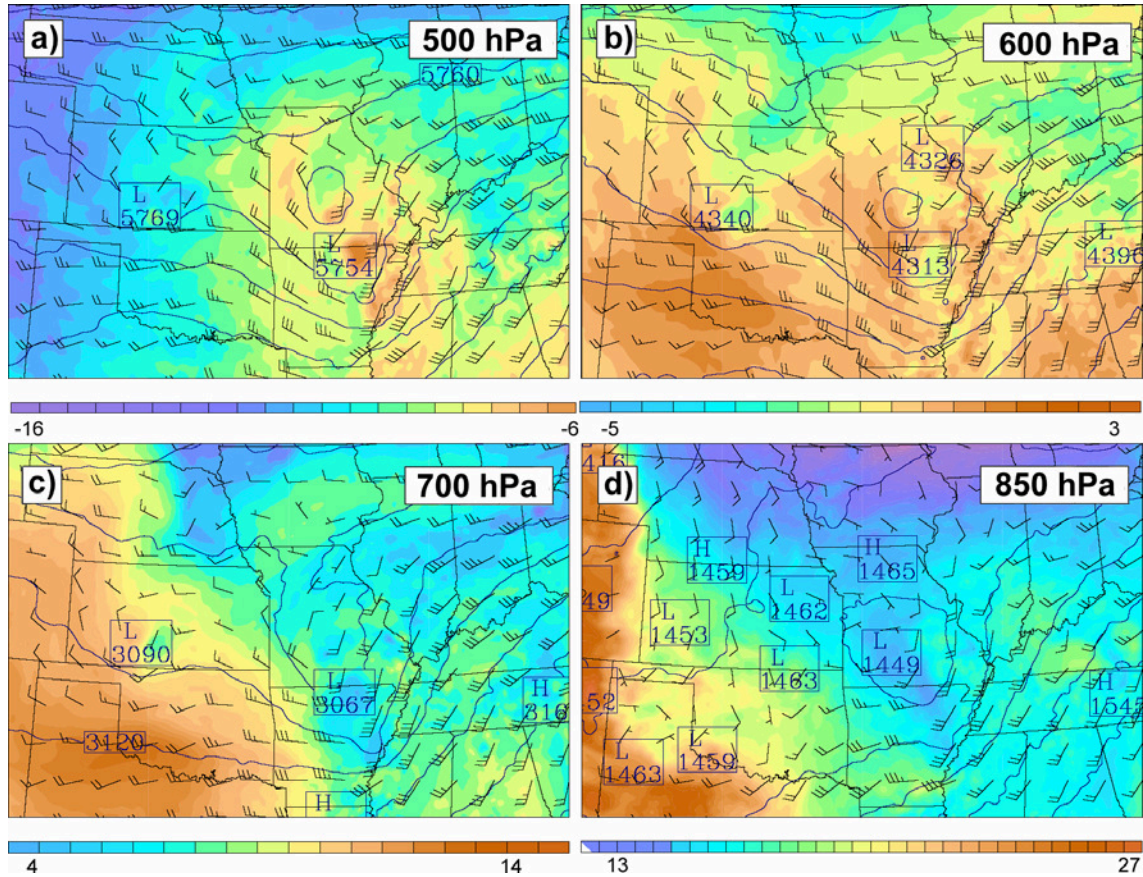
FIG. 3.15. WRF-4 initialized at 0000 UTC 11 June forecasts of temperature (shaded in degrees C), height (contoured in blue every 20 m) and wind (one full barb denotes 10 kt) at 1800 UTC 11 June at (a) 500 hPa, (b) 600 hPa, (c) 700 hPa and (d) 850 hPa.
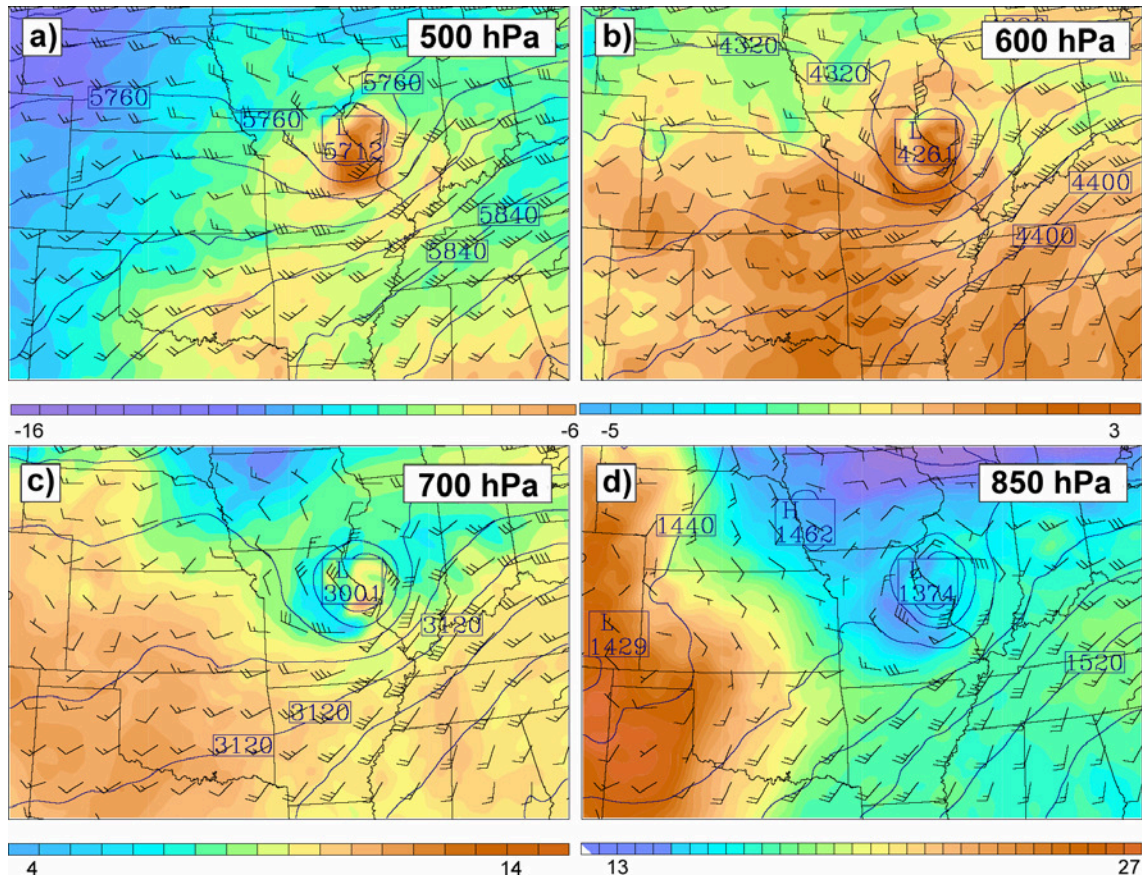
FIG. 3.16. MM5-10 initialized at 0000 UTC 10 June forecasts of temperature (shaded in degrees C), height (contoured in blue every 20 m) and wind (one full barb denotes 10 kt) at 1800 UTC 11 June at (a) 500 hPa, (b) 600 hPa, (c) 700 hPa and (d) 850 hPa.

height field and a cyclonic circulation at all levels, with the deepest relative heights and strongest cyclonic circulation at 500 and 600 hPa. The MM5-10 forecasts in Fig. 3.16 similarly accurately simulate the vertical thermodynamic structure of the MCV, with a strong cold core at 850 hPa and a strong warm core at 500 hPa (though too warm), transitioning between 600 and 700 hPa. While it forecasts a strong circulation at all levels, it incorrectly forecasts it strongest at 700 and 850 hPa (Fig. 3.16c–d), whereas the BAMEX dropsonde data shows the strongest circulation at 500 and 600 hPa (Fig. 2.28 and 2.29).

As the high-resolution WRF model displays improved performance over the other three models when forecasting secondary convection and midlevel vortex strength on 11 June, it likewise outperforms these models regarding surface low development during the afternoon of 11 June (MM5 and WRF-10 forecasts not shown). WRF-4 maintains the surface low between 1002 and 1005 hPa in Figs. 3.17d–f, and does not aggressively and unrealistically deepen the low as a result of convective feedback, as occurs in the other three simulations. The WRF-4 forecasts compare well to actual surface observations which show a surface low of 1006 hPa at 1500 UTC (Fig. 2.20) deepening to slightly below 1005 hPa through 0000 UTC (Figs. 2.21–2.23) with a closed circulation clearly defined at 1800 UTC in Fig. 2.21. Although the WRF-4 forecast surface circulation appears three hours too late at 2100 UTC in Fig. 3.17c, the dynamics behind the surface low development appear to correspond the most with actual observations. It was shown in Chapter II (Figs. 2.21 and 2.35) that the surface low developed on the northeastern edge of a surface cold pool. Similarly, the WRF-4
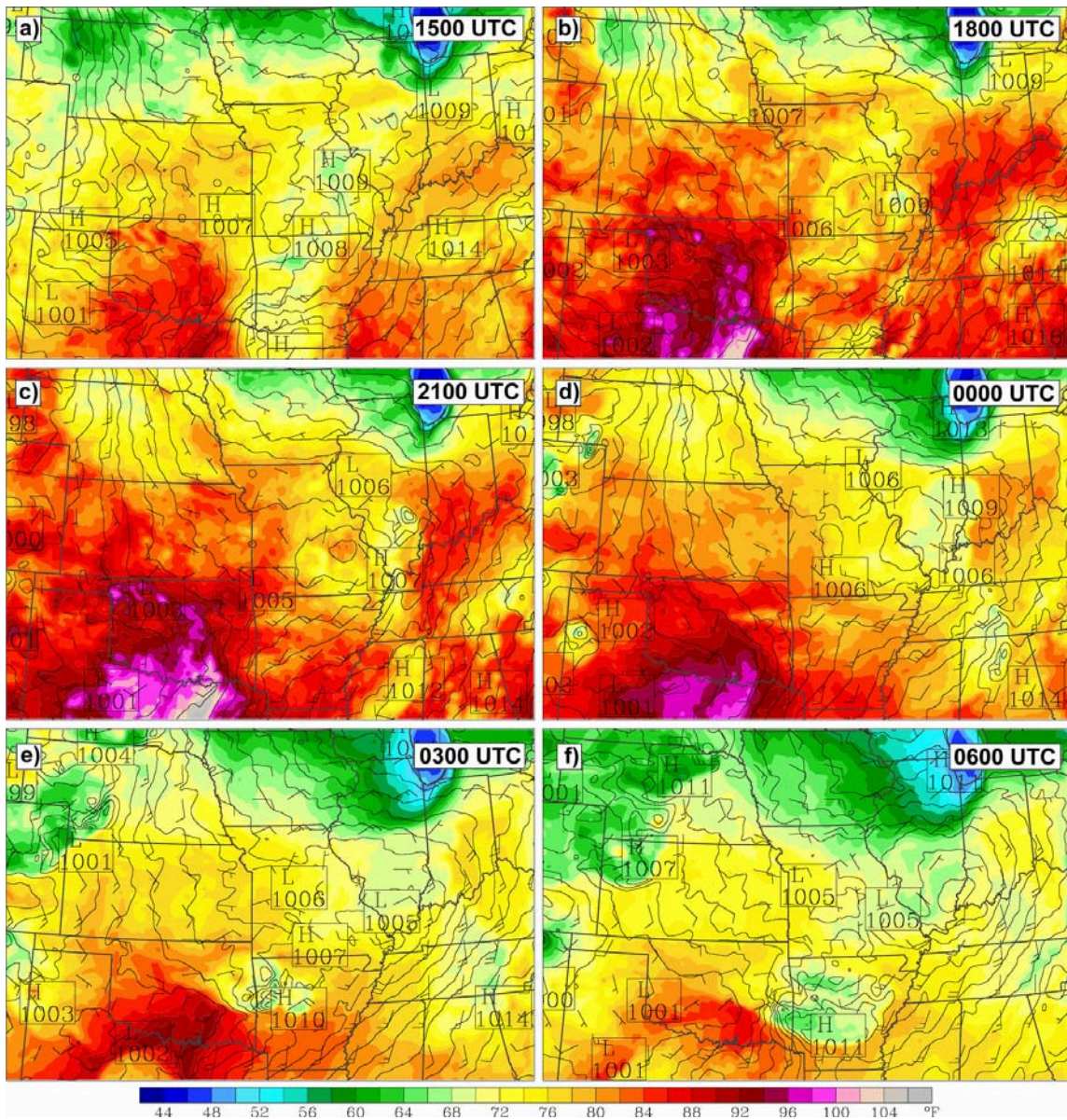
FIG. 3.17. WRF-4 initialized 0000 UTC 11 June forecasts of surface temperature (shaded), mean sea level pressure (black solid, contoured every millibar) and 10-m winds (one full barb denotes 10 kt) at 3-hour intervals beginning 1500 UTC 11 June.

forecasts the surface low to the northeast of a cold surface temperature anomaly at 2100 UTC in Fig. 3.17c. The accuracy displayed by the WRF-4 in this section makes it reasonable to believe its deterministic forecasts will be beneficial for a dynamic investigation of an MCV system.

3.4. Synopsis of WRF-4 MCV forecasts

Since it is determined that WRF-4 deterministic forecasts perform well enough to be reliable for a dynamic analysis, this section will examine its forecasts in more detail to provide a thorough overview of its forecasts during MCV evolution. Again, this part of the study employs WRF-4A forecasts for analysis of the initial MCS and the resulting development of the MCV (stage I) and WRF-4B is used to analyze secondary convection during the next diurnal cycle and the evolution of the surface vortex (stage II).

3.4.1. Stage I: MCV formation

Figure 3.18 provides a closer look at the WRF-4A simulated MCS and MCV through forecasts of radar reflectivity and 500-hPa height and wind. The first convection to initiate at 2100 UTC in Fig. 3.18a forms in the immediate vicinity of the 500-hPa shortwave over the Texas panhandle (vertical structure of the midlevel wave shown in east-west cross section in Fig. 3.19). Convection quickly expands and by 0000 UTC two distinct bow-echoes have evolved over western and northern Oklahoma. These two systems merge three hours later, and by 0600 UTC, WRF-4A predicts a solid line of convection extending from north central Oklahoma into northern Texas. This
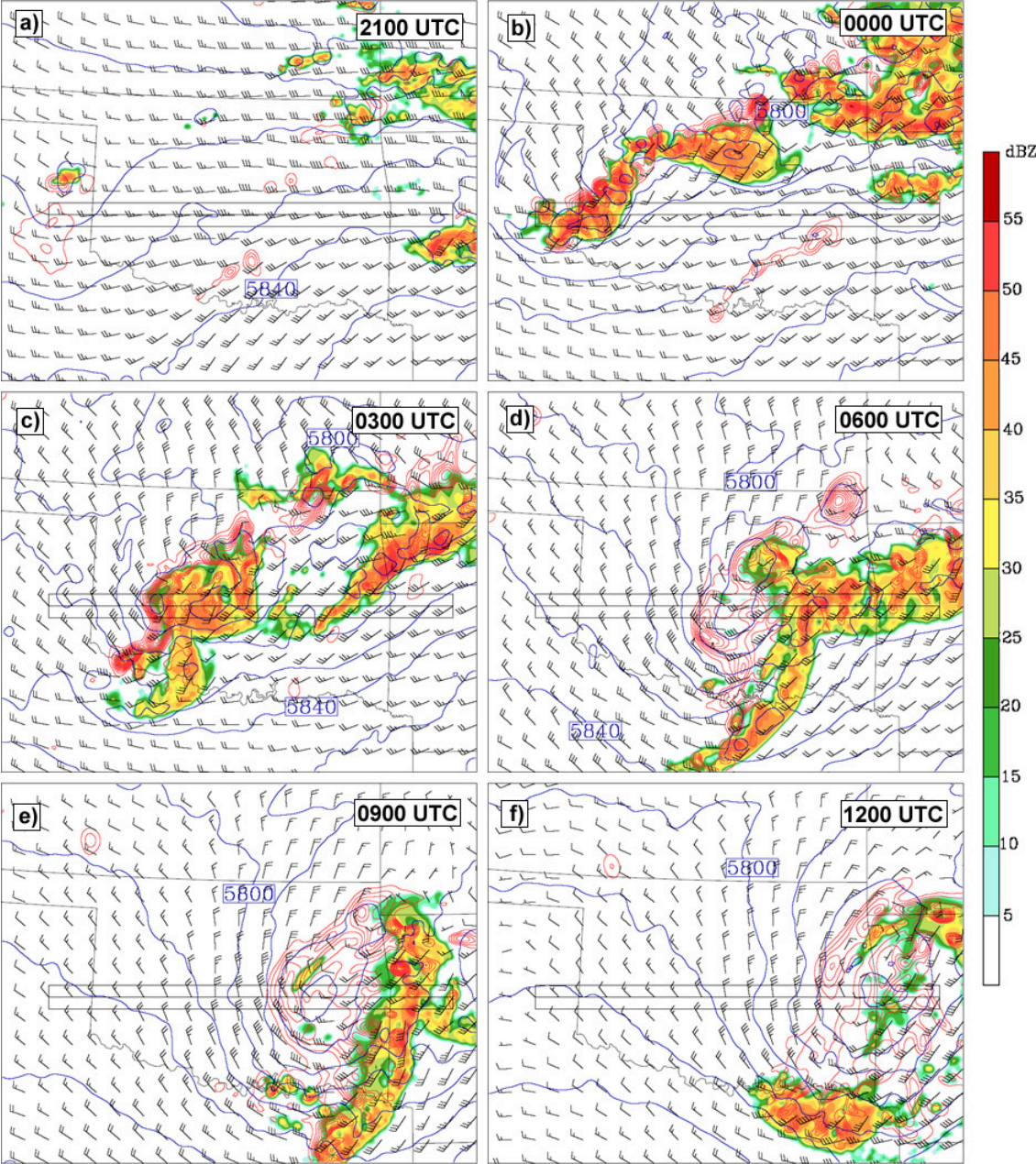
FIG. 3.18. WRF-4A forecasts for reflectivity (shaded), 500 hPa height (in meters, contoured in blue) and 500 hPa relative vorticity (contoured in red every 10^{-4} s^{-1}) at three-hour intervals beginning 2100 UTC 10 June.
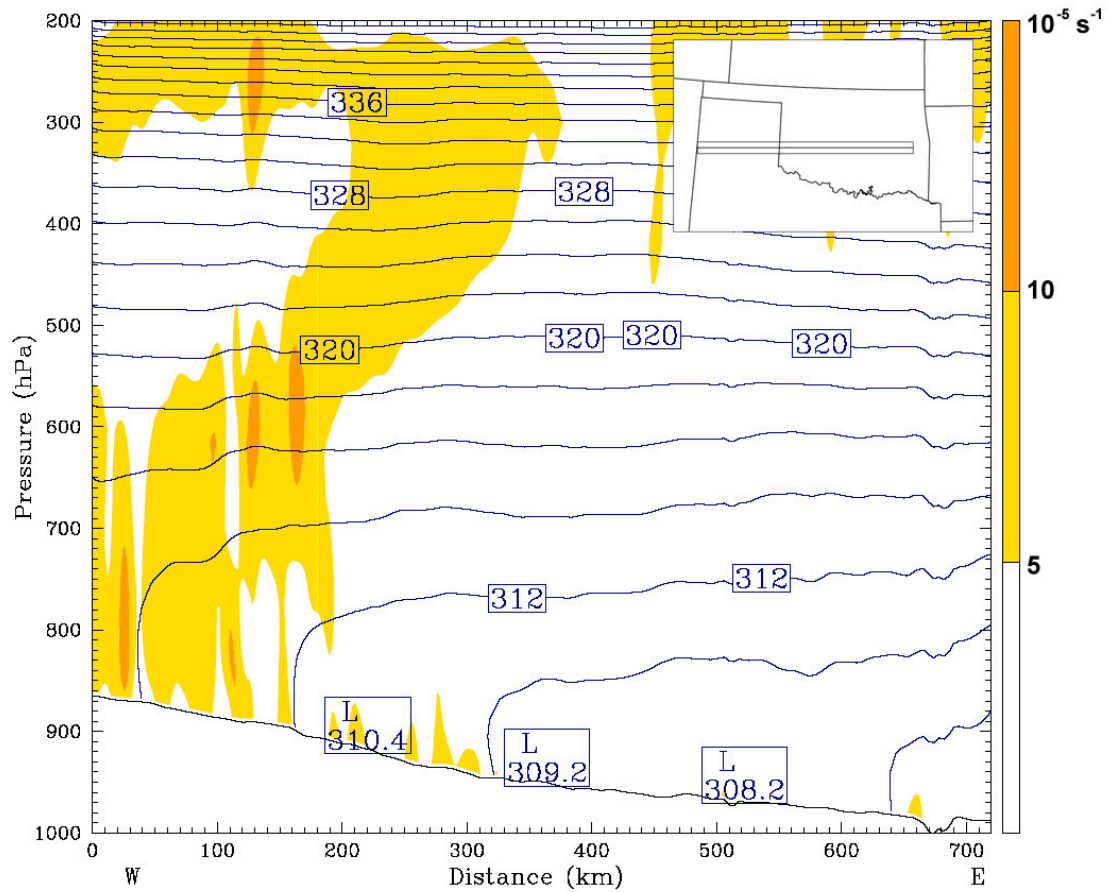
FIG. 3.19. 2100 UTC 10 June relative vorticity contoured every 5×10^{-4} s^{-1} averaged 20-km either side of east-west cross section denoted as horizontal line in upper right panel.

MCS weakens by 0900 UTC as the system enters western Arkansas, and by 1200 UTC, much of the precipitation has dissipated and a clear rotation pattern is evident in the forecast reflectivity.

The development of the MCV is seen in the 500 hPa vorticity, height and wind that is overlain on the reflectivity images. Convection first initiates in the immediate vicinity of the midlevel shortwave at 2100 UTC, just north of the area of 10×10^{-5} s^{-1} 500-hPa vorticity in the Texas panhandle. At 0000 UTC, as convection expands, strong midlevel vorticity has grown in coverage and strength (130×10^{-5} s^{-1}), but is limited to the immediate vicinity of convection over western Oklahoma, displaced slightly behind it. A second vorticity maximum has appeared behind convection that has initiated over north central Oklahoma. 500-hPa heights around both areas of convection are decreasing, and since the western Oklahoma convection is directly inside the midlevel shortwave, the wave deepens at this time. Unlike the vorticity maxima, the height minima are situated directly over both areas of convection. As the two areas of convection merge at 0300 UTC, the enhanced midlevel vorticity is now displaced slightly behind the developing MCS, but two distinct vorticity maxima are still evident, both sustaining a maximum value of 130×10^{-5} s^{-1}. The midlevel shortwave continues to deepen slightly, and a closed 5800 m 500-hPa isoheight appears over central Oklahoma, immediately behind the convective line and aligned with the northern vorticity maxima. No signs of a closed circulation are apparent at this time. Three hours later, the MCS has continued to race across Oklahoma and the vorticity maxima behind it have merged into one anomaly, but at 120×10^{-5} s^{-1} it is slightly weaker. On the other hand, the low

has deepened to 5790 m behind the convection and now coincides with the location of

maximum vorticity. The vorticity maximum continues to weaken through 31 hours to

90×10^{-5} s^{-1} (not shown), and restrengthens to 120×10^{-5} s^{-1} at 0900 UTC, by which time

it is displaced roughly 150 km to the west of the weakening MCS and heights fall further

to 5770 m. At 1200 UTC as the MCS dissipates, the vorticity maximum weakens to 90

$\times 10^{-5}$ s^{-1} over western Arkansas, but the low in the height field maintains a minimum

value of 5770 m and the area of lower heights expands in area. It is also at this time that

a closed circulation appears in the 500 hPa wind field.

3.4.2. Stage II: Secondary convection and surface vortex development

Figure 3.20 presents the WRF-4B forecasts of radar reflectivity and 600-hPa

height and wind during the second stage of the MCV on 11 June. Of particular note is

that the forecast MCV is over central Arkansas at 1600 UTC (Fig. 3.20a) which is

displaced about 200 km to the south of the synoptic-scale midlevel circulation over

southwest Missouri. Unlike the WRF-4 forecasts initialized at 0000 UTC 10 June, this

simulation keeps the bulk of the Oklahoma convection to the south of the existing

midlevel circulation (not shown), resulting in separate midlevel vortices at 1600 UTC 11

June. At this time, WRF-4B forecasts a decaying MCS moving across southwest

Arkansas (not shown). A broken line of convection exists farther north into eastern

Missouri, and the midlevel shortwave is centered over southwest Missouri, displaced

about 100 km to the west of the northernmost point of convection (Fig. 3.20a). By 2000

UTC (Fig. 3.20c), convection has become much stronger and more widespread along the
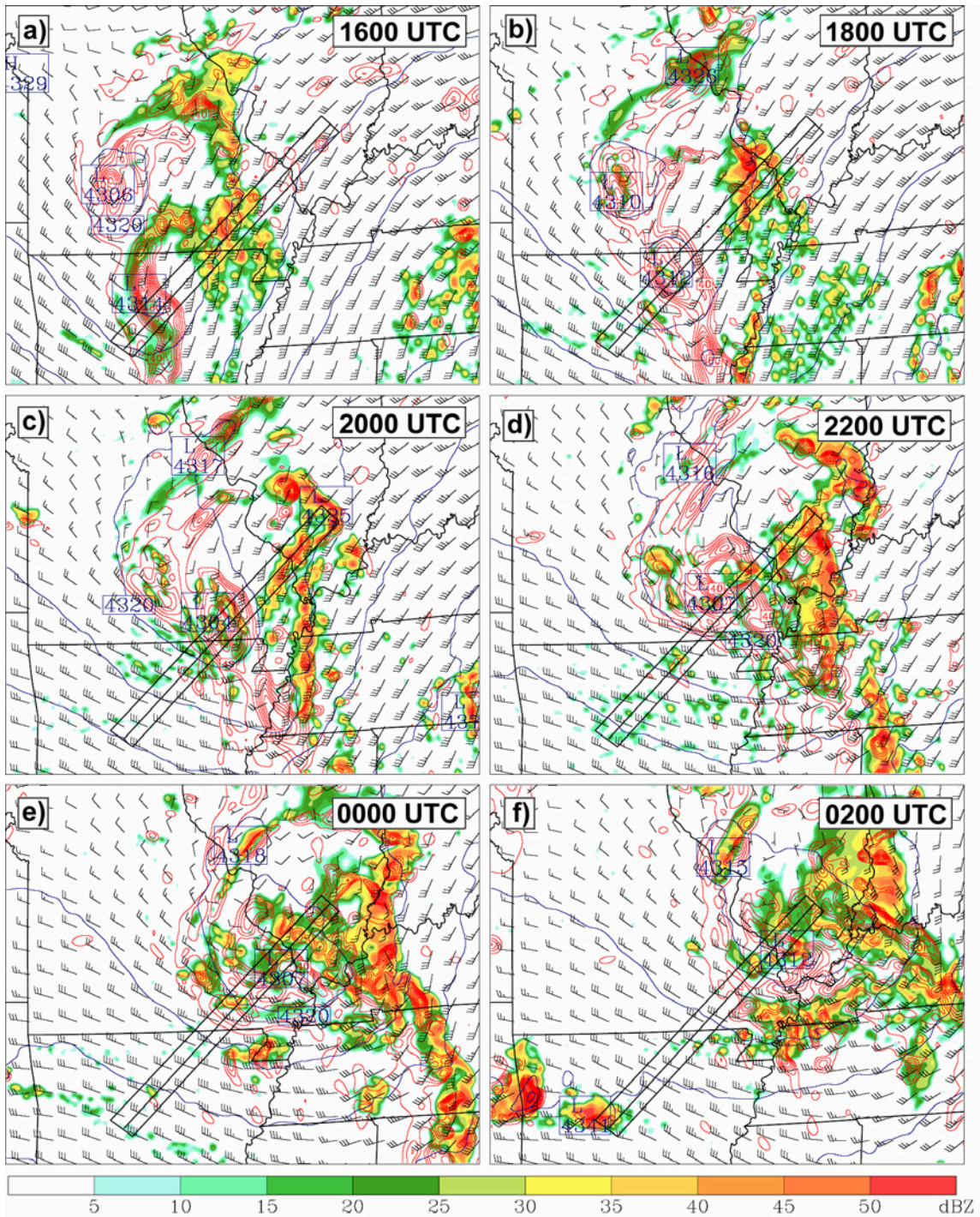
FIG. 3.20. WRF-4B forecasts for reflectivity (shaded), 600 hPa height (in meters, contoured in blue) and 500 hPa relative vorticity (contoured in red every 10^{-4} s^{-1}) at two-hour intervals beginning 1600 UTC 11 June. Black solid box represents path of MCV.

entire eastern periphery of the MCV, from Illinois through western Tennessee into

Alabama. Closer to the MCV center, weak convection fires in northern Arkansas at

1800 UTC, and becomes more widespread throughout southeast Missouri through 0000

UTC. At 2200 UTC (Fig. 3.20d), the two midlevel vortices merge over southeast

Missouri. After 0000 UTC, convection in all portions of the MCV circulation begins to

weaken, but remains active through the end of the forecast period at 1200 UTC (not

shown). The midlevel shortwave over Arkansas reaches its deepest strength of 4304 m at

2000 UTC (Fig. 3.20c) as weak convection fires directly beneath it. After merging with

the southern Missouri disturbance at 2200 UTC, the MCV keeps a low of 4307 m

through 0000 UTC before beginning to fill in and weaken after that point (Fig. 3.20f).

Figure 3.21 shows a closer examination of the forecast surface field from 1600

UTC 11 June to 0200 UTC 12 June. A surface circulation appears at 1600 UTC over

southwest Missouri inside the surface cold pool (Fig. 3.21a). Two hours later, the

circulation becomes slightly better defined over central Missouri as it becomes displaced

from the cold pool so that it now resides in a local surface temperature maximum. At

this time, a closed surface low of 1005 hPa appears. By 2000 UTC (Fig. 3.21c), the low

deepens to below 1004 hPa and is situated in a small warm anomaly which is 6 to 10

degrees Fahrenheit warmer than its surroundings. The circulation also expands during

this time period. As convection becomes widespread near the low center by 0000 UTC

(Fig. 3.20e), the warm anomaly at the surface dissipates and the surface low begins to

move along the temperature gradient left over from convection to the north in southern

Illinois (Fig. 3.21e). It maintains its intensity at 1004 hPa through 0200 UTC (Fig. 3.21f)
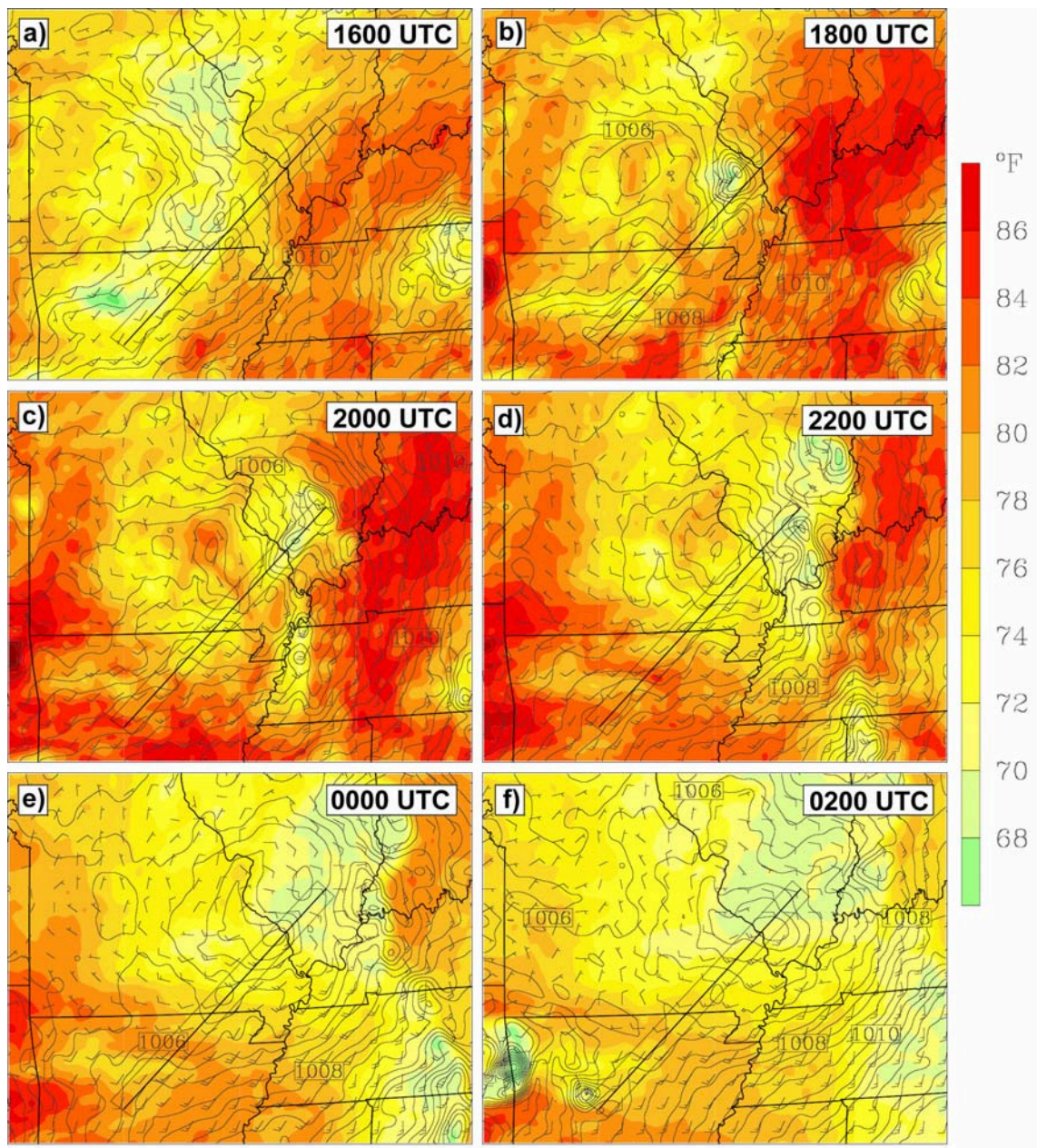
FIG. 3.21. WRF-4B forecasts of surface temperature (shaded), mean sea level pressure (black solid, contoured every millibar) and 10-m winds (one full barb denotes 10 kt) at two-hour intervals beginning 1600 UTC 11 June. Black solid box represents path of MCV.

and the circulation pattern remains the same. By 0600 UTC (not shown), the low has

deepened further to 1003 hPa, although ambient surface pressures are rising by this time,

so that the low is deepening further relative to the environment. The circulation also

intensifies through this period. At this point the circulation is situated along the surface

boundary, and the resulting wind pattern is now influencing cold air advection from

northern Illinois and warm air advection from the Tennessee Valley. It is at this point

that the surface low has clearly entered a baroclinic environment and is now evolving

into a typical extratropical cyclone. The surface circulation continues to grow through

1200 UTC (not shown) as the low further deepens relative to surrounding areas. The

forecast transition to an extratropical system accurately reflects the behavior of the

actual MCV which was evidenced in Chapter II (Fig. 2.24).

3.5. Discussion

The wide range of model forecasts presented in this chapter illustrates the very

large uncertainty facing MCV predictability. The extreme sensitivity of an MCV to

moist convective processes suggests that ability to accurately predict convection is

crucial in ability to predict an MCV circulation. This concept is evidenced in section 3.3,

as the parameterized WRF-10 and MM5-30 perform poorly in almost all stages of the

MCV. In section 3.3.1 it was demonstrated that the under-prediction of the Oklahoma

MCS by these two models seriously hindered their forecasts of a well-defined midlevel

circulation at later times. On the other hand, the convective parameterization appears

susceptible to over-forecasting precipitation and serious convective feedback issues as

well, seen with the unrealistic deepening of the surface low in the presence of strong convection directly over the MCV in MM5-30 and WRF-10.   Additionally, the strength of the midlevel vortex at 0000 UTC 11 June is shown to be important in simulations of the Oklahoma MCS, as those models which forecasted the weaker midlevel shortwave at that time (MM5-30 and WRF-10) failed to produce significant convection through the evening. Furthermore, lead-time appears to be a serious issue in forecasting the convection. Both WRF-4 and MM5-10 forecasts initialized at 0000 UTC 11 June (when widespread convection had already formed) fail to initiate convection in a timely manner and this inaccuracy in convective forecasts has a significant impact on the resulting MCV.

The impacts of increased horizontal resolution do not appear to be as significant a factor in MCV predictability as convective parameterization, as the explicit convective forecasts of MM5-10 often perform better than the parameterized WRF-10, despite using the same horizontal resolution. However, throughout the entire MCV lifecycle, the best performance is that of WRF-4 which uses the highest horizontal resolution of all four models in addition to its explicit convective forecasts. This fine resolution allows the WRF-4 to better simulate small-scale convective processes such as mesoscale updrafts, cold pools and latent heating, which quite possibly is the reason behind its outstanding performance displayed here. For this reason, the deterministic forecasts of WRF-4 are determined to be useful for future dynamic investigations of the IOP 8 MCV and other such systems.

CHAPTER IV

STATISTICAL EVALUATION OF MCV DYNAMICS AND PREDICTABILITY

THROUGH ENSEMBLE FORECASTING

4.1. Introduction

The dynamic processes associated with the IOP 8 MCV as illustrated in Chapters II and III are subjected to further examination in this chapter through a statistical approach using ensemble forecasts. This part of the study utilizes the two-way nested NCAR/PSU nonhydrostatic Mesoscale Model MM5, version 2 (Dudhia 1993), initialized at 0000 UTC on 10 June, extending 48 hours from initialization at three-hour forecast increments. The model is run at a 10-km horizontal resolution and uses 241×181 grid points and 27 vertical layers. The Mellor-Yamada PBL scheme (Mellor and Yamada 1982) is employed, and convection is explicitly forecast using the Reisner microphysics scheme with graupel (Reisner et al. 1998). Both control and perturbed simulations use the operational Eta model as lateral boundary conditions.

Similar to Zhang (2005), twenty ensemble forecasts are generated using balanced random perturbations, produced by randomly selecting initial perturbations from the background error covariance used by the MM5 three-dimensional variational (3DVAR) data assimilation system developed at NCAR (Barker et al. 2004). Twenty sets of random but balanced initial perturbations of the streamfunction are produced and transformed to derive perturbations of wind, temperature and pressure. These

perturbations are added to the reference MM5 analysis at 0000 UTC 10 June to generate

twenty ensemble forecasts (Zhang 2005).

4.2. Ensemble performance

Zhang (2005) described how the ensemble mean often provides the best estimate

of the future state of the atmosphere. This section provides an overview of the ensemble

forecasts and a dynamic comparison of the ensemble mean compared to observations

and deterministic WRF-4 forecasts from Chapter III. Error associated with the ensemble

mean forecast is further investigated through an analysis of ensemble spread and an

evaluation of select ensemble members.

4.2.1. Ensemble mean

Figure 4.1 displays the ensemble mean forecast of 500-hPa wind, height and

relative vorticity along with simulated radar reflectivity at 1200 UTC 10 June and at 6-

hour intervals through the lifecycle of the IOP 8 MCV through 1200 UTC 12 June. The

forecast at 1200 UTC 10 June, 12 hours before MCS initiation, is show in Fig. 4.1a. A

shortwave trough is evident over the New Mexico/Texas border, with an associated

mean relative vorticity maximum of 10^{-4} s^{-1} in West Texas. This forecast verifies well

with the 500-hPa upper air observations in Fig. 2.4 which shows the 5820 m isoheight in

roughly in the same location. The control MM5-10 forecast of the midlevel pattern at

that time (Fig. 3.3b) is similar to both the ensemble mean forecast and upper air

observations, albeit slightly weaker with the depth of the shortwave over Texas and New
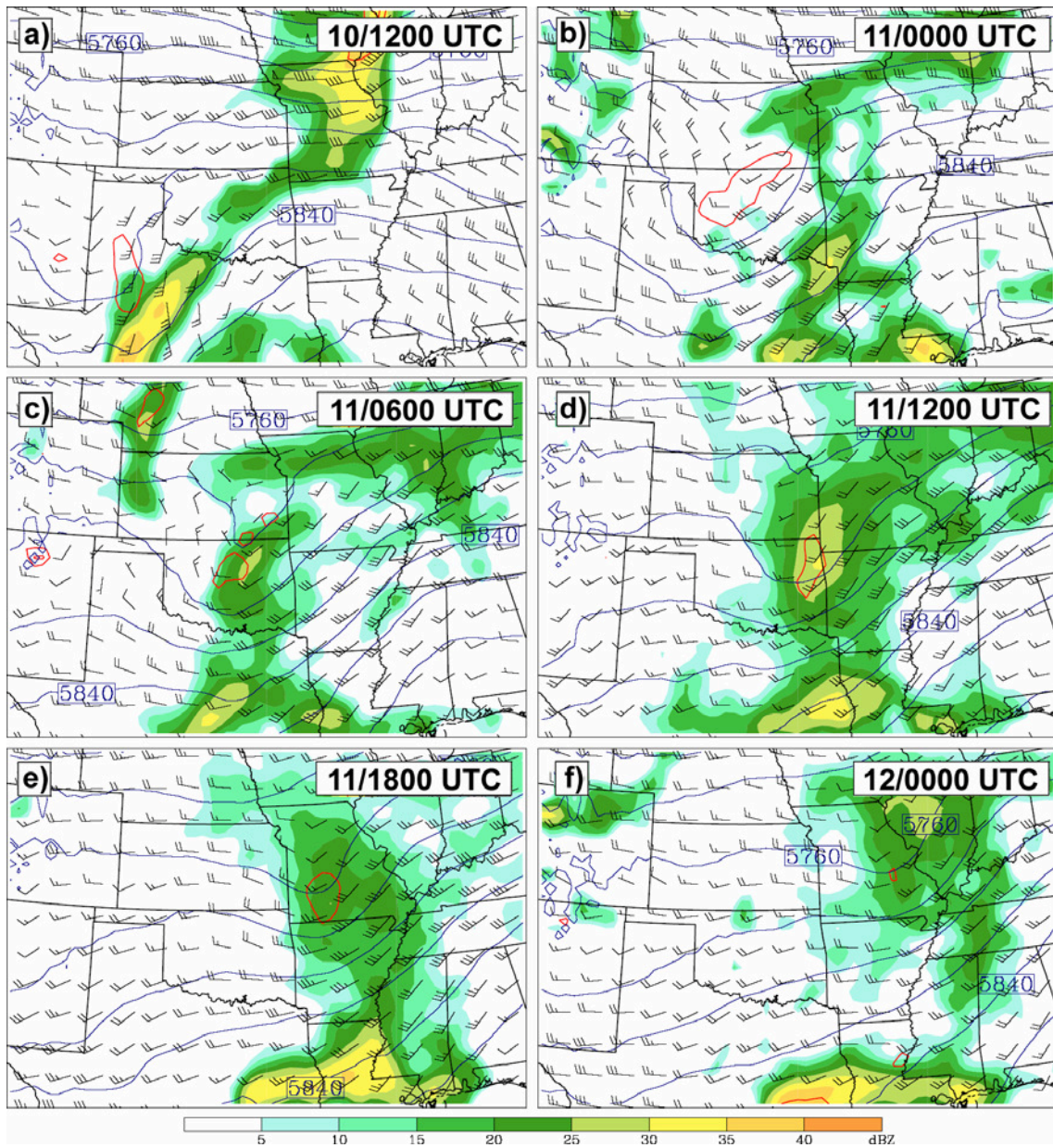
FIG. 4.1. MM5-10 ensemble mean forecast of reflectivity (shaded), 500 hPa relative vorticity (contoured in red every 10^{-4} s^{-1}) heights (m) and wind (one full barb denotes 10 kt) at 1200 UTC 10 June and at 6-hour intervals beginning 0000 UTC 11 June.

Mexico. The WRF-4A forecast (Fig. 3.5b) is even shallower with the depth of the

midlevel shortwave. Additionally, the ensemble mean forecasts a large area of mean

reflectivity greater than 35 dBZ just to the east of the mean midlevel shortwave over

west Texas (Fig. 4.1a). This forecast is much stronger and farther west with convection

than what was detected by radar at that time (Fig. 2.3e), and corresponds best with radar

observations six hours earlier (Fig. 2.3c). Conversely, MM5-10 and WRF-4 simulations

forecast very little to no convection at 1200 UTC (Figs. 3.3a and 3.5a). This comparison

reveals that the ensemble mean forecast performs better than the control simulation as

well as the WRF-4 deterministic forecasts analyzed in Chapter III in the time period

preceding MCS initiation.

Next, Fig. 4.1b provides the ensemble mean forecasts of reflectivity and the 500-

hPa flow pattern at 0000 UTC 11 June, corresponding to the time of MCS initiation (Fig.

2.11b), and at 1200 UTC 11 June, when the MCV circulation had become well-defined

on radar (Fig. 2.11f). While the forecast depth of the 0000 UTC 11 June midlevel

shortwave forecast by the ensemble mean in Fig. 4.1b verifies well with observed 500-

hPa data at that time (Fig. 2.6), the simultaneous mean reflectivity forecast in Oklahoma

is very weak and does not match actual radar observations (Fig. 2.11b). Additionally,

the ensemble mean forecasts too much convection to the east of the shortwave over

Arkansas and eastern Texas at that time. The control MM5-10 does not forecast

convection at all at this time, and incorrectly forecasts the midlevel shortwave trough

slightly weaker than that of the ensemble mean (Fig. 3.7b). While the WRF-4 is

likewise too shallow with the midlevel shortwave at 0000 UTC (Fig. 3.9b), its

convective forecast at that time is far superior to that of the MM5-10 or the ensemble mean. At 0600 UTC (Fig. 4.1c), the ensemble mean forecasts convection in the vicinity of the 500-hPa shortwave over Oklahoma, which matches well with the location of actual convection at that time (2.11d). The control MM5-10 forecasts stronger convection than the ensemble mean, but is too far north and not as widespread (Fig. 3.7d).

Six hours later (Fig. 4.1d) the ensemble mean forecasts a deeper midlevel wave but weakens the 500-hPa vorticity and does not forecast a well-defined circulation (Fig. 2.11f). However, it forecasts a widespread area of weak reflectivity directly over the midlevel shortwave (over the Oklahoma/Arkansas border) which reasonably resembles actual radar in Fig. 2.11f and is very close to the location of the actual midlevel circulation. On the other hand, the control MM5-10 forecasts convection much too strong at that time (Fig. 3.7f) and has displaced the midlevel shortwave trough about 400km too far north over central Missouri. The forecast midlevel circulation pattern, however, is much more accurate than that forecast by the ensemble mean (Fig. 4.1c). Neither the control MM5-10 nor the ensemble mean perform as well as the WRF-4 at this time, which forecasts a well-defined midlevel circulation and weakening reflectivity (Fig. 3.9f) which very closely resembles the midlevel rotation pattern seen in radar in Fig. 2.11f. Hence for the forecast MCV formation, the ensemble mean performs better than the control MM5-10 simulation regarding the midlevel pattern leading to MCS initiation at 0000 UTC and the location of the midlevel disturbance 12 hours later, but fails to forecast a well-defined MCV (though, as will be discussed later, individual

ensemble members do forecast the vortex). Both the ensemble mean and control MM5-10 simulation however fall short of the WRF-4 which displays superior performance during all stages of MCV formation.

Figure 4.1e shows the forecast at 1800 UTC when widespread secondary convection began to develop ahead of the actual MCV (Fig. 2.14). The forecasts at this time also compare to dropsonde data, and are given in more detail in Fig. 4.2 which shows the ensemble mean forecasts of temperature, height and wind at four levels. The ensemble mean forecasts the deepest wave and strongest circulation at 600 hPa which matches the dropsonde observations (Fig. 2.29), though unlike the dropsondes and the control MM5 (Fig. 3.16), the ensemble mean does not produce a closed circulation at any level. Also, the ensemble mean forecasts a transition from a warm-core system to cold core between 600 and 700 hPa (Figs. 4.2b–c) which match dropsonde observations in Figs. 2.29 and 2.30. However, its forecasts of the 500-hPa warm core and 850-hPa cold core (Figs. 4.2a and 4.2d) are too weak, and are not as accurate as the respective temperatures forecast by the control MM5-10 at those levels (Figs. 3.16a and 3.16d). Therefore the ensemble mean, while forecasting the MCV much too weak, does forecast correctly the vertical structure of the midlevel vortex, though is much less accurate than the control simulation.

Finally Fig. 4.1f displays the ensemble mean forecast at 0000 UTC 12 June. The forecast midlevel relative vorticity has weakened dramatically by this time, and the 500-hPa flow in the vicinity of the shortwave trough is very broad and open, as opposed to the continued closed circulation evident in radar loops at this 0000 UTC 12 June (still
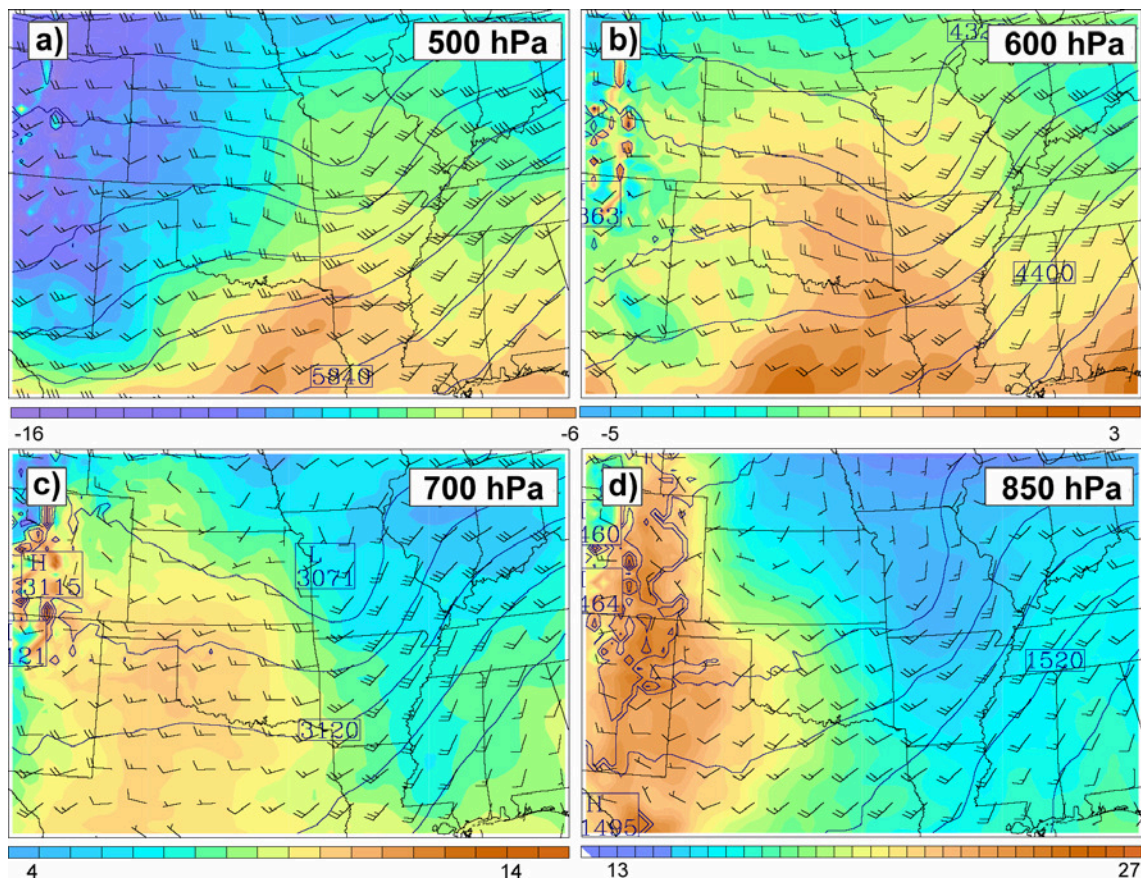
FIG. 4.2. MM5-10 ensemble mean forecasts of temperature (shaded in degrees C), height (contoured in blue every 20 m) and wind (one full barb denotes 10 kt) at 1800 UTC 11 June at (a) 500 hPa, (b) 600 hPa, (c) 700 hPa and (d) 850 hPa.

radar image in Fig. 2.14d). In addition, the ensemble mean places the shortwave trough

over northeast Missouri, whereas the center of circulation is detected on radar about 300

km to the south at this time over extreme southeast Missouri. The MM5 ensemble mean

forecasts a large area of convection over and to the west of the midlevel shortwave

trough (Fig. 4.1d), which is reasonably accurate compared to the widespread

precipitation seen on radar reflectivity in Fig. 2.14d. The control MM5-10 forecasts a

much stronger closed midlevel circulation at this time (Fig. 3.14d), as well as convection

over the MCV center and to its east. However this model is much too far northeast with

the MCV circulation over eastern Illinois. WRF-4B again shows the most accurate

forecast of the MCV and secondary convection at this time (Fig. 3.13d), with a well-

defined cyclonic circulation over southeast Missouri and widespread convection to the

north and east, corresponding well with actual radar reflectivity (Fig. 2.14d).

Through the comparison of the MM5 ensemble mean with the control MM5-10

and WRF-4 forecasts, it is evident that the ensemble mean performs better than the

control MM5-10 regarding strength and placement of large scale features and convection,

but fails to accurately forecast a well-defined MCV. The ensemble mean is most

accurate 12 to 24 hours after initialization (before MCS initiation on 0000 UTC 11 June).

After that time, the control MM5-10 displays much better accuracy in forecasting the

MCV circulation than the ensemble mean due to the lack of a well-defined circulation in

several ensemble forecasts. The ensemble mean is more accurate than both the control

MM5-10 and WRF-4 in forecasting the general upper air pattern leading up to MCS

initiation (1200 UTC 10 June through 0000 UTC 11 June), but significantly lags the

WRF-4 in MCV simulation after that point. Thus, the ensemble mean is reliable in predicting large-scale non-convective atmospheric processes in this case, but its accuracy deteriorates at the onset of the convection-sensitive MCV lifecycle.

4.2.2. Ensemble members

The cause of the relatively poor performance by the ensemble mean after MCV formation in Fig. 4.1 is seen when examining the ensemble members themselves. There is considerable spread among the twenty ensemble members, among which EN-31 and EN-35 perform poorly. Members EN-36 and EN-40 display fair performance, while EN-33 and EN-34 show the most accurate forecasts of all ensemble members. Figure 4.3 displays the predicted 300 hPa height, wind and potential vorticity of each of these ensemble members at 1800 UTC 10 June, or roughly six hours before MCS initiation. These figures illustrate the forecast upper tropospheric structure leading up to the development of the MCS over Oklahoma during the local evening hours of 10 June. The most notable difference among the six forecasts is the presence of potential vorticity perturbations in the vicinity of forecast convection ahead of the upper level wave forecast by EN-31 and EN-35. Otherwise, the upper-air forecasts at this time are relatively similar with only slight variances regarding the depth of the wave over New Mexico and west Texas.

Figure 4.4 shows the reflectivity forecast by these same ensemble members at 0600 UTC 11 June. It was at this time that the observed MCS had reached maturity and spanned the entire state of Oklahoma (Fig. 2.11d). Despite the relatively low variation
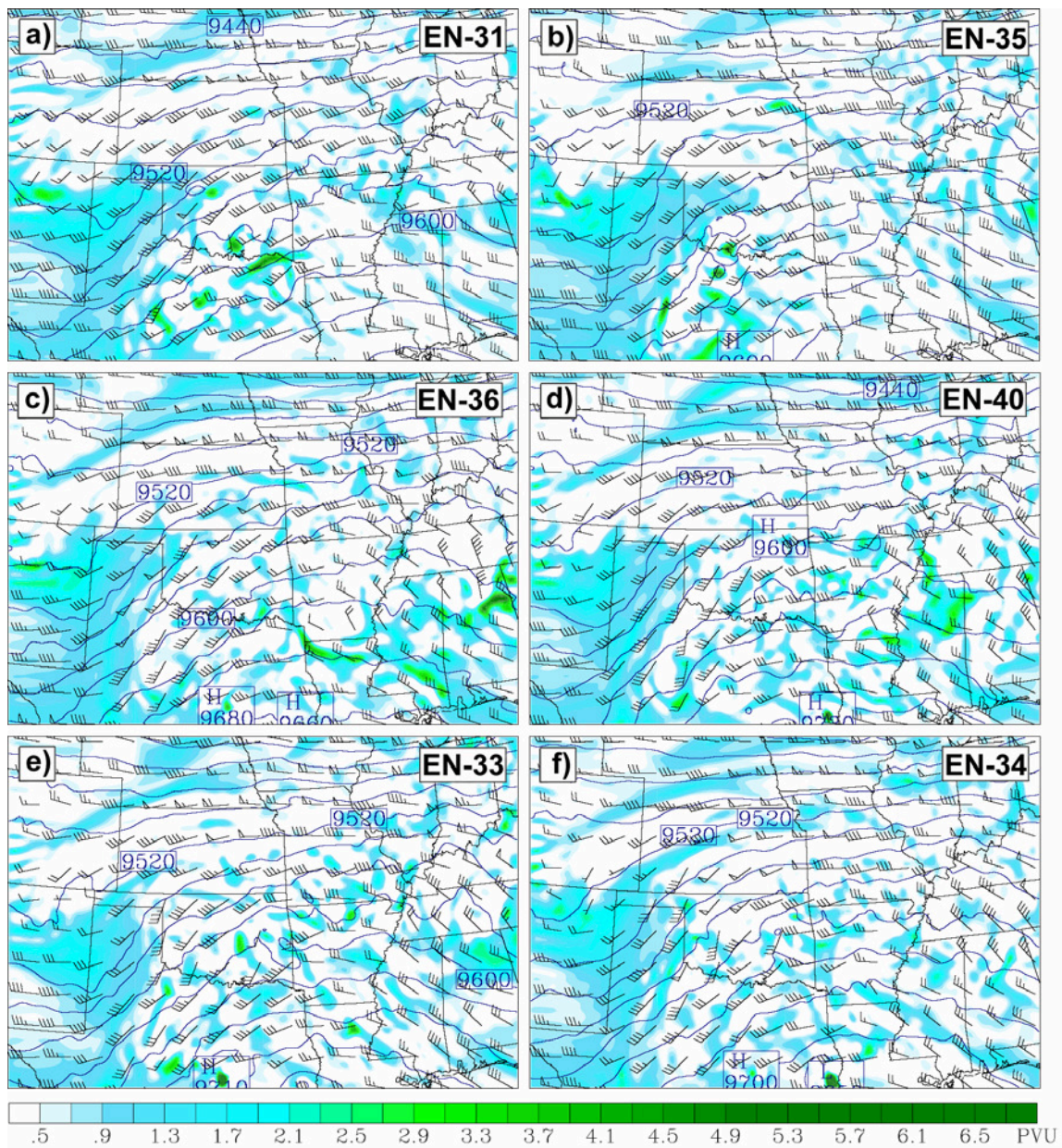
FIG. 4.3. Six chosen ensemble forecasts of 300-hPa potential vorticity (shaded), height (contoured every 20 m) and wind vector in knots at 1800 UTC 10 June.
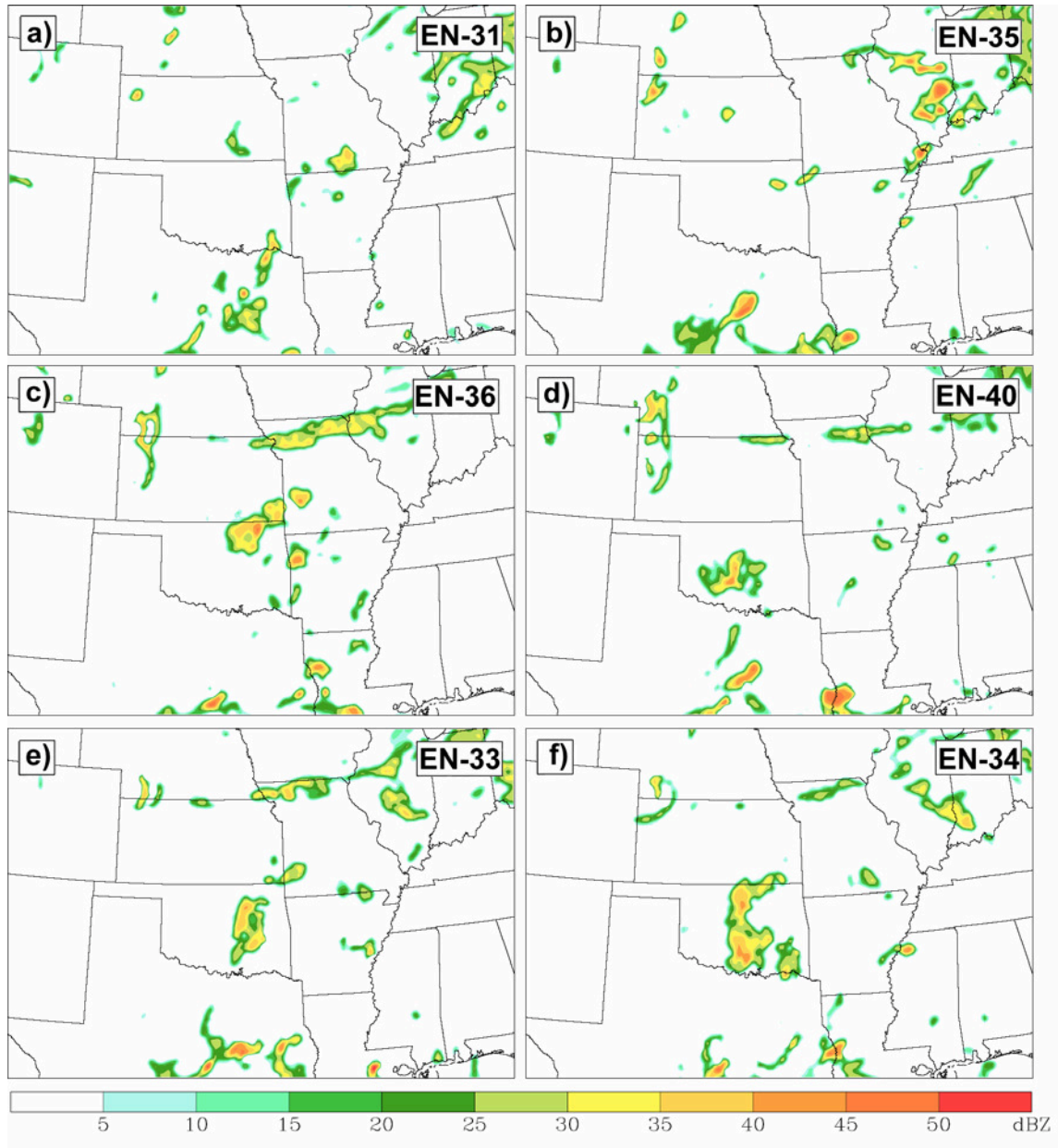
FIG. 4.4. Six chosen ensemble forecasts of simulated radar reflectivity at 0600 UTC 11 June.

among forecasts of the upper level system twelve hours earlier, the reflectivity forecasts at this time encompass a much greater range, varying from almost no convection over Oklahoma at all (EN-31 and EN-35; Figs. 4.4a and 4.4b respectively) to a well-organized strong convective system (EN-34; Fig. 4.4f).

Reflectivity forecasts at 1200 UTC 11 June for the same members are presented in Fig. 4.5, the time at which the IOP 8 MCV circulation had been clearly noticeable on radar within a weakening convective system (Fig. 2.11f). As with the reflectivity forecasts six hours prior, the ensemble forecasts for 1200 UTC show a great deal of variation, including unorganized weak activity (EN-31; Fig. 4.5a), widespread unorganized convection (EN-36; Fig. 4.5c), strong organized convection (EN-40; Fig. 4.5d) and an apparent MCV (EN-33, EN34; Figs. 4.5e and 4.5f respectively). It is noted that EN-34 which shows the most accurate forecast of the MCV at that time also shows the best performance predicting the Oklahoma MCS at 0600 UTC. Those members which exhibit poor forecasts of the MCV at 1200 UTC also poorly forecast convection six hours prior to that time, implying a dependence of MCV predictability on the ability to accurately predict the MCS.

A further look into ensemble forecasts of the IOP 8 MCV is given in Fig. 4.6 which presents forecasts of 600 hPa height, wind and potential vorticity at 1200 UTC 11 June, the same time as the reflectivity forecasts in Fig. 4.5. EN-31 and EN-35, which had forecasted little to no convection between 0600 UTC and 1200 UTC, also do not predict an MCV at this time (Fig. 4.6a,b). While the other four members predict a midlevel circulation, they vary in location, depth and strength. The only members to
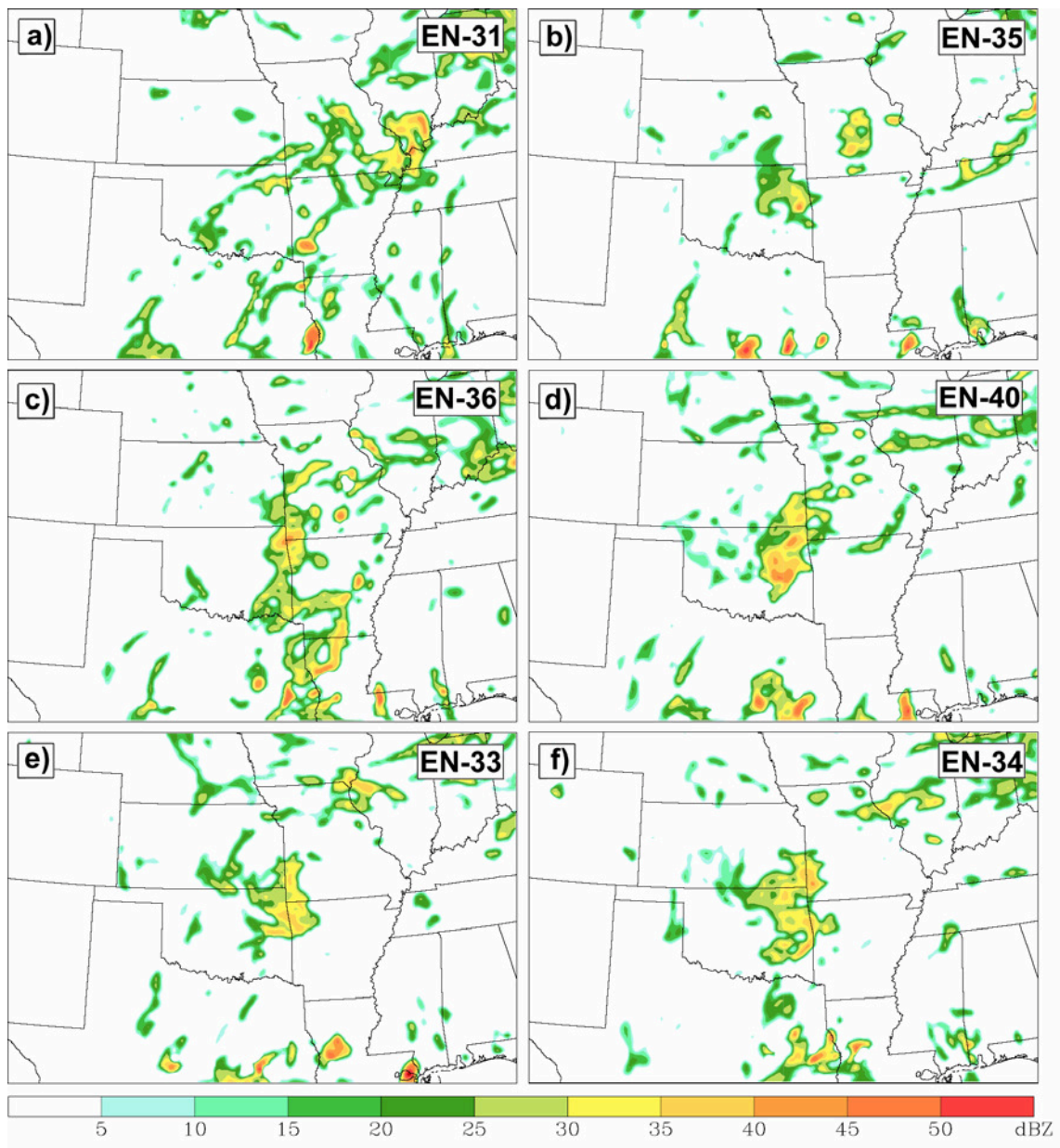
FIG. 4.5. Six chosen ensemble forecasts of simulated radar reflectivity at 1200 UTC 11 June.
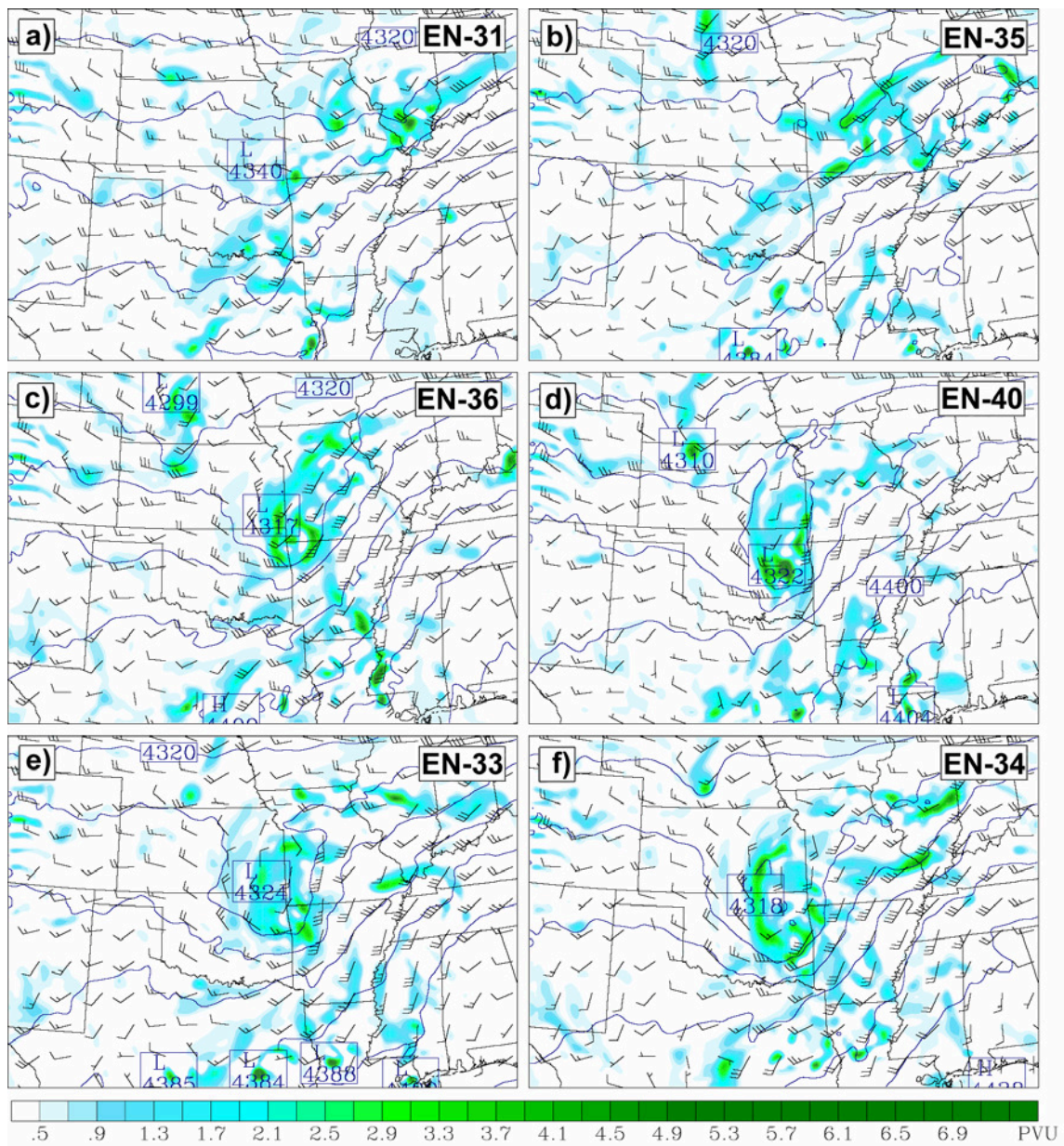
FIG. 4.6. Six chosen ensemble forecasts of 600-hPa potential vorticity (shaded), height (contoured every 20 m) and wind vector in knots at 1200 UTC 11 June.

forecast a closed circulation at this time are EN-33 and EN-34 (Figs. 4.6e,f). The same

members had likewise exhibited the best performance forecasting convection,

illustrating the importance of strong, long-lived convection in creating a well-defined

MCV through creation of heating-induced midlevel potential vorticity.

Next, the variety in forecasts of the mature MCV, including secondary

convection and surface cyclone development among ensemble members is examined.

Ensemble forecasts of 600-hPa temperature, height and wind at 1800 UTC 11 June are

given in Fig. 4.7. These forecasts can be compared to 600-hPa dropsonde observations

of the MCV in Fig. 2.29, which had detected a cyclonic circulation over southern

Missouri and northern Arkansas coincident with a warm core of 1 ºC and a low in the

height field of below 4000 m. The warm core and cyclonic circulation are not present in

the forecasts of EN-31 and EN-35 (Figs. 4.7a,b) due to the lack of an MCV. The other

four members forecast a low in the 600-hPa height field near 4300 m, though no

ensemble member forecasts heights as low as were detected in the dropsonde data.

Though EN-36 forecasts the deepest low of these four members, (Fig. 4.7c), it forecasts

the weakest circulation and coolest midlevel temperatures compared to the other

members and the dropsonde data in Fig. 2.29. Figure 4.8 shows reflectivity forecasts for

each ensemble member at 1800 UTC 11 June, the time at which widespread secondary

convection had developed in real time (Fig. 2.14b). As with convection at previous

times, these figures demonstrate the wide range of convective forecasts at this time,

ranging from almost no convection at all near the MCV (EN-31 and EN-35; Figs. 4.8a,b)

to widespread activity directly over the midlevel circulation (EN-34; Fig. 4.8f). Of the
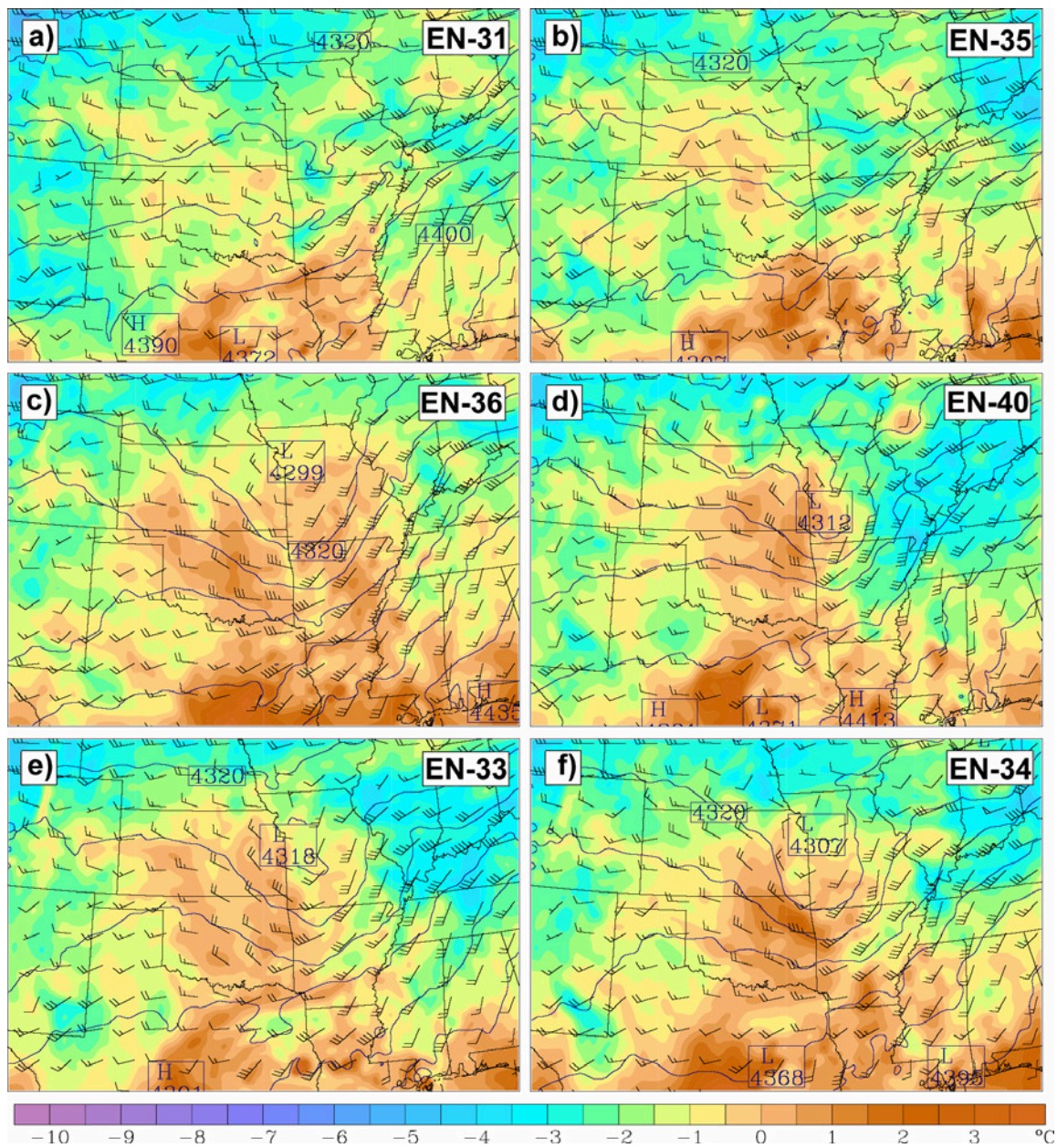
FIG. 4.7. Six chosen ensemble forecasts of 600-hPa temperature (shaded in degrees C), height (contoured every 20 m) and wind vector in knots at 1800 UTC 11 June.
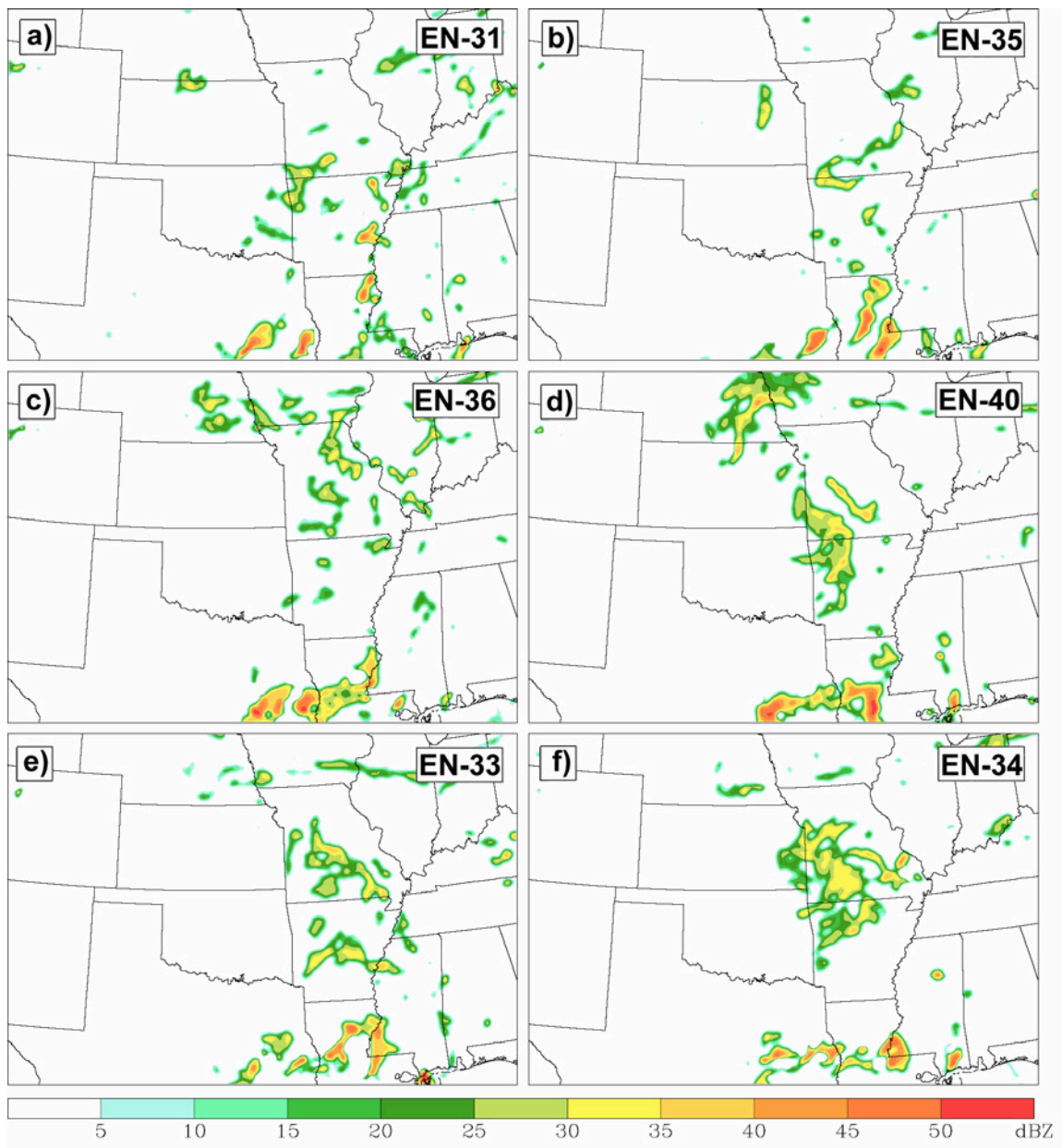
FIG. 4.8. Six chosen ensemble forecasts of simulated radar reflectivity at 1800 UTC 11 June.

four good members, EN-36 forecasts the weakest convection (Fig. 4.8c) corresponding

with its poorer forecast of the MCV in Fig. 4.7c. This disparity illustrates sensitivity of

forecasting moist convection to the MCV forecast.

Finally, member forecasts of surface wind, pressure and temperature at 0000

UTC 12 June are given in Fig. 4.9. It was at this time that a relatively strong surface

cyclone had begun to develop with a well-defined surface circulation over southeast

Missouri and a surface pressure of 1004 hPa (Fig. 2.23).   The most superb forecast once

again comes from EN-33 and EN-34, which predict a closed surface circulation at this

time, as well as a strong surface cold pool (temperature near 65 degrees Fahrenheit) and

a surface pressure below 1006 hPa (Figs. 4.9e–f). Signs of a surface circulation among

the other members are very weak to non-existent, and the pressures and surface

temperatures are quite a bit higher.

The six chosen ensemble member forecasts presented in Figs. 4.3–8 illustrate the

wide variety of simulated results of this system despite only slight variations in initial

forecasts. Of particular interest is the way certain members maintain their skill in

forecasting the IOP 8 MCV through the development of the initial MCS and continuing

through the penetration of the MCV circulation to the surface. As illustrated here, EN-

33 and EN-34, which exhibit the best forecast of the initial MCS, also show the best

performance in predicting the MCV at 1200 UTC 11 June and the surface low at 0000

UTC 12 June. At the same time, EN-31 and EN-35, which forecast very little

convection at the time of the initial MCS, also exhibit very poor performance in

forecasting the midlevel circulation at 1200 UTC 11 June and surface low development
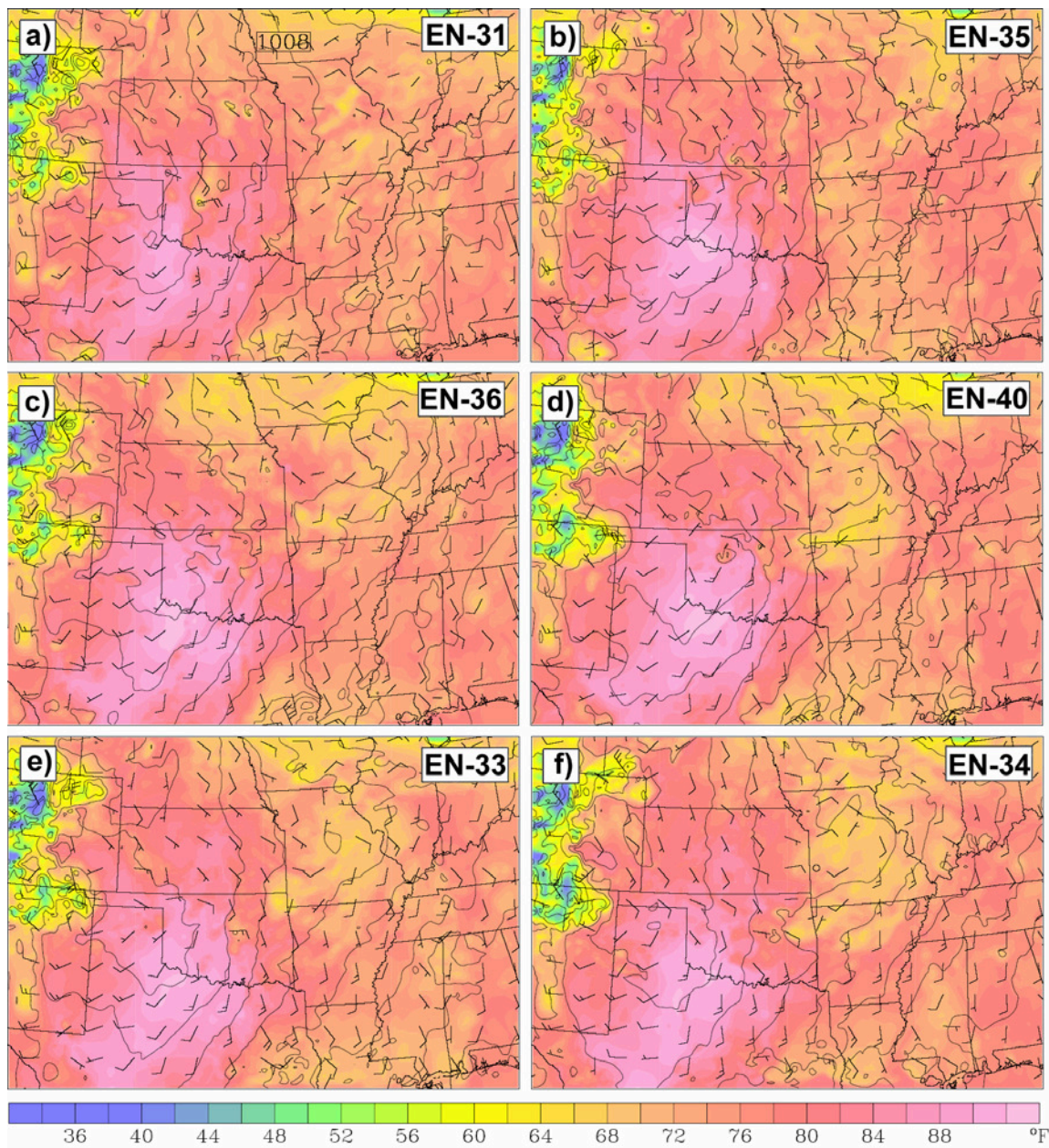
FIG. 4.9. Six chosen ensemble forecasts of surface temperature (shaded), mean sea level pressure (contoured every 2 hPa) and 10-m wind vector in knots at 0000 UTC 12 June.

at 0000 UTC 12 June. Thus, these chosen ensemble member forecasts illustrate the

major role of moist convection in the predictability of this MCV and the significant

forecast divergence that results. Because the best forecasts are at the edge of the

ensemble spread, the ensemble mean forecast, described in section 4.2.1, becomes less

reliable after MCV formation (Fig. 4.1). The correlation among convection and the

MCV, along with many other forecast variables, will be further examined in section

4.3.3.

4.2.3. Ensemble error growth

The ensemble spread analyzed in section 4.2.1 is represented quantitatively in

this section using the root-mean of difference total energy (RM_DTE), where

$$DTE = 0.5(u'u'+v'v'+kT'T') \tag{4.1}$$

where primes denote the difference between any two members and $k = C_p/T_r$ ($C_p =$

1004.9 J kg^{-1} K^{-1} and the reference temperature $T_r = 270K$) (Zhang et al. 2004). Figures

4.10 and 4.11 show the horizontal distribution of vertically averaged RM_DTE for six-

hour intervals beginning at 0600 UTC 10 June, or six hours after initialization. The most

significant regions of error growth (> 5 ms^{-1}) through 1800 UTC 10 June (Figs. 4.10a–c)

are found in the immediate vicinity of moist convection and the midlevel shortwave

trough, consistent with Zhang et al. (2003). Beginning at 0600 UTC 11 June (Fig.

4.11a), roughly the time of MCV formation, a region of maximum ensemble spread

greater than 4 m s^{-1} becomes associated with the MCV over central Oklahoma and

reaches a maximum value of 5 m s^{-1} at 1200 UTC. After that time, RM_DTE slightly
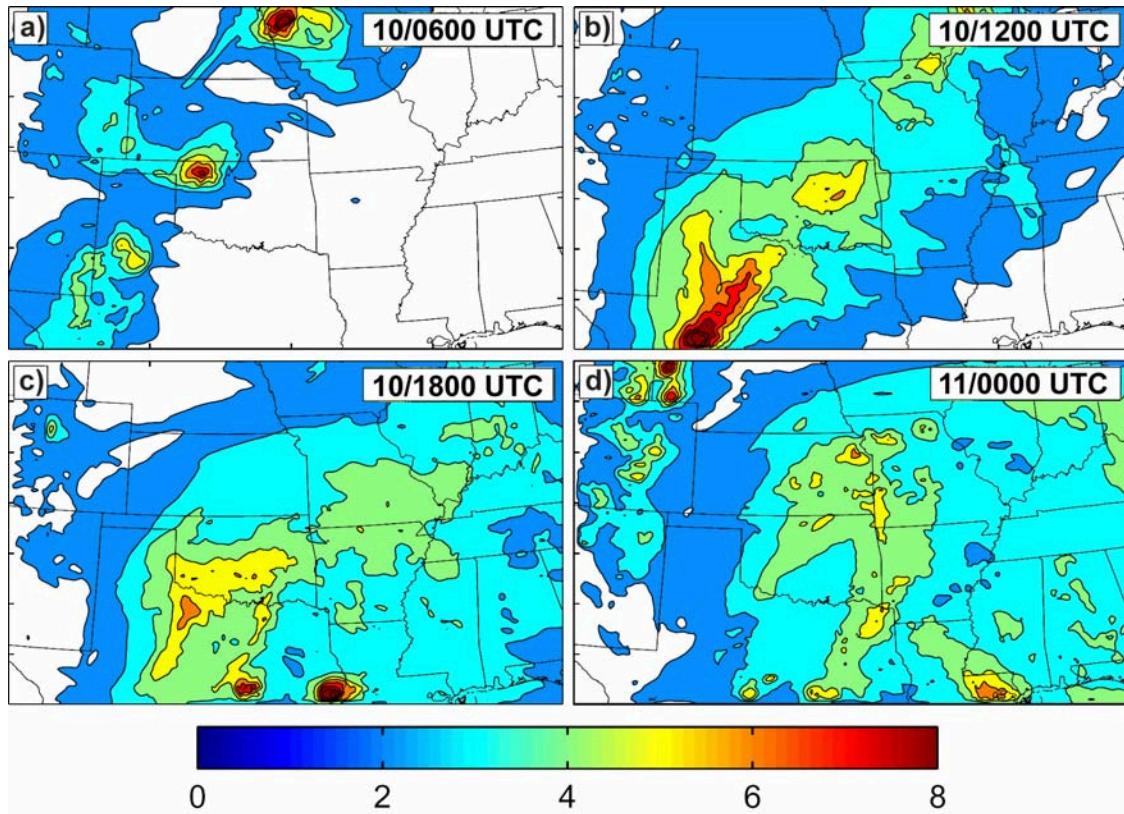
FIG. 4.10. Horizontal distribution of vertically-averaged RM_DTE at 6-hour intervals starting 0600 UTC 10 June.
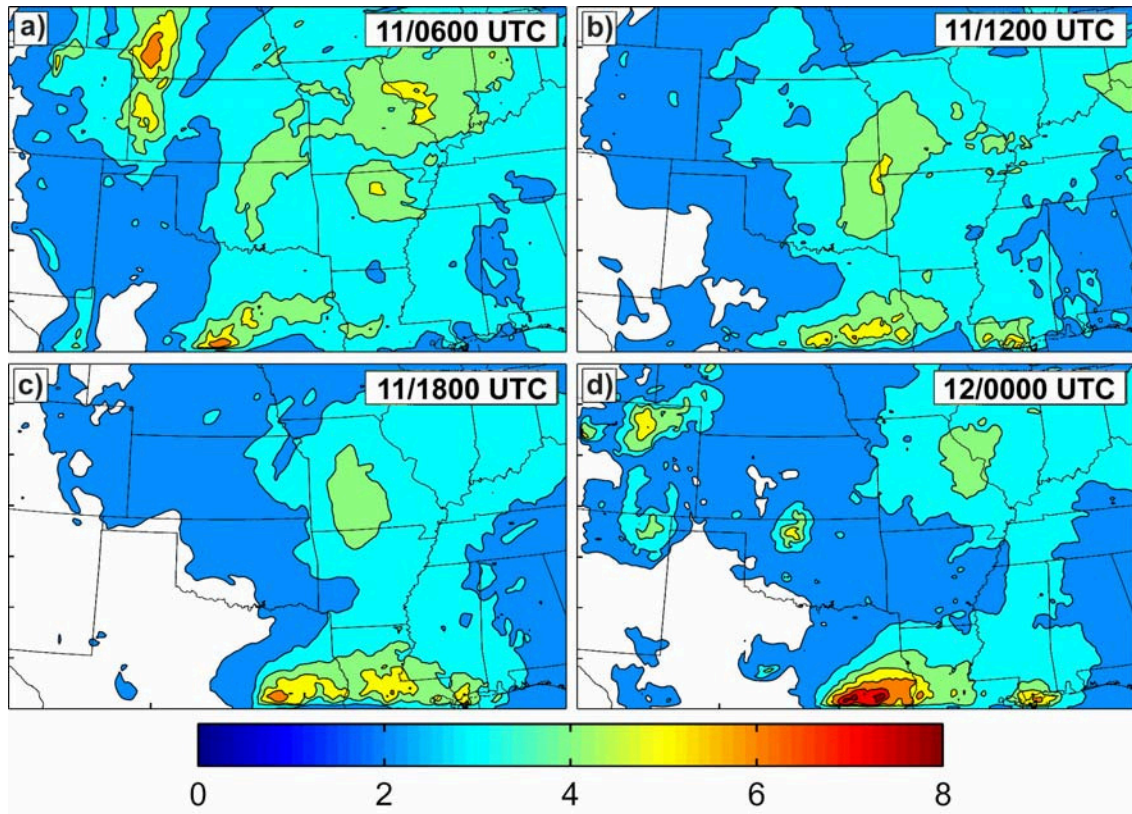
FIG. 4.11. Horizontal distribution of vertically-averaged RM_DTE at 6-hour intervals starting 0600 UTC 11 June.

decreases following the MCV through the end of the forecast period, except for a local maximum at the southern-most portion of the display domain where strong convection is forecast (Figs. 4.11c,d).

The corresponding vertical distribution of horizontally-averaged RM_DTE is given in Fig. 4.12a, analyzed in three-hour intervals beginning with model initialization at 0000 UTC 10 June. Initial ensemble spread by the balanced initialization method (denoted as green dotted line in Fig. 4.12a) is maximized in the upper and lower troposphere. RM_DTE at the tropopause and near the surface grows through 0000 UTC 11 June (black dotted line in Fig. 4.12a). At the same time, a third local error maximum grows in the middle troposphere between 0000 UTC and 0600 UTC, centered between 500- and 600-hPa, the same layer where initial error was lowest. RM_DTE at this level peaks between 0300 and 0600 UTC, likely associated with the developing mean convection through that time (Fig. 4.1) and the associated latent heating. The slight decrease in error growth after this time (Fig. 4.12b) is attributed to the fact that many ensembles do not forecast an MCV or widespread secondary convection after 1200 UTC 11 June, thus their forecasts are relatively similar (albeit bad), which may not be representative for the uncertainty associated with moist convection forecast at this later time.
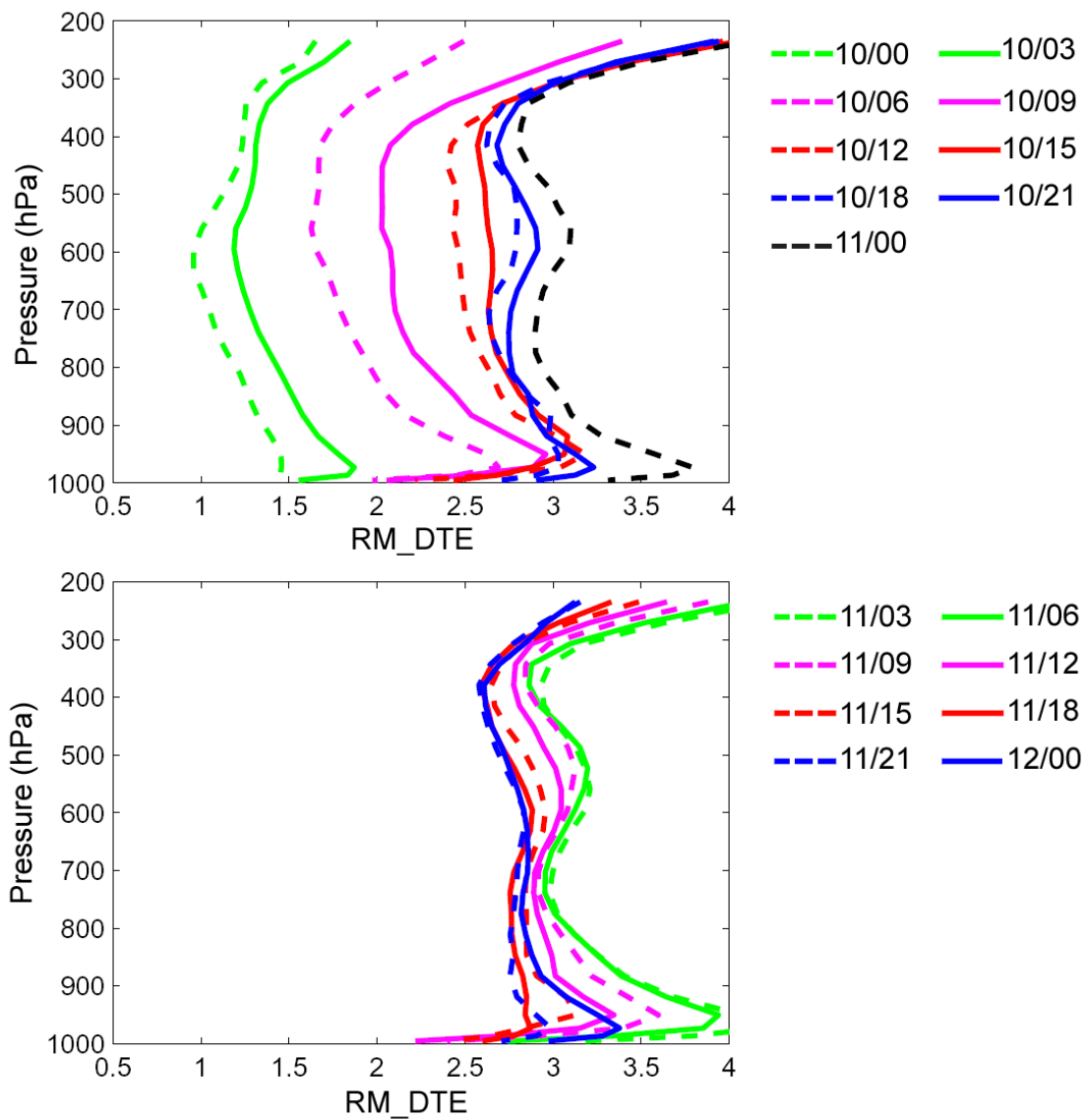
FIG. 4.12. Vertical distribution of vertically-averaged RM_DTE at three hour intervals beginning 0000 UTC 10 June.

4.3. Structure and dynamics of error correlation

In this section, error correlation structure is evaluated to give further insight into the dynamics of the IOP 8 MCV. The correlation coefficient r is calculated among a set of n data points using

$$Cor\left\{x_{i_1 j_1 k_1}, y_{i_2 j_2 k_2}\right\} = \frac{\frac{1}{N-1}\sum_{n=1}^{N}\left(x_{i_1 j_1 k_1 n} - \overline{x_{i_1 j_1 k_1}}\right)\left(y_{i_2 j_2 k_2 n} - \overline{y_{i_2 j_2 k_2}}\right)}{\left[\frac{1}{N-1}\sum_{n-1}^{N}\left(x_{i_1 j_1 k_1 n} - \overline{x_{i_1 j_1 k_1}}\right)^2\right]^{1/2}\left[\frac{1}{N-1}\sum_{n-1}^{N}\left(y_{i_2 j_2 k_2 n} - \overline{y_{i_2 j_2 k_2}}\right)^2\right]^{1/2}} \quad ,(4.2)$$

where x and y denote two model state variables. Two types of correlation are used: cross correlation, which is defined as the correlation between two different forecast variables at the same grid point, and cross-spatial correlation, defined as the correlation between different variables at different grid points. The correlations examined in this section focus on the atmospheric processes that were deemed important to the MCV lifecycle in previous literature and in Chapters II and III of this study. Specifically, the correlation analysis will focus on the relationship between the strength of the MCV at different times through its lifecycle to the 10 June West Texas convection, the strength of the shortwave trough at the time of MCS initiation, the strength and areal coverage of secondary convection, and ambient wind shear during the second diurnal cycle.

4.3.1. MCV Precursor: West Texas MCS and resulting midlevel circulation

In Chapter II, the strength of the initial shortwave was considered a factor in the strength of the Oklahoma MCS of late 10 June and thus the strength of the MCV. In addition, it was speculated that convection over New Mexico and west Texas during the

early morning of 10 June acted to strengthen the midlevel shortwave before MCS

initiation over Oklahoma. Here this hypothesis is tested by examining the probabilistic

forecasts relating the initial shortwave and convection over the extreme southwestern

Plains to the MCS over the southern and central Plains on early 11 June and the strength

of the MCV.

To represent convection during the local morning of 10 June over New Mexico

and Texas this part of the probabilistic dynamics study uses surface temperature, with

lower temperatures indicative of a stronger surface cold pool. While a more direct

representation of convection through hydrometeor mixing ratio could also be used, the

forecast surface cold pools generally encompass a larger area than localized convective

updrafts and detectable longer than hydrometeors. Since the cooling effects of

evaporative cooling generally linger for a few hours after precipitation has ended, the

surface temperatures are analyzed at 1500 UTC, the latest time at which any ensembles

forecast convection over West Texas, so that those members which produce convection

at any time during the local morning of 10 June will be included in the correlation

analysis.

The structure of the midlevel shortwave at 0000 UTC 11 June, the time

immediately before the ensemble-mean had initiated convection (Fig. 4.1b), is illustrated

in Fig. 4.13 in which the ensemble-mean 600-hPa PV is presented in green. The mean

PV is oriented in a southwest to northeast elongated fashion from northwest Texas to

eastern Kansas, along the center of the midlevel trough, and reaches a maximum of

roughly 2.3 PVU over western Oklahoma. The ensemble-average 1500 UTC 10 June

surface temperature is shaded in gray in Fig. 4.13 and shows a clear negative

temperature anomaly of up to 6 degrees exists in southwest Texas where convection is

most commonly found among ensemble members at that time and three hours earlier

(ensemble mean convection at 1200 UTC shown in Fig. 4.1a). The correlation among

the point of maximum 600 hPa potential vorticity at 0000 UTC 11 June (point A) to the

surface temperature field nine hours earlier is shown in Fig. 4.13a. A weak negative

correlation of over 0.3 exists over a large part of western Texas and eastern New Mexico,

and is strongest in the northeastern part of the coldest mean temperatures where a small

negative correlation of 0.5 is found (point B). This correlation pattern is implicative of a

relation between convection near the upper wave at 1500 UTC to the strength of the

midlevel vortex nine hours later. In addition, the weak negative correlation to the north

and west of the mean surface cold pool indicates that a stronger midlevel vortex is also

related to convection which initiates earlier and farther northwest.

Similarly, a negative correlation exists between the surface temperature at point

B and the region of maximum vorticity at 0000 UTC (Fig. 4.13b). Positive correlations

of over 0.5 exist on the western and eastern edges of the PV center. This correlation

pattern suggests that stronger early morning convection is generally associated with a

smaller, stronger midlevel vortex in the afternoon and vice versa. This relationship is

exemplified in Fig. 4.14 by comparing the reflectivity forecasts of EN-31 and EN-34 at

1200 UTC 10 June to their respective 600-hPa potential vorticity forecasts twelve hours

later. EN-31 forecasts weaker convection over a more constrained area than EN-34, and

consequently its forecast surface cold pool is much smaller. Similar to its limited

FIG. 4.13. The forecast estimated correlation between (a) 0000 UTC 11 June 600 hPa potential vorticity at point A and any 1500 UTC 10 June surface temperature, and (b) 1500 UTC 10 June surface temperature at point B to any 0000 UTC 11 June 600 hPa potential vorticity. Positive correlation values are in solid blue contours and negative in dashed contour starting at ±0.3 and with intervals of 0.2. Mean potential vorticity contoured in green with contour intervals of 0.5 PVU and mean surface temperature shaded every 2 degrees C.
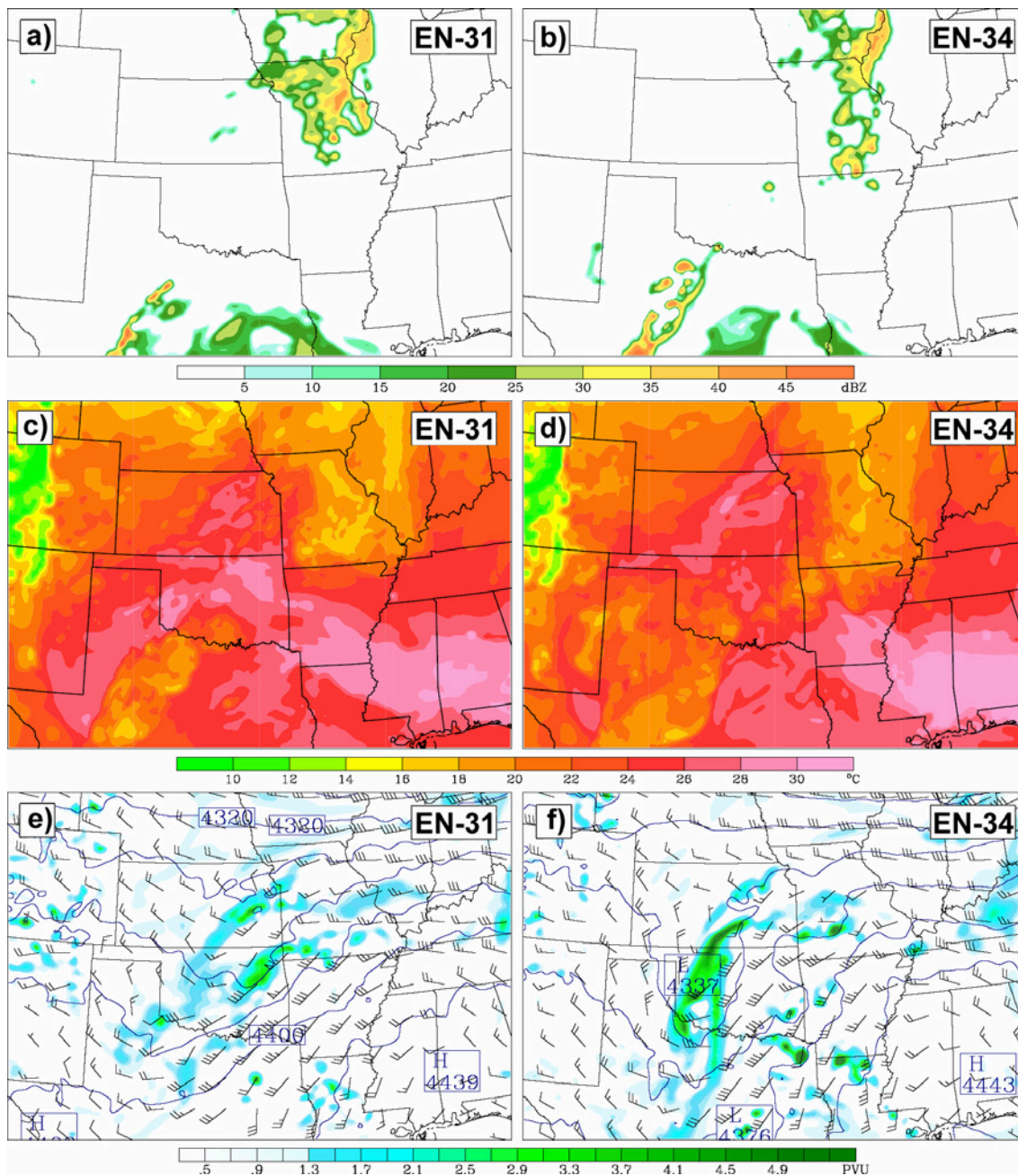
FIG. 4.14. (a,b) Ensemble forecast reflectivity at 1200 UTC 10 June, (c,d) forecast surface temperature in degrees Celsius at 1500 UTC 10 June and (e,f) 600-hPa potential vorticity (shaded), height (contoured every 10 m) and wind vector in knots at 0000 UTC 11 June.

forecast of convection, EN-31 forecasts a much weaker and broader PV anomaly at 0000

UTC, with the PV maximum actually focused ahead of the midlevel trough. Conversely,

EN-34 forecasts more widespread convection, and its forecast PV at 0000 UTC is

significantly stronger and more concentrated along the base of the midlevel shortwave.

A better illustration of the structure of the PV correlation to 10 June convection

is given in an east/west cross section in Fig. 4.15 across the vorticity maximum at 0000

UTC 11 June (represented as a red line in Fig. 4.13b). The disturbance is located

primarily in the upper troposphere with a PV perturbation extending down to the

midlevels where a second PV maximum is located. The negative correlation with the

surface cold pool from 9 hours earlier is primarily over the middle troposphere

perturbation. This correlation suggests that a stronger cold pool, and hence stronger

convection, acts to strengthen the PV in the middle levels of the troposphere, most likely

due to convective heating, and this strengthened PV maintains at least some of its

magnitude up until convective initialization that evening around 0000 UTC. It is

certainly possible that the correlation is due to the fact that stronger and more

widespread convection on early 10 June will be associated with a stronger initial

midlevel wave which translates to a stronger vortex later on. However, since the

negative correlation shown in Fig. 4.15 is focused primarily below the typical region of

maximum convective heating (described in section 3.3.1), it appears that PV is created in

the middle and lower levels of the troposphere by early morning convection which acts

to strengthen the midlevel disturbance, and this intensity is at least somewhat maintained

throughout the day. Thus, it is further demonstrated that the convection of the morning
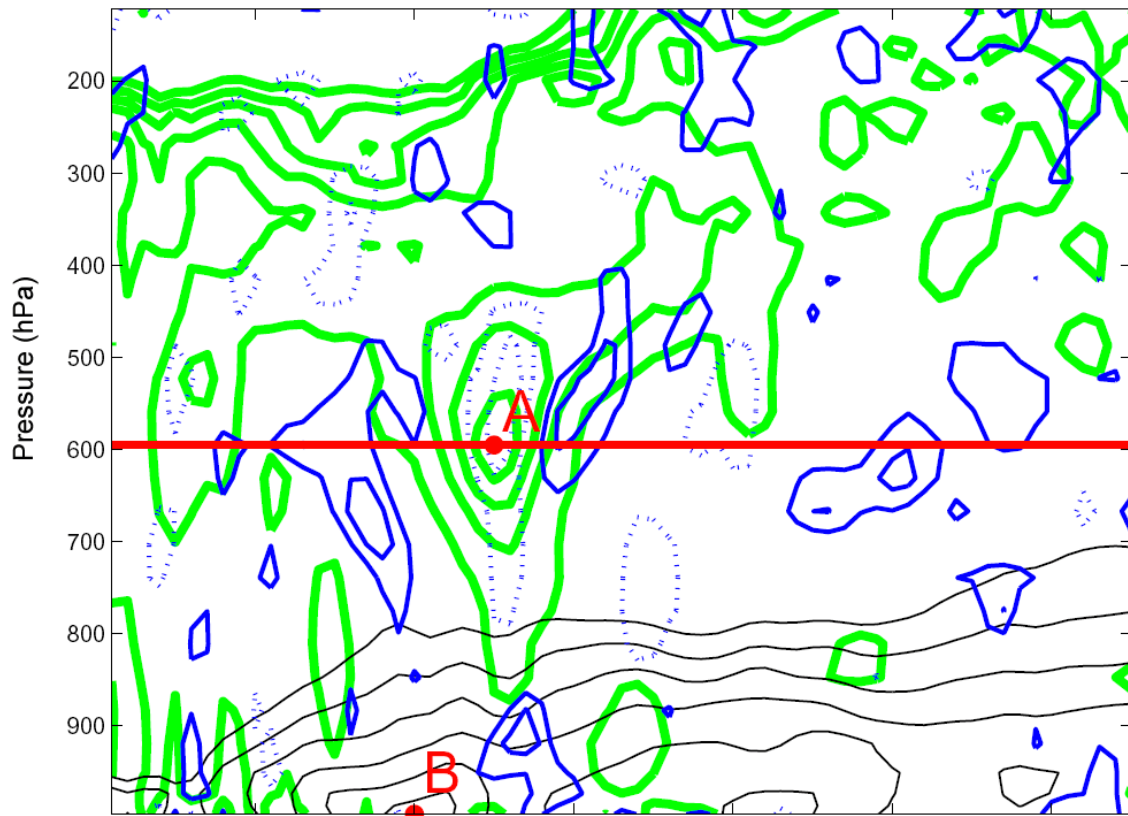
FIG. 4.15. The forecast estimated correlation between 1500 UTC 10 June surface temperature at point B in Fig. 4.11b to any 0000 UTC 11 June potential vorticity along vertical cross section denoted as red line in Fig. 4.11b. Positive correlation values are in solid blue contours and negative in dashed contour starting at ±0.3 and with intervals of 0.2. Mean potential vorticity shaded every 0.5 PVU.

of 10 June may indeed be a factor in the strength of the midlevel vortex at 0000 UTC 11 June by contributing to enhanced midlevel vorticity and a possible MCV.

The correlation patterns in Fig. 4.13 is examined further in Fig. 4.16a which gives the correlation between the 1500 UTC 10 June surface temperature at point A (representative of convection) to 300 hPa PV six hours earlier (before most ensemble members forecast convection). A moderate negative correlation exists over the 300 hPa wave in southeast New Mexico, suggesting that a stronger upper-level wave at 0900 UTC is related to stronger convection during the next several hours. Also of note in Fig. 4.16a is the strong positive correlation immediately ahead of the upper PV anomaly in western Texas. This correlation appears to be the direct result of tropospheric PV destruction resulting from convection over that region in a few ensemble members at that time. Figure 4.16b shows the correlation between 0900 UTC 10 June PV at 300 hPa at point B to 600 hPa 0000 UTC PV. A positive correlation exists over the center of the midlevel PV maximum, very similar in structure to the correlation from 1500 UTC surface temperature to midlevel PV in Fig. 4.13b. Figure 4.17 gives the correlation from the point of maximum 600-hPa potential vorticity at 0000 UTC 11 June to PV at the same level at 0900 UTC 10 June. No significant correlation exists upstream (eastern New Mexico) which suggests that the correlations over the midlevel shortwave at 0000 UTC 11 June in Figs. 4.13b and 4.16b are not strictly due to the simple translation of stronger midlevel PV through time. The correlations in Figs. 4.13 and 4.16 then suggest that a stronger midlevel shortwave at 0000 UTC 11 June is correlated with a stronger
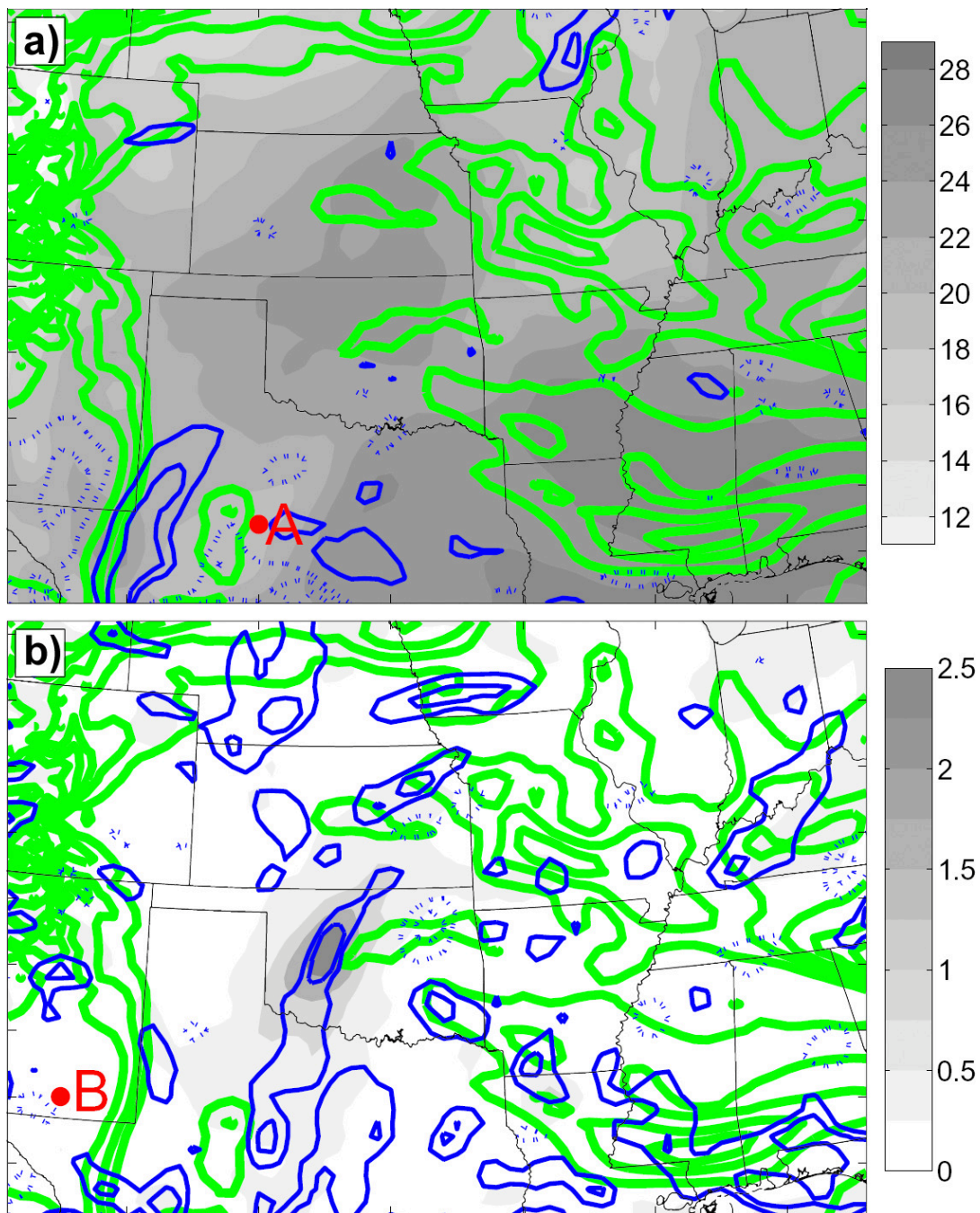
FIG. 4.16. The forecast estimated correlation between (a) 1500 UTC 10 June surface temperature at point A to any 0900 UTC 10 June 300 hPa potential vorticity (mean 300 hPa potential vorticity contoured in green every 0.5 PVU and mean temperature shaded every 2 degrees C), and (b) 0900 UTC 10 June potential vorticity at point B to any 0000 UTC 11 June 600 hPa potential vorticity (mean 300 hPa potential vorticity contoured in green every 0.5 PVU and mean 600 hPa potential vorticity shaded every 0.5 PVU). Positive correlation values are in solid blue contours and negative in dashed contour starting at ±0.3 and with intervals of 0.2.
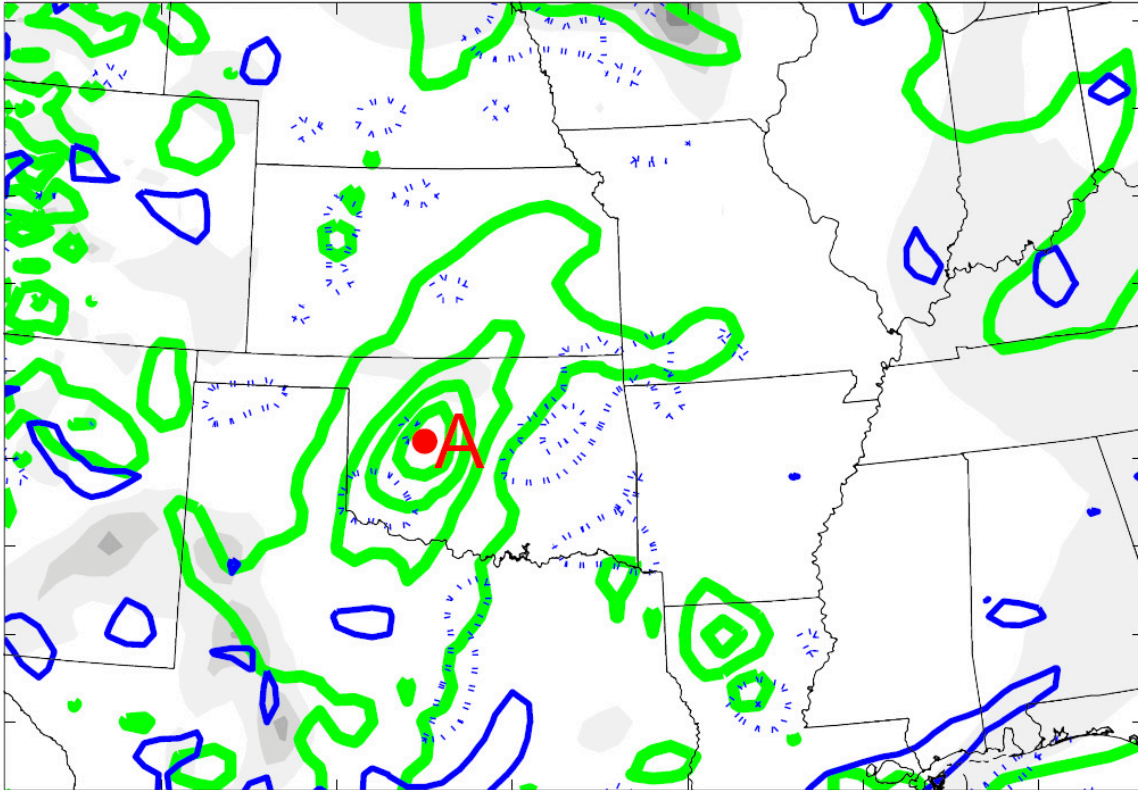
FIG. 4.17. The forecast estimated correlation between 0000 UTC 11 June 600-hPa potential vorticity at point A and any 0900 UTC 10 June 600 hPa potential vorticity. Positive correlation values are in solid blue contours and negative in dashed contour starting at ±0.3 and with intervals of 0.2. Mean 0900 UTC potential vorticity contoured in green with contour intervals of 0.5 PVU and mean 0000 UTC potential vorticity shaded every 0.5 PVU.

shortwave at 0900 UTC 10 June, via the enhancement of convection during the morning hours of 10 June.

4.3.2. 0000 UTC 11 June shortwave and 1200 UTC 11 June MCV

Since stronger convection of 10 June favors a deeper midlevel vortex, it then becomes advantageous to investigate the effect of initial midlevel vortex strength to the Oklahoma MCS and thus the MCV of 11 June. To determine the connection between a preexisting vortex and MCV formation, correlation between midlevel vorticity at 0000 UTC 11 June to 600 hPa potential vorticity at 0900 UTC 11 June is analyzed. It is around this time that most ensemble members forecast a mature MCV. Figure 4.18a shows the correlation between the location of the maximum 600 hPa vorticity at 0000 UTC 11 June (point A) and the 600 hPa PV field nine hours later. A positive correlation of over 0.5 is shown near and slightly west of the maximum PV at that time, suggesting that a stronger vortex yields a slightly slower and stronger midlevel PV disturbance at 0900 UTC. This correlation supports the concept of ambient vorticity being an important factor, possibly due to stronger convection favored by a stronger shortwave, or may simply be a sign that a stronger initial midlevel shortwave maintains its strength nine hours later. It is noted that a second positive correlation of over 0.5 exists near the location of the midlevel vortex at 0000 UTC. The cause of this correlation is unclear.

Similarly, the correlation between the point of highest potential vorticity at 0900 UTC 11 June (point B in Fig. 4.18a) and the midlevel vorticity field nine hours prior in Fig. 4.30b suggests that the stronger MCV is correlated with a stronger, but not
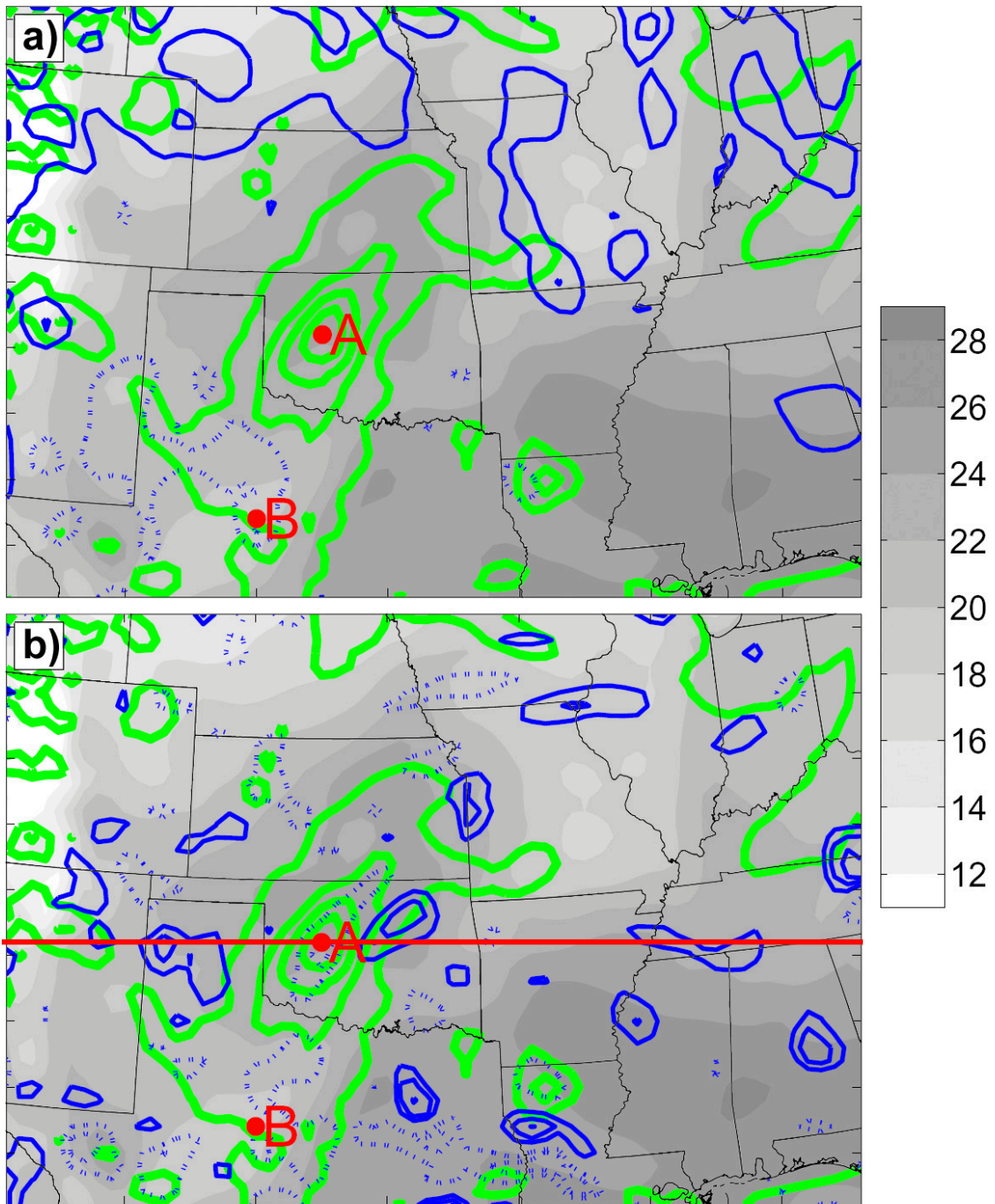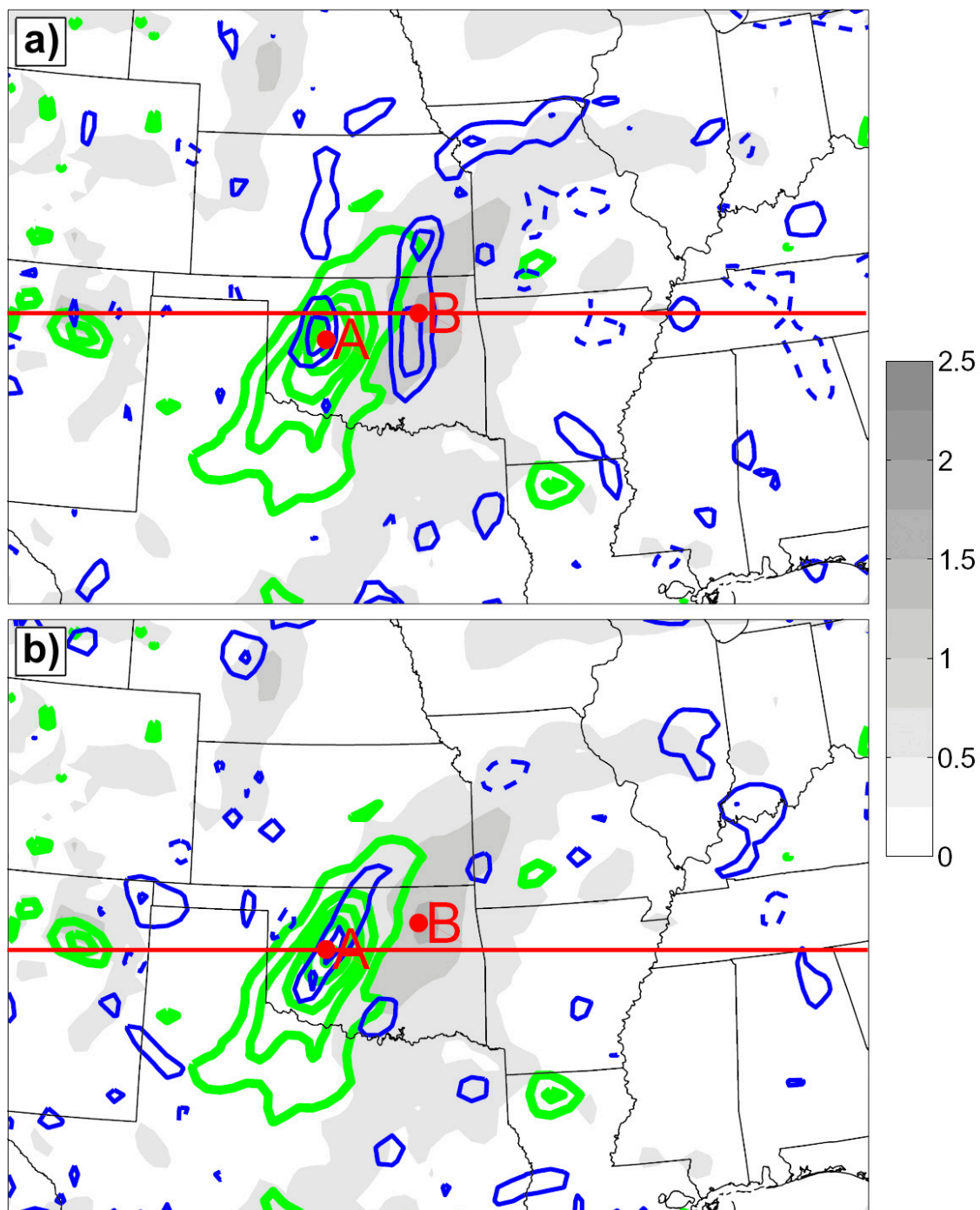
FIG. 4.18. The forecast estimated correlation between (a) 0000 UTC 11 June 600-hPa relative vorticity at point A and any 1200 UTC 11 June 600-hPa potential vorticity, and (b) 1200 UTC 11 June potential vorticity at point B to any 0000 UTC 11 June 600 hPa relative vorticity. Positive correlation values are in solid blue contours and negative in dashed contour starting at ±0.3 and with intervals of 0.2. Mean relative vorticity contoured in green with contour intervals of 0.5×10^{-4} s^{-1} and mean potential vorticity shaded every 0.5 PVU.

necessarily larger, initial midlevel shortwave as a small moderate positive correlation

exists directly over the center of the strongest 0000 UTC 11 June midlevel vortex. This

correlation pattern is supported by the individual ensemble forecasts in Figs. 4.19 and

4.20 which show the forecasts of 600-hPa relative vorticity at 0000 UTC 11 June and

600-hPa potential vorticity at 0900 UTC 11 June respectively. Members EN-34 and EN-

33 (Figs. 4.19c –d) forecast high vorticity over the midlevel shortwave trough at 0000

UTC 11 June whereas EN-31 is much weaker with vorticity and places the vorticity

maximum to the east of the shortwave trough axis (Fig. 4.19b). Accordingly, members

EN-34 and EN-33 forecast strong potential vorticity perturbations nine hours later (Figs.

4.20c–d) whereas EN-31 does not. This correlation among relative vorticity in the

vicinity of the shortwave trough at 0000 UTC 11 June to the strength of the PV

perturbations nine hours later supports the idea of stronger ambient vorticity leading to a

stronger MCV.

It is noted that stronger vorticity may aid the magnitude of convective heating

which would in turn yield a stronger MCV and could affect the correlation pattern in Fig.

4.18. To account for this possibility, Fig. 4.21 presents two scatter plots relating the

point of strongest 600-hPa PV at 1200 UTC 11 June to the strength of the maximum

600-hPa relative vorticity at 0000 UTC 11 June (Fig. 4.21a), and to the strength of the

strongest convection between 0000 UTC and 0600 UTC 11 June (Fig. 4.21b). For this

analysis, six ensemble members which did not produce significant convection or an

MCV were eliminated. The correlation between the 1200 UTC 11 June 600-hPa PV and

the 600-hPa relative vorticity at 0000 UTC 11 June (0.5105) is significantly higher than
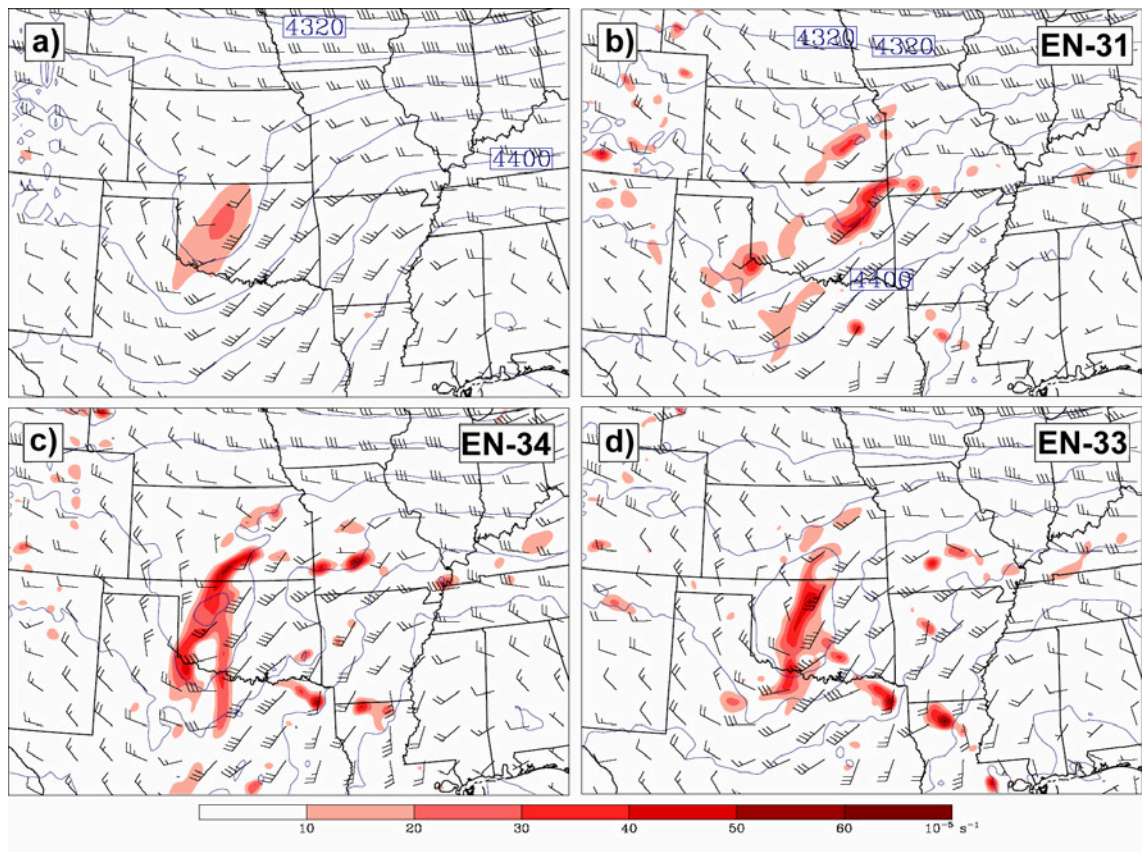
FIG. 4.19.   (a) Ensemble mean forecast and (b–d) individual ensemble forecasts of 600-hPa relative vorticity (shaded), height (contoured every 20 m) and wind vector in knots at 0000 UTC 11 June.
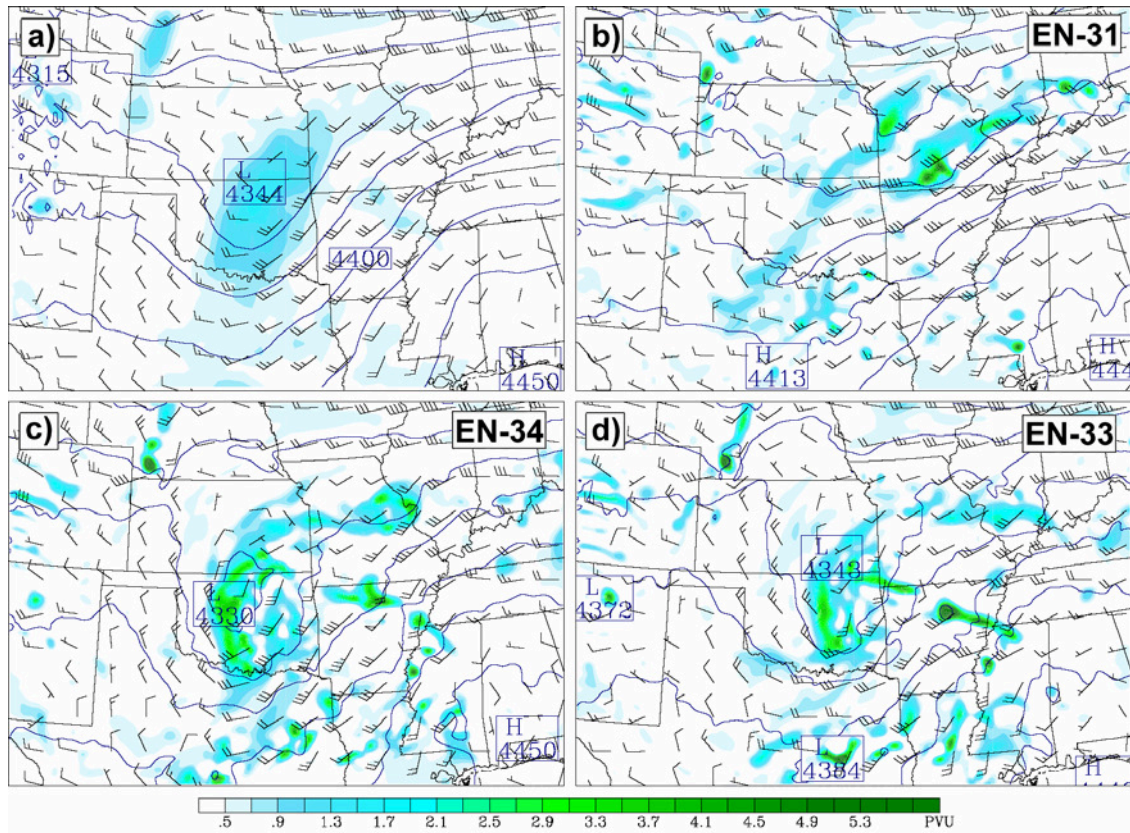
FIG. 4.20. (a) Ensemble mean forecast and (b–d) individual ensemble forecasts of 600-hPa potential vorticity (shaded), height (contoured every 20 m) and wind vector in knots at 0900 UTC 11 June.
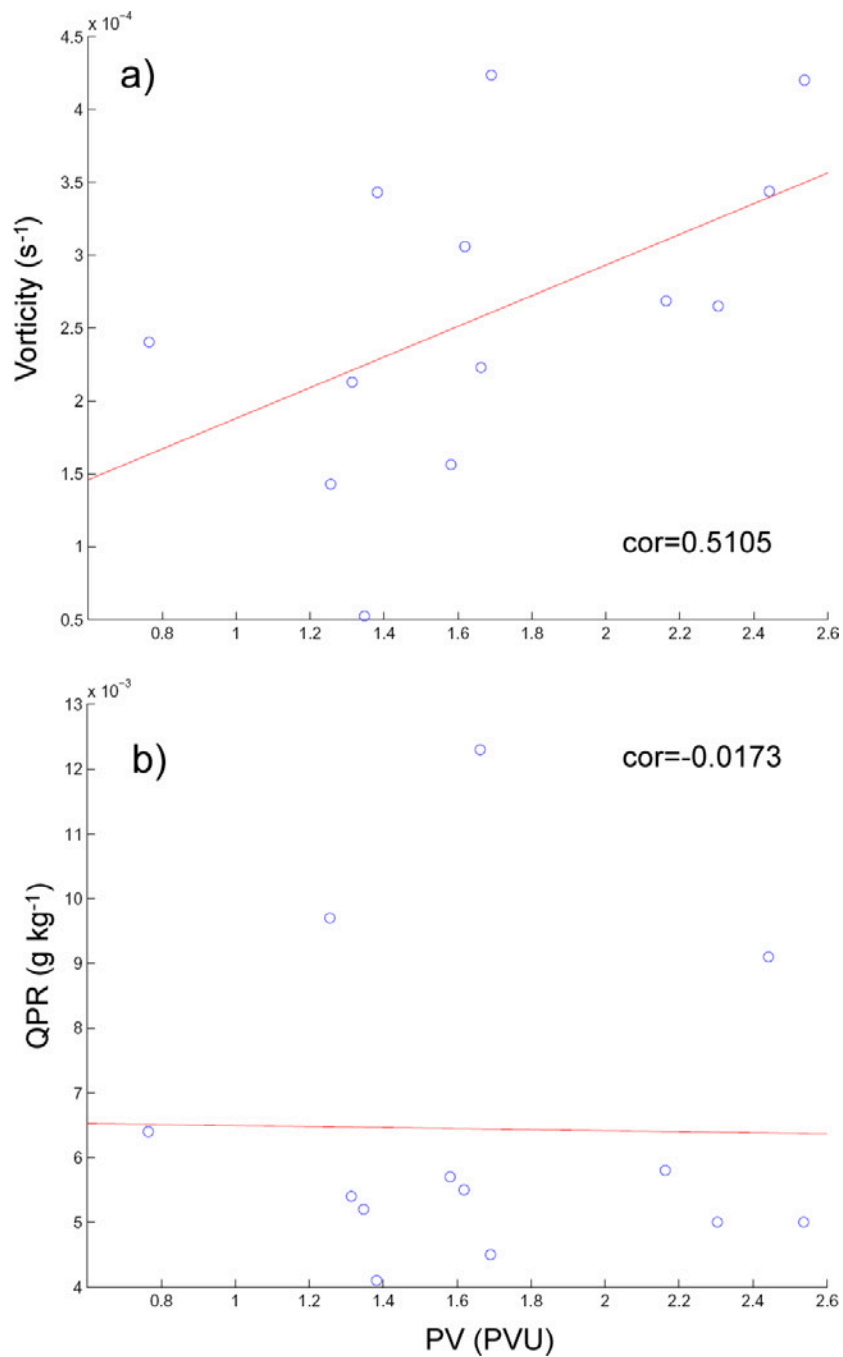
FIG. 4.21. Scatter plots of ensemble maximum 600-hPa potential vorticity at 1200 UTC 11 June and (a) maximum 600-hPa vorticity at 0000 UTC 11 June and (b) ensemble maximum integrated precipitation hydrometeor mixing ratio (QPR) between 0000 and 0600 UTC 11 June. Linear best-fit line in red.

that to convection (-0.0173), with a much more sloped regression line. These figures support the hypothesis that the strength of the MCV at 1200 UTC 11 June is directly related to the strength of the preexisting 600-hPa vorticity among ensemble members.

Cross sections across the disturbances at 0000 and 1200 UTC 11 June are given in Fig. 4.22 and are denoted as red horizontal lines in Figs. 4.18a and 4.18b. The correlations in Figs. 4.22a and 4.22b match those with respect to Figs 4.18a and 4.18b respectively. Figure 4.22a shows that the positive correlation among the point of highest midlevel vorticity at 0000 UTC to the PV field nine hours later is centered at 600 hPa. The vertical correlation structure presented in the cross section in Fig. 4.22b shows that a stronger PV anomaly at 1200 UTC 11 June is correlated with a stronger initial vortex also centered at 600 hPa. The correlation may be due to advection of midlevel PV or to another process unable to be determined in this analysis. Since no other significant positive correlation exists at any other vertical level, it can be assumed that a stronger vortex at 0900 UTC is not due to simply a stronger initial upper wave. It was hypothesized in Chapter I that a preexisting vortex was necessary for providing a mechanism to concentrate the mergers of PV perturbations and to lower the local Rossby radius such that convective heating is more effective in inducing a balanced response from the atmosphere. While this analysis illustrates the significance of a preexisting midlevel disturbance to the eventual strength of the MCV, it cannot be determined through this study any such processes that are responsible for this relationship.
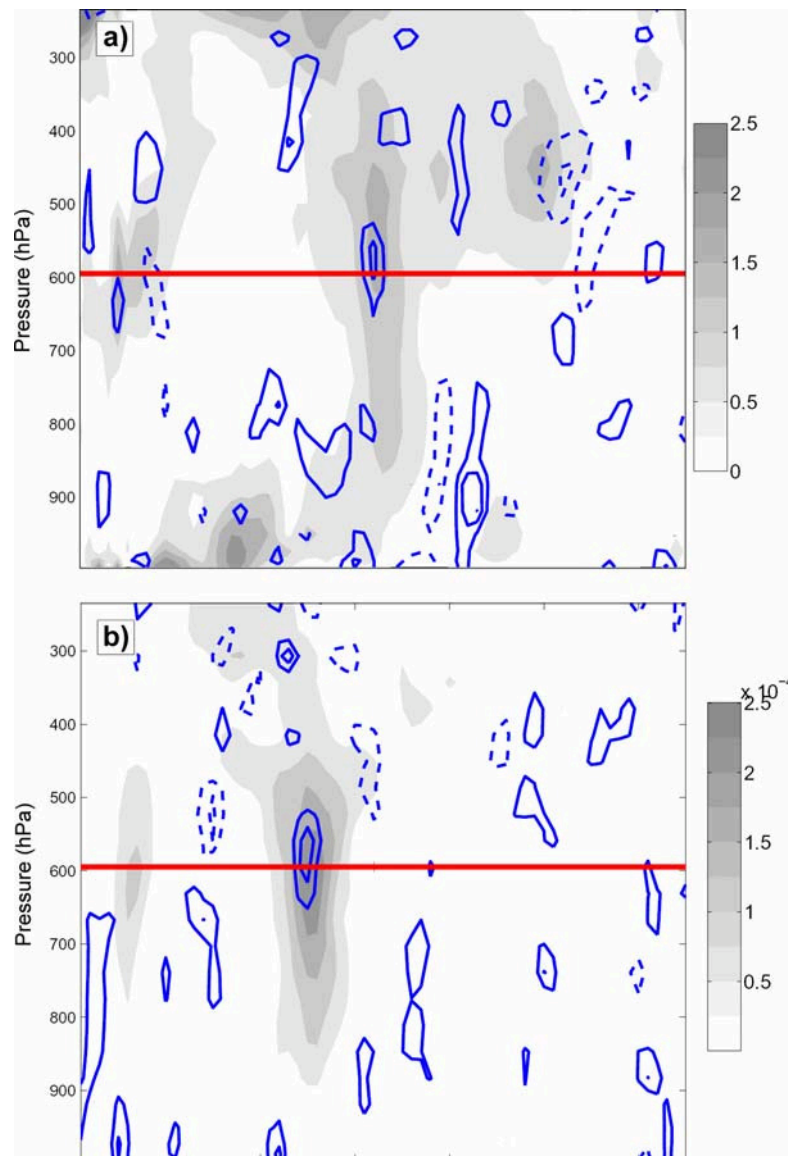
FIG. 4.22. (a) The forecast estimated correlation between 0000 UTC 11 June 600-hPa relative vorticity at point A in Fig. 4.16a and any 1200 UTC 11 June 600-hPa potential vorticity along vertical cross section denoted as red line in Fig. 4.16a. Mean potential vorticity shaded every 0.5 PVU. (b) The forecast estimated correlation between 1200 UTC 11 June potential vorticity at point B in Fig. 4.16b to any 0000 UTC 11 June 600 hPa relative vorticity along vertical cross section denoted as red line in Fig. 4.16b. Mean relative vorticity shaded every 0.5×10^{-4} s^{-1}. Positive correlation values are in solid blue contours and negative in dashed contour starting at ±0.3 and with intervals of 0.2.

4.3.3. Secondary convection and midlevel vortex strength

In this section, MCV dynamics are examined during the second diurnal cycle (36–48h), in which secondary convection is expected to play a critical role in the evolution of this system. It was speculated in Chapter II that convection near the MCV is critical to both the longevity and downward development of the MCV circulation. Here, the relationship between MCV strength and secondary convection is examined using the statistical ensemble methods.

A Lagrangian coordinate system is used for correlation analysis during this stage of the MCV, centered on the midlevel circulation center for each member. This coordinate system is utilized since variability among ensemble members is much greater at this stage, and vortex position varies by over 100 km which significantly impacts ensemble mean values as well as error covariance structure. Additionally, six members which failed to produce significant convection overnight 11 June are omitted for analysis at this time, since their lack of an MCV circulation at the beginning of the time period is useless to the investigation of MCV dynamics involving subsequent convection.

To represent the MCV, 600 hPa potential vorticity is examined at 2100 UTC 11 June, the time at which the ensemble mean PV is strongest. Figure 4.23 displays the correlation between potential vorticity at the vortex center and hydrometeor mixing ratio. It is noted that the mean PV in Fig. 4.23 is not strongest over the circulation center but is displaced directly south of the vortex and extends southeastward for over 200 km. This displacement of PV from the center of circulation is due to the superposition of the MCV circulation and the environmental winds and will be addressed later in this section.

FIG. 4.23. The forecast estimated correlation between (a) 2100 UTC 11 June 600-hPa potential vorticity at circulation center at each time (represented by red X) and any 2100 UTC 11 June column-integrated precipitation hydrometeor mixing ratio. Positive correlation values are in solid blue contours and negative in dashed contour starting at ±0.3 and with intervals of 0.2. Mean potential vorticity contoured in green with contour intervals of 0.5 PVU and mean column-integrated precipitation hydrometeor mixing ratio shaded every 0.5×10^{-3} g kg^{-1}.

The average precipitation in Fig. 4.23 is forecast over a large area on the east side of the mean circulation center, with the heaviest mean precipitation located roughly 80 km to the east of the mean vortex. A weak correlation between PV at the vortex center to precipitation exists over the region of maximum mean precipitation and stretches to just east of the circulation center. As the correlation is directly over the ensemble mean precipitation maximum, it appears that highest precipitation rates correlate at least slightly to a stronger MCV. To determine if earlier convection plays a role in the eventual strength of the PV at the circulation center, the correlation between 600 hPa potential vorticity at 2100 UTC to convection three hours earlier is also examined (Fig. 4.24). At this time the maximum mean precipitation is displaced roughly 150 km to the southeast of the circulation center at 1800 UTC, about 70 km farther than the displacement of convection in Fig. 4.23 showing that mean convection is moving inward toward the circulation center from 1800 UTC to 2100 UTC. Similar to the case in Fig. 4.23, the potential vorticity at the circulation center in Fig. 4.24 is positively correlated with precipitation near the region of maximum convection. The correlation here is slightly higher than that to convection at 2100 UTC and encompasses a slightly larger area. Again, the PV at the circulation center appears correlated with the highest precipitation, especially that closer to the vortex.

The relationship between PV and convection is further analyzed with precipitation at 1500 UTC given in Fig. 4.25. The highest mean precipitation is focused roughly 350 km to the southeast of the vortex which further shows the maximum mean convection moving closer to the circulation center from 1500 UTC through 2100 UTC.
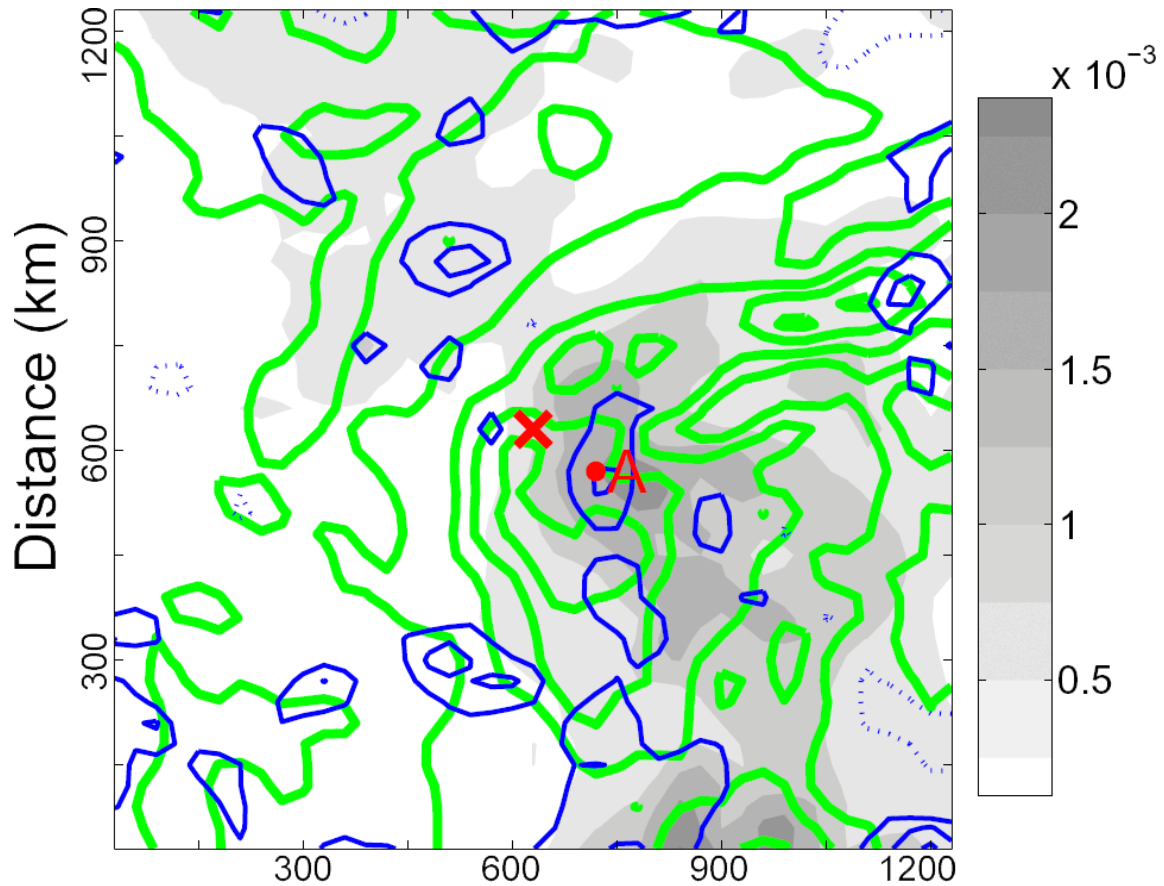
FIG. 4.24. The forecast estimated correlation between 2100 UTC 11 June 600-hPa potential vorticity at circulation center at each time (represented by red X) and any 1800 UTC 11 June column-integrated precipitation hydrometeor mixing ratio. Positive correlation values are in solid blue contours and negative in dashed contour starting at ±0.3 and with intervals of 0.2. Mean potential vorticity contoured in green with contour intervals of 0.5 PVU and mean column-integrated precipitation hydrometeor mixing ratio shaded every 0.5×10^{-3} g kg^{-1}.
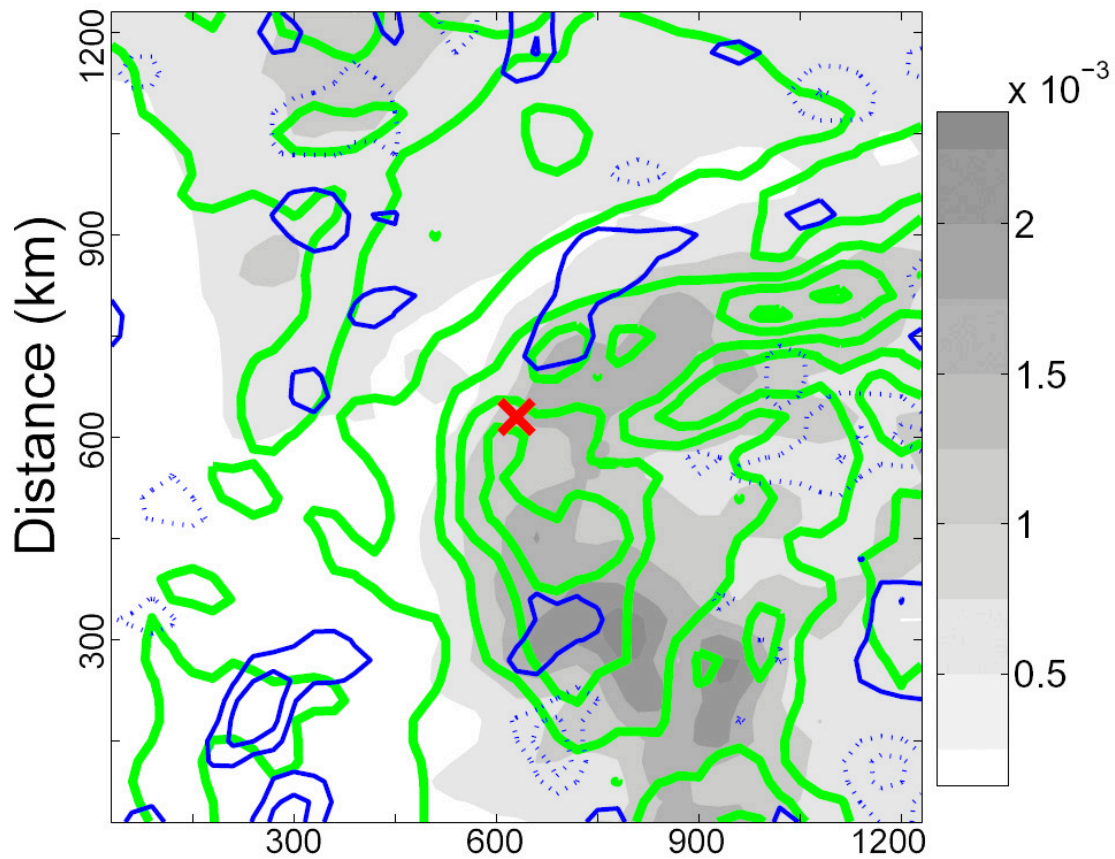
FIG. 4.25. The forecast estimated correlation between (a) 2100 UTC 11 June 600-hPa potential vorticity at circulation center at each time (represented by red X) and any 1500 UTC 11 June column-integrated precipitation hydrometeor mixing ratio. Positive correlation values are in solid blue contours and negative in dashed contour starting at ±0.3 and with intervals of 0.2. Mean potential vorticity contoured in green with contour intervals of 0.5 PVU and mean column-integrated precipitation hydrometeor mixing ratio shaded every 0.5×10^{-3} g kg^{-1}.

Only a slight positive correlation is found near the area of strongest mean convection to

the southeast, with a stronger negative correlation south of it, in an area of relatively low

mean precipitation. The connection is weaker than that with convection at 2100 UTC or

1800 UTC. The correlations presented here show that the PV at the circulation center at

2100 UTC is related to convection which moves closer to that point through time. This

relationship illustrates how convection acts to strengthen PV at later stages through the

advection of heating-induced PV anomalies.

The center reference point in Figs. 4.23–4.25 was chosen as the circulation center

in the absolute wind field and is not representative of the actual MCV center due to the

superposition of MCV-induced shear onto background winds. Therefore MCV-relative

winds are considered by subtracting the approximate velocity of the MCV circulation (8

ms^{-1} from 240 degrees), and the difference between the two wind fields is given in Fig.

4.26. By subtracting the MCV motion in Fig. 4.26b, the MCV circulation becomes

much more clearly defined, displaced approximately 170 km to the southeast of the

circulation in the absolute wind field.

The same correlations in Figs. 4.23–4.25 are examined using PV at the point of

the actual MCV circulation at 2100 UTC (determined in Fig. 4.26b) to precipitation

across the domain in Figs. 4.27–4.29. Figure 4.27 presents the mean convection at 1500

UTC relative to the MCV center, which is displaced 150 km to the south of the vortex at

that time. No significant correlation exists over the large area of mean convection to the

east of the MCV at that time. A positive correlation exists to the north of the MCV

associated with the synoptic-scale cold front, and a more significant correlation exists to
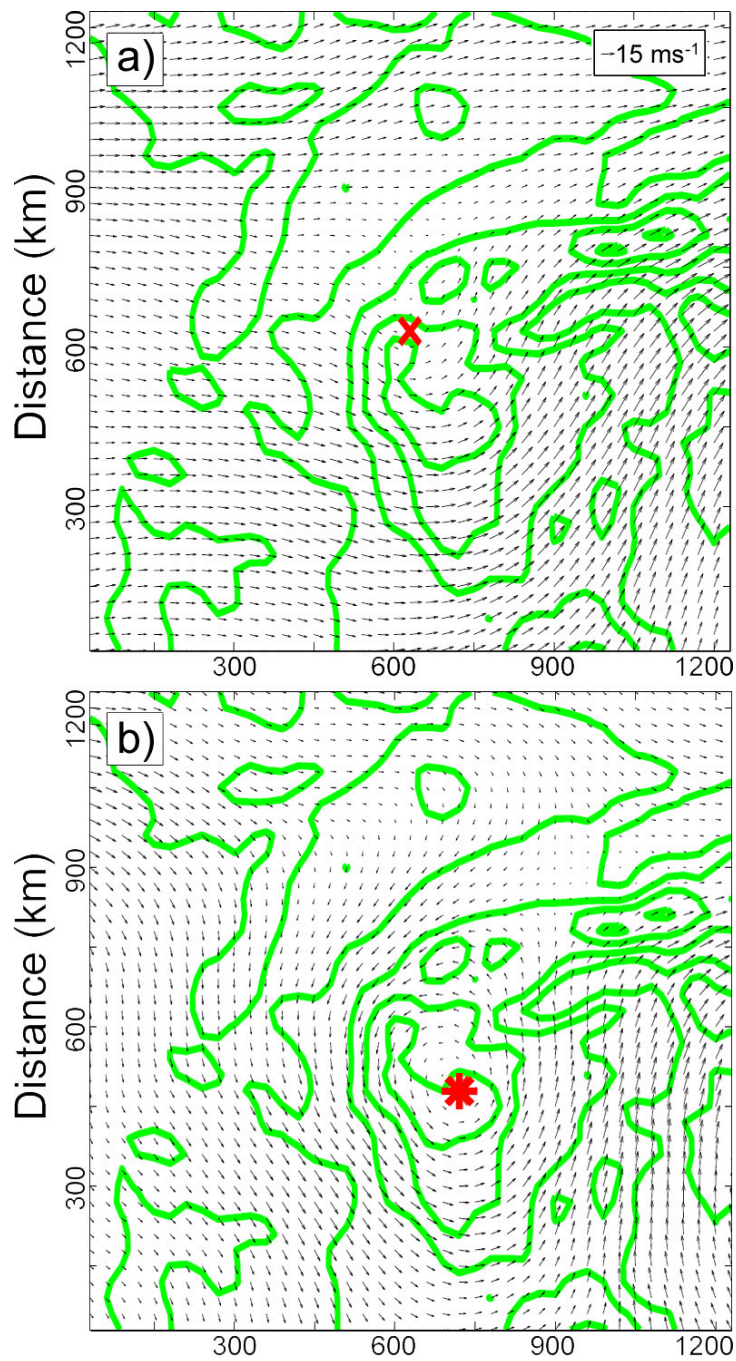
FIG. 4.26. Ensemble mean 2100 UTC 11 June 600-hPa potential vorticity (contoured in green every 0.5 PVU) and (a) total mean wind vector, (b) MCV-relative wind vector. Approximate circulation centers denoted by red X in (a) and red star in (b).
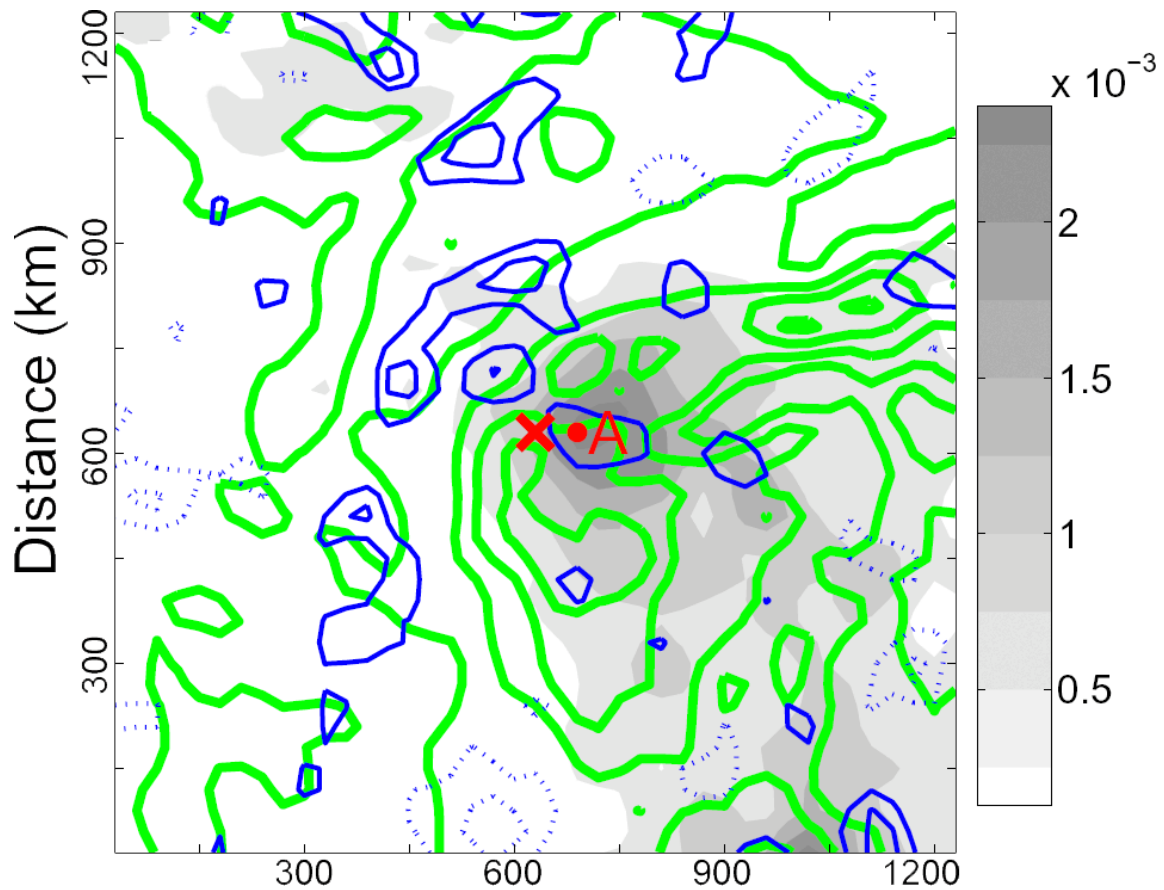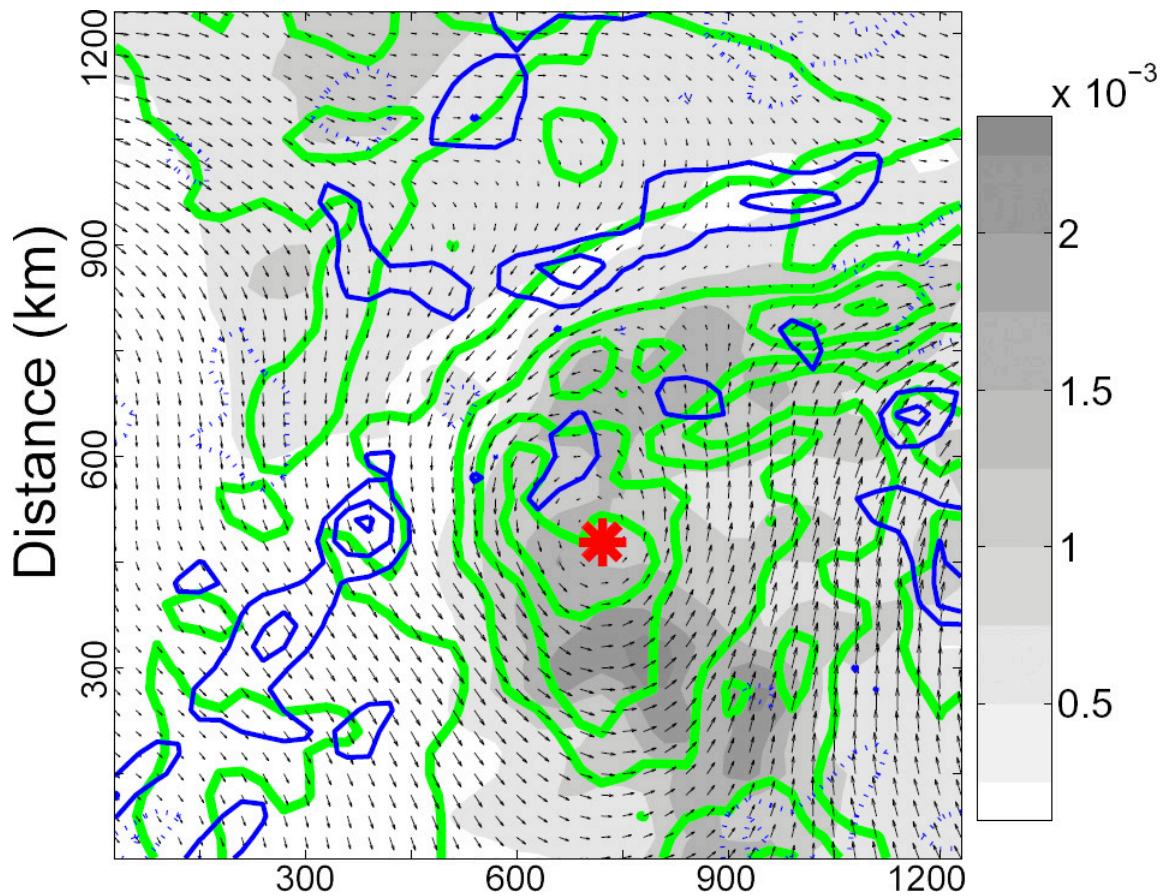
FIG. 4.27. The forecast estimated correlation between (a) 2100 UTC 11 June 600-hPa potential vorticity at MCV center (represented by red star) and any 1500 UTC 11 June column-integrated precipitation hydrometeor mixing ratio. Positive correlation values are in solid blue contours and negative in dashed contour starting at ±0.3 and with intervals of 0.2. Mean potential vorticity contoured in green with contour intervals of 0.5 PVU, mean column-integrated precipitation hydrometeor mixing ratio shaded every 0.5×10^{-3} g kg^{-1} and mean MCV-relative wind denoted by vectors.
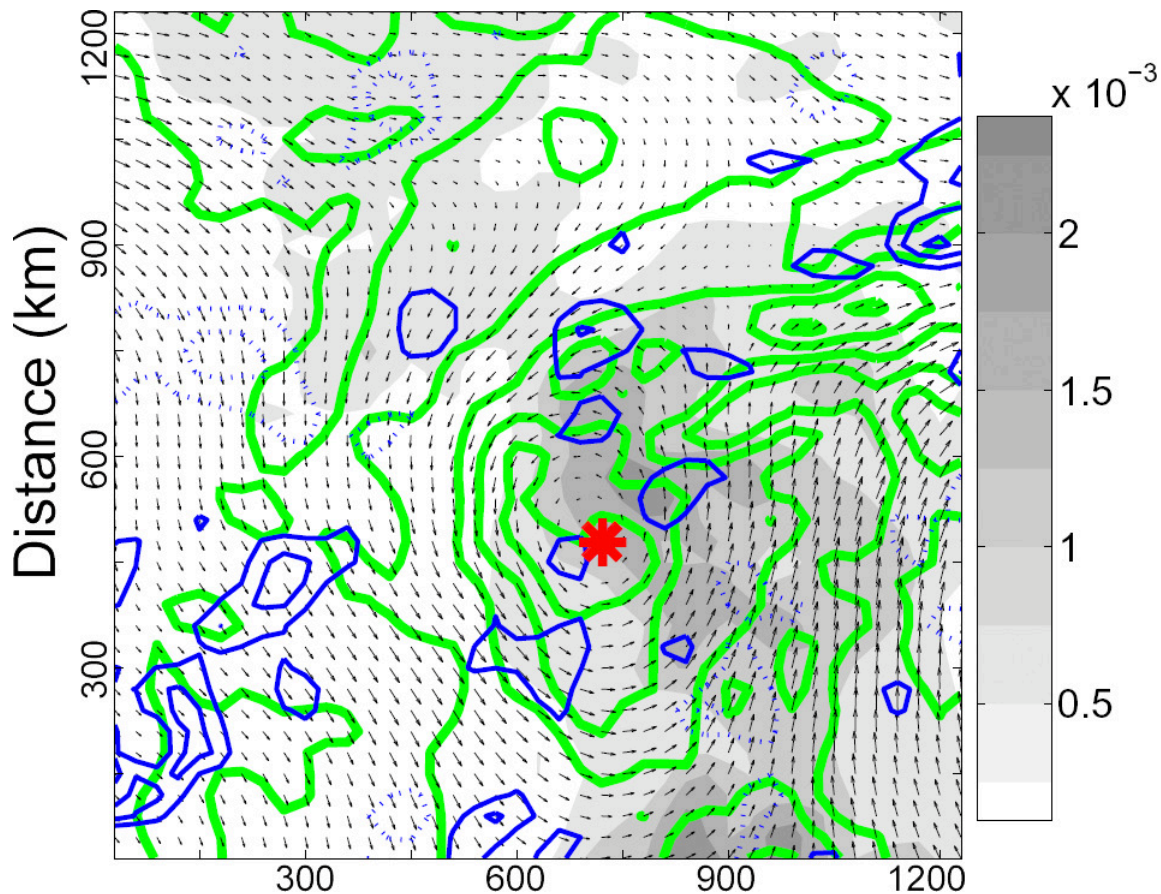
FIG. 4.28. The forecast estimated correlation between (a) 2100 UTC 11 June 600-hPa potential vorticity at MCV center (represented by red star) and any 1800 UTC 11 June column-integrated precipitation hydrometeor mixing ratio. Positive correlation values are in solid blue contours and negative in dashed contour starting at ±0.3 and with intervals of 0.2. Mean potential vorticity contoured in green with contour intervals of 0.5 PVU, mean column-integrated precipitation hydrometeor mixing ratio shaded every 0.5 × 10^{-3} g kg^{-1} and mean MCV-relative wind denoted by vectors.
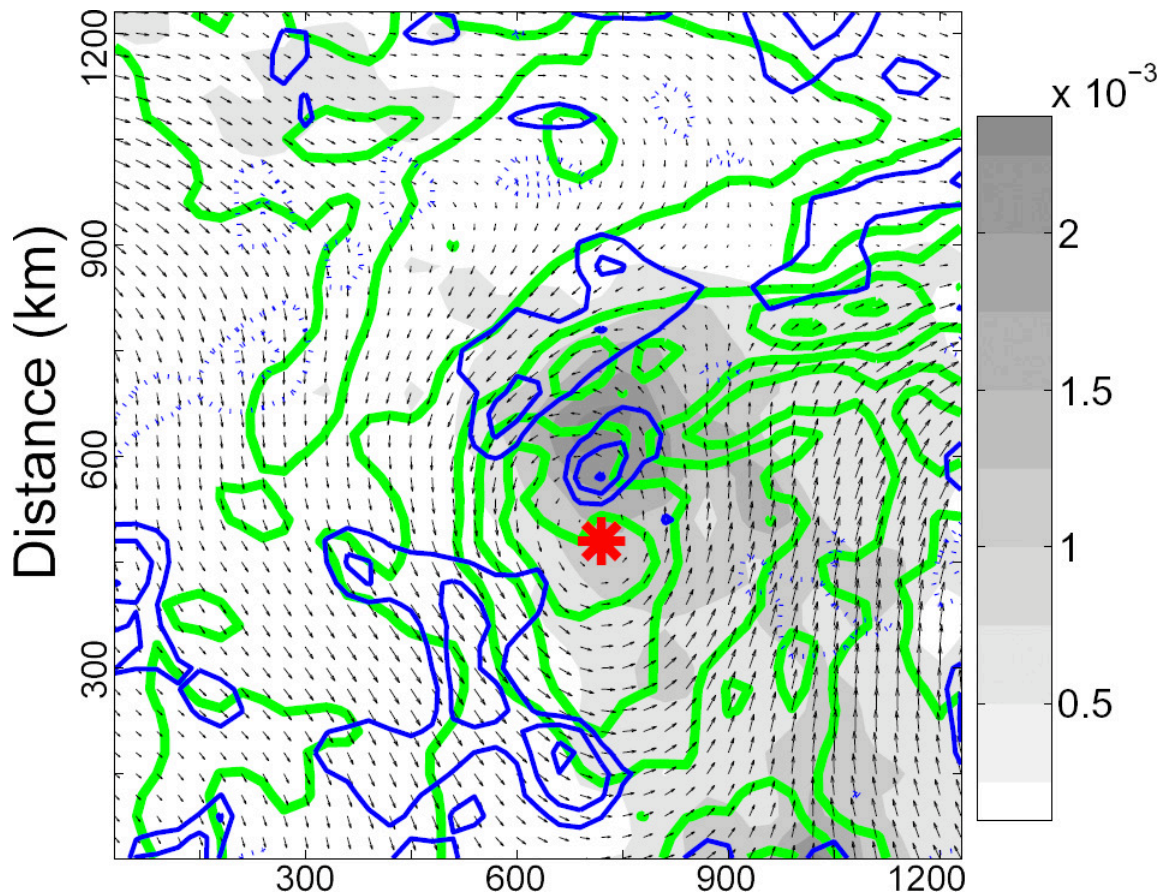
FIG. 4.29. The forecast estimated correlation between (a) 2100 UTC 11 June 600-hPa potential vorticity at MCV center (represented by red star) and any 2100 UTC 11 June column-integrated precipitation hydrometeor mixing ratio. Positive correlation values are in solid blue contours and negative in dashed contour starting at ±0.3 and with intervals of 0.2. Mean potential vorticity contoured in green with contour intervals of 0.5 PVU, mean column-integrated precipitation hydrometeor mixing ratio shaded every 0.5 × 10^{-3} g kg^{-1} and mean MCV-relative wind denoted by vectors.

the west of the MCV. The reason for this correlation is unable to be determined. In Fig.

4.28 the mean convection at 1800 UTC has moved to the east of the MCV and is roughly

50 km closer to the vortex center than at 1500 UTC. It is also at this time that a weak

positive correlation between PV at the MCV center to convection is evident near the

ensemble mean maximum precipitation, with other small correlations evident elsewhere

within the region of mean convection. Finally at 2100 UTC (Fig. 4.29), the maximum

mean precipitation has circulated to the north of the MCV, maintaining a distance of

about 100 km from the MCV center. At this time, a significant positive correlation is

evident close to the maximum mean precipitation, along with other positive correlations

along the western and northern peripheries of the area of mean convection. The positive

correlation patterns shown in Figs. 4.27–4.29 show that a stronger MCV is related with

stronger convection at the same time, both near the maximum area of mean precipitation

and along the western edge of the mean precipitation area, suggesting a correlation with

more widespread convection. Though the maximum mean convection moves slightly

closer to the MCV center between 1500 UTC and 1800 UTC, its motion is generally

around the MCV circulation in a cyclonic manner, staying close to the radius of

maximum winds.

4.3.4. Environmental support of convection and midlevel vortex strength

In this section, the same statistical approach applied in section 4.3.3 is used to

examine correlation among the vortex and ambient shear (calculated as the magnitude of

the shear vector). As discussed in Chapter I, Trier et al. (2000a) found that MCVs are

favored in environments of weaker shear, but not weak enough so that secondary

convection is hindered. Their statistical findings of 17 MCVs and associated shear in

their paths are presented in Table 4.1.

TABLE 4.1. Association of secondary convection with environmental parameters from Trier et al. (2000a). Mean values for population subsets are given with standard deviations in parenthesis.

Subset of population	Sample size	Vertical shear (10^{-3} s^{-1})	
		0.5–2.5 km	2.0–6.0 km
Entire MCV population	17	4.06 (2.18)	1.73 (0.95)
No secondary convection	7	4.10 (2.66)	2.21 (1.21)
Secondary convection	10	3.75 (1.71)	1.40 (0.49)
Secondary MCS	6	3.93 (1.99)	1.49 (0.55)
Secondary cells	4	3.48 (1.12)	1.26 (0.33)

Figure 4.30a displays the correlation between 1800 UTC 600 hPa potential

vorticity at the absolute circulation center and 0.5 – 2.5 km shear three hours earlier.

Both fields are plotted in a Lagrangian coordinate relative to the absolute circulation

center at each time (represented as a red X). In the path of the MCV, mean low-level

shear increases to 4–5 × 10^{-3} s^{-1}, maximized to the south of the MCV path and

concentrated along the PV gradient. The most significant correlation pattern (> 0.5)

appears over this area, extending northward toward the eastern flank of the MCV.

Comparison with precipitation at the same time (Fig. 4.24a) shows that this area of

positive correlation is situated in the vicinity of the heaviest mean convection. Since

convection is favored in environments of higher low-level shear, it would then appear

that the positive correlation between the strength of the MCV and the low-level shear
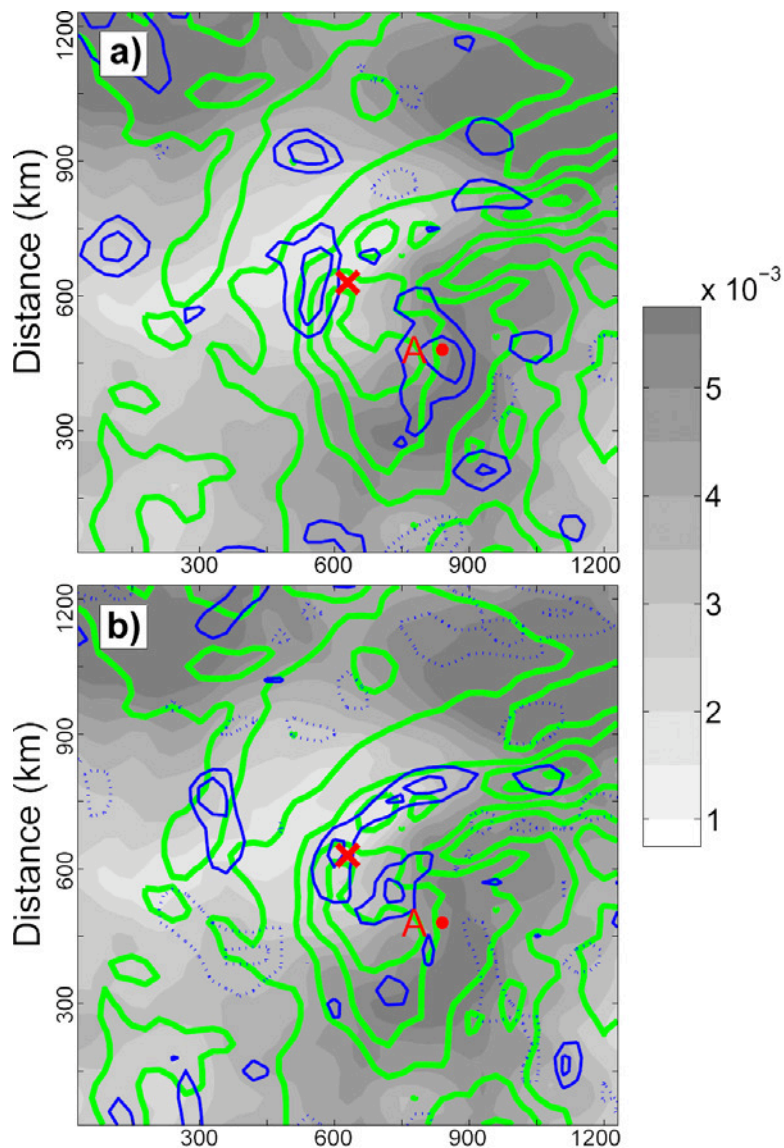
FIG. 4.30. The forecast estimated correlation between (a) 2100 UTC 11 June 600-hPa potential vorticity at circulation center at each time (represented by red X) and any 1800 UTC 11 June 0.5–2.5 km shear, and (b) 1800 UTC 11 June 0.5–2.5 km shear at point A to any 2100 UTC 11 June 600 hPa potential vorticity. Positive correlation values are in solid blue contours and negative in dashed contour starting at ±0.3 and with intervals of 0.2. Mean potential vorticity contoured in green with contour intervals of 0.5 PVU and mean shear shaded every 0.5×10^{-3} s^{-1}.

ahead of the circulation center can be tied through convection. This concept is supported by the point-to-point correlation between low-level shear and precipitation (Fig. 4.31) which shows a widespread positive correlation in the southeastern flank of the MCV as well as to the northeast. As correlations from low-level shear to both convection and potential vorticity are situated over the region of highest shear (4–5×10^{-3} s^{-1}), it is suggested here that environments of very high low-level shear ahead of the MCV are conducive to convection and thus a stronger vortex at later time periods. It is also noted that convectively-generated surface cold pools can enhance low-level shear and may be partially behind the positive correlations in Fig. 4.31. Interestingly, no negative correlation exists at the MCV center (at either 1800 UTC or 2100 UTC; not shown), as would be expected following the conclusions of Trier et al. 2000b, who suspected stronger and longer lived MCVs were favored in environments of limited shear.

Next, the relationship between the MCV at 2100 UTC and midlevel shear (2.0–6.0 km) at the same time is investigated. Figure 4.32a displays the correlation among 600 hPa potential vorticity at the vortex center at 2100 UTC to midlevel shear three hours beforehand. The mean environment ahead of the vortex center is characterized by 3–4×10^{-3} s^{-1} shear, which is over two standard deviations greater than the mean value attained by Trier et al. 2000a (Table 4.1). As is the case with low-level shear, a positive correlation exists to the southeast and northeast of the circulation center, near the gradient of potential vorticity and in the general region of convection along the outer flank of the MCV. The highest positive correlation near and ahead of the MCV is near the region of lowest midlevel shear, generally less than 3×10^{-3} s^{-1}. The cross
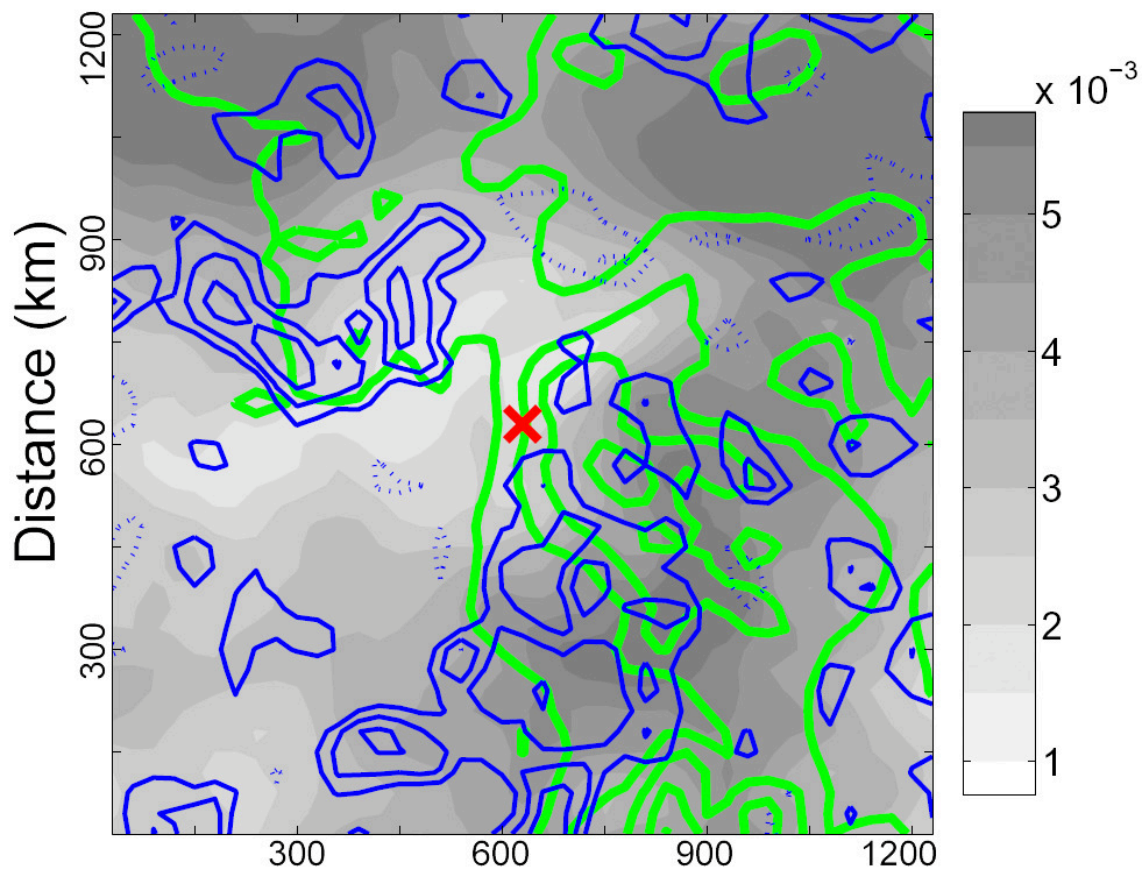
FIG. 4.31. The forecast estimated point by point correlation between 1800 UTC 11 June 0.5–2.5 km shear and 1800 UTC 11 June column-integrated precipitation hydrometeor mixing ratio. Positive correlation values are in solid blue contours and negative in dashed contour starting at ±0.3 and with intervals of 0.2. Mean column-integrated precipitation hydrometeor mixing ratio contoured in green with contour intervals of 0.5×10^{-3} g kg^{-1} and mean shear shaded every 0.5×10^{-3} s^{-1}. Coordinates centered on 600-hPa circulation center at each time represented by red X.
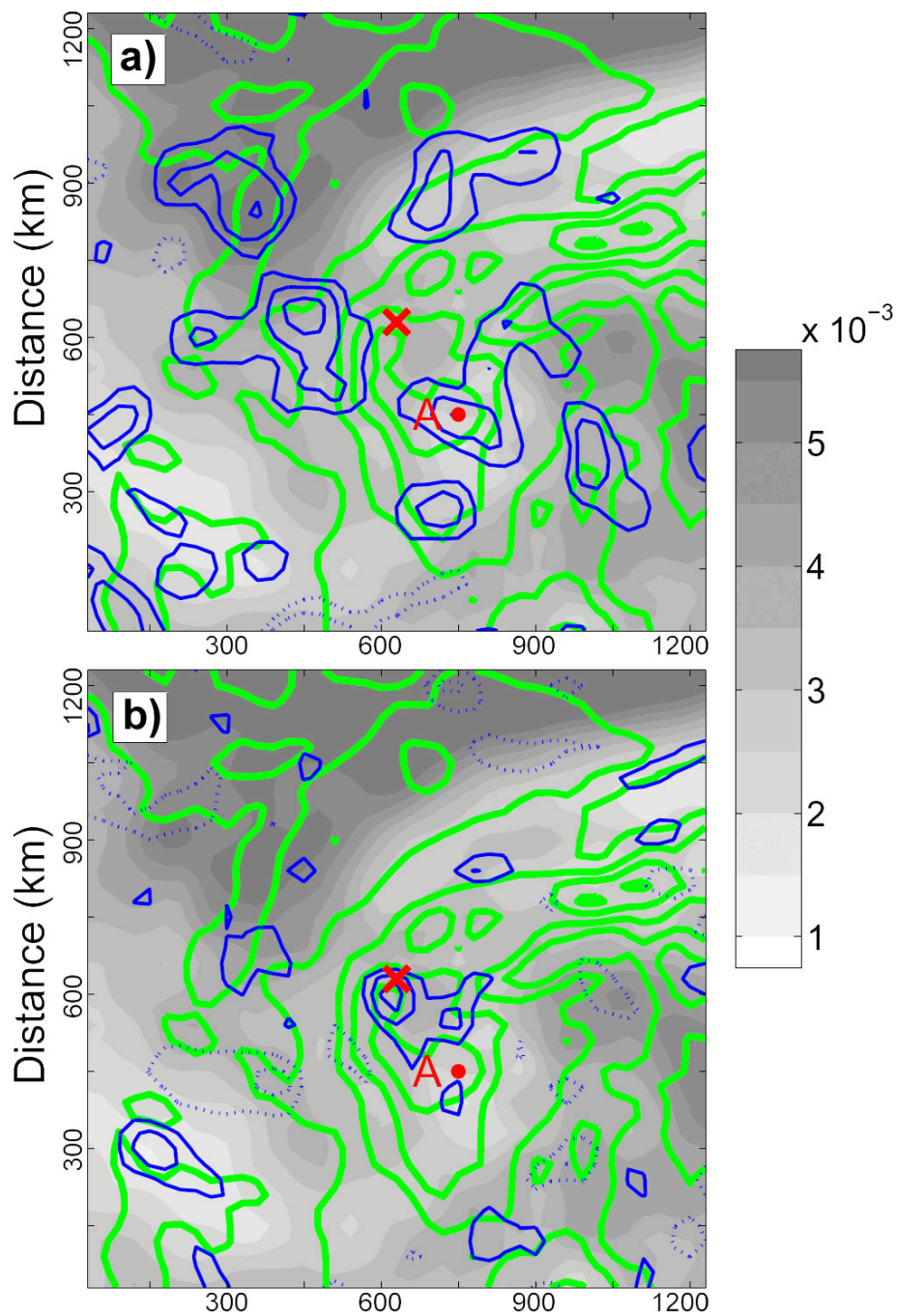
FIG. 4.32. The forecast estimated correlation between (a) 2100 UTC 11 June 600-hPa potential vorticity at circulation center at each time (represented by red X) and any 1800 UTC 11 June 2.0–6.0 km shear, and (b) 1800 UTC 11 June 2.0–6.0 km shear at point A to any 2100 UTC 11 June 600 hPa potential vorticity. Positive correlation values are in solid blue contours and negative in dashed contour starting at ±0.3 and with intervals of 0.2. Mean potential vorticity contoured in green with contour intervals of 0.5 PVU and mean shear shaded every 0.5×10^{-3} s^{-1}.

correlation among midlevel shear and precipitation (Fig. 4.33) also shows a similar

pattern where the highest positive correlations are found generally in areas where shear

is less than 3×10^{-3} s^{-1}. This general correlation pattern is indicative of a limit at which

shear becomes important to the dynamics of this system and associated convection. As

was the case with low-level shear, no negative correlations exist anywhere near the

MCV.

Similar correlations between the MCV and ambient shear are examined in Figs.

4.34 and 4.35, but for PV analyzed at the actual MCV center (section 4.3.3).   A very

large are of positive correlation between 600-hPa PV at the MCV center (red star) and

0.5–2.5 km shear exists over the southern edge of the MCV (Fig. 4.34a). Taking the

reverse correlation of low-level shear at the point of highest correlation in Fig. 4.34a

(point A) to the 600-hPa PV field shows a very strong positive correlation over the MCV

as well as over the absolute center of circulation to the northwest. Similarly, the

correlation between 600-hPa PV at the MCV center (red star) to 2.0–6.0 km shear is

given in Fig. 4.35a. Positive correlations exist around the edge of the MCV circulation,

with a correlation of over 0.5 in the path of the MCV. Taking the reverse correlation

from shear at this point (point A) in Fig. 4.35b to PV shows that the correlation is

strongest over the MCV center and extends toward the absolute circulation center

(similar to the correlation pattern in Fig. 4.34b). Again, no significant negative

correlation is present in either Fig. 4.34 or 4.35, which further suggests that weakening

of the MCV through shear-induced tilting may not be a significant factor in this

simulated MCV.
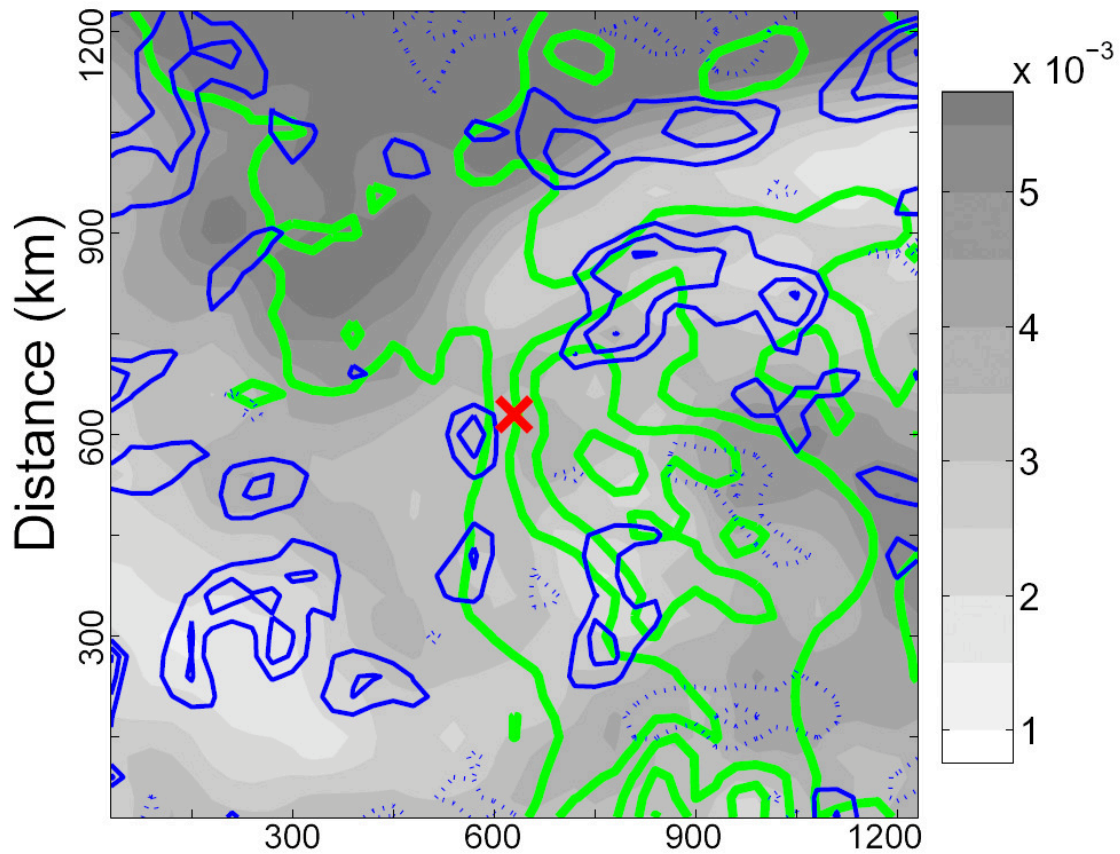
FIG. 4.33. The forecast estimated point by point correlation between 1800 UTC 11 June 2.0–6.0 km shear and 1800 UTC 11 June column-integrated precipitation hydrometeor mixing ratio. Positive correlation values are in solid blue contours and negative in dashed contour starting at ±0.3 and with intervals of 0.2. Mean column-integrated precipitation hydrometeor mixing ratio contoured in green with contour intervals of 0.5×10^{-3} g kg^{-1} and mean shear shaded every 0.5×10^{-3} s^{-1}. Coordinates centered on 600-hPa circulation center at each time represented by red X.
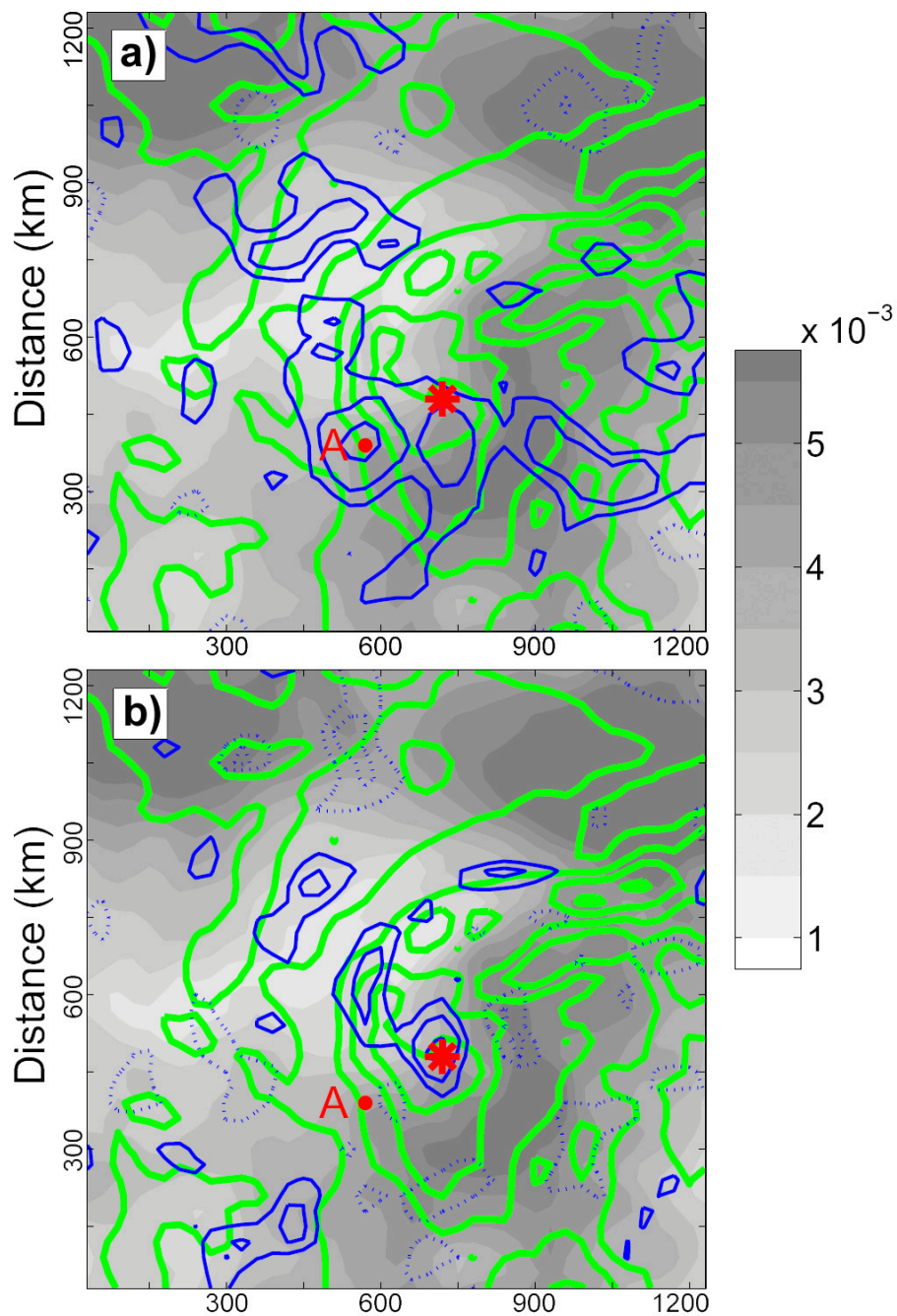
FIG. 4.34. The forecast estimated correlation between (a) 2100 UTC 11 June 600-hPa potential vorticity at MCV center at each time (represented by red star) and any 1800 UTC 11 June 0.5–2.5 km shear, and (b) 1800 UTC 11 June 0.5–2.5 km shear at point A to any 2100 UTC 11 June 600 hPa potential vorticity. Positive correlation values are in solid blue contours and negative in dashed contour starting at ±0.3 and with intervals of 0.2. Mean potential vorticity contoured in green with contour intervals of 0.5 PVU and mean shear shaded every 0.5×10^{-3} s^{-1}.
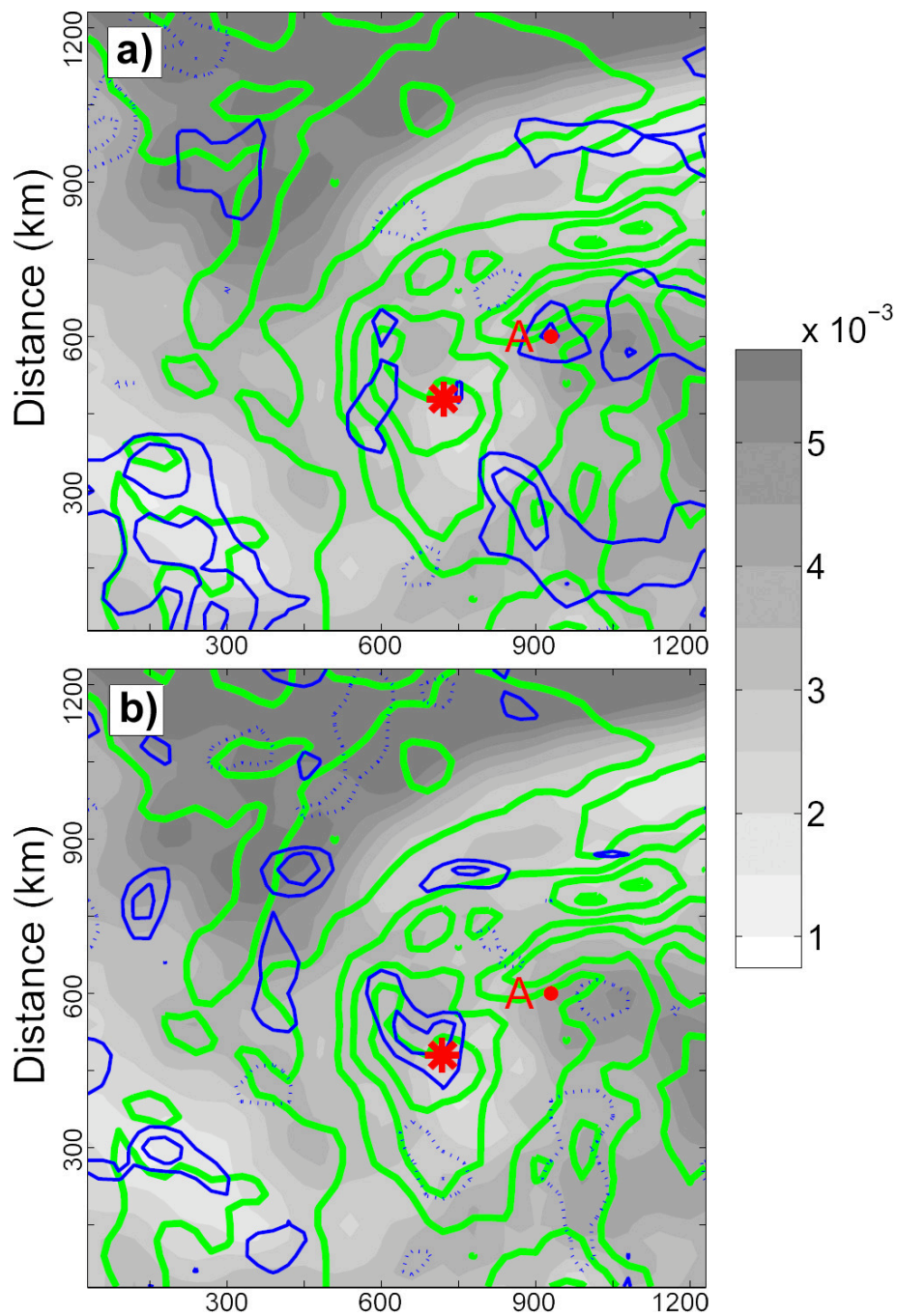
FIG. 4.35. The forecast estimated correlation between (a) 2100 UTC 11 June 600-hPa potential vorticity at MCV center at each time (represented by red star) and any 1800 UTC 11 June 2.0–6.0 km shear, and (b) 1800 UTC 11 June 2.0–6.0 km shear at point A to any 2100 UTC 11 June 600 hPa potential vorticity. Positive correlation values are in solid blue contours and negative in dashed contour starting at ±0.3 and with intervals of 0.2. Mean potential vorticity contoured in green with contour intervals of 0.5 PVU and mean shear shaded every 0.5×10^{-3} s^{-1}.

Figure 4.36 supports the idea that stronger MCVs are associated with stronger shear by showing the 2100 UTC 11 June PV and shear forecasts of two different ensemble members. EN-31 forecasts no MCV and only weak midlevel PV, and likewise forecasts weak shear at both the 0.5–2.5 and 2.0–6.0 layers. Conversely, EN-33, which forecasts a strong MCV at this time, forecasts a more widespread area of higher low-level and midlevel shear both over the MCV and downstream of it. Thus, these two ensemble forecasts further illustrate the relationship between a stronger MCV and higher environmental shear in the case of the IOP 8 MCV. This strong positive correlation is likely associated with the vertical displacement mechanism described by Trier et al. (2000b), where balanced lifting of warm, unstable air over the surface cold pool will create an absolutely unstable environment and enhance convection near the MCV center. Higher shear will also tilt a vortex so that the upper-level cold anomaly is situated over warm and unstable air ahead of a vortex, leading to greater atmospheric destabilization suitable for convection. MCV-induced shear may affect these correlation patterns, though to what degree is unknown.

As Trier et al. (2000a) found strong MCVs to be favored in environments in which shear is neither too weak nor too strong, this preferred shear pattern would not be detectable using the linear correlations employed in this section. Figs. 4.37 presents a scatter plot of maximum PV (averaged 30-km in each direction) versus shear (averaged 60-km each direction over a point 300 km downstream of the MCV center) at 1800 UTC to see if a nonlinear preferred shear pattern exists among ensemble members. No significant pattern is evident in the correlation of PV and shear at any level. Hence,
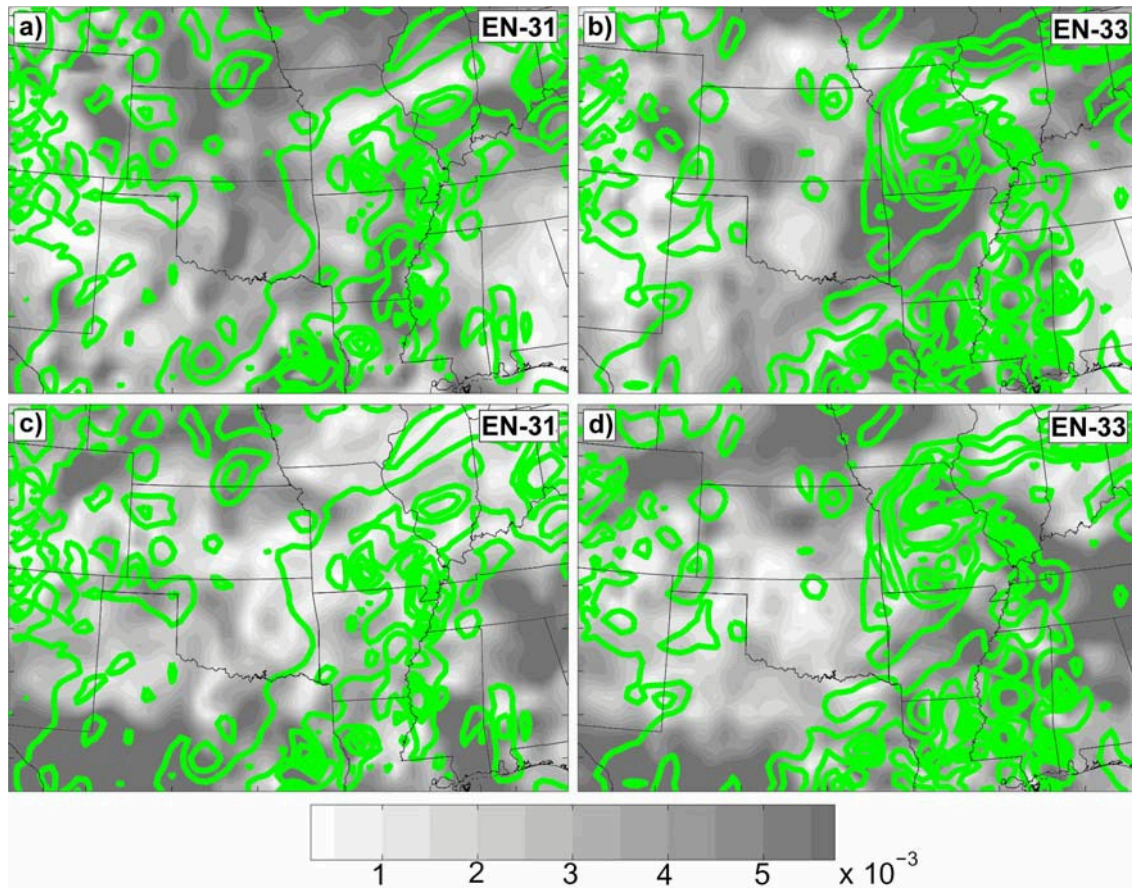
FIG. 4.36. Ensemble forecasts of 2100 UTC 11 June 600-hPa potential vorticity (contoured in green every 0.5 PVU) and (a,b) 0.5–2.5km shear and (c,d) 2.0–6.0 km shear (shaded in s^{-1}).
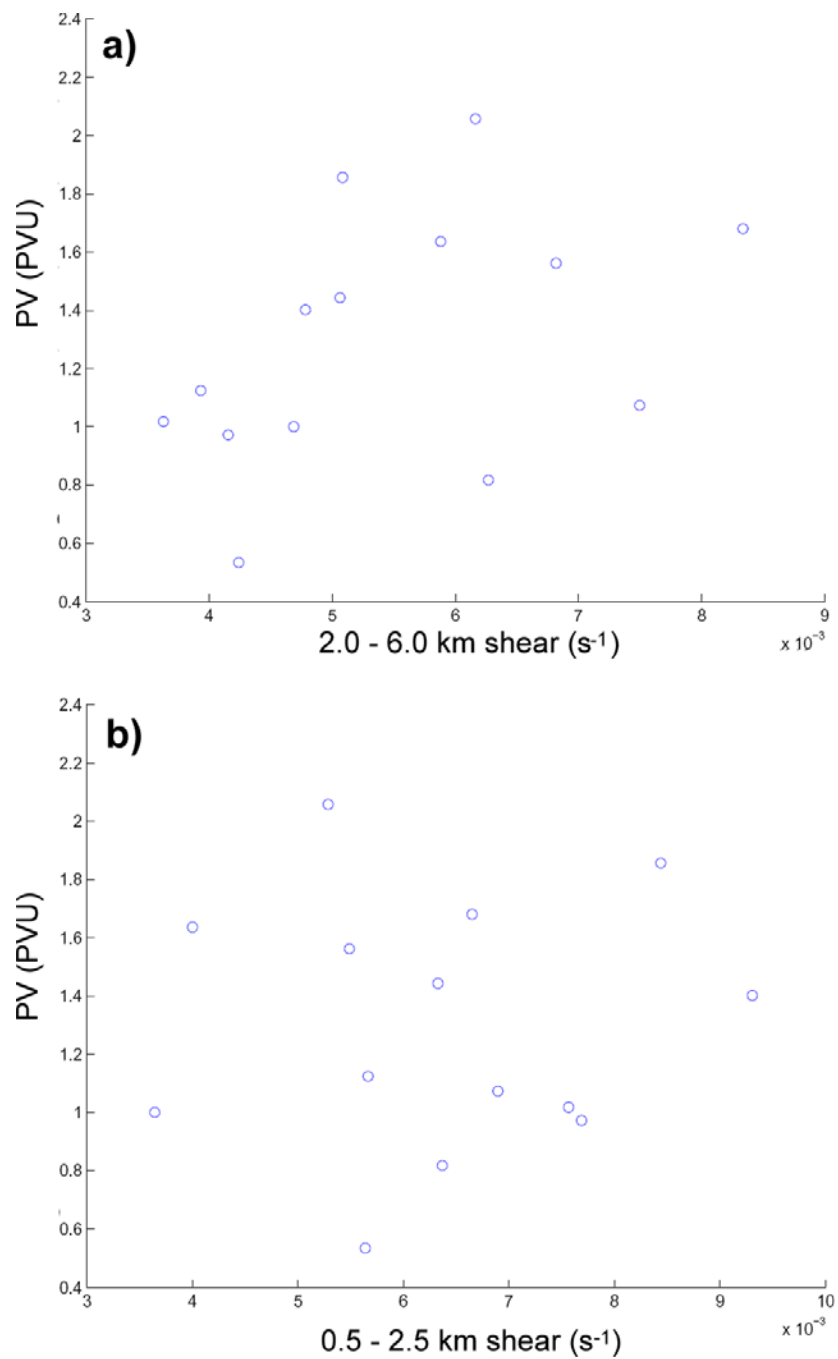
FIG. 4.37. Scatter plots of ensemble PV at the MCV center and (a) 2.0 – 6.0 km shear and (b) 0.5 – 2.5 km shear averaged 60-km in each direction over a point 300 km ahead of the MCV at 1800 UTC 11 June.

plots of individual ensemble data, like the other correlations presented in this section, do not support the findings of Trier et al. (2000a).

4.3.5. Low-level vortex growth

Section 4.3.3 illustrated how a stronger MCV is associated with stronger and more widespread convection, and in Chapter I it was described how secondary convection directly over the MCV can be critical in focusing PV in the lower troposphere and leading to surface vortex growth. The latter hypothesis is tested by calculating the correlation coefficient between the vorticity at the surface at 2100 UTC 11 June to convection (represented by integrated precipitation hydrometeor mixing ratio) directly above it. A very strong positive correlation of 0.8368 is found. This correlation is supported by Figs. 4.38 and 4.39 which show the forecasts of convection at 2100 UTC and the surface wind field at the same time respectively. Member EN-31 does not forecast convection near the surface low at all (Fig. 4.38b), and thus does not forecast a surface circulation (Fig. 4.39b). On the other hand, EN-34 and EN-33 both produce convection directly over the MCV (Figs. 4.38c and 4.38d respectively) and also forecast a closed circulation in the surface winds (Figs. 4.39c and 4.39d). Furthermore, member EN-34 is strongest with its forecast convection and is accordingly 1-hPa deeper with the surface low, and forecasts a slightly stronger circulation in the surface winds (Fig. 4.39c). The strong correlation between surface vorticity and convection among the vortex, illustrated by the individual ensemble analysis, solidly reinforces the hypothesis that secondary convection is critical to vortex growth to the surface.
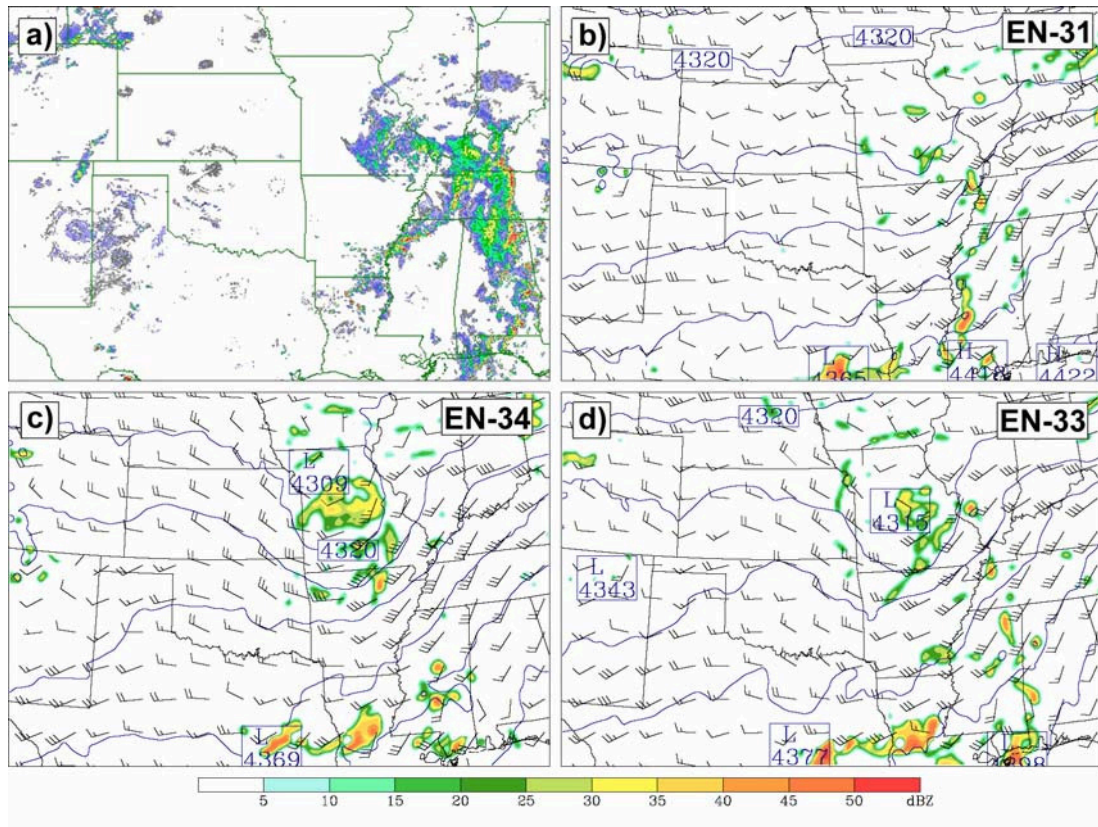
FIG. 4.38. (a) Composite WSR-88D reflectivity at 2100 UTC 11 June and (b–d) ensemble forecasts of simulated radar reflectivity (shaded), 600-hPa heights (contoured every 10 m) and wind in knots at 2100 UTC 11 June.
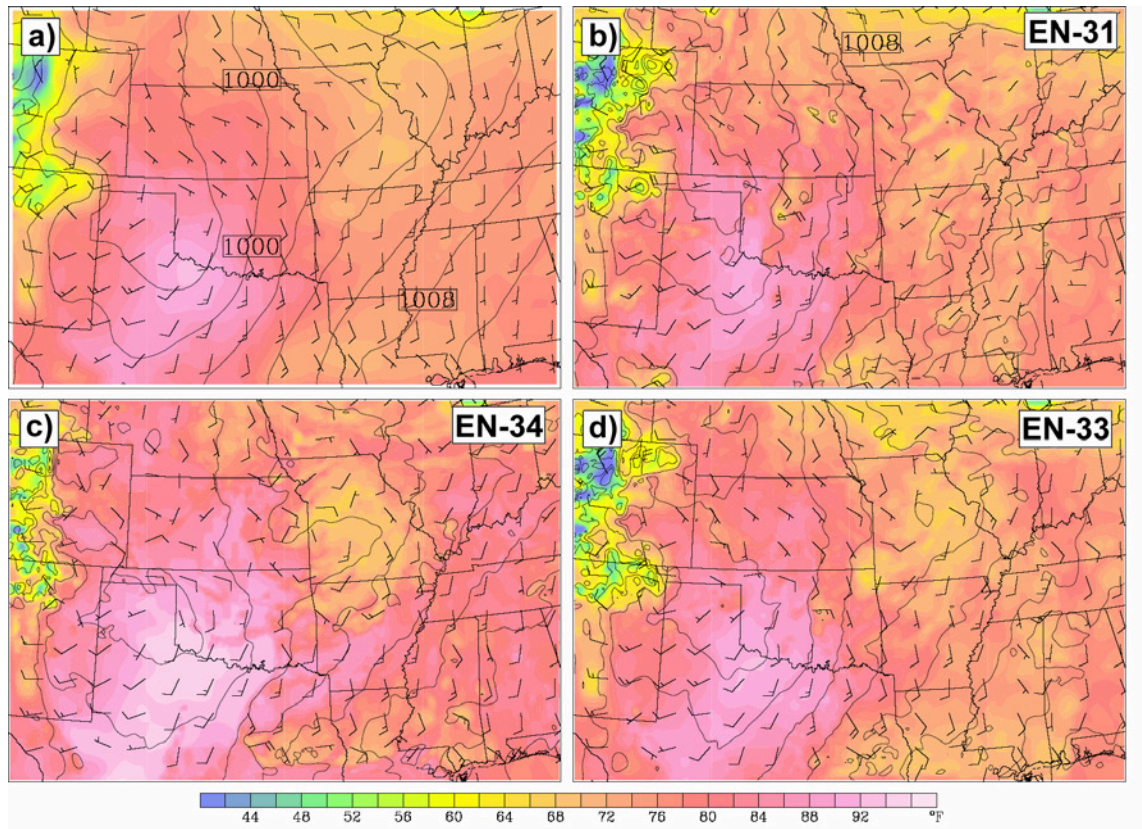
FIG. 4.39. (a) Ensemble mean forecast and (b–d) individual ensemble forecasts of surface temperature (shaded), mean sea level pressure (contoured every 2 hPa) and 10-m wind vector in knots at 0000 UTC 12 June.

It was further hypothesized in Chapter II that vortex growth at the immediate

surface would be favored toward the edge of a surface cold pool, where vertical

distances between potential temperature surfaces would be vertically separated further,

thus enhancing vortex stretching in the lower troposphere as well as increasing the

penetration depth of the midlevel vortex. This theory is tested in Fig. 4.40, where a

cross section is drawn in the Lagrangian frame relative to the surface vorticity maximum.

It is shown that the highest mean low-level vorticity is focused in the peak of the mean

surface cold pool rather than at the edge. The correlation between surface vorticity at

point A and $d\theta/dz$ is shown. A significant but shallow positive correlation exists directly

over the surface vortex, in the region of weakest stratification in the lowest layer of the

troposphere (most likely a shallow boundary layer). This correlation is the opposite of

what was expected, but corresponds to the results of section 4.3.3 where ensemble

member EN-34 had forecasted a deepening surface low as a result of increased PV,

correlated with an increase in stratification of potential temperatures in the lowest layer

of the atmosphere. An interesting structure to the correlation pattern is evident as the

positive correlation in the lower troposphere is roughly angled along the zone of

stratification at the western edge of the surface cold pool, extending from the center of

the cold anomaly, near the center of vorticity at the surface, up to near 950 hPa at the top

of the cold pool on the western side. As this correlation occurs in the deepest section of

the cold pool at the surface, it would be suggested that a deeper cold pool is conducive to

a stronger surface vortex and is supported by the individual ensemble analysis of EN-34
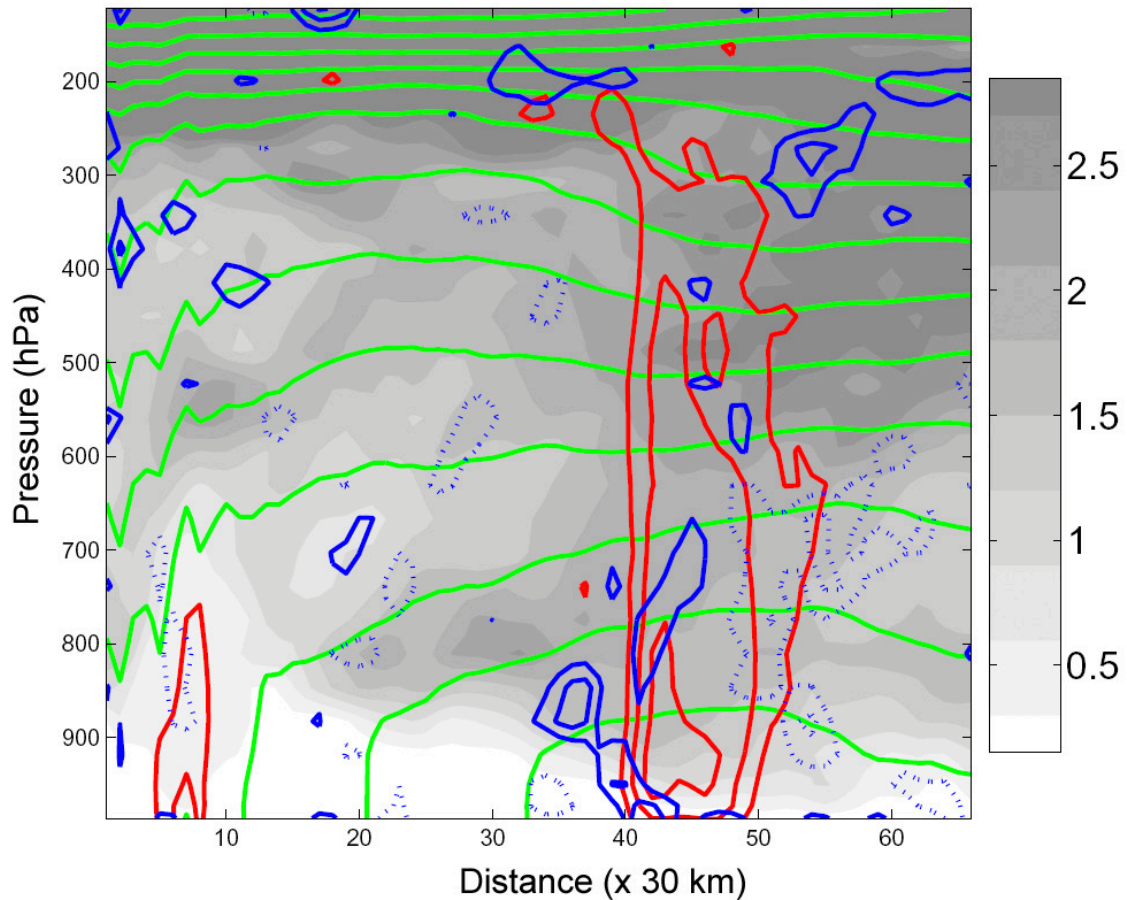
FIG. 4.40. The forecast estimated correlation between maximum 2100 UTC 11 June surface vorticity to any 2100 UTC 11 June dθ/dz along vertical cross section drawn along east-west plane centered on location of maximum surface vorticity for each member. Positive correlation values are in solid blue contours and negative in dashed contour starting at ±0.3 and with intervals of 0.2. Potential temperature contoured in green every 5 K, relative vorticity contoured in red every 0.5 × 10^{-4} s^{-1} and dθ/dz shaded every 0.5 K.

in Fig 4.39c. The relation to a strengthened cold pool may simply be the result of stronger convection immediately over the surface vortex.

Surface vortex development is further evaluated in Fig. 4.41 which displays vertical cross sections of potential vorticity and potential temperature centered on the surface low for EN-33 and EN-34 at 2100 UTC 11 June and 0000 UTC 12 June. Both members show a PV maximum near 600 hPa at 2100 UTC, however since the MCV is out of the cross section for EN-34 the potential vorticity displayed in this figure is much weaker than that of EN-33. For both members, this PV grows downward three hours later as convective heating refocuses PV further down in the troposphere (convection shown in Fig. 4.38). Additionally, both members forecast a secondary vorticity maximum near the surface. EN-34 forecasts a potential vorticity increase from 2100 UTC to 0000 UTC near the surface vortex with an associated increase in vorticity. However, EN-33 forecasts the surface PV anomaly to decrease during the same time, while vorticity itself strengthens. Reasoning behind the difference in surface PV structure can be seen when looking at the three-hour difference in stratification, presented in Fig. 4.42. The increase in PV forecasted by EN-34 is in a zone of increasing low-level stratification, possibly due to a strengthening surface cold pool. Additionally, simulated reflectivity in Fig. 4.38 shows that EN-34 forecasts relatively strong and widespread convection directly over the developing surface vortex, which may have been strong enough for low- and midlevel convective warming to influence an increase in PV all the way to the surface. Conversely, the increase in surface vorticity forecasted by EN-33 is associated with a strong decrease in stratification immediately at
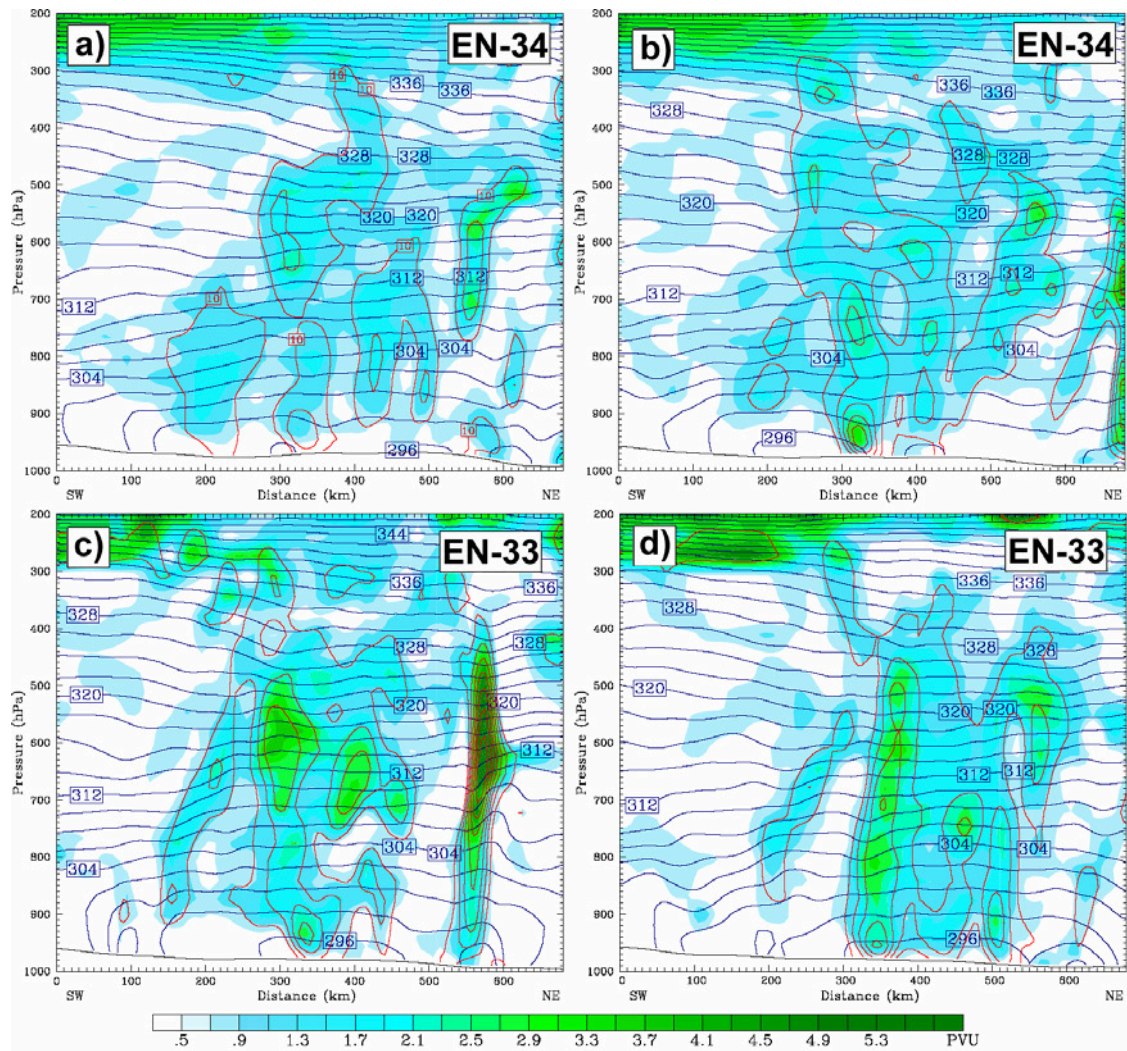
FIG. 4.41. Ensemble forecasts of potential vorticity (shaded), relative vorticity (contoured in red every 10^{-4} s^{-1}) and potential temperature (contoured in blue every 2 K) along an east-west oriented vertical cross section centered over the maximum surface vorticity for each figure.
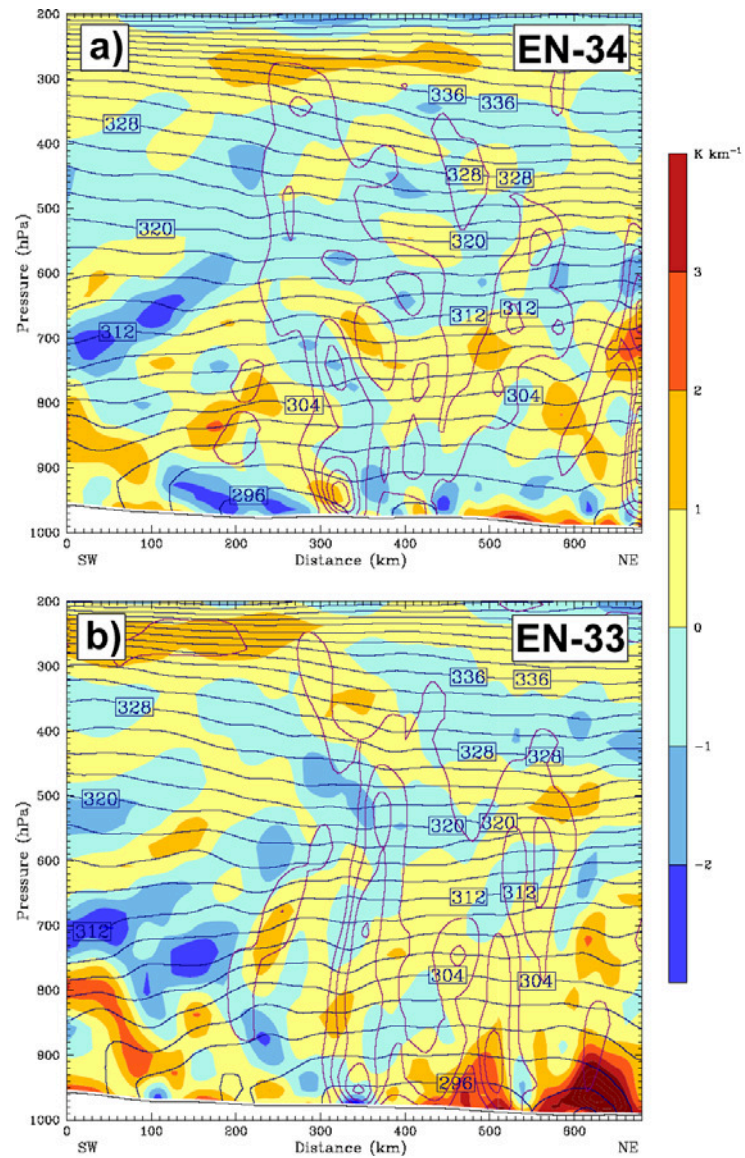
FIG. 4.42. Ensemble forecasts of three-hour difference dθ/dz (shaded), relative vorticity (contoured in purple every 10^{-4} s^{-1}) and potential temperature (contoured in blue every 2 K) at 0000 UTC 12 June along an east-west oriented vertical cross section centered over the maximum surface vorticity.

the surface, yet is accompanied by an increase in lower tropospheric PV directly above it as convection increases. The differences between the two ensemble members illustrate how more than one method exists for MCV vortex growth at the surface despite the common factor with convection.

4.4. Ensemble sensitivity to horizontal resolution and convective parameterization

Runs of both the high-resolution MM5-10 (explicitly forecast convection) and low-resolution MM5-30 (parameterized convection) were considered for the statistical analysis in this chapter. The similarities and differences between the two model runs are examined in this chapter to illustrate the importance of the high-horizontal resolution and explicit convective forecasts employed by the MM5-10 ensembles. Figures 4.43–45 present the differences among correlation structure between potential vorticity at three different times during the MCV lifecycle, looking at both the 10-km and 30-km MM5 models. In Fig. 4.43, the correlation coefficient is calculated between 300-hPa potential vorticity at 1200 UTC 10 June and 600-hPa potential vorticity at 0000 UTC 11 June. Figures 4.43a and 4.43b show the correlation between the point of maximum 600-hPa potential vorticity at 0000 UTC 11 June (point B) and the 300-hPa potential vorticity field at 1200 UTC for the 30-km and 10-km runs respectively. Figures 4.43c and 4.43d show the reverse correlation of those in Figs. 4.43a and 4.43b respectively, taken at point A. Differences among the two models regarding the initial upper wave at 1200 UTC (shaded) are small, with the 30-km being slightly stronger with the lead shortwave over western Texas. However, at 0000 UTC, significant differences are seen between
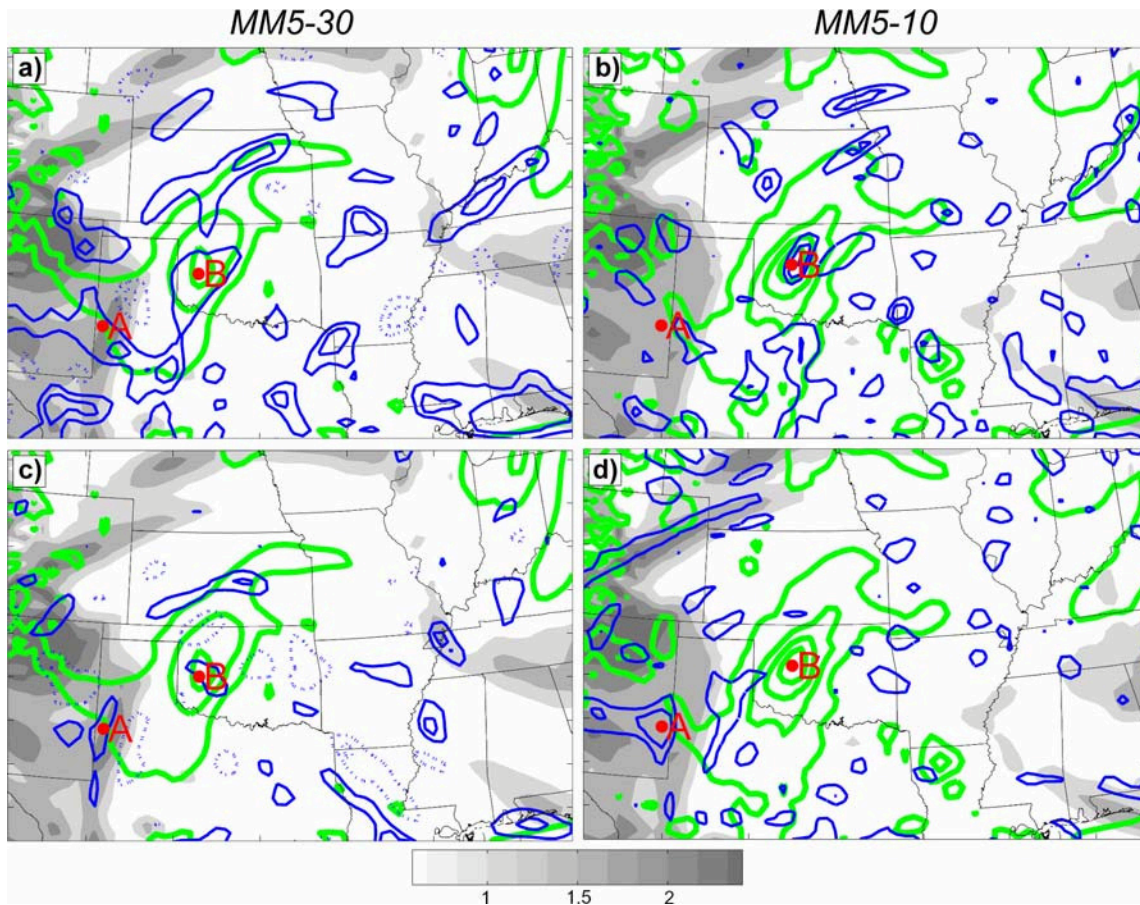
FIG. 4.43. The forecast estimated correlation between (a, b) 0000 UTC 11 June 600 hPa relative vorticity at point B and any 1200 UTC 10 June 300-hPa potential vorticity, and (c, d) 1200 UTC 10 June 300-hPa potential vorticity at point A to any 0000 UTC 11 June 600 hPa potential vorticity. Forecasts from the 30-km MM5 are shown in (a, c) and forecast from the 10-km MM5 are given in (b, d). Positive correlation values are in solid blue contours and negative in dashed contour starting at ±0.3 and with intervals of 0.2. Mean 1200 UTC potential vorticity shaded every 0.5 PVU and mean 0000 UTC potential vorticity contoured in green every 0.5 PVU.
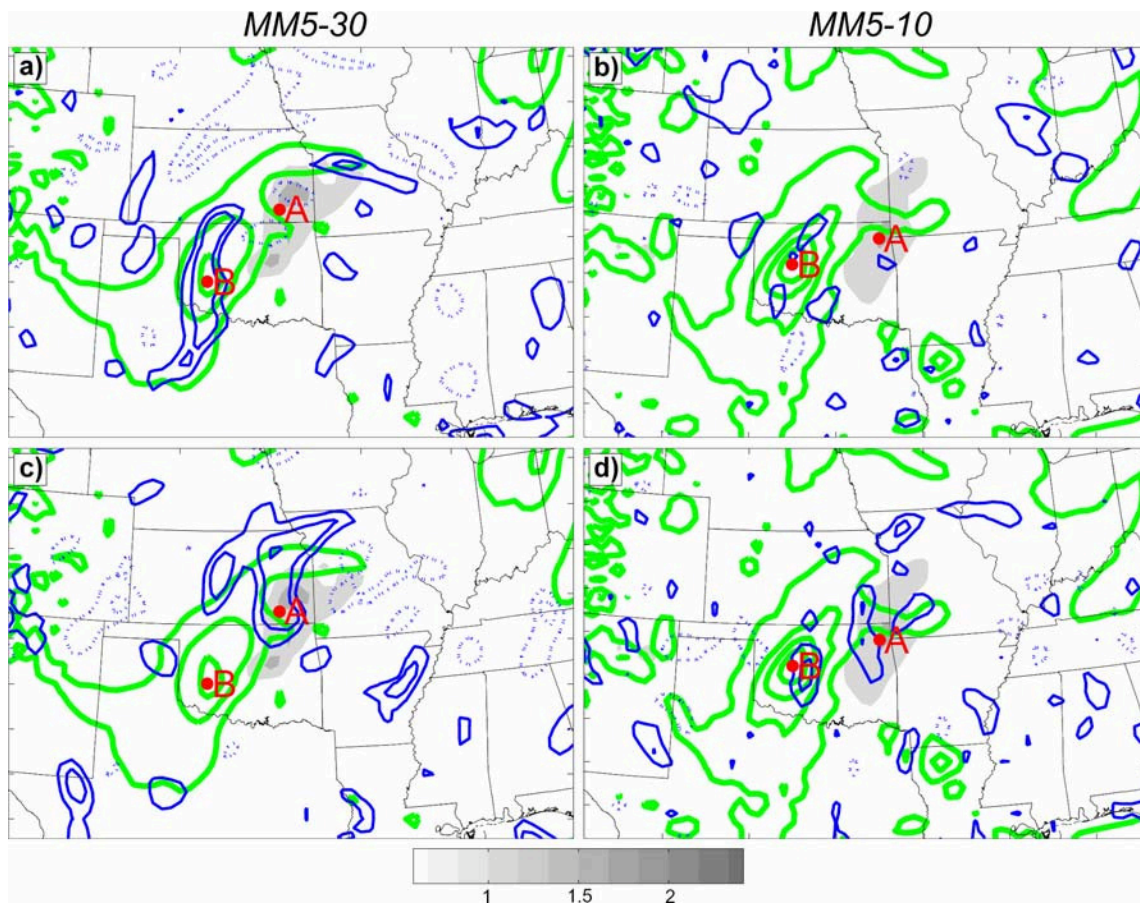
FIG. 4.44. The forecast estimated correlation between (a, b) 1200 UTC 11 June 600 hPa relative vorticity at point A and any 0000 UTC 10 June 600-hPa potential vorticity, and (c, d) 0000 UTC 10 June 600-hPa potential vorticity at point B to any 1200 UTC 11 June 600 hPa potential vorticity. Forecasts from the 30-km MM5 are shown in (a, c) and forecast from the 10-km MM5 are given in (b, d). Positive correlation values are in solid blue contours and negative in dashed contour starting at ±0.3 and with intervals of 0.2. Mean 1200 UTC potential vorticity shaded every 0.5 PVU and mean 0000 UTC potential vorticity contoured in green every 0.5 PVU.
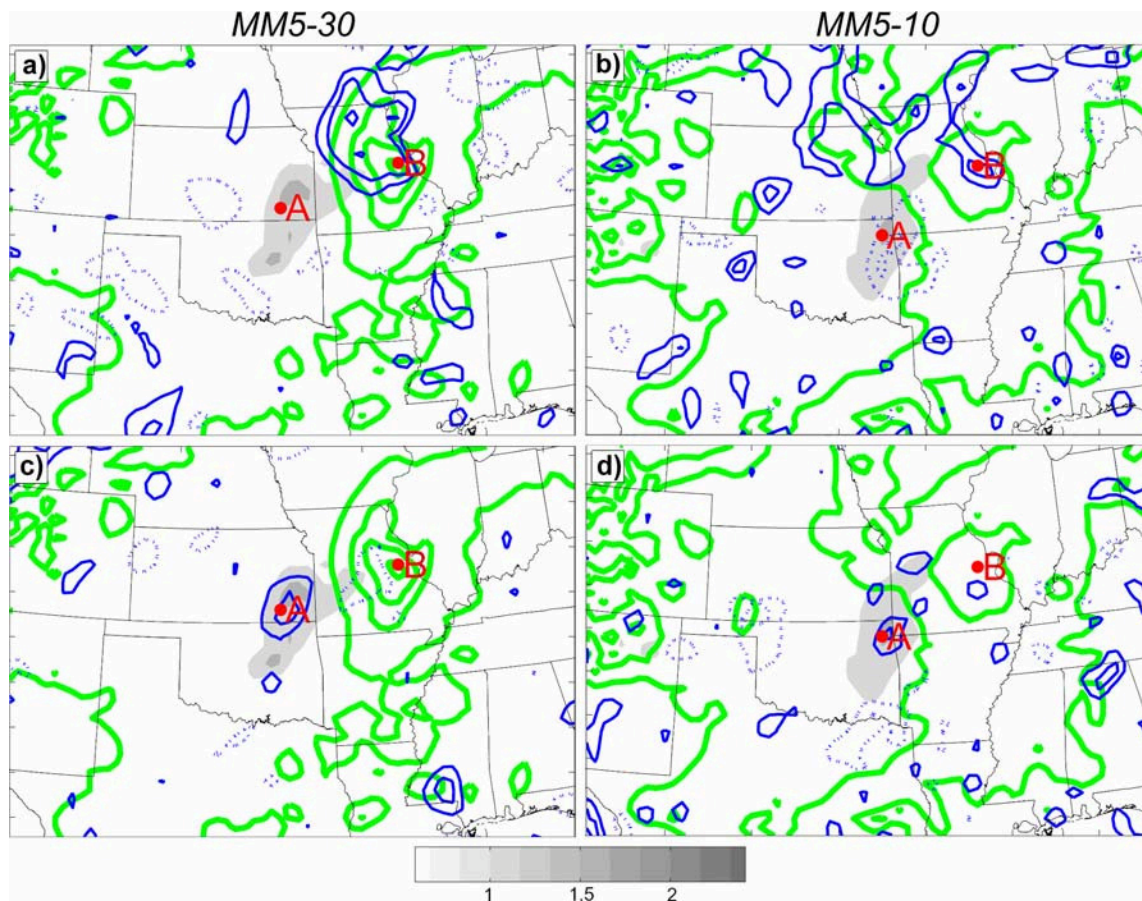
FIG. 4.45. The forecast estimated correlation between (a, b) 1200 UTC 11 June 600-hPa potential vorticity at point A and any 0000 UTC 12 June 600-hPa potential vorticity, and (c, d) 0000 UTC 12 June 600-hPa potential vorticity at point B to any 1200 UTC 11 June 600 hPa relative vorticity. Forecasts from the 30-km MM5 are shown in (a, c) and forecast from the 10-km MM5 are given in (b, d). Positive correlation values are in solid blue contours and negative in dashed contour starting at ±0.3 and with intervals of 0.2. Mean 1200 UTC potential vorticity shaded every 0.5 PVU and mean 0000 UTC potential vorticity contoured in green every 0.5 PVU.

midlevel potential vorticity forecasts, with the high-resolution MM5 being quite a bit stronger with the mean midlevel wave. Correlation structure between PV at each time shows slight differences between the 10-km and 30-km runs. Looking at the low-resolution forecast, the correlation from the lead upper wave (point A) to the midlevel vorticity at 0000 UTC is weak (Fig 4.43a). Contrastingly, the 10-km MM5 produces a more significant correlation pattern over the midlevel wave at that time (Fig. 4.43b). The reverse correlations show more significant differences, with the correlation from the maximum midlevel potential vorticity at 0000 UTC to the upper level PV at 1200 UTC being much weaker with the 30-km (Fig. 4.43c) than with the 10-km version (Fig. 4.43d).

The PV-to-PV correlation structure continues to show differences when midlevel PV at 0000 UTC 11 June is compared to midlevel PV twelve hours later in Fig. 4.44. However, in this case, it is the low-resolution MM5 that shows significant correlation structure (Figs. 4.44a and 4.44c) compared to those within the high-resolution version (Figs. 4.44b and 4.44d), despite the 36-hour forecasts of mean midlevel potential vorticity being relatively similar. Likewise, the correlations among midlevel potential vorticity at 1200 UTC to that twelve hours later (Fig. 4.45) continue to show much more significant correlation structure from the low-resolution version. It is presumed that the convective forecasts are responsible for the considerable disparity in correlation structure between the low-resolution and high-resolution MM5 models. Since the MCV is highly dependent on former convective processes, the forecasts from the low-resolution MM5 are not as reliable, since convection is only parameterized, and the low horizontal resolution can make convective impact on a single grid point too significant,

sometimes leading to serious convective feedback issues. This inadequacy in convective forecasting appears to be a significant factor in the more significant correlation patterns seen in Figs. 4.44 and 4.45, as convective feedback can greatly influence the dynamics behind correlation structure. Alternative reasoning for the stronger correlation could be the lack of convection within several MM5-30 ensemble members. For this reason, the 10-km MM5 model was employed for the statistical analysis in this study, with anticipated improved insight into correlation structure and MCV dynamics due to the explicit nature of forecast convection and higher horizontal resolution.

4.5. Summary and discussion

In this chapter, ensemble forecasting is used as a new method of investigating MCV dynamics. It is shown that slight perturbations in initial conditions will escalate into a very large ensemble spread due to the high sensitivity of an MCV to moist convective processes. Moist convection from as early as the local morning of 10 June is shown to have a significant impact on the lifecycle of the MCV through 48 hours. Through diabatically-induced PV perturbations, stronger convection in West Texas feeds onto the existing midlevel shortwave itself, and a stronger wave in turn yields stronger and more widespread convection in Oklahoma, which then feeds back onto the midlevel wave to create an MCV. It is also shown that the stronger the MCV, the more favored secondary convection will be, which in turn allows vortex penetration to the surface. The extreme sensitivity of each of these processes to preceding moist convection results

in large ensemble spread and a great deal of forecast uncertainty regarding the lifecycle of an MCV.

The discrepancy among ensemble members allows for innovative insight into MCV dynamics through the analysis of various ensemble forecasts, both in a case-by-case and statistical manner. It is concluded that convectively-driven diabatic processes are crucial in the formation of an MCV through PV generation, which not only results from latent heating in the middle troposphere but also from evaporative cooling near the surface. Furthermore, it is shown that a stronger MCV during the second diurnal cycle is associated with stronger and more widespread secondary convection. Through enhanced secondary convection, vortex penetration to the surface is shown to be strongly related to overhead convection, as a very strong correlation of over 0.8 was found between the strength of the low-level vortex and convection immediately above it among ensemble members. Because of the significance of convection both over the vortex and ahead of it, an atmosphere that is more conducive for convection will be more conducive to a long-lived MCV as well. This includes an atmosphere of higher vertical shear, which was hypothesized by Trier et al. (2000b) to favor the displacement of warm moist air ahead of an MCV up over the cold pool, creating an absolutely unstable layer near the center of the MCV. Thus, despite its potential to tilt and weaken an MCV, stronger shear ahead of an MCV is determined to associated with a stronger, longer lived vortex, possibly through enhanced convection.

CHAPTER V

CONCLUSION

This study has presented some predictability issues surrounding the evolution of the BAMEX IOP 8 MCV and provided an investigation of the dynamics surrounding this system using both high-resolution WRF deterministic forecasts and ensemble forecasting, both of which have only been recently introduced and are still subject to ongoing studies. The dynamic analysis attained through the use of these two methods through a framework provided by past studies provided excellent insight into the ability of the WRF model and ensemble forecasting to accurately predict the lifecycle of an MCV.

The BAMEX IOP 8 MCV included one of the most detailed data sets of any previous MCV system, as it not only formed in the most dense network of upper air profilers in Oklahoma, but the BAMEX campaign released numerous dropsondes into the system as it reached its mature stage. Through analysis of this data, combined with radar, satellite and surface observations, several hypotheses were formed regarding the processes important to the lifecycle of the MCV. First was that convection over New Mexico and west Texas early on 10 June may have amplified a preexisting midlevel shortwave trough, which translated to the development of the MCV later that day when convection developed within the circulation. Second was that the rotation evident in radar loops around 0600 UTC 11 June had developed around 500 to 600 hPa three hours

earlier as detected by the NOAA wind profiler network. Additionally, BAMEX dropsonde data suggests that the circulation had grown downward by 1800 UTC 11 June to near 850 hPa. This downward development of vorticity coincided with the development of widespread strong convection along the eastern periphery of the MCV circulation as well as weak convection immediately over the MCV center. A closed surface circulation appeared in surface observations around this time as well, and strengthened throughout the day before merging with a nearby front and becoming baroclinic in structure.

The forecasts of several numerical models, varying in horizontal resolution, initialization date and convective parameterization, were analyzed to evaluate ability to accurately predict the lifecycle of the BAMEX IOP 8 MCV, verified by observational data. The study found that models which employ convective parameterization are unable to reliably forecast this system due to the highly sensitive nature of the MCV to convection at all stages. Their forecasts widely range from no MCV at all when no convection is produced to an extreme deepening of the system due to severe convective feedback. Furthermore, the high horizontal resolution of the WRF-4 led to a superior forecast of the MCV at all stages from MCS initiation to the development of the surface vortex 24 hours later. This model was found to have impressive ability to predict an MCV.

Issues surrounding MCV predictability were further evaluated through ensemble forecasts. Large ensemble spread following the development of the MCV illustrated the extreme sensitivity of an MCV to convection and the significant forecast error that

results. An analysis of individual ensemble members confirmed the critical nature of convection to the development and longevity of an MCV, as members which did not forecast strong convection as early as 10 June failed to accurately predict the MCV at later times.

Statistical analyses of ensemble members supported the conclusions reached through analysis of observational data and the deterministic WRF forecasts in a statistical manner. A modest correlation was found among ensemble members between the strength of early 10 June convection over New Mexico and West Texas and the strength of the midlevel shortwave at 0000 UTC 11 June. The strength of the shortwave at this time was then found to be correlated with the strength of the MCV 12 hours later. Plots of individual ensemble data confirmed that preexisting midlevel vorticity is important in the eventual development of an MCV. Additionally, convection over the MCV was found to be critical to surface low development the following day, as a very high correlation was found among ensemble members between the strength of the surface vortex and convection immediately above it. Analysis of individual ensemble members demonstrated that mechanisms such as vorticity stretching at the edge of a surface cold pool may be a beneficial factor to surface vortex growth, but not as significant as secondary convection in the center of the vortex. The strength of the vortex at midlevels was found to be correlated with stronger convection at that time, and the maximum mean convection was found to advect cyclonically around the MCV over a six hour period. Additionally, stronger vortices were found to be favored in environments of higher environmental shear ahead of an MCV since they were more

conducive to convection. Since the ensemble forecasts showed secondary convection to be related to the longevity and strength of the MCV, weakening effects due to shearing the vortex were likely insignificant, especially since no negative correlations between MCV strength and ambient shear were found.

It is emphasized that the results presented in this study are valid for only one case. The varied nature of ways an MCV may form and evolve, as proven by past studies, illustrates the importance of examining a wide range of MCVs. The use of the high-resolution WRF and ensemble forecasting in this study proved to be of significant value in understanding the dynamics and predictability of one MCV case. Applying these methods to subsequent MCV cases will broaden the awareness of MCV dynamics and lead to a better understanding of the extent to which these systems can accurately be predicted.

REFERENCES

Anthes, R. A., 1983: Regional models of the atmosphere in middle latitudes. *Mon. Wea. Rev.*, **111,** 1306–1335.

Barker, D. M., W. Huang, Y. R. Guo, A. J. Bourgeois and Q. N. Xiao, 2004: A three-dimensional variational data assimilation system for MM5: Implementation and initial results. *Mon. Wea. Rev.,* **132,** 897–914.

Bartels, D. L., and R. A. Maddox, 1991: Midlevel cyclonic vortices generated by mesoscale convective systems. *Mon. Wea. Rev.*, **119,** 104–118.

Black, T. L., 1994: The new NMC mesoscale Eta model: Description and forecast examples. *Wea. Forecasting,* **9,** 265-278.

Bosart, L. F., and F. Sanders, 1981: The Johnstown flood of July 1977: A long-lived convective system. *J. Atmos. Sci.,* **38,** 1616–1642.

Buizza, R., and P. Chessa, 2002: Prediction of the U.S. storm of 24–26 January 2000 with the ECMWF ensemble prediction system. *Mon. Wea. Rev.,* **130,** 1531–1551.

Chen, S. S., and W. M. Frank, 1993: A numerical study of the genesis of extratropical convective mesovortices. Part I: Evolution and dynamics. *J. Atmos. Sci.,* **50,** 2401–2426.

Cohn, S. E., and D. F. Parrish, 1991: The behavior of forecast error covariances for a Kalman filter in two dimensions. *Mon. Wea. Rev.*, **119**, 1757-1785.

Cohn, S. E., 1997: An introduction to estimation theory. *J. Meteor. Soc. Jap.*, **75(1B)**, 257-288.

Daley, R., 1992: Estimating model-error covariances for applications to atmospheric data assimilation. *Mon. Wea. Rev.*, **120**, 1735-1746.

Davis, C., and L. F. Bosart, 2001: Numerical simulations of the genesis of Hurricane Diana (1984) Part I: Control simulation. *Mon. Wea. Rev.,* **129**, 1859-1881.

Davis, C., N. Atkins, D. Bartels, L. Bosart, M. Coniglio, et al., 2004: The bow echo and MCV experiment. *Bull. Amer. Meteor. Soc.,* **85,** 1075-1093.

Davis, C. A., and M. L. Weisman, 1994: Balanced dynamics of mesoscale vortices produced in simulated convective systems. *J. Atmos. Sci.,* **51,** 2005–2030.

Dudhia, J., 1993: A nonhydrostatic version of the Penn State/NCAR Mesoscale Model: Validation tests and simulation of an Atlantic cyclone and cold front. *Mon. Wea. Rev.,* **115,** 488-504.

Ertel, H., 1942: Ein Neuer hydrodynamischer Wirbelsatz. *Met. Z.,* **59,** 273-281.

Evensen, G., 1994: Sequential data assimilation with a nonlinear quasi-geostrophic model using Monte Carlo methods to forecast error statistics. *J. Geophys. Res.*, **99(C5)**, 10,143–10,162.

Fritsch, J. M., J. D. Murphy and J. S. Kain, 1994: Warm core vortex amplification over land. *J. Atmos. Sci.,* **51,** 1780–1807.

Galarneau, T. J. Jr., and L. F. Bosart, 2004: The long-lived MCV of 11-13 June 2003 during BAMEX. Preprints of the 22nd Conference on Severe Local Storms, American Meteorological Society, 4-8 October 2004, Hyannis, MA, paper 5.4.

Grell, G. A., 1993: Prognostic evaluation of assumptions used by cumulus parameterizations. *Mon. Wea. Rev.,* **121,** 1493-1513.

Gyakum, J. R., 1983: On the evolution of the *QE II* storm. II: Dynamic and thermodynamic structure. *Mon. Wea. Rev.*, **111,** 1156–1173.

Haynes, P. H., and M. E. McIntyre, 1987: On the evolution of vorticity and potential vorticity in the presence of diabatic heating and frictional or other forces. *J. Atmos. Sci.,* **44,** 828–841.

Hertenstein, R. F.A., and W. H. Schubert, 1991: Potential vorticity anomalies associated with squall lines. *Mon. Wea. Rev.*, **119,** 1663–1672.

Hirschberg, P. A., and J. M. Fritsch, 1991: Tropopause undulations and the development of extratropical cyclones. Part II: Diagnostic analysis and conceptual model. *Mon. Wea. Rev.,* **119,** 518–550.

Holton, J. R., 1972: An introduction to dynamic meteorology. International Geophysical Series, Vol. 16, Academic Press, 319 pp.

Hoskins, B. J., M. E. McIntyre and A.W. Robertson, 1985: On the use and significance of isentropic potential vorticity maps. *Quart. J. Roy. Meteor. Soc.,* **111,** 877-946.

Houze, R.A., S. Brodzik, C. Schumacher, S. E. Yuter and C. R. Williams, 2004: Uncertainties in oceanic radar rain maps at Kwajalein and implications for satellite validation. *J. App. Meteor.,* **43,** 1114–1132.

Kain, J. S., and J. M. Fritsch, 1993: Convective parameterization for mesoscale models: The Kain-Fritsch scheme. *The Representation of Cumulus Convection in Numerical Models, Meteor. Monogr.,* No. 46, K. A. Emanuel and D. J. Raymond, Eds. Amer. Meteor. Soc., 165-170.

Kirk, J. R., 2003: Comparing the dynamical development of two mesoscale convective vortices. *Mon. Wea. Rev.*, **131,** 862–890.

Lin, Y.-L, R. D. Farley, and H. D. Orville, 1983: Bulk parameterization of the snow field in a cloud model. *J. Clim. Appl. Met.,* **22,** 1065-1092.

Lorenz, E. N., 1969: The predictability of a flow which possesses many scales of motion. *Tellus,* **21,** 289–307.

Mellor, G. L., and T. Yamada, 1982: Development of a turbulence closure model for geophysical fluid problems. *Rev. Geophys. Space Phys.,* **20,** 851-875.

Michalakes, J., S. Chen, J. Dudhia, L. Hart, J. Klemp, J. Middlecoff, and W. Skamarock 2001: Development of a next generation regional Weather Research and Forecast model. Proc. of the Ninth ECMWF Workshop on the Use of High Performance Computing in Meteorology. Eds. Walter Zwieflhofer and Norbert Kreitz. World Scientific, Singapore, 269-276.

Molteni, F., R. Buizza, T. N. Palmer, and T. Petroliagis, 1996: The ECMWF ensemble prediction system. Methodology and validation. *Quart. J. Roy. Meteor. Soc.,* **122**, 73–120.

Montgomery, M. T., and J. Enagonio, 1998: Tropical cyclogenesis via convectively forced vortex rossby waves in a three-dimensional quasigeostrophic model. *J. Atmos. Sci.,* **55,** 3176–3207.

Noh, Y., W. G. Cheon, and S. Raasch, 2001: The improvement of the K-profile model for the PBL using LES. Preprints of the International Workshop of Next Feneration NWP Model, Seoul Korea, 65-66.

Olsson, P. Q., and W. R. Cotton, 1997: Balanced and unbalanced circulations in a primitive equation simulation of a midlatitude MCC. Part I: The numerical simulation. *J. Atmos. Sci.,* **54,** 457–478.

Raymond, D. J., and H. Jiang, 1990: A theory for long-lived mesoscale convective systems. *J. Atmos. Sci.,* **47,** 3067–3077.

Raymond, D.J., 1992: Nonlinear balance, and potential-vorticity thinking at large Rossby number. *Quart. J. Roy. Meteor. Soc.*, **118**, 987-1015.

Reisner, J., R. J. Rasmussen, and R. T. Bruintjes, 1998: Explicit forecasting of supercooled liquid water in winter storms using the MM5 Mesoscale Model. *Quart. J. Roy. Meteor. Soc.,* **124B,** 1071-1107.

Ritchie, E. A., and G. J. Holland, 1997: Scale interactions during the formation of typhoon Irving. *Mon. Wea. Rev.,* **125,** 1377–1396.

Rogers, R. F., and J. M. Fritsch, 2001: Surface cyclogenesis from convectively driven amplification of midlevel mesoscale convective vortices. *Mon. Wea. Rev.,* **129,** 605–637.

Rossby, C. G., 1940: Planetary flow patterns in the atmosphere. *Quart. J. R. Met. Soc.,* **66,** Suppl., 68-87.

Schubert, W. F., J. J. Hack, P. L. Dias and S. R. Fulton, 1980: Geostrophic adjustment in an axisymmetric vortex. *J. Atmos. Sci.,* **37,** 1464–1484.

Talagrand, O., 1997: Assimilation of observations, an introduction. *J. Meteor. Soc. Jap.*, **75(1B)**, 191-209.

Thorpe, A. J., 1985: Diagnosis of balanced vortex structure using potential vorticity. *J. Atmos. Sci.,* **42,** 397–406.

Toth, Z., and E. Kalnay, 1997: Ensemble forecasting at NCEP and the breeding method. *Mon. Wea. Rev.,* **126**, 3292–3302.

Tracton, M. S., 1973: The role of cumulus convection in the development of extratropical cyclones. *Mon. Wea. Rev.,* **101,** 573–593.

Tracton, M. S., E. Kalnay, 1993: Operational ensemble prediction at the National Meteorological Center: Practical aspects. *Wea. Forecasting*, **8**, 379-400.

Trier, S. B., C. A. Davis, and J. D. Tuttle, 2000a: Long-lived mesoconvective vortices and their environment. Part I: Observations from the central United States during the 1998 warm season. *Mon. Wea. Rev.,* **128,** 3376–3395.

Trier, S. B., C. A. Davis, and W. C. Skamarock, 2000b: Long-lived mesoconvective vortices and their environment. Part II: Induced thermodynamic destabilization in idealized simulations. *Mon. Wea. Rev.,* **128**, 3396–3412.

Zhang, D., and J. M. Fritsch, 1986: Numerical simulation of the meso-β scale structure and evolution of the 1977 Johnstown flood. Part I: Model description and verification. *J. Atmos. Sci.,* **43,** 1913–1944.

Zhang, D., and J. M. Fritsch, 1987: Numerical simulation of the meso-β scale structure and evolution of the 1977 Johnstown flood. Part II: Inertially stable warm-core vortex and the mesoscale convective complex. *J. Atmos. Sci.,* **44,** 2593–2612.

Zhang, D., and J. M. Fritsch, 1988: A numerical investigation of a convectively generated, inertially stable, extratropical warm-core mesovortex over land. Part I: Structure and evolution. *Mon. Wea. Rev.,* **116,** 2660–2687.

Zhang, F., 2005: Dynamics and structure of mesoscale error covariance in a winter cyclone estimated through short-range ensemble forecasts. *Mon. Wea. Rev.*, accepted.

Zhang, F., A. Odins, and J. W. Nielsen-Gammon, 2005: Mesoscale predictability of an extreme warm-season rainfall event. *Wea. Forecasting*, in review.

Zhang, F., C. Snyder, and R. Rotunno, 2002: Mesoscale predictability of the 'surprise' snowstorm of 24-25 January 2000. *Mon. Wea. Rev.*, **130,** 1617-1632.

Zhang, F., C. Snyder, and R. Rotunno, 2003: Effects of moist convection on mesoscale predictability. *J. Atmos. Sci.,* **60**, 1173–1185.

VITA

Daniel Patrick Hawblitzel was born in Kansas City, Missouri on June 20, 1980. He graduated from the University of Missouri – Columbia in May 2002 with a Bachelor of Science degree in soil and atmospheric sciences. As an undergraduate student he worked as an agricultural forecaster for the University of Missouri Extension program and served as president of the University of Missouri Chapter of the American Meteorological Society. In August 2002, he began graduate school at Texas A&M University in the Department of Atmospheric Sciences. Daniel Hawblitzel can be contacted at his permanent address at 6709 North Indiana Avenue, Kansas City, Missouri, 64119.